Large Eddy Simulation of Tidal Turbines

Pablo Ouro Barba

School of Engineering

Cardiff University, Wales, UK

Supervised by:

Prof. Thorsten Stoesser and Prof. Roger Falconer

This thesis is submitted in partial fulfilment of the requirements for the degree of

Doctor of Philosophy (Ph.D.)

2017

DECLARATION

This work has not been submitted in substance for any other degree or award at this or any other university or place of learning, nor is being submitted concurrently in candidature for any degree or other award.

Signed ..... (candidate) Date .....

STATEMENT 1

This thesis is being submitted in partial fulfilment of the requirements for the degree of PhD.

Signed ..... (candidate) Date .....

STATEMENT 2

This thesis is the result of my own independent work/investigation, except where otherwise stated, and the thesis has not been edited by a third party beyond what is permitted by Cardiff Universitys Policy on the Use of Third Party Editors by Research Degree Students. Other sources are acknowledged by explicit references. The views expressed are my own.

Signed ..... (candidate) Date .....

STATEMENT 3

I hereby give consent for my thesis, if accepted, to be available online in the Universitys Open Access repository and for inter-library loan, and for the title and summary to be made available to outside organisations.

Signed ..... (candidate) Date .....

STATEMENT 4: PREVIOUSLY APPROVED BAR ON ACCESS

I hereby give consent for my thesis, if accepted, to be available online in the University's Open Access repository and for inter-library loans **after expiry of a bar on access previously approved by the Academic Standards & Quality Committee**.

Signed ..... (candidate) Date .....

Acknowledgements

I would like to thank Professor Thorsten Stoesser for supervising my research at the School of Engineering at Cardiff University. During this time, I have largely improved my skills and expertise that surely will be very valuable in my future career as researcher. Valuable inputs from Professor Roger Falconer have been also helpful, and are here appreciated.

During these years I have shared many hours of coding and post-processing with my workmates to whom I am greatly thankful. I would like to give a special mention to those that have become close friends to me and have been a great support during these years: Bruño, Luis, Ken, Sandeep, Yan, Filipa, Nico, John, Alex, Thanasis, etc. I also thank to those involved in the IAHR Cardiff Young Professional Network as it has been a great experience for me.

The collaboration with Tidal Energy Limited became a relevant part of my research. I do appreciate all the help and support from Magnus Harrold and Peter Bromley during this time.

My two short visits at University of A Coruña with Dr. Luis Ramírez and Dr. Xesús Nogueira were very helpful for my research. I thank them for their advise and opportunity to work together, which I hope continues in the future. My former MSc thesis advisor, Dr. Luis Cea, has been a great support with his always helpful words and advice.

Thanks to all the people involved from ARCCA and HPC Wales, and specially to Thomas Green. My research would have not been possible without all the support and guidance I received since the beginning. I also thank ECCOMAS for the grant I received to assist to the European CFD conference in 2014.

Last but not least, I am very thankful to my parents Olga and Jesús, my brother Jesús, my grandparents Maximino, Olga, Jesús and Ana, the rest of my family, and to my always companion Yanina. This thesis has been a long journey and having them by my side, with their unlimited support and help, has been key to accomplish it with such success. Gracias.

Cardiff, 2017 Pablo Ouro Barba

Abstract

Understanding of hydrodynamics involved in the flow around tidal turbines is essential to enhance their performance and resilience, as they are designed to operate in harsh marine environments. During their lifespan, they are subjected to high velocities with large levels of turbulence that demand their design to be greatly optimised. Experimental tests have provided valuable information about the performance of tidal stream devices but these are often conducted in constricted flumes featuring turbulent flow conditions different to those found at deployment sites. Additionally, measuring velocities at prospective sites is costly and often difficult.

Numerical methods arise as a tool to be used complementary to the experiments in investigations of tidal stream turbines. In this thesis, a high-fidelity large-eddy simulation computational approach is adopted and includes the immersed boundary method for body representation, due to its ability to deal with complex moving geometries. The combination of these numerical methods offers a great balance between computational resources and accuracy. The approach is applied and validated with simulations of vertical and horizontal axis tidal turbines, among other challenging cases such as a pitching airfoil. An extensive validation of predicted hydrodynamics, wake developed downstream of the devices or structural loadings, outlines the accuracy of the proposed computational approach. In the simulations of vertical axis tidal turbines, the blade-vortex interaction is highlighted as the main phenomenon dominating the physics of these devices. The horizontal axis tidal turbine is simulated under different flow and turbulence intensity conditions, in both flat and irregular

channel bathymetries. This thesis seeks to assess and enhance the performance, resilience and survivability of marine hydrokinetic devices in their future deployment at sea.

Contents

Declaration iii

Acknowledgements vi

Abstract ix

Contents ix

Related Publications xv

Nomenclature xv

List of Figures xix

List of Tables xxviii

1 Introduction 1

1.1 Motivation 1

1.2 Current challenges faced by tidal turbines 7

1.3 Objectives & accomplishments 12

2 Numerical framework 16

2.1 Governing Equations 16

2.2 Fractional-step method 20

2.3 Simulation of moving bodies 22

2.4 The immersed boundary method . . . 25
2.4.1 Direct forcing immersed boundary method . . . 27
2.4.2 Application of the IB method to simulate VATTs . . . 31
2.4.3 Application of the IB method to simulate HATTs . . . 36
2.5 Summary . . . 39

3 Hybrid parallelisation of the Eulerian-Lagrangian solver 41
3.1 Introduction . . . 41
3.2 Parallelisation strategy . . . 44
3.2.1 Eulerian field parallelisation using MPI . . . 44
3.2.2 OpenMP implementation . . . 45
3.2.3 Hybrid MPI/OpenMP stategy . . . 46
3.3 Parallel performance assessment . . . 49
3.3.1 Case 1: Simulation of a Vertical Axis Tidal Turbine . . . 50
3.3.2 Case 2: Simulation of a Pitching Airfoil . . . 59
3.4 Summary . . . 62

4 Dynamic stall in pitching airfoils 65
4.1 Introduction . . . 65
4.2 Dynamic stall on Vertical Axis Turbines . . . 68
4.3 Computational setup . . . 72
4.4 Code validation . . . 75
4.4.1 Cases I.a and I.b . . . 78
4.4.2 Case II . . . 91
4.5 Summary . . . 94

5 Simulation of Vertical Axis Tidal Turbines 97
5.1 Introduction . . . 97
5.2 VATT subjected to laminar flow . . . 100
5.3 VATT subjected to turbulent flow . . . 102
5.3.1 Grid size and time step sensitivity . . . 103
5.3.2 Turbine Performance . . . 107
5.3.3 Downstream wake prediction for λ=2 . . . 111

5.3.4 Blade-vortex interaction . . . 114
5.3.5 Power spectral density . . . 120
5.4 Summary . . . 122

6 Simulation of Horizontal Axis Tidal Turbines 125
6.1 Introduction . . . 125
6.2 Experimental setup description . . . 128
6.3 Hydrodynamics validation . . . 130
6.3.1 Simulation setup . . . 130
6.3.2 Numerical parameter sensitivity and validation . . . 132
6.4 Results and Discussions . . . 133
6.4.1 Hydrodynamics during turbine operation . . . 133
6.4.2 Hydrodynamic loadings at the blade-hub juncture . . . 136
6.5 Effect of free-stream turbulence on rotor hydrodynamics . . . 139
6.5.1 Influence on the turbine hydrodynamics . . . 140
6.5.2 Effect of free-stream turbulence on hydrodynamic loadings 148
6.6 HATT over a bed of dunes . . . 149
6.6.1 Single dune precursor simulation . . . 151
6.6.2 HATT over a bed of dunes . . . 155
6.6.3 Impact of bed-induced turbulence on hydrodynamic loadings 166
6.7 Summary . . . 171

7 Conclusions and outlook 175

Appendices 181
A Synthetic Eddy Method . . . 181

References 185

The publications derived from the work undertaken in this thesis are enumerated: one book chapter, four conference papers, and several journal papers have been submitted.

Journal papers

1. **P. Ouro**, T. Stoesser. An immersed boundary-based large-eddy simulation approach to predict the performance of vertical axis tidal turbines. *Computers & Fluids*. 152: 74-87. 2017
2. **P. Ouro**, M. Harrold, T. Stoesser, P. Bromley. Hydrodynamic performance and structural assessment of a horizontal axis tidal turbine prototype. *Journal of Fluids and Structures*. 71: 78-95. 2017
3. **P. Ouro**, T. Stoesser. Effect of the Environmental Turbulence on the Performance and Survivability of tidal turbines. *Submitted to Journal of Flow, Turbulence and Combustion*.
4. **P. Ouro**, T. Stoesser, L Ramierz. Effect of blade cambering on the dynamic stall in view of designing vertical axis tidal turbines. *Submitted to ASME Journal of Fluids Engineering*.
5. **P. Ouro**, B. Fraga, T. Stoesser. Speedup of an Eulerian-Lagrangian large-eddy simulation solver by hybrid MPI/OpenMP parallelisation. *Under preparation*.
6. **P. Ouro**, L. Cea, L. Ramirez, X. Nogueira. An immersed boundary method for unstructured meshes in depth averaged shallow water models. *International Journal for Numerical Methods in Fluids*. 81: 672-688. 2016

7. L. Ramirez, X. Nogueira, **P. Ouro**, F. Navarina, S. Kheladi, I. Colominas. A higher-order finite volume method for overlapping grids. *Archives of Computational Methods in Engineering*. Accepted. 2017

Book chapters

1. **P. Ouro**, T. Stoesser, R. McSherry. Large-Eddy Simulation of a Vertical Axis Tidal Turbine using Immersed Boundary Method. *CFD for Wind and Tidal Offshore Turbines*, Springer. Chapter 5, 49–58. 2015

Conference papers

1. **P. Ouro**. Large-Eddy Simulation of Vertical Axis Tidal Turbines: study of the blockage effect. *36^{th} IAHR World Congress*. The Hague, Netherlands. 2015
2. **P. Ouro**, T. Stoesser. Large-Eddy Simulation of Tidal Turbines Using the Immersed Boundary Method. *5^{th} Oxford Tidal Energy Workshop*. Oxford, United Kingdom. 2016
3. **P. Ouro**, T. Stoesser. Wake generated downstream a vertical axis tidal turbine. *12^{th} European Wave and Tidal Energy Conference*. Cork, Ireland. 2017

Nomenclature

Abbreviations

ALE	Arbitrary Lagrangian Eulerian
CFD	Computational Fluid Dynamics
CFL	Courant-Friedrichs-Lewy condition
DNS	Direct Numerical Simulation
EL	Eulerian-Lagrangian
FSI	Fluid-Structure Interaction
HATT	Horizontal Axis Tidal Turbine
HAWT	Horizontal Axis Wind Turbine
IB	Immersed Boundary
LES	Large Eddy Simulation
LEV	Leading Edge Vortex
MDF	Multi-Direct Forcing
MPI	Message Passing Interface
OpenMP	Open Multi-Processing
PSD	Power Spectral Density
r.h.s	Right hand side
RANS	Reynolds Averaged Navier-Stokes
SEM	Synthetic Eddy Method
SGS	Sub-Grid Scale
TEV	Trailing Edge Vortex
TKE	Turbulent Kinetic Energy
VATT	Vertical Axis Tidal Turbine
VAWT	Vertical Axis Wind Turbine

Dimensionless parameters

Fr	Froude number
Ma	Mach number
Re	Reynolds number

Greek Symbols

α	Local angle of attack
β	Effective angle of attack
δ	Interpolating delta function
η	Distance between vortical structures
κ	Oscillation frequency
λ	Tip speed ratio
ν	Kinematic viscosity
Ω	Rotational velocity
ω_i	Vorticity in the i-direction
∂	Indicates partial derivation operation
ϕ	Kernel function
π	Number pi
ρ	Fluid density
σ	Turbine solidity
θ	Rotated angle
ε	Dissipation

Roman Symbols

$\tilde{p}$	Pseudo-pressure
A	Swept Area
C	Turbine's centre coordinates
C_D	Drag coefficient
C_L	Lift coefficient
C_M	Moment coefficient
C_N	Normal coefficient
C_P	Power coefficient
C_Q	Torque coefficient
C_T	Thrust coefficient
D	Drag force

F	Lagrangian force
f	Eulerian force
I	Turbulence intensity
k	Turbulent kinetic energy
L	Lift force
M_r	Torsional or pitching moment
M_θ	Bending moment
N	Normal force
P	Power
p	Pressure
Q	Tangential force or torque
T	Axial force or thrust
t	Time
U	Lagrangian marker velocity
u	Eulerian velocity
U^*	Forced Lagrangian velocity
u_*	Eulerian friction velocity
V	Volume
X	Lagrangian coordinates
x	Eulerian coordinate

Superscripts

$(\cdot)'$	Fluctuation value
$(\cdot)*$	Normalised variable
$(\cdot)^+$	Variable in wall-units
$(\cdot)^c$	Variable referred to cambered airfoil
$(\cdot)^Q$	Variable calculated based on tangential forces
$(\cdot)^s$	Variable referred to straight airfoil
$(\cdot)^T$	Variable calculated based on thrust forces
$\overline{(\cdot)}$	Time-averaged variable

Subscripts

$(\cdot)_0$	Referred to initial conditions or at the inlet
$(\cdot)_c$	Variable based on the chord length
$(\cdot)_D$	Variable based on the diameter

$(\cdot)_L$	Referred to Lagrangian marker
$(\cdot)_T$	Referred to turbine
$(\cdot)_W$	Referred to water
$(\cdot)_{ds}$	Variable referred to dynamic stall
$(\cdot)_{hub}$	Variable referred to turbine blade tip
$(\cdot)_{hub}$	Variable referred to turbine hub
$(\cdot)_{RMS}$	Root Mean Square error
$(\cdot)_{ss}$	Variable referred to static stall

List of Figures

1.1 Spring peak flow along the UK coastline. Source: RenewableUK. . 3
1.2 Locations of a) potential tidal range, tidal stream and wave energy projects along the UK coastline, and b) number of turbines used in the tidal range and tidal stream projects. Source: RenewableUK. 4
1.3 Maturity curve of the main tidal energy devices, from concept to pre-commercial prototype development. 6
1.4 Atlantis' AR1000 tidal turbine. Source: Tidalenergytoday.com. . . 8
1.5 Tocardo's tidal turbines array. Source: Tidalenergytoday.com. . . 8
1.6 DeltaStream turbine. Source: Tidalenergytoday.com. 8
1.7 VATT prototype from Han et al. [2013] tested in their stage I phase. 8
1.8 Flapping membrane developed by EEL Energy tested at IFREMER. Source: Eel-energy. 8
1.9 Tidal kite prototype developed by Minesto Ltd. Source: Minesto Limited. 8
1.10 Representation of the harsh marine conditions where tidal turbines operate in. 9
1.11 Fouling generated on the foundation of an offshore wind turbine. . 10
1.12 Verdant tidal current turbine after a structural failure in a blade. Source: Li et al. [2016b] 11

2.1 Schematic representation of the computational fluid and solid domains. 16

2.2 Energy spectrum representation distinguishing the production, inertial, and dissipation ranges. Dotted line denotes the Kolmogorov turbulence decay law. 18
2.3 Two-dimensional representation of the Cartesian staggered grid. The neighbours used in the interpolation for a Lagrangian marker (filled red circle) are the black-filled symbols found within the square boundary. **x** represents pressure nodes, □ are $x-$velocity nodes, ◯ are y-velocity nodes, and red circles are the Lagrangian markers. ΔV_L denotes the Lagrangian marker volume. 21
2.4 NACA 0012 represented using an Arbitrary Lagrangian Eulerian method. From Ramírez [2015]. 24
2.5 NACA 0012 represented using a Chimera or overset method. From Ramírez et al. [2017]. 25
2.6 NACA 0012 represented using the immersed boundary method. . 25
2.7 Kernels functions used to compute the interpolating delta functions. 29
2.8 Graphical description of the main parameters to be considered on the rotational movement of the VATT. 34
2.9 Representation of the bending (M_θ^T and M_θ^Q) and pitching (M_r) moments generated in a HATT. a) Perspective view of the turbine blades. b) Zoom-in of the blade section outlined in a) representing the calculation of the pitching moment. The hub is removed for sake of simplicity. 37

3.1 Representation of the communication between 4 sub-domains using layers of 3 ghost cells. The drawn cells correspond to the pressure mesh. 45
3.2 Schematic representation of the solving procedure in Hydro3D using 4 MPI tasks configuration. In this example, sub-domains 1 and 3 have Lagrangian particles and are provided with 3 OpenMP threads. Top left box indices indicates the MPI rank and t_i indicates the OpenMP thread number. MDF indicates Multi-Direct Forcing. 48

3.3 Schematic distribution of 38 MPI ranks among 4 SMP nodes for which 12 can demand up to 2 OpenMP threads. 50
3.4 Eulerian sub-domains distribution with indication of the LMR levels, and the VATT blades with contours of normalised time-averaged streamwise velocity. 52
3.5 Physical average runtime due to computation of convection and diffusion, Poisson pressure equation, and the IB method subroutines, and total time per time step for meshes a) M1 and b) M2. Speedup in the code performance regarding the IB method computations and total time per time step for meshes c) M1 and d) M2. 55
3.6 Comparison of the physical runtime and speedup due to computing the convection, diffusion and pressure terms, the IB method subroutine, and total time per time step due to schedule directives in OpenMP, using a) 2 threads, and b) 4 threads. 56
3.7 Comparison of the overhead on the code computations when using the multi-direct forcing scheme. 58
3.8 Comparison of the extra overhead on the code computations when using different kernel functions. 59
3.9 Distribution of the LMR levels in the mesh used for the pitching airfoil simulations. The sub-domains enclosed within the red boundaries demand multi-threading. 61
3.10 Performance of the hybrid MPI/OpenMP parallelisation on the pitching airfoil simulations achieved for the mesh P1 (left column) and P2 (right column). 62

4.1 a) Effective angle of attack, α, described by a turbine blade during the first half of the revolution for different tip speed ratios, where α_{ss} and α_{ds} denote static and dynamic stall angles respectively. b) Regions of dynamic stall experienced by a VAT blade when rotating at $\lambda = 2.0$. 70
4.2 Evolution of the reduced frequency, k^*, with the tip speed ratio, λ, considering different curvature parameters, c/R. 71

4.3 Representation of the pitching cycle described by a NACA 0012. α_{max} and α_{min} represent the maximum and minimum pitch angles. 73
4.4 Dimensions of the numerical domain used for the pitching airfoil simulations. 74
4.5 Phase averaged aerodynamic coefficients from case I.a. a) Lift and b) drag coefficients using different mesh resolutions, and c) lift and d) drag coefficients with different time step values. Comparison of the present LES with experiments (Lee and Gerontakos [2004]) and 3D DES (Wang et al. [2012]). 77
4.6 Description of the flow pattern developed for the NACA 0012 (left) and NACA 4412 (right) at different phases of the upstroke pitching motion previous to deep stall with normalised z-vorticity ($\omega_z c/U_0$) contours. 80
4.7 Description of the flow pattern developed for the NACA 0012 (left) and NACA 4412 (right) at different phases of the upstroke pitching motion during post-stall conditions with normalised z-vorticity ($\omega_z c/U_0$) contours. 82
4.8 Description of the flow pattern developed for the NACA 0012 (left) and NACA 4412 (right) at different phases of the downstroke pitching motion with normalised z-vorticity ($\omega_z c/U_0$) contours. 84
4.9 Iso-surfaces of normalised spanwise vorticity ($\omega_z c/U_0 = \pm 30$) coloured with normalised streamwise velocity (U/U_0) for the NACA 4412 at three pitch angles. 85
4.10 Iso-surfaces of normalised streamwise vorticity for the NACA 4412 at 11.54° ↑, with blue and red surfaces corresponding to $\omega_x c/U_0 =$ 8 and -8, respectively. 86
4.11 Plan-view of the turbulent structures generated during the pitching cycle of the NACA 4412 represented with iso-surfaces of Q-criterion=300 coloured with instantaneous streamwise velocities. (a) to (g) show the top-view at different pitch angles, and (h) shows the bottom-view at the minimum angle of attack of $\alpha = -5°$. 87

4.12 Comparison of the phase averaged computed C_L (a) and b)), C_D (c) and d)) and C_M (e) and f)) for the NACA 0012 and 4412 and experimental results (Lee and Gerontakos [2004]). Straight and dashed lines denote upstroke and downstroke movements respectively. 89
4.13 Comparison of the phase averaged computed lift-to-drag coefficient (C_L/C_D) for the NACA 0012 and 4412. Straight and dashed lines denote upstroke and downstroke movements respectively. 92
4.14 Contours of $\omega_z c/U_0$ describing the flow pattern experienced by the NACA 0012 during 10 phases of the pitching cycle in case II. . . . 93
4.15 Computed coefficients for the case II. Comparison of the experimental results from Lee and Su [2015] with the computed a) C_L and b) C_M. 94

5.1 Normalised velocity magnitude contours at θ = a) 0°, b) 30°, c) 60°, and d) 90° after the first VATT blade has rotated three full revolutions with the laminar flow conditions. 101
5.2 Hydrodynamic a) torque and b) normal coefficients of the VATT under a laminar flow. Comparison between the present results using different time step values, and those from body-fitted models of Ferrer and Willden [2015]; Ramírez et al. [2015]. 102
5.3 Sketch of the domain used for the LES of the VATT under turbulent flow. The sub-domain divisions is represented by straight lines. 104
5.4 Comparison of the computed power coefficient generated by one blade using the different mesh resolutions. 105
5.5 L_2 norm error analysis for the turbine under turbulent flow regarding the different values of normalised a) mesh resolution and b) time step size. 106
5.6 Mean power coefficient for the entire turbine versus tip speed ratio curve: Experimental (Roa et al. [2010]), RANS (Maître et al. [2013]; McNaughton et al. [2014]) and present LES results. 107

5.7 Coefficient of power, C_P, as a function of rotated angle, θ, of one turbine blade for λ= a) 1.5, b) 2.0 and c) 2.5, and C_P of the entire turbine for λ= d) 1.5, e) 2.0 and f) 2.5. Comparison between experiments and RANS k-ω SST (Maître et al. [2013]), RANS k-ω SST LRE (McNaughton et al. [2014]), and present LES. 109
5.8 Coefficient of lift, C_L, as a function of effective angle of attack, α, of one turbine blade for λ= a) 1.5, b) 2.0 and c) 2.5. Comparison of present LES with RANS results from Maître et al. [2013]; McNaughton et al. [2014]. 111
5.9 Contours of normalised a) streamwise velocity and b) z-vorticity at $z/c = 1$ for the turbine rotating at $\lambda = 2.0$. 112
5.10 Profiles of normalised mean streamwise velocity profiles at $x/D =$ a) 1.0, b) 1.5, c) 2.0, and d) 2.5; and normalised mean TKE at $x/D =$ e) 1.0, f) 1.5, g) 2.0, and h) 2.5 with comparison of the present LES results with RANS and experimental data from Mercier et al. [2014]. 113
5.11 Schematic of the vortex shedding sequence in the flow around a VATT rotating at $\lambda = 2.14$ described by Brochier et al. [1986]. . . 115
5.12 Blade-vortex interaction of the VATT at $\lambda = 2.0$. 117
5.13 Blade-vortex interaction of the VATT at $\lambda = 1.0$. 118
5.14 Blade-vortex interaction of the VATT at $\lambda = 3.0$. 119
5.15 Dynamic stall regions along the revolution of a VATT at tip speed ratios of a) 1.0, b) 2.0, and c) 3.0. 121
5.16 a) Time series of u- and v-velocities and their b) power spectral density at the point P located at $x/R = 0.80$, $y/R = -0.60$. Dashed line represents the -5/3 slope from Kolmogorov's law. . . 122

6.1 The 1:30-scale HATT prototype tested at Cardiff University's hydraulic flume. 129
6.2 Streamwise velocity signal obtained with ADV placed upstream the turbine for 300s. 130

6.3 a) Numerical domain with the inlet velocity profile sketched; b) Longitudinal plane along $y/D = 1.5$ (through centre of rotor) showing the mesh distribution with increased resolution around the rotor using local mesh refinement. 131
6.4 a) Instantaneous normalised torque along 3 revolutions with the turbine rotating at λ=λ_{opt} when using different meshes and time steps. b) Normalised computed power coefficient compared with the experimental results for the four different tip speed ratios analysed. 133
6.5 Visualisation of the flow structures generated by the turbine rotating at $\lambda = \lambda_{opt}$ represented by pressure iso-surfaces coloured with instantaneous non-dimensional streamwise velocity values. 134
6.6 Top view of the HATT rotating at λ=λ_{opt}. a) 3D streamlines and vertical contour plane at $z/H = 0.42$ both coloured with the non-dimensional instantaneous streamwise velocity. b) Generated flow structures downstream the turbine's rotor represented with iso-surfaces of $\lambda_2 D/U_0 = -420$ with a z-plane at $z/H = 0.50$. . . . 135
6.7 Evolution along the second and third revolutions ($360° < \theta < 1080°$) when the turbine rotates at λ=0.75, 1.00 and 1.25λ_{opt} of: the bending moment coefficients due to a) thrust ($C_{M_\theta^T}$) and b) tangential ($C_{M_\theta^Q}$) forces, and the pitching moments coefficients due to c) thrust ($C_{M_r^T}$) and d) tangential ($C_{M_r^Q}$) forces.Results for a single blade. 137
6.8 Average value and fluctuation range of the a) blade root bending moment coefficients, $C_{M_\theta^T}$ and $C_{M_\theta^Q}$, and b) the blade root torsional moment coefficients, $C_{M_r^T}$ and $C_{M_r^Q}$. 138
6.9 XY-planes at the middle of the channel ($z/H = 0.5$) representing the turbine's wake after it rotates 2240°. a) Mean and b) instantaneous non-dimensional streamwise velocity for the uniform inflow case, and c) mean and d) instantaneous non-dimensional streamwise velocity for the turbulent inflow case. 140

6.10 XZ-planes at the middle of the channel ($y/B = 0.5$) representing the turbine's wake after rotating 2240°. a) Mean and b) instantaneous normalised streamwise velocity with uniform inflow ($I = 0\%$), and c) mean and d) instantaneous non-dimensional streamwise velocity with turbulent inflow ($I = 10\%$). 142
6.11 Profiles of velocity deficit along the turbine's wake centreline. Results from the LES with turbulent and non-turbulent inflow conditions are plotted together with data from experimental (Myers et al. [2013]) and numerical studies (Blackmore et al. [2014]). . . . 143
6.12 XZ-planes at the middle of the channel ($y/B = 0.5$) representing the turbine's wake after rotating 2240°. a) Mean and b) instantaneous non-dimensional turbulent kinetic energy for the uniform inflow, and c) mean and d) instantaneous non-dimensional turbulent kinetic energy for the $I = 10\%$ case. 144
6.13 X-planes located at 0.33D, 1.0D, 2.0D and 3.5D downstream the turbine representing the non-dimensional turbulent kinetic energy contours when an inlet turbulence intensity of a) $I = 0\%$ and b) $I = 10\%$ is used. The dotted circle represents the turbine's swept area. 146
6.14 Contours of time-averaged primary Reynolds shear stresses, $u'v'/U_0^2$, at a XZ-plane at $y/B = 0.5$ when the turbine rotates 2240° for a) laminar and b) artificial turbulent inflow cases. 147
6.15 Instantaneous normalised torque value generated by the turbine blades along $180° < \theta < 1260°$ when $I = 0\%$ and $I = 10\%$ are prescribed at the inflow. 149
6.16 Distribution during $180° < \theta < 1260°$ of bending moment due to a) thrust and b) tangential forces, and pitching moments due to c) axial and d) tangential forces, when the turbine rotates at $\lambda = \lambda_{opt}$ influenced by the free-stream turbulence. 150
6.17 Bathymetry of Ramsey Sound (Wales) where the HATT is designed to be deployed. From: Evans et al. [2015]. 152
6.18 Complete domain representation of the channel with dune-bed bathymetry used for the HATT simulation. 153

6.19 Time-averaged normalised streamwise velocity contours and streamlines for the precursor dune simulation. 154
6.20 Comparison of present results (red line) with experiments (symbols) from Stoesser et al. [2008] of normalised mean: a) streamwise velocities, b) streamwise (straight line) and cross-flow (dashed line) direction velocity fluctuations, c) vertical velocity fluctuations. 156
6.21 Contours of time-averaged values of a) streamwise velocities and b) TKE, corresponding to the simulation of the HATT over a bed of dunes. 157
6.22 Centreline profile at $z = z_{hub}$ with normalised time-averaged values of a) streamwise velocity and turbulence intensity (%), and b) Reynolds stresses and turbulent kinetic energy. 159
6.23 Instantaneous flow structures generated in the first dune and which eventually interact with the tidal turbine. Iso-surfaces of pressure fluctuation are coloured with mean streamwise velocity values. . . 161
6.24 Main flow features developed from the fluid-structure interaction of the HATT and the uneven bed shape represented with contours of normalised instantaneous a) streamwise velocities, b) spanwise velocities, and c) turbulent kinetic energy. 162
6.25 X-planes located at x/D=0.5, 1.5, 3.5, and 7.5 downstream the turbine. Left column shows mean streamwise velocities, centre column time-averaged turbulent kinetic energy, and right column instantaneous turbulent kinetic energy. Dashed line depicts the turbine swept perimeter. For legend values the reader is referred to Fig. 6.21. 164
6.26 Relative pressure contours at $y/D = 0$ with $\lambda_2 D/U_0 = -200$ iso-surfaces coloured with streamwise velocity values. Points P1, P2 and P3 are used to collect velocity signals. 165
6.27 Time series of a) streamwise (red line) and vertical (black line) velocities upstream the turbine obtained at P1, b) normalised power coefficient, and c) flap-wise and d) edge-wise bending moments. . 167
6.28 Power spectral density of u- and w-velocity signals collected at P1, P2 and P3 for the HATT rotating over a bed of dunes. 170

1 Artificial turbulent velocity field using SEM. Contours of normalised a) streamwise and b) vertical velocities. 183

List of Tables

3.1 Short description of the OpenMP Schedule directives. 46

3.2 Details of the configurations used to test the hybrid parallelisation scheme in the simulation of a VATT: Eulerian cell size normalised with the chord length, number of Lagrangian markers representing the airfoil, number of MPI tasks, and which of them demand multi-threading. 51

3.3 Details of the configurations used to test the hybrid MPI/OpenMP parallelisation in the simulation of the pitching airfoil: grid resolution normalised with the chord length, total number of Eulerian cells, number of Lagrangian markers representing the airfoil, number of MPI tasks, and which of them demand multi-threading. . . 60

4.1 Description of the main parameters characterising the pitching airfoil cases and the experimental campaigns used as reference. . . . 73

4.2 Details of the normalised mesh resolutions and the number of divions along the airfoil's surface used during the sensibility study for case I.a. 75

5.1 Details of mesh resolutions tested, number of divions along the airfoil's surface, N_L, and time-avergared power coefficient generated by the 3 blades. 104

6.1 List of references of some high-fidelity numerical simulations of HATT that used the LES closure. Both body geometry description typology, number of CPUs used to run the simulations are specified, and CPU hours of the simulated cases. 127
6.2 Details of the meshes used during the spatial resolution sensibility study of the HATT simulation. 132
6.3 Value of the bending moment coefficients obtained at different turbulence intensity values with the turbine rotating at $\lambda = \lambda_{opt}$. . . 151
6.4 Average, maxima, and amplitude of the bending moments for the three blades in the simulation of a HATT over a bed of dunes. . . 168

Chapter 1

Introduction

1.1 Motivation

Constantly growing population is not just enlarging the difficulty of solving actual environmental issues but is also creating new and complicated challenges that also need to be correctly addressed. According to the International Energy Agency (IEA) the energy demand will increase 40% in 2040. This fact together with the climate change and the yet dependence on carbon based energy resources demands quick changes towards using environment friendly solutions. Motivated by this need, renewable energy sectors have remarkably developed during the last decades, and the interest in developing new alternatives from carbon-free resources is also increasing. The IEA has reported that renewable energy could become the largest source of electricity over coal, nuclear power, and natural gas within 15 years. Despite this promising scenario, the biggest questions upon renewable energy sources are their efficiency, especially for solar energy panels. Moreover, high-costs can also be a limiting factor for alternative sources of energy. Nonetheless, these technologies are advancing very quick year after year improving their cost-efficiency rate, and becoming more affordable.

At present, wind and solar energy sectors dominate the renewable energy map. Wind energy industry is well-developed and uses technologically mature turbine designs, which is the result of the research that has been undertaken since 1990s.

Solar energy avoids the environmental (visual and noise generation) impact that wind turbines have but solar cells performance is still lower than that of wind turbines. They also have a rheological behaviour that makes their efficiency to diminish year after year, with an expected lifespan of 25 years. The main weakness of wind and solar energies lies on their dependence on the weather conditions, i.e wind gusts and sunlight hours and intensity respectively, which causes intermittent energy generation.

Alternatively to this stochastic energy generation resources, marine energy is becoming a promising renewable energy source with an estimated power to be harnessed worldwide of 1TW. The areas with the largest available potential of marine energy resources are in USA, Canada, UK and France. Some studies suggested that European marine capacity is around 12.5GW, which can generate an equivalent of 48TWh per annum according to the report from Fraenkel [2002]. Recent studies, e.g. Douziech et al. [2016], support marine energy as a new green technology with similar environmental impacts, such as carbon payback time or life cost assessment, to that of offshore wind or solar photovoltaic.

There are different alternatives to extract energy from oceans such as technologies based on salinity gradient or temperature differences in the water, although most marine energy projects are designed to harness energy from tides or waves (Magagna and Uihlein [2015]). Tidal streams are generated as a result of the movement of tides, which are occurs during day and night, and can be predicted for long periods of time. Such regularity and predictability are the main incentives for pushing the development of the tidal energy industry with the long-term aim of designing more cost-effective tidal devices.

Two tidal energy technologies should be distinguished as they become the most promising in the short/medium term development of marine renewable energy: tidal stream and tidal range. The former uses turbines to extract kinetic energy from tidal currents while the latter is based on enclosing a sea region with a continuous barrage and due to water head height difference energy is generated through turbines (Angeloudis et al. [2016]). A comprehensive state-of-the-art review of tidal range technology is presented in Waters and Aggidis [2016].

Despite the rationale and their promising role behind tidal energy technologies in the future energy mix, they are in their early days as highlighted by the reduced

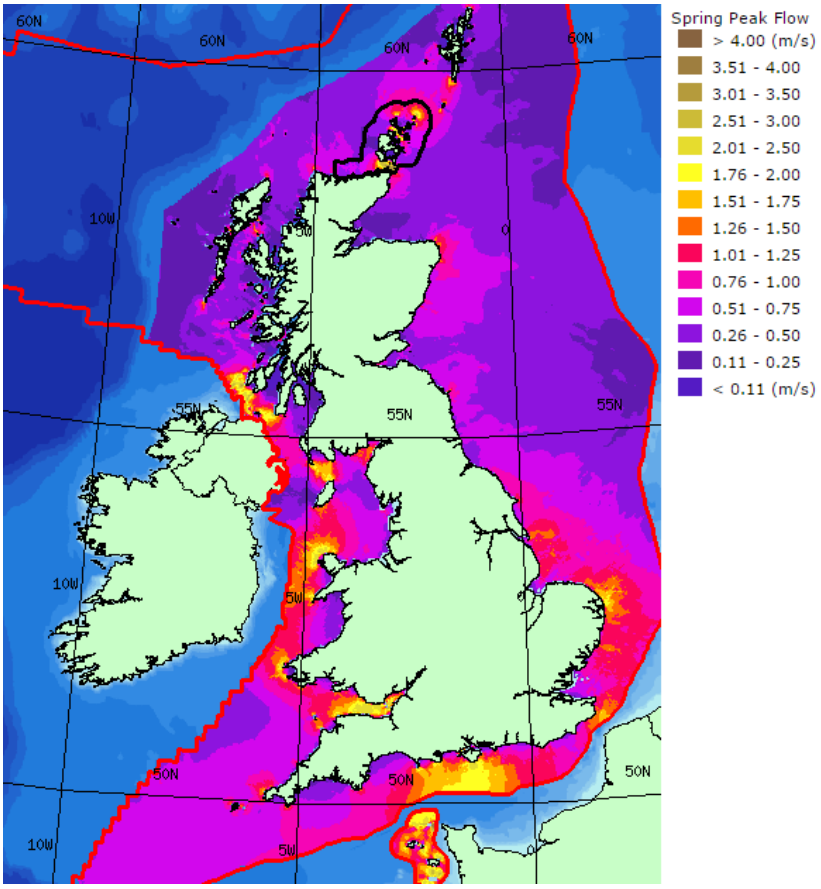

Figure 1.1: Spring peak flow along the UK coastline. Source: RenewableUK.

number of tidal-related projects that have achieved commercial stages, with most of them still at testing processes. Along the UK there is a great potential for energy extraction from tides as highlighted in Fig. 1.1 that presents the peak Spring flows along the UK coastline and highlights that flow speeds up to 3-4m/s can be achieved. It is at some of these locations where the main projects undergoing/planned in the UK are located as presented in Fig. 1.2a) based on RenewableUK data. These are located mainly along the Scottish coast, Anglesey Peninsula (Wales), off the coast of Pembrokeshire (Wales) or the Severn estuary, which has the second largest tidal range worldwide (Ahmadian and Falconer [2012]). All these projects could provide up to a 10% of UK's electricity needs and their carbon footprint and environmental risks are much lower than those associated to new nuclear plants or coal burning factories.

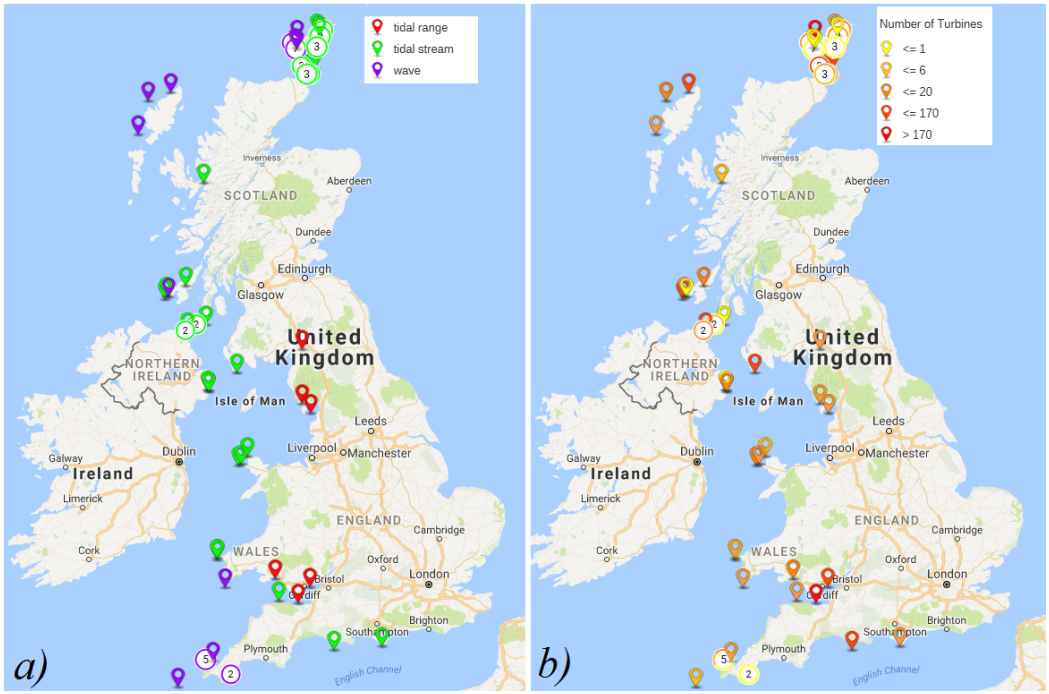

Figure 1.2: Locations of a) potential tidal range, tidal stream and wave energy projects along the UK coastline, and b) number of turbines used in the tidal range and tidal stream projects. Source: RenewableUK.

According to the European Marine Observation and Data Network (EMODnet) Human Activities team UK gathers 65% of the tidal energy projects along the European Union. Noteworthy is the wide range of technologies to be used from horizontal axis tidal turbines to tidal kites. The projects location using tidal stream turbines depicted in Fig. 1.2a) and b) agree well with the high peak flow areas in Fig. 1.1, i.e. northern Scotland and Severn estuary. Complementary confirmation to such promising scenario of UK's potential locations for marine energy is found in the UK Atlas of Offshore renewable energy (www.renewables-atlas.info/).

Tidal stream energy harnessing devices

To date, the most used devices for marine currents energy extraction purposes are tidal turbines, among which the most commonly found are Horizontal Axis Tidal Turbines (HATT) and Vertical Axis Tidal Turbines (VATT). These devices

are also known as hydrokinetic or tidal stream turbines whose driving principle is to extract kinetic energy from water velocities. Their main advantage lays in their higher efficiency when compared to other marine energy devices, such as oscillating membranes or salinity gradient technologies. This is especially noticeable for HATTs whose technology development has been benefited from the mature wind industry technology, where horizontal axis turbines dominate the market with more than 90% of the commercial prototypes (Khan et al. [2009]). This situation has benefited many HATTs prototypes, which have achieved commercial stages after undertaken the tests needed to be fully licensed to operate. On the other hand, most VATTs are still in prototype testing and design stages focused on solving issues related to their efficiency, which is lower than that of HATTs. Thus, the current VATT projects are focused on this need for improving its hydrodynamic characteristics towards feasible future commercialisation.

The foremost advantage of HATTs over VATTs is their higher efficiency derived from a more advanced technology development. Another common problem on VATT designs is their self-starting problems (Khan et al. [2009]; Worasinchai et al. [2016]). However, VATT can be considered more convenient for tidal stream environments mainly due to the following properties:

1. VATTs are omni-directional, i.e. their operation and efficiency is independent of the flow direction, whereas HATTs depend on yaw-mechanisms that can lead to mechanical problems. Hence, VATTs are ideal to work under tidal currents as stream directions vary along the tidal cycle.

2. They rotate at lower tip speed ratio than HATTs, which is believed to be more environmentally friendly as the blade passing frequency relative to the fluid velocity is lower and thus fish can travel through them more easily. Additionally, they are supposed to work better in low-to-medium tidal velocities as they need a lower cut-in velocity. Major concerns on working HATTs are fish endangerment and noise-production (Khan et al. [2009]), which have led to issues with environmental agencies as they might affect fish migration (Institute Electric Power Research [2012]).

3. VATTs make better use of shallow tidal stream flows as they maximise the use of the available cross-section, i.e. their squared-shape projected area

adapts better than the circular swept area of HATTs (Shives and Crawford [2017]). This is an important consideration when a minimum clearance between the minimum water level and top tip height is needed in order to prevent impacts with travelling vessels.

4. Their simpler design allows to locate mechanical components, e.g. generator, gearbox..., either below the rotor or above, which permits placing them on the seabed or near the surface as a floating device, respectively. This flexibility should be consider in order to evaluate the option with the lowest maintenance works as they can suppose a big economical cost Vazquez and Iglesias [2016].

Such differences on the development of HATT and VATT technologies are depicted in Fig. 1.3, which establishes a commonly acknowledged time-gap of about 20 years to VATTs behind HATTs designs. Additionally, Magagna and Uihlein [2015] reported that 76% of R&D investment is dedicated to HATTs whereas VATTs receive a rough 2% of the total, which is not optimal for VATTs in order to reduce the gap with HATTs and achieve a similar development stage.

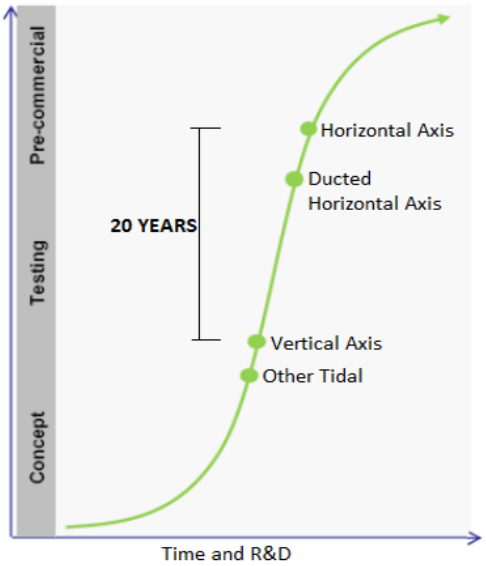

Figure 1.3: Maturity curve of the main tidal energy devices, from concept to pre-commercial prototype development.

Commercial prototypes

Some HATT devices at advanced development stages are the Atlantis' AR1000 turbine shown in Fig. 1.4 that was placed in Pentland Firth (Scotland); the array of five Tocardo tidal turbines to be placed in Eastern Scheldt (The Netherlands), Fig. 1.5; or the DeltaStream turbine from Tidal Energy Ltd. presented in Fig. 1.6 which is projected to be deployed in Ramsey Sound and St. David's Head (Wales). These turbines are at pre-commercial stages except the Atlantis' turbine which has been already installed in the first phase of the MeyGen project together with another 3 Andritz turbines. Many other devices and tidal developers can be found in Magagna and Uihlein [2015] and Khan et al. [2009]. On the other hand, the amount of pre-commercial or commercial VATTs is very scarce. Fig. 1.7 shows the prototype used by Han et al. [2013] in their Stage I testing in South Korea.

Despite turbines being the most used devices to harness tidal energy, there are more device typologies also targeted for tidal energy extraction. Some examples worth to be highlighted are the oscillating membrane developed by EEL Energy, shown in Fig. 1.8, or the kite-like design developed by Minesto Ltd. shown in Fig. 1.9. These designs feature important advantages to be considered in marine environments, such as reduced fish mortality when compared to tidal turbines. Although their performance is also expected to be lower than that of turbines, a large amount of EU funding has been assigned in 2016 to continue their development, with special interest in their future commercialisation and deployment, e.g. Minesto's kite in Anglesey (Wales).

1.2 Current challenges faced by tidal turbines

Several official organisations have reported on the promising scenario of tidal energy, such as the European Commission (see European Commision [2014a,b]) or the International Energy Agency's Ocean Energy Systems Initiative (Copping et al. [2013]). These reports agree in a common remark: tidal energy is at a critical step as many issues need to be approached and solved before deploying cost-effective commercial devices. The main concerns arise from technological issues gathering their reliability and performance as these devices work under

Figure 1.4: Atlantis' AR1000 tidal turbine. Source: Tidalenergytoday.com.

Figure 1.5: Tocardo's tidal turbines array. Source: Tidalenergytoday.com.

Figure 1.6: DeltaStream turbine. Source: Tidalenergytoday.com.

Figure 1.7: VATT prototype from Han et al. [2013] tested in their stage I phase.

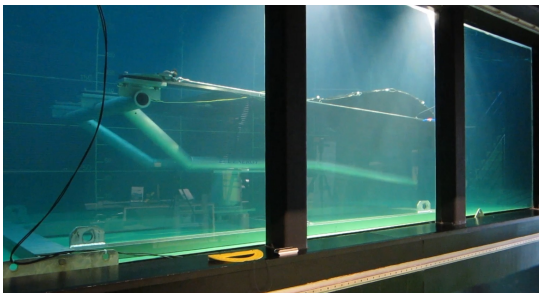

Figure 1.8: Flapping membrane developed by EEL Energy tested at IFREMER. Source: Eel-energy.

Figure 1.9: Tidal kite prototype developed by Minesto Ltd. Source: Minesto Limited.

very challenging environments, but also on their survivability under extreme conditions about which very little research has been done to date. The lack of technology readiness provokes that the levelised cost-of-energy associated to tidal

turbines (and other ocean energy devices) is yet too high, and hence its current development pace is slower than predicted.

Fig. 1.10 outlines the complex environment in which tidal turbines operate showing that these devices suffer from the action of waves, and high turbulence intensity levels induced from irregular seabed and non-uniform approaching velocity. The latter is characterised by different spatial (e.g. turbulent velocity distribution) and temporal scales (e.g. intertidal movement), which makes it difficult to reproduce accurately. In arrays of turbines, the turbine-to-turbine interaction adds even more complexity to the problem.

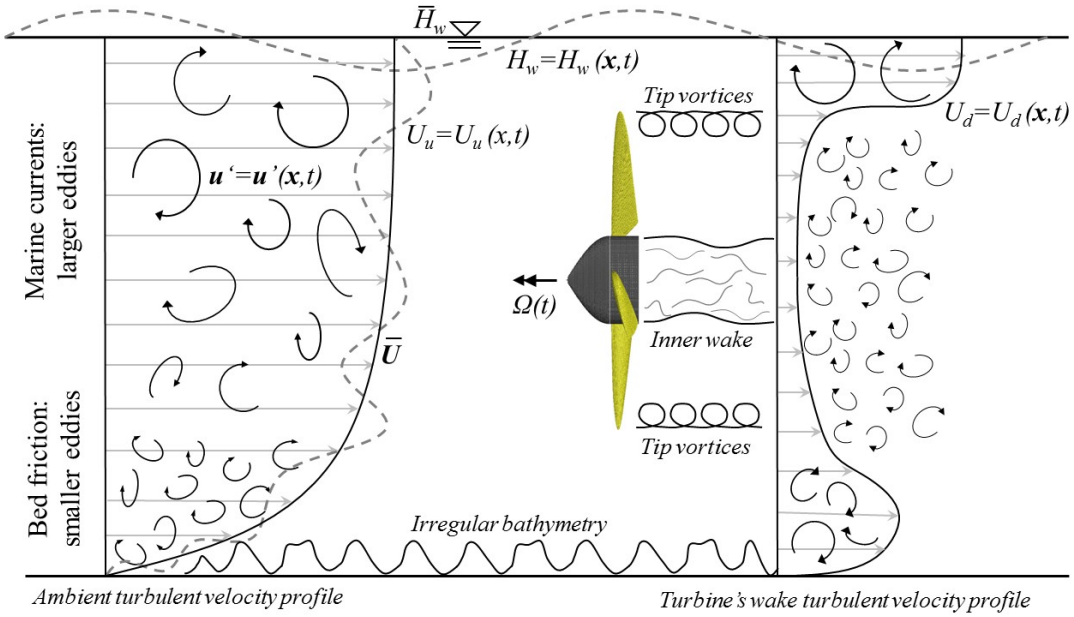

Figure 1.10: Representation of the harsh marine conditions where tidal turbines operate in.

Reliability

Tidal turbines are often designed for a lifetime of 20 to 25 years (Harper and Hallett [2015]; Parkinson and Collier [2016]). During such long periods of time, the marine environment will originate issues that demand scheduled maintenance, such as high material corrosion due to water salinity, generation of marine fouling (see Fig. 1.11) increasing mechanical losses, etc. The aforementioned factors can

require frequent cleaning and repairing processes that are very costly as they imply the use of vessels and accessing or lifting the device, among others. Thus, it is vital to minimise these inspections/reparations as much as possible in order to improve the economic viability of tidal energy devices. Chen and Lam [2015] reviewed many of these problems and presented possible solutions, e.g. using composite blades that prevent corrosion and have high structural resistance.

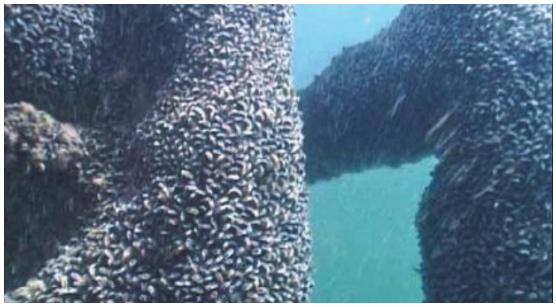

Figure 1.11: Fouling generated on the foundation of an offshore wind turbine.

Performance

The power generation capabilities of tidal turbines is an intrinsic aspect of the turbine blades design. Mechanical and electrical losses are not accounted in this thesis as these are also found in wind turbines and are unavoidable. To improve the current levelised cost-of-energy, efficient turbines have to be designed, Douziech et al. [2016]. For this purpose, experimental tests using different rotor designs are usually performed but these are specially costly. Numerical methods arise to be an affordable complimentary approach to carry out rotor performance improvements. To make these computational approaches feasible, they have to be well validated with experimental tests data. This is one of the main topics of this thesis with the validation of a numerical approach for vertical and horizontal axis tidal turbines. The numerical models can provide a larger dataset of information compared to experiments, which mean they provide important insights of the fluid flow around a turbine. Additionally, they are a valuable tool to be used towards the development of turbine arrays where experimental testing is remarkably difficult to perform. Nevertheless, the optimisation of tidal turbine

rotors has not been approached as, to the best of the author's knowledge, there is no published research on this topic although it has been widely applied for wind turbines.

Survivability

A main concern for the future development of tidal turbines is the little information available on their survivability under the harsh marine environment. Tidal turbines are meant to be placed in high-velocity range areas where there is a large amount of kinetic energy to be converted into electricity. This means that tidal turbines are meant to operate under very challenging conditions throughout their lifetime. Therefore, careful and detailed research needs to be undertaken in order to understand how tidal currents affect the turbine considering high water velocities and turbulence intensities, and how the turbine affect the surrounding water flow, e.g. in terms of wake development and velocity deficit recovery. At their deployment location, high turbulence intensities up to 20-25% could be expected (Milne et al. [2016]) together with a mix of large scale processes, e.g. tidal cycles, and localised issues, e.g. waves, recirculation areas or turbulence from the bed friction.

The illustration in Fig. 1.10 presents and summarises some of these phenomena that will affect the survivability and performance of the turbine. These challenging conditions make tidal turbines prone to failure due to extreme loads, such as the experienced by Verdant's turbine as depicted in Fig. 1.12. Thus, an accurate estimation of the loads to be supported by tidal stream turbines is required so it lasts the expected 20-25 years, and minimises maintenance operations.

1.3 Objectives & accomplishments

The main aim of this thesis is the development and application of a computational methodology to simulate the near-field hydrodynamics of tidal turbines with emphasis on their performance and survivability. The former is approached with the validation and application of the proposed high-fidelity numerical approach to both vertical and horizontal axis tidal turbines. The latter is accomplished

Figure 1.12: Verdant tidal current turbine after a structural failure in a blade. Source: Li et al. [2016b]

with the study of the effect of artificial and natural turbulent environmental flows on the structural loadings of a horizontal axis tidal turbine. The accomplishment of these objectives aim at improving the development of tidal turbines as a promising carbon free energy.

The main challenge was the refinement of the immersed boundary method in Hydro3D which lack of automatism, MPI and OpenMP parallelisation, and ability to calculate structural loadings. Adopting this IB method into a LES solver would allow to perform high-accuracy tidal turbine simulations. The complex geometries used to represent airfoils and turbines (especially the horizontal axis turbine) demanded to a front-tracking algorithm that generates the required geometry in a triangular mesh format and which could be imported into the immersed boundary method. The author invested a great amount of time during this thesis developing such an automated, numerically stable, adaptable and accurate scheme which is presented in Chapter 2. The successfully validation and application is presented in Chapters 3 to 6.

- Chapter 2: the governing equations used in the in-house code Hydro3D are presented together with the description of the fractional-step method adopted to perform large eddy simulation. A direct forcing immersed boundary adopted for the body representation method was developed into Hydro3D and refined to its application to predict the hydrodynamics of both vertical and horizontal axis tidal turbines and resulting structural loadings.

- Chapter 3: a refined hybrid parallelisation approach is implemented into Hydro3D. This scheme is mainly based on automatising the immersed boundary method and its parallelisation using MPI using a novel 'scattering-gathering-master' strategy and adding OpenMP into the MPI parallelisation scheme. The hybrid MPI/OpenMP approach aims at reducing the computational load due to the immersed boundary method computations, which could become a bottleneck during the simulations when a large amount of immersed boundary points are used.

- Chapter 4: dynamic stall is one of the most relevant phenomenon in the hydrodynamics of tidal stream turbines. The prediction of dynamic stall in moving airfoils is a challenging case which demands the computational approach to resolve well the near-wall velocities and hence serves to highlight the accuracy of the proposed approach. Its behaviour varies depending on many parameters that characterise the fluid flow regime and the turbine blades motion. In order to verify that the present computational approach is able to resolve the main characteristics of dynamic stall, three different scenarios are simulated and validated with experimental and numerical data. The effect of blade cambering is also studied by comparing the hydrodynamic coefficients and flow development around a NACA 0012 with a NACA 4412.

- Chapter 5: the computational approach is applied to the simulation of vertical axis tidal turbines. An initial validation is performed with the simulation of a three-bladed VATT under laminar flow with the aim at comparing the forces output with body-conformal methods. This case allows to quantify the accuracy of the IB method to represent moving turbine blades compared to body fitted models which are the mainly approached used by researches/industry for these applications. Thereafter, a VATT under turbulent flow is analysed, validated, and compared with experimental data and RANS results from other published works. The validation of the predicted hydrodynamics and wake downstream outlines the accuracy of the method. The remarkable blade-vortex interaction that characterise VATTs is also highlighted for different rotational speeds.

- Chapter 6: in collaboration with Tidal Energy Limited, a horizontal axis tidal turbine prototype is analysed and validated with experimental results based on power coefficient predictions. The survivability of tidal turbines is often linked to the environmental turbulence present in the oncoming flow, which causes important variations on the power output and more importantly on the structural loads. Such effect is analysed under uniform and turbulent inflows. The latter is generated using an artificial turbulent velocity field via Synthetic Eddy Method with different turbulence intensities. Additionally an exhaustive analysis of the bending and torsional moments is performed to evaluate the mean and extreme load values suffered by the turbine blades. A final case of the HATT over a bed of dunes is presented as a realistic turbulent environmental flow. The energetic flow structures generated upstream the turbine directly impact the power generation and increase the fatigue loads, which compromises the resilience of the device.

Chapter 2

Numerical framework

2.1 Governing Equations

The Navier-Stokes equations are used to resolve three-dimensional, unsteady, turbulent, incompressible fluids in a Cartesian rectangular grid. The fluid domain, Ω_f, is represented in Fig. 2.1 together with the outer boundary, $\partial\Omega_f$, and $S = \Omega_f \cap \Omega_s$ denotes the boundary between the fluid domain and the solid body (Ω_s) moving with a velocity U^*.

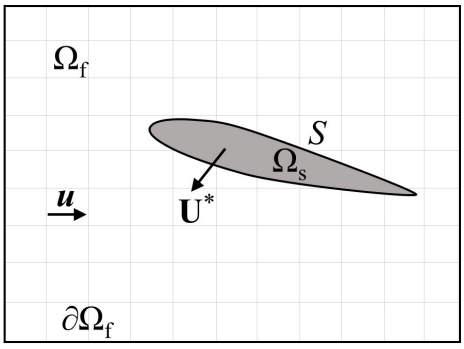

Figure 2.1: Schematic representation of the computational fluid and solid domains.

In the Large-Eddy Simulation (LES) framework, the continuity and momentum equations are spatially filtered and normalised with the Reynolds number

Re, and are presented in Eq. 2.1 and 2.2 respectively. The governing equations are solved in the whole fluid domain Ω_f.

$$\frac{\partial u_i}{\partial x_i} = 0 \tag{2.1}$$

$$\frac{\partial u_i}{\partial t} + \frac{\partial u_i u_j}{\partial x_j} = -\frac{\partial p}{\partial x_i} + \nu \frac{\partial^2 u_i}{\partial x_i \partial x_j} - \frac{\partial \tau_{ij}}{\partial x_j} + f_i \tag{2.2}$$

The variable u_i (i or j=1,2,3) denote the filtered resolved velocity components, p is the filtered resolved pressure divided by density, and ν is the kinematic viscosity of the fluid. The term f_i represents the source/sink term due to the Immersed Boundary (IB) method (Fadlun et al. [2000]; Uhlmann [2005]), which is explained in detail in Section 2.4.

The resolution of the spatial and temporal flow scales present in flows with medium-to-high Reynolds number would require extremely fine grids and small time steps, which is practically unaffordable. This approach is well-known as Direct Numerical Simulation (DNS) and is yet prohibitive for most Hydraulic and Environmental engineering applications, Stoesser [2014]. The method of LES arises as an alternative to DNS which still performs high-fidelity simulations resolving the energetic flow structures while models via spatial filtering the isotropic small scale ones, Leonard [1975]. The filtering is implicit of the adopted numerical grid in which only those scales larger than the grid size are resolved and then those smaller than the grid cell are accounted by the SGS model, Rodi et al. [2013]. This assumption filtering process is reasonable as the small scales are isotropic and thus easier to model than the large scales which are more energetic and anisotropic, Stoesser [2014]. Further reduction of the LES requirements can be achieved using, for instance, a Local Mesh Refinement (LMR) method which allows to use fine grid resolutions in the areas of interest while coarser ones in which such a resolution is not needed, Cevheri et al. [2016]. On the other hand, Reynolds Averaged Navier-Stokes (RANS) closures use time-averaging velocity fields that fail to predict accurately the flow when this is notably unsteady and dominated by a large range of turbulent flow structure. This thesis focuses on the flow around tidal turbines, which is dominated by large-scale turbulent structures, and thus RANS is not considered as it is not capable to resolve accurately

these flow phenomena.

The energy production and cascade process for the large scales would be identical for LES and DNS, whilst differences are observed on the spectral distribution of energy in the vicinity of the cut-off wave number, at which the SGS model induces a much faster energy dissipation. In general, the finer the grid, the smaller is the portion of the spectrum that requires modelling, so the capabilities of the SGS model become particularly relevant when the LES is performed in coarse grids. Fig. 2.2 presents the typical energy spectrum with the three distinguished regions: I denotes the energy production range, II is the inertial subrange that follows the Kolmogorov decay law with -5/3 slope, and III is the energy dissipation sub-range. In a well-resolved LES, the cut-off separating the resolved and modelled length scales is usually found in the inertial subrange prior to the dissipation range, as depicted from Fig. 2.2. Hence, the most important interaction to be accomplished by the SGS model is that between the large-scale energy-containing unresolved scales and the smallest resolved scales.

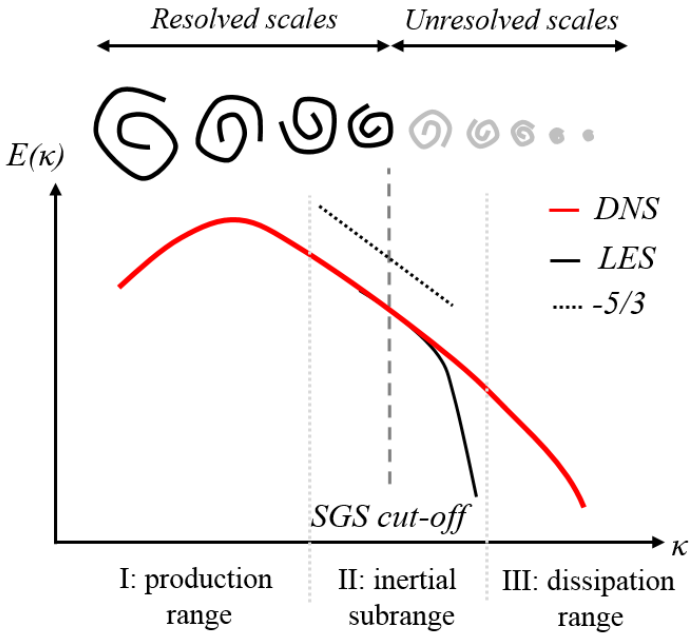

Figure 2.2: Energy spectrum representation distinguishing the production, inertial, and dissipation ranges. Dotted line denotes the Kolmogorov turbulence decay law.

An important requirement of a SGS model is to provide physically correct dissipation which is the only way turbulent kinetic energy is removed from the resolved scales, Davidson [2015]. A too large dissipation would artificially increase the diffusive fluxes leading to excessive damping of the resolved scales, whereas a too small SGS-model dissipation would result in a pile up of energy around the cut-off wavenumber.

In this thesis, the Smagorinsky (Smagorinsky [1963]) and Wall-Adapting Local Eddy viscosity (WALE) (Nicoud and Ducros [1999]) SGS models are adopted. The unresolved velocity fluctuations are accounted using a subgrid stress tensor, τ_{ij}, included in the momentum equation (Eq. 2.2), and reads

$$\tau_{ij} = \tau_{ij}^{a} + \frac{1}{3}\tau_{kk}\delta_{ij} \tag{2.3}$$

Here, the former term corresponds to the anisotropic component, and the latter to the isotropic components, where δ_{ij} is the Kronecker delta. In the standard Smagorinsky SGS model, the eddy or turbulent viscosity, ν_t, is approximated as,

$$\nu_t = (C_s\Delta)^2 \cdot |S_{ij}| \qquad \text{, where } |S_{ij}| = \sqrt{2S_{ij}S_{ij}} \tag{2.4}$$

$$S_{ij} = \frac{1}{2}\left(\frac{\partial u_i}{\partial x_j} + \frac{\partial u_j}{\partial x_i}\right) \tag{2.5}$$

Here C_s is the Smagorinsky constant set to 0.1 (Rodi et al. [2013]), $\Delta = (\Delta x \Delta y \Delta z)^{1/3}$ is the filter size equal to the mesh cell size, and S_{ij} is the resolved rate of strain from the filtered resolved velocities. This artificial viscosity is then used to calculate the anisotropic subgrid stress tensor, as

$$\tau_{ij}^{a} = -2\nu_t \overline{S}_{ij} \tag{2.6}$$

Regarding the sensibility to the SGS model on the wake produced downstream a HATT, Sarlak et al. [2015] investigated six different variations of the standard and dynamic Smagorinsky SGS models. Their results shown negligible influence of the different SGS models variations in the power output, although quite small variations were found on the wake velocity. TKE profiles and 3D flow visualisa-

tions showed that the less dissipative the SGS model, the quicker the breakdown of the large flow structures. Additionally, the evaluation of the ν_t/ν ratio can be used to assess how much the SGS model contributes to the total dissipation, and thus to discuss the resolution between well-resolved LES and DNS, Davidson [2009].

The WALE model, introduced by Nicoud and Ducros [1999], has gained popularity as is can account for wall effects without employing wall-damping functions which makes it a suitable to the simulation of immersed bodies in which the fluid mesh is not conformed to their geometry (Cevheri et al. [2016]). One of the main advantages of the model is that it predicts correctly the behaviour of the eddy viscosity near solid surfaces. The turbulent viscosity is calculated from the resolved velocity-gradients tensor $g_{ij} = \partial u_i/\partial x_j$, as follows:

$$\nu_t = (C_w \Delta)^2 \frac{(S^d_{ij} S^d_{ij})^{3/2}}{(\overline{S}_{ij}\overline{S}_{ij})^{5/2} + (S^d_{ij} S^d_{ij})^{5/4}} \tag{2.7}$$

where S^d_{ij} is the traceless symmetric part of the square of the velocity gradient tensor (g_{ij}) presented in Eq. 2.8, S_{ij} is the resolved rate of strain from Eq. 2.5 calculated from the filtered resolved fluid velocities, and C_w is the constant of the WALE model assumed to be 0.46 as considered in Cevheri et al. [2016]).

$$S^d_{ij} = \frac{1}{2}(\overline{g}^2_{ij} + \overline{g}^2_{ij}) - \frac{1}{3}\delta_{ij}\overline{g}^2_{kk} \tag{2.8}$$

2.2 Fractional-step method

The spatially filtered Navier-Stokes equations in the LES framework presented in Eq. 2.1 and 2.2 are advanced in time using the so-called fractional-step method based on the projection method developed by Chorin [1968]. The main advantage of this method is that the velocity and pressure computations are decoupled. In the present framework, the fluid is solved in a Cartesian rectangular grid with staggered storage of the velocities using central fourth-order finite-differences approximations. In a staggered grid, velocity vectors are stored at the middle of the cell faces while the pressure is stored in the cell centre. Hence, four different

grids are used to compute u, v, w and p. Fig. 2.3 exhibits a two-dimensional representation of a staggered grid with uniform grid spacing and Lagrangian markers used in the immersed boundary method.

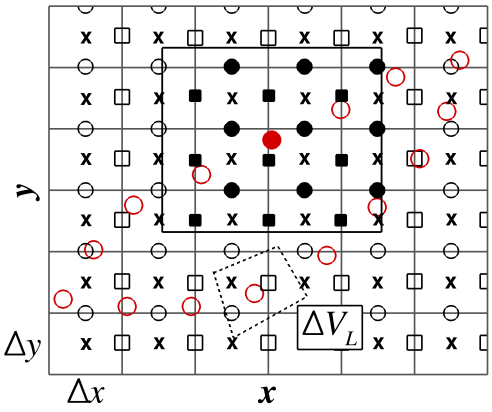

Figure 2.3: Two-dimensional representation of the Cartesian staggered grid. The neighbours used in the interpolation for a Lagrangian marker (filled red circle) are the black-filled symbols found within the square boundary. **x** represents pressure nodes, □ are $x-$velocity nodes, ◯ are y-velocity nodes, and red circles are the Lagrangian markers. ΔV_L denotes the Lagrangian marker volume.

The fractional-step method uses the Helmholtz decomposition to obtain the velocity field from a solenoidal and an irrotational vector fields through several computational steps. The first is to predict a non-solenoidal or non-divergence free velocity, $\tilde{\mathbf{u}}$, from the explicit computation of the convection and diffusion terms, and the pressure term with the values from the previous time step. The velocity $\tilde{\mathbf{u}}$ at the time step t is calculated using a low-storage three-steps Runge-Kutta scheme to compute the convective and diffusive terms (Cevheri et al. [2016]), as

$$\frac{\tilde{\mathbf{u}} - \mathbf{u}^{l-1}}{\Delta t} = \nu\alpha_l \nabla^2 \mathbf{u}^{l-1} - \alpha_l \nabla p^{l-1} - \alpha_l[(\mathbf{u}\cdot\nabla)\mathbf{u}]^{l-1} - \beta_l[(\mathbf{u}\cdot\nabla)\mathbf{u}]^{l-2} \quad (2.9)$$

where l (=1,2,3) is the Runge-Kutta sub-step for which l=1 denotes values from the previous time step $t-1$, and α_l and β_l stand as the Runge-Kutta coefficients with values: α_1=β_1=1/3, α_2=β_2=1/6, and α_3=β_3= 1/2.

An additional correction to $\tilde{\mathbf{u}}$ is required due to the presence of external forces,

e.g. forces from Lagrangian bodies, in order to obtain the updated intermediate velocity $\tilde{\mathbf{u}}^*$. The immersed boundary method is extensively used throughout this publication, and its effect on the velocity field is achieved through the forcing term $\boldsymbol{f}$ on the r.h.s of Eq. 2.2. Thus, the corrected predicted velocity field, $\tilde{\mathbf{u}}^*$, is updated as

$$\tilde{\mathbf{u}}^* = \tilde{\mathbf{u}} + \boldsymbol{f}\Delta t \tag{2.10}$$

This intermediate velocity does not accomplish the solenoidal or divergence-free condition. Thus, a projection scalar function $\tilde{p}$, often referred to as pseudo-pressure that has no physical meaning, is calculated via the incompressibility condition so the predicted intermediate velocity field fulfils the divergence-free condition. The pseudo-pressure field is obtained in Eq. 2.11 from the resolution of the Poisson equation accomplished using an iterative multi-grid technique.

$$\nabla^2\tilde{p} = \frac{\nabla \cdot \tilde{\mathbf{u}}^*}{\Delta t} \tag{2.11}$$

The predicted velocity field is then projected onto the divergence-free field using the pseudo-pressure gradient correction to obtain the velocity field at the actual time step $\mathbf{u}^t$, as

$$\mathbf{u}^t = \tilde{\mathbf{u}}^* - \Delta t\nabla\tilde{p} \tag{2.12}$$

Finally, the value of the pressure field at the current time step, p^t, results from the value at the previous time step, p^{t-1}, and the pseudo-pressure field, as

$$p^t = p^{t-1} + \tilde{p} - \frac{\nu\Delta t}{2}\nabla^2\tilde{p} \tag{2.13}$$

2.3 Simulation of moving bodies

The simulation of moving solid bodies is a common problematic found in a wide range of applications, such as in biological flows simulating flying insects or hu-

man heart valves (de Tullio and Pascazio [2016]; Sotiropoulos and Yang [2014]), or in engineering problems such as tidal stream turbines. This flow simulations of moving boundaries supposes a big computational challenge demanding the mesh to be somehow adapted to the analysed geometry along with its movement. Mesh-adaptation procedures used in body-fitted mesh typologies are not exempt of complexity, and often demand techniques that are very computationally demanding. These disadvantages restrict the adaptability of the numerical models to many applications adding an extra computational effort to the already large cost of performing LES or DNS. The techniques more commonly used in this area are the Arbitrary Lagrangian Eulerian (ALE) approaches, Chimera or overset methods, and Eulerian-Lagrangian methods, e.g. the immersed boundary method. Fig. 2.4 to 2.6 shows how the meshes are conformed for the simulation of the flow around a NACA 0012 using the different approaches, which are briefly described in the following.

ALE methods are the most commonly used both in Academia and industry. As shown in Fig. 2.4, the fluid mesh is built as a continuum domain featuring an internal solid boundary that conforms the analysed bodies (Ramírez [2015]; Sarrate et al. [2001]). This computational domain can be partitioned into multiple blocks to increase the simulation speed. In those cases when dynamic bodies are simulated, the boundary representing the obstacle describes an imposed movement (Ramírez et al. [2015]) or moves as a consequence from the fluid action (Han et al. [2015]). The main advantage is the imposition of the boundary conditions along the body surface using boundary layer cells. On the contrary, problems arise when large deformations are experienced, and they are also computationally expensive as a result of the obligatory re-meshing at each step and consequent variable re-allocation. Novel methodologies have been developed to model specific problems such as sliding mesh or rotating domains where part of the mesh is steady while another, where the body is embedded, is dynamic (Ferrer and Willden [2015]; McNaughton et al. [2014]). Nevertheless, additional complexity is added as the communication between meshes is also challenging in order to maintain the high-order of the approach, Ramírez et al. [2015]. Some examples of ALE techniques applied to tidal stream turbines are the works of Afgan et al. [2013]; McNaughton et al. [2014].

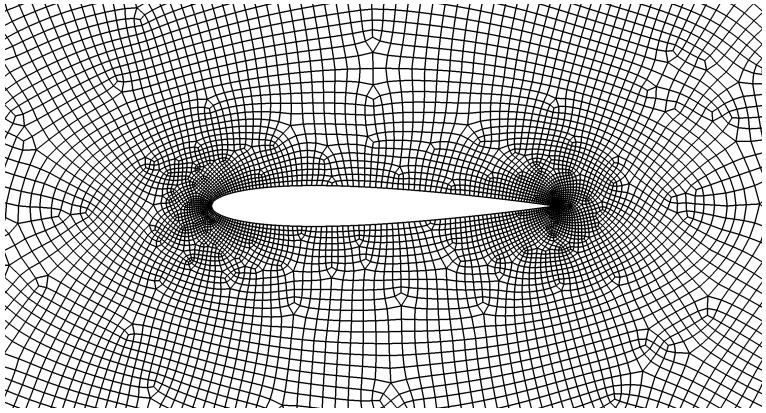

Figure 2.4: NACA 0012 represented using an Arbitrary Lagrangian Eulerian method. From Ramírez [2015].

Chimera methods were firstly introduced by Steger et al. [1982]. These methodologies are often referred to as overset or overlapping meshes, and are commonly based on a set of two or more meshes: fixed mesh that remains unchanged along the simulation and moving mesh(es) that usually represents the body-fitted geometry (Galbraith et al. [2014]; Nakata and Liu [2012]). Fig. 2.5 depicts the two grid typologies used in the simulation of a NACA 0012, Ramírez et al. [2017]. In Chimera methods the fluid flow is resolved through a series of steps. Firstly, the fluid is calculated at the fixed mesh. Then, via interpolation functions (e.g. using Moving Least Squares approximations) the variables from the fixed mesh are interpolated to the moving domain. In the latter the governing equations are also solved so the fluid is adapted to the influence of the embedded geometry. The obvious advantage of these overset approaches compared to ALE methods is the absence of re-meshing procedures, accurate reproduction of the boundary conditions at the solid interface, and provision of an easy mechanism to deal with the relative motions in dynamic bodies simulations. As a drawback, overlapping methods require the resolution of the Navier-Stokes equations in the different reference frames corresponding to each of meshes used, and which are often of different topologies, e.g. a fixed Cartesian rectangular mesh and a moving unstructured mesh (see Fig. 2.5). An example of application to wind turbines is the work of Li et al. [2012].

On the contrary to the previous methods, in the framework of Eulerian-

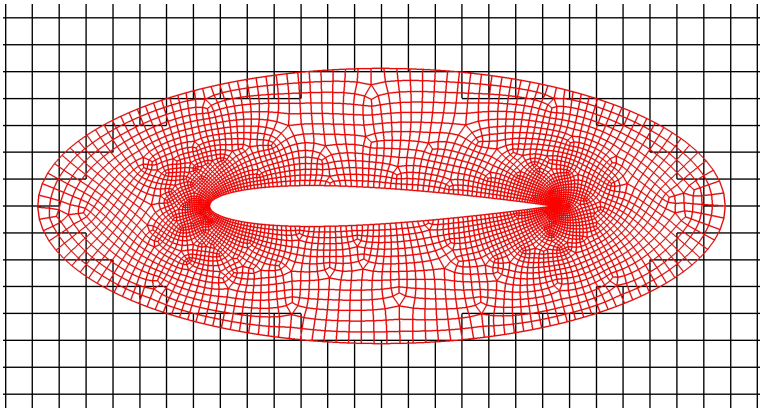

Figure 2.5: NACA 0012 represented using a Chimera or overset method. From Ramírez et al. [2017].

Lagrangian (EL) approaches the use of Immersed Boundary (IB) methods is becoming more frequent with an extended range of applications. In these methods, the mesh where the fluid is solved is fixed and is not conformed to the body geometry. The representation of the solid boundary is accomplished with a solid mesh using either a continuum or discrete approaches, as later explained in Section 2.4, and which is decoupled from the fixed fluid mesh framework. The main advantages of the IB methods are their easier implementation compared to ALE and Chimera approaches, and great ability to deal with complex geometries, movements and deformations. However, the lack of body conformal meshes provokes that the boundary conditions along the solid interface are not accurately fulfilled, and it can also present spurious force oscillations and pressure fluctuations, Cristallo and Verzicco [2006]; Lee et al. [2011]. Nonetheless, their moderate demanded computational cost makes them an affordable choice to simulate moving geometries at medium Reynolds numbers using a feasible amount of computational resources to perform LES or DNS within a reasonable time frame.

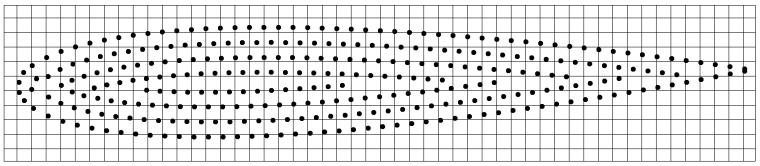

Figure 2.6: NACA 0012 represented using the immersed boundary method.

2.4 The immersed boundary method

The immersed boundary method was originally developed by Peskin [1972] with the aim at developing a methodology for the simulation of heart valves. His accomplishment was achieved thanks to the previous advancements of Chorin [1968] developing the projection method, which is the base of the widely used fractional-step method. Peskin developed a non-body conformal methodology that constituted a computationally cheap while accurate approach to biomechanical flows, especially in the cardiac flows area. Nevertheless, it was not until 1990s, when the popularity of the IB method increased notably and the research community explored new improvements onto the method so as to enlarge its range of applications and accuracy, e.g. Saiki and Biringen [1996]. The fact that the IB method has the capacity to be combined with structured meshes (usually rectangular Cartesian meshes) is a remarkable advantage as it allows the use of efficient flow solvers, such as fast Poisson equation solvers, Sotiropoulos and Yang [2014]. The reduction in computational cost of using the IB method compared to body-fitted models was already highlighted by Fadlun et al. [2000].

Mainly two IB method varieties can be distinguished regarding the body representation. These are the continuum and discrete approaches. The continuum models use the geometrical description of a continuous surface to project the velocities over the normal vector to the body surface. It usually involves the categorisation of the Eulerian cells into solid, fluid or intermediate, i.e. influenced by the IB, using techniques as ray-tracing. Examples of this methodology can be found in Iaccarino [2004]; Kim et al. [2001], and Kang et al. [2012] with the simulation of a HATT.

The discrete models are those where the body is built as a set of individual Lagrangian points that conform its shape, as depicted from Fig. 2.6. Generally, the boundary velocity is set onto the Eulerian grid via a two-way interpolation procedure. Uhlmann [2005] developed the direct forcing (DF) method using a discrete description based on the previous work from Fadlun et al. [2000]. Uhlmann [2005] used delta functions previously employed by Peskin [2002] and Roma et al. [1999] to exchange information between the fluid and solid frameworks, which provided a smoother force output than previous discrete methods. Further refinements

came from the work of Wang et al. [2008a] who outlines that Uhlmann's direct forcing is unable to completely satisfy the no-slip condition at the boundary as some residual velocities remain within the solid region. Hence, they introduced the Multi-Direct Forcing (MDF) method that consists on an iterative solution of the DF equations in a multi-correction fashion. On the other hand, Yang et al. [2009] developed an alternative formulation of the delta functions that smooth the force oscillations. Vanella and Balaras [2009] adopted Moving-Least Squares (MLS) approximations to build the interpolation functions, whose main advantage is that MLS guarantees the partition of unity whereas when using delta functions this is only satisfied if the discrete Lagrangian grid resolution is that of the Eulerian mesh, Uhlmann [2005]. Ouro et al. [2016] introduced the DF-MLS methodology for the application of the IB method to unstructured meshes. Pinelli et al. [2010] performed a similar work on the adaptation of the Reproducing Kernel Particle Method (RKPM), which yields on the same basis than MLS, and also provided an accurate reconstruction of interpolation functions.

In the current thesis, a refined version of the DF-IB method from Uhlmann [2005] is used and described in Section 2.4.1, due to its ability to deal with moving geometries, feasible computational effort, adaptability to complex geometries such as hydrofoils or horizontal axis tidal turbine designs, and good numerical stability.

Fluid-structure interaction advancements

The cited works on improving the IB method have notably benefited the research community enlarging the areas of application. The fact that the equations governing the solid body are treated separately to the fluid equations eases the implementation of Fluid-Structure Interaction (FSI) algorithms. Uhlmann [2005] applied the DF to particle laden flows prescribing a rigid behaviour of these. Additional degrees of freedom have been added to the methodology with the studies of Deen et al. [2009] where deformable bubbles were simulated, Le et al. [2009] with the simulation of deformable red-blood cells, Yang and Stern [2012] presented a wide range of FSI application of rigid bodies, Tian et al. [2014] who did a special stress on the application of the IB method to biological flows, and Favier et al. [2016]; Pinelli et al. [2017] focused on flexible filaments for aeronautic

and hydraulic engineering applications. Sotiropoulos and Yang [2014] reviewed the state-of-the-art of the IB method for FSI applications and showed a wide range of problems addressed by their research group. These are some examples of the past and current research undertaken using the IB method, and this thesis focuses on widening this range of applicability. Note that the present FSI simulation stand only as the interaction between the solid structure and the fluid flow without a one-way or two-way coupling between the structural and fluid solvers.

2.4.1 Direct forcing immersed boundary method

In the direct forcing immersed boundary method the solid geometry is discretised into a finite amount of Lagrangian markers or points, which is often denoted as Lagrangian grid. This set of points is physically decoupled from the fluid mesh as the latter is not conformed to the geometry of the solid. Instead, the Lagrangian markers are embedded within the fluid mesh as previously shown in Fig. 2.3, and through the direct forcing equations the solid points and fluid cells are communicated. Using this set of equations (explained below) each Lagrangian marker enforces a desired velocity onto the surrounding fluid cells through a forcing term, $\boldsymbol{f}$, added in the r.h.s of Eq. 2.2, which eventually gives the method its name. From hereinafter, letter case denote Eulerian variable whilst upper case are referred to Lagrangian variables.

The direct forcing method follows a multi-step predictor-corrector procedure, which is adapted as follows: First, the predicted Eulerian velocities ($\tilde{\mathbf{u}}$) are calculated from Eq. 2.9. These are interpolated to the Lagrangian grid using an interpolation function, which in the present publication is a delta function (δ), for the transfer of information to each Lagrangian marker L from its closest n_e number of Eulerian neighbours, so as to obtain the interpolated Lagrangian velocity $\mathbf{U}_L$ as,

$$\mathbf{U}_L = \sum_{ijk=1}^{n_e} \tilde{\mathbf{u}}_{ijk} \cdot \delta(\mathbf{x}_{ijk} - \mathbf{X}_L) \cdot \Delta\mathbf{x}_{ijk} \tag{2.14}$$

where $\mathbf{x}_{ijk}$ is the vector of coordinates of the Eulerian mesh cell ijk, $\mathbf{X}_L$ $(=(X_L,Y_L,Z_L)^T)$

is the location of the Lagrangian marker L, and $\Delta\mathbf{x}_{ijk}{=}\Delta x{\cdot}\Delta y{\cdot}\Delta z$ is the Eulerian cell volume.

The interpolating delta function is calculated in Eq. 2.15 from the multiplication of three one-dimensional kernels, ϕ. The accuracy of this interpolating procedure lies on that of the kernel. Many authors proposed different version of this function, such as Peskin [2002], Roma et al. [1999]. Nevertheless, these functions can produce considerable spurious force oscillations, Lee et al. [2011]. With the purpose of reducing these oscillations, Yang et al. [2009] performed the smoothing of the kernel functions from the former references, and achieved a remarkable reduction on the force oscillations. Fig. 2.7 shows the shape of the kernel ϕ_3, ϕ_3^* and ϕ_4^* from Yang et al. [2009] that feature a different distribution of the interpolation values.

$$\delta(\mathbf{x}_{ijk}-\mathbf{X}_L)=\frac{1}{\Delta\mathbf{x}_{ijk}}\phi\left(\frac{x_{ijk}-X_L}{\Delta x}\right)\phi\left(\frac{y_{ijk}-Y_L}{\Delta y}\right)\phi\left(\frac{z_{ijk}-Z_L}{\Delta z}\right) \quad (2.15)$$

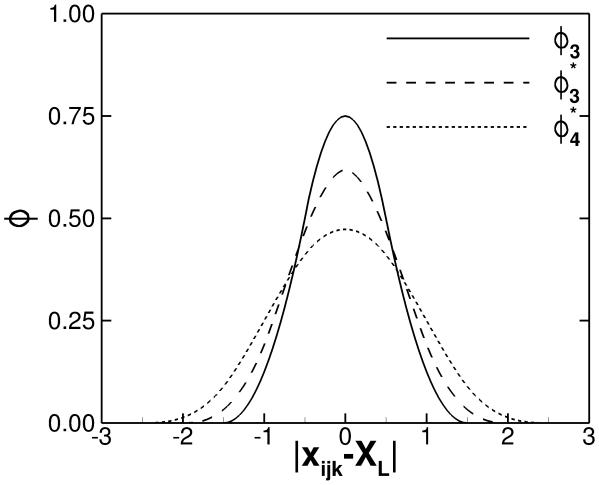

Figure 2.7: Kernels functions used to compute the interpolating delta functions.

These kernels are tested for the laminar VATT presented in Section 5 and it was found that ϕ_3 experienced the largest oscillations on the force outputs while ϕ_3^* and ϕ_4^* obtained similar values. However, as ϕ_4^* has a larger stencil (kernel width) gathering 128 neighbours, it requires a higher computational effort during

the neighbour searching than ϕ_3^*, which uses 64 neighbours. Hence, ϕ_3^* is chosen for the simulations of this publication as it offers the best compromise between accuracy and computational effort.

The second step of the direct forcing method is to compute the force $\mathbf{F}_L$ that each Lagrangian marker needs to exert onto the fluid in order to satisfy the no-slip condition at the marker's position. This force term is calculated as the difference between the desired (or forced) velocity at the marker, $\mathbf{U}_L^*$, and the velocity $\mathbf{U}_L$ previously interpolated from the fluid mesh in Eq. 2.14, as

$$\mathbf{F}_L = \frac{\mathbf{U}_L^* - \mathbf{U}_L}{\Delta t} \tag{2.16}$$

The computation of the forced boundary velocity is performed depending on whether the solid body is moving, and considering this motion is prescribed or calculated from a FSI algorithm. When the body is static, then $\mathbf{U}_L^* = 0$. In case the body is moving as a reaction from the action of the fluid, then a FSI algorithm is needed to compute the enforced velocity (Yang and Stern [2013]; Yang et al. [2015]). The latest scenario considers that the solid body is moving at a prescribed velocity and pattern, which permits the analytical calculation of its coordinates at any time during the simulation. Hence, for the latter case, the forced Lagrangian velocity, $\mathbf{U}_L^*$, is easily computed as,

$$\mathbf{U}_\mathbf{L}^* = (U_L^*, V_L^*, W_L^*)^T = \frac{\partial \mathbf{X}_L}{\partial t} = \left(\frac{\partial X_L}{\partial t}, \frac{\partial Y_L}{\partial t}, \frac{\partial Z_L}{\partial t} \right)^T \tag{2.17}$$

The third step constitutes the backwards procedure where the Lagrangian force is transferred back to the Eulerian mesh cells in order to obtain the Eulerian force $\boldsymbol{f}$. This reverse interpolation of $\mathbf{F}_L$ from the closest n_L Lagrangian markers to each Eulerian cell, for which the same delta function values from the forwards interpolation in Eq. 2.14 are used, is performed as,

$$\boldsymbol{f}(\mathbf{x}_{ijk}) = \sum_{L=1}^{n_L} \mathbf{F}_L \cdot \delta(\mathbf{X}_L - \mathbf{x}_{ijk}) \cdot \Delta V_L \tag{2.18}$$

Note that during the forwards interpolation (from Eulerian to Lagrangian) the fluid cell volume $\Delta\mathbf{x}_{ijk}$ is used, while the backwards process (Eq. 2.18) uses the volume assigned to each of the Lagrangian markers ΔV_L. According to Uhlmann [2005], the direct forcing method requires that the force transferred to the fluid has to be the same than the one transferred to the solid. The equilibrium condition to be fulfilled is presented in Eq. 2.19, where N_e is referred to all Eulerian cells that suffer from the IB method correction. Hence, the Lagrangian volume ΔV_L is approximately equal to Δx_{ijk}. This is an important remark to be considered during the generation of complex geometries.

$$\sum_{ijk=1}^{N_e} \boldsymbol{f}(\mathbf{x}_{ijk}) \cdot \Delta x_{ijk} = \sum_{L=1}^{N_L} \mathbf{F}_L \cdot \Delta V_L \tag{2.19}$$

In the final corrector step, the predicted Eulerian velocity, $\tilde{\mathbf{u}}$, is updated in Eq. 2.10 in order to calculate the predicted Eulerian velocity after the IB method correction, $\tilde{\mathbf{u}}^*$.

2.4.2 Application of the IB method to simulate VATTs

For the application of the IB method to vertical axis tidal turbines, the turbine blade geometry is generated by a discrete mesh. This is accomplished using a Delaunay triangulation algorithm featuring a resolution similar to the Eulerian fluid mesh, as requisition in the direct forcing method equilibrium condition from Eq. 2.19. A front-tracking algorithm (El-Hamalawi [2004]) generates the desired hydrofoil shape as an unstructured mesh and also provides geometrical properties such as area or centre of gravity. The nodes of the generated unstructured grid are adopted as the Lagrangian markers to represent the turbine's geometry. The rotation of the turbine's blades is prescribed at a constant rotational velocity, Ω, describing a circular movement about the turbine's central shaft whose location $\mathbf{C}_x$ is denoted as,

$$\mathbf{C}_\mathbf{x} = (C_x, C_y, C_z)^T \tag{2.20}$$

For the time advancement of the blades fixed time step values are employed. This avoids triggering spurious force oscillations when using variable time step, as Lee et al. [2011]; Shin et al. [2008] reported. The turbine rotates counter-clockwise about the z-axis as depicted in Fig. 2.8, and for the calculation of velocities and coordinates the rotation matrix $\mathbb{R}$ is employed, and reads:

$$\mathbb{R}(\theta_L) = \begin{pmatrix} cos(\theta_L) & sin(\theta_L) & 0 \\ -sin(\theta_L) & cos(\theta_L) & 0 \\ 0 & 0 & 1 \end{pmatrix} \tag{2.21}$$

The initial position of the turbine is at $\theta_L = 0°$. Local Cartesian coordinates ($\mathbf{X}_{L_0}$), initial rotated angle (θ_{L_0}), and radius (R_L) of each Lagrangian marker comprising the turbine blades are calculated at the beginning of the simulations as:

$$\mathbf{X}_{L_0} = (X_{L_0}, Y_{L_0}, Z_{L_0})^T \tag{2.22}$$

$$R_0 = \sqrt{(X_{L_0})^2 + (Y_{L_0})^2} \tag{2.23}$$

$$\theta_{L_0} = \text{atan}(X_{L_0}/Y_{L_0}) \tag{2.24}$$

The rotated angle at the time t is $\theta_L = \theta_L(t) = \theta_{0_L} + \Omega t$, for which Ω stands as the rotational velocity of the turbine. Hence, the position of the Lagrangian markers ($\mathbf{X}_L$) at a given time step is determined as:

$$\mathbf{X}_L^T = \mathbf{C_x}^T + \mathbb{R}(\theta_L) \cdot \mathbf{X}_{L_0}^T \tag{2.25}$$

Taking into consideration that the VATT movement is prescribed, its circular movement can be described more easily using polar coordinates. The actual Lagrangian coordinates can be calculated directly from Eq. 2.26 at any time t.

The forced Lagrangian velocity is calculated applying Eq. 2.17.

$$\mathbf{X}_L = \begin{pmatrix} X_L \\ Y_L \\ Z_L \end{pmatrix} = \begin{pmatrix} C_x \\ C_y \\ C_z \end{pmatrix} + \begin{pmatrix} -R_L \cdot sin(\theta_L) \\ R_L \cdot cos(\theta_L) \\ Z_{L_0} \end{pmatrix} \tag{2.26}$$

$$\mathbf{U}^*_\mathbf{L} = \begin{pmatrix} U^*_L \\ V^*_L \\ W^*_L \end{pmatrix} = \begin{pmatrix} -R_L \cdot \Omega \cdot cos(\theta_L) \\ -R_L \cdot \Omega \cdot sin(\theta_L) \\ 0 \end{pmatrix} \tag{2.27}$$

Fig. 2.8 sketches the blades of the VATT together with the two coordinate systems used: (X,Y,Z) and (R, θ) for the Cartesian and polar references respectively. This figure depicts all relevant geometrical variables, acting fluid forces (lift, L, and drag, D), and normal n and tangential t vectors to the blade movement, which are used to determine the normal force, N, and torque, Q, respectively.

Forces distribution

The solid reaction force ($\mathbf{F} = (F_x, F_y, F_z)^T$) acting on each blade is determined as the sum of the forces calculated in Eq. 2.16 from all markers comprising each blade as:

$$\mathbf{F} = \int_{blade} \rho \mathbf{F}_L dV_L \tag{2.28}$$

where ρ stands for the fluid density. The x-component of $\mathbf{F}$ is also referred as thrust force, T. The turbine blades are considered infinitely long, i.e. assuming two-dimensionality of the system, and hence forces in the vertical are deemed irrelevant. The local angle of attack (α) is determined as the angle derived from the unperturbed incident velocity and the rotational speed of the blade regardless its geometry along its whole rotation as in McLaren [2011], and presented in

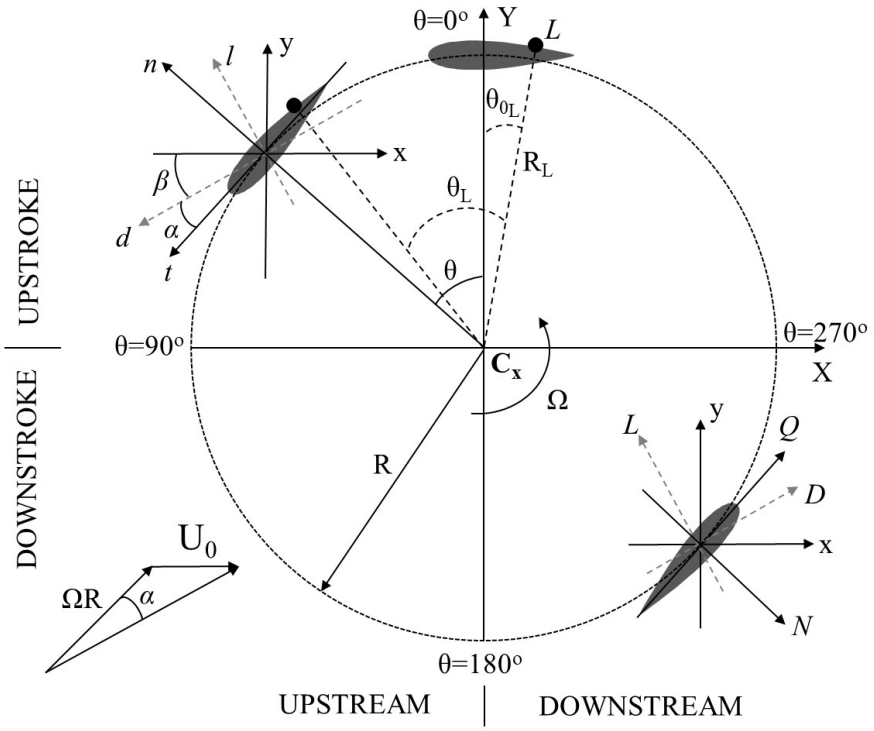

Figure 2.8: Graphical description of the main parameters to be considered on the rotational movement of the VATT.

Eq. 2.29, together with the effective angle of attack β described by the blade.

$$\alpha = \text{atan}\left(\frac{-\sin(\theta)}{\lambda + \cos(\theta)}\right); \qquad \beta = \theta - \alpha \tag{2.29}$$

where λ is known as the tip speed ratio, and is defined as:

$$\lambda = \frac{\Omega R}{U_0} \tag{2.30}$$

This parameter indicates the relation between the tangential or tip speed, ΩR, in comparison to the free-stream velocity, U_0.

Drag and lift forces on the blades are calculated using the x- and y- compo-

nents of **F** projected onto the reference frame (d, l) using the angle β as follows:

$$\begin{pmatrix} D \\ L \end{pmatrix} = \begin{pmatrix} cos(\beta) & sin(\beta) \\ -sin(\beta) & cos(\beta) \end{pmatrix} \begin{pmatrix} F_x \\ F_y \end{pmatrix} \tag{2.31}$$

Following the same notation than Maître et al. [2013]; McNaughton et al. [2014], the drag (C_D) and lift (C_L) coefficients are normalised by the tangential rotational velocity, ΩR, and read:

$$C_L = \frac{L}{1/2\rho(\Omega R)^2 cH} \tag{2.32}$$

$$C_D = \frac{D}{1/2\rho(\Omega R)^2 cH} \tag{2.33}$$

where c stands for the blade chord length and H is the spanwise length of the blades.

The torque and normal forces are obtained by projecting lift and drag forces over the local angle of attack α, representing the effective parallel and perpendicular position of the blade according to the effective local velocity. Eq. 2.34 shows how the torque and normal forces are calculated and their coefficients are normalised by the free-stream velocity (U_0) instead of the tip speed previously used for C_L and C_D.

$$\begin{pmatrix} Q \\ N \end{pmatrix} = \begin{pmatrix} cos(\alpha) & sin(\alpha) \\ -sin(\alpha) & cos(\alpha) \end{pmatrix} \begin{pmatrix} D \\ L \end{pmatrix} \begin{pmatrix} R & 1 \end{pmatrix} \tag{2.34}$$

$$C_Q = \frac{Q}{1/2\rho U_0^2 AR} \tag{2.35}$$

$$C_N = \frac{N}{1/2\rho U_0^2 A} \tag{2.36}$$

where $A = 2RH$ is the turbine's projected area. Finally, the performance of the turbine is often represented by to the power coefficient, C_P. This is calculated as the ratio between the power available in the water, P_W, and the power generated

by the total number of blades (N_b) comprising the turbine, P_T, as,

$$C_P = \frac{P_T}{P_W} = \frac{N_b \cdot \Omega \cdot Q}{1/2\rho U_0^3 A} \tag{2.37}$$

2.4.3 Application of the IB method to simulate HATTs

The simulation of HATTs using the IB method is similar to its application to VATT although the rotation axis is different, and the geometry is purely three-dimensional. The HATT geometry is also generated by a discrete mesh using a Delaunay triangulation. The turbine rotates counter-clockwise with a prescribed constant rotational velocity around the centre $\mathbf{C}_x$, as indicated in Fig. 2.9a. The initial variables that need to be calculated are the local Cartesian coordinates ($\mathbf{X}_{L_0}$) of the markers, and initial described angle and radius which are calculated differently to the VATT, and read:

$$R_0 = \sqrt{(Y_{L_0})^2 + (Z_{L_0})^2} \tag{2.38}$$

$$\theta_{L_0} = \text{atan}(Y_{L_0}/Z_{L_0}) \tag{2.39}$$

The rotated angle of each marker moving at time t is $\theta_L = \theta_L(t) = \theta_{0_L} + \Omega t$, and thus its position is calculated as,

$$\mathbf{X}_L = \begin{pmatrix} X_L \\ Y_L \\ Z_L \end{pmatrix} = \begin{pmatrix} C_x \\ C_y \\ C_z \end{pmatrix} + \begin{pmatrix} X_{L_0} \\ R_L \cdot \sin(\theta_L) \\ R_L \cdot \cos(\theta_L) \end{pmatrix} \tag{2.40}$$

The torque generated by the turbine is computed in Eq. 2.41 using the y- and z-force components. Finally, the power coefficient of a HATT is calculated as in Eq. 2.37 with $A = \pi R^2$ denoting the turbine swept area.

$$Q = \sum_{L=1}^{N_L} (F_{y_L} \cdot cos(\theta_L) + F_{z_L} \cdot sin(\theta_L)) \cdot R_L \tag{2.41}$$

Calculation of hydrodynamic loadings on the HATT blades

In addition to evaluate of the hydrodynamic performance of an operating HATT, its structural analysis is performed using the IB method forces. This highlights the potential of the approach to analyse fluid-structure interaction problems, Yang and Stern [2012]. The aim is to quantify the major loadings at the blade-hub junction as this connection is one of the section supporting large stresses, and with the goal to avoid structural failure of the turbine. In the present methodology, the structural loads are directly computed by integration of the IB nodal forces (Eq. 2.28). Note that the blades are deemed non-deformable, so the normal forces are not considered for the structural analysis, and nor is gravity included.

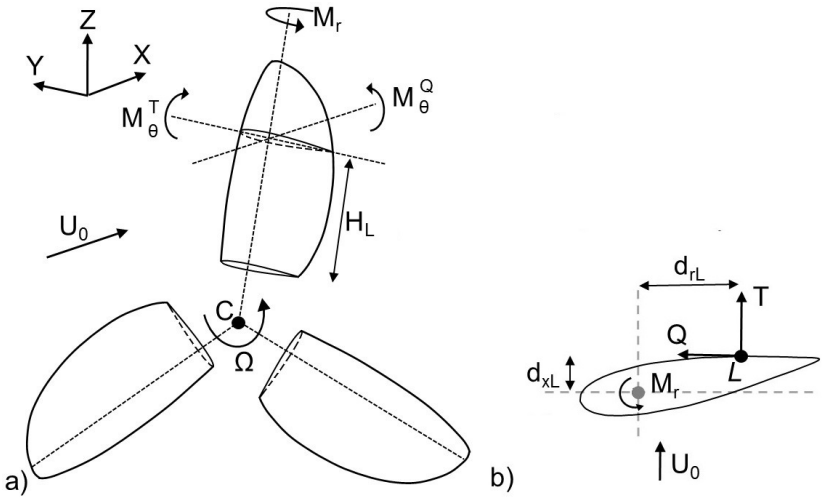

Figure 2.9: Representation of the bending (M_θ^T and M_θ^Q) and pitching (M_r) moments generated in a HATT. a) Perspective view of the turbine blades. b) Zoom-in of the blade section outlined in a) representing the calculation of the pitching moment. The hub is removed for sake of simplicity.

The bending moments produced by thrust and tangential forces of the Lagrangian markers comprising each blade, are denoted as M_θ^T (called flap-wise moment) and M_θ^Q (denoted edge-wise moment), and calculated in Eq. 2.42 and 2.43 respectively. The lever arm, H_L, is the radial distance between the marker L and

the blade-hub junction, and is depicted in Fig. 2.9a).

$$M_\theta^T = \sum_{L=1}^{N_L} T_L \cdot H_L \tag{2.42}$$

$$M_\theta^Q = \sum_{L=1}^{N_L} Q_L \cdot H_L \tag{2.43}$$

Similar calculations are done for the contributions of thrust and tangential forces to the torsional or pitching moment, denoted as M_r^T and M_r^Q and determined using Eq. 2.44 and 2.45. The lever arms are d_{x_L} and d_{r_L} for the thrust and tangential forces respectively, which are calculated as the distance between gravity centre of each blade section and the Lagrangian marker, as Fig. 2.9b) shows.

$$M_r^T = \sum_{L=1}^{N_L} T_L \cdot d_{r_L} \tag{2.44}$$

$$M_r^Q = \sum_{L=1}^{N_L} Q_L \cdot d_{x_L} \tag{2.45}$$

The normalisation of the structural moments from the thrust ($C_{M_\theta^T}$ and $C_{M_r^T}$) and tangential force components ($C_{M_\theta^Q}$ and $C_{M_r^Q}$), is as follows:

$$C_{M_\theta^T} = \frac{{M_\theta}^T}{1/2\rho U_0^2 AR} \tag{2.46}$$

$$C_{M_\theta^Q} = \frac{{M_\theta}^Q}{1/2\rho U_0^2 AR} \tag{2.47}$$

$$C_{M_r^T} = \frac{{M_r}^T}{1/2\rho U_0^2 AR} \tag{2.48}$$

$$C_{M_r^Q} = \frac{{M_r}^Q}{1/2\rho U_0^2 AR} \tag{2.49}$$

2.5 Summary

The numerical framework used to resolve the governing equations in the in-house code Hydro3D has been presented. A brief introduction to the most common approaches to simulate moving bodies has been described. The time advancement using the fractional-step method has been explained. A refined direct forcing immersed boundary method has been implemented into the large eddy simulation based solver, which provides Hydro3D the adaptability to simulate complex geometries. Its application to both vertical and horizontal axis tidal turbines, as well as other bluff bodies such as airfoils, has been explained in detail. The decoupling between fluid and solid frameworks allow to perform the structural of the stresses at the blade-hub junction for the horizontal axis tidal turbine. This calculation has been explained and is later on used to determined maximum stresses and equivalent loads for fatigue loading cycles.

Chapter 3

Hybrid parallelisation of the Eulerian-Lagrangian solver

3.1 Introduction

Constantly increasing computational resources have aided/accelerated the development of sophisticated CFD codes (Sotiropoulos [2015]). Currently it is possible to solve accurately and time-dependently turbulent flows at low to moderately high Reynolds numbers in complex geometries (Stoesser [2014]). Nonetheless, there is still a number of flow predictions limited by computer hardware, for instance: flows featuring a very wide range of temporal and spatial scales, which require excessively fine numerical grids and small time steps; flows including rapidly moving boundaries in the context of fluid-structure interaction, e.g. tidal turbines; or multiphase flows transporting enormous amounts of small particulates (Fraga and Stoesser [2016]; Fraga et al. [2016]). Overcoming these limitations is key to the advancement of CFD. Nowadays, most CFD codes are sped-up by parallelisation allowing an efficient usage of modern computer hardware. The three main parallelisation strategies most commonly used in CFD codes (Afzal et al. [2016]) are: distributed memory (through Message Passing Interface, MPI), shared memory (through OpenMP) or a combination of both. Alternatively, graphics card based GPUs can be employed (Buck et al. [2004]; Ji et al. [2015];

Tutkun and Edis [2017]) but this is not subject of the present research.

MPI is the most commonly used protocol of distributed memory computation. It is used for the communication of the sub-domains into which the computational domain is divided (Wang et al. [2008b]), and each one solves the same code, i.e. on basis of the Single Program Multiple Data (SPMD) paradigm. The key to this strategy is the communication between sub-domains: the exchange of information across sub-domain interfaces must ensure the coherence of the simulation as a whole, Cevheri et al. [2016]. This pure MPI parallelisation offers a tremendous performance increase, but its implementation is not straightforward and implies substantial changes to a non-paralellised code, which can result in considerable decrease of code efficiency if the amount of information exchanged between processors is large, Jin et al. [2011]. Nevertheless, MPI appears to be an ideal solution for distributed memory systems, such as high-performance computers (HPC), notwithstanding that MPI works well on shared memory machines, such as desktop computers and workstations.

OpenMP operates with shared memory on single computer nodes such as desktops, workstations, or nodes-of-a-cluster. Its implementation does not require substantial changes into the code at hand, which results in faster implementation and easier portability. On the other hand, parallelisation efficiency could be lower than that of MPI, and the feasible maximum problem size of the simulation is constrained by the hardware available on the computing node. The limited parallelisation efficiency is due to the presence of a non-parallelised part of the code among the sequential code. The schedule directives in OpenMP help to achieve a better load balancing within the parallelised sections (Rabenseifner et al. [2009]).

The mixed use of MPI and OpenMP in a hybrid parallelisation strategy can lead to an important increase in the code performance as demonstrated in the following works. Chorley and Walker [2010] tested a hybrid MPI/OpenMP version of the molecular dynamics application DL_POLY3.0. The hybrid version outperformed the pure MPI scheme when large number of cores were used, whilst the latter achieved a better performance when using a small number of cores due to communication overheads between the OpenMP threads. Mininni et al. [2011] tested a mixed scheme in a pseudospectral code in two clusters, and achieved

different performance outputs on each one. Their results showed that the code's speedup using the hybrid scheme is augmented when the number of cores is large compared to that of the pure MPI. Yakubov et al. [2013] implemented a similar strategy to an Euler-Lagrange framework to simulate the flow around an airfoil where bubbles were injected into cavitation regions. Despite a good code performance was proved, no sensibility study was performed regarding the inclusion of OpenMP threads. Shi et al. [2015] performed a detailed study on how distributing differently MPI tasks and OpenMP threads could provide a disparity in the code performance results in application to Taylor-Couette flows. In the application to the finite element model Fluidity, Guo et al. [2015] achieved an improved performance using a hybrid scheme compared to pure MPI, which was basically attributed to enhancing communication procedures. Noteworthy is that the development of hybrid MPI/OpenMP parallelisation strategies is of interest to many research areas, which share the same need for improving the performance of a code followed by the increasing availability of computational resources. However, the development of mixed strategies can bring load-balancing or communication issues which makes their implementation almost case dependent.

Aim of the chapter

The implementation of a hybrid MPI/OpenMP parallelisation strategy into Hydro3D is presented. The computation of the Lagrangian part regarding the IB method greatly challenges the computer hardware, which serves as motivation to add a fine-grained parallelisation via OpenMP into the coarse-grained MPI parallelisation of Hydro3D. Whilst distributed memory is very efficient for the computation of the Eulerian flow field, the clustered distribution of Lagrangian points can compromise the load balance of the calculations when they are concentrated in specific areas of the fluid domain. The proposed mixed approach attempts to increase the performance of Hydro3D by combining the advantages of both MPI and OpenMP.

The hybrid MPI/OpenMP parallelisation strategy is presented in Section 3.2. Details on the separate MPI and OpenMP implementations are described in Section 3.2.1 and 3.2.2, whereas Section 3.2.3 focuses on the development of the

hybrid scheme. The performance of the mixed scheme in Hydro3D is discussed in 3.3 with application to the simulations of the flow around a vertical axis tidal turbine and a pitching airfoil. Special emphasis is put on the synchronisation between threads and processors within the hybrid parallelisation loops using different OpenMP schedule directives.

3.2 Parallelisation strategy

The parallel execution of the code Hydro3D is accomplished using MPI, which features a Local Mesh Refinement (LMR) methodology that permits to refine certain sub-domains achieving the required resolutions at certain areas. The implementation of the LMR method is presented by Cevheri et al. [2016] who highlighted the notable reduction in the number of processors required when using LMR instead of using uniform meshes while maintaining the same resolution at the relevant areas of the fluid domain, e.g. near the walls. Taking advantage of LMR, Hydro3D can perform expensive LES with a feasible amount of computational resources. The hybrid MPI/OpenMP scheme implementation is detailed before analysing its efficiency in the selected problems where the scheme targets at enhancing the speedup compared to that of a pure MPI configuration.

All simulations of this publication are carried out on HPC WALES' supercomputer which hosts 128 SMP (Symmetric Multi-Processing) nodes. Each computer has 2 sockets, containing an Intel Xeon E5-2670 (Sandy Bridge) 2.60 GHz processor with 8 cores per socket. This gives 16 cores per node and 64GB (DDR3-1600Mhz ECC SDR) RAM per node. Nodes are interconnected with an Infiniband (Connect2-X) 4x QDR/PCIe gen2 16x network infrastructure (40Gbps HS/LL QDR, 1.2μsec latency). The compilation of the code is accomplished using the version 15.0 and 5.1 of the Intel and MPI compilers, respectively.

3.2.1 Eulerian field parallelisation using MPI

The concept of MPI-based LES computations is to divide the computational domain of the Eulerian field into sub-domains or blocks, and parallel execute them using multiple processing units by means of the SPMD. These blocks are assigned

to different ranks and message-passing communication is accomplished via MPI. The blocks overlap at their boundaries by one or several layers of Eulerian nodes (ghost cells or halos) through which information is exchanged. Fig. 3.1 depicts four sub-domains with three layers of ghost cells. Each sub-domain overlaps with its immediate neighbours and the information stored in the ghost cells is exchanged when needed, guaranteeing a continuous Eulerian field across block interfaces. This is a standard procedure on the parallelisation of block-structured grids (Gropp et al. [1994]; Walker [1992]) and increases the calculation speed of the solution of the Poisson equation when using a multigrid solver (Versteeg and Malalasekera [2007]) because a big matrix solution problem is broken down into many small sub-problems, which can be solved more efficiently. Regarding the thread-core affinity improvement, SMP-style (sequential) MPI task assignation is employed. In this manner, consecutive MPI tasks meant to deal with neighbouring sub-domains during the calculation rely within the same node, thus reducing the communication time to accomplish the exchange of information, Rabenseifner et al. [2009].

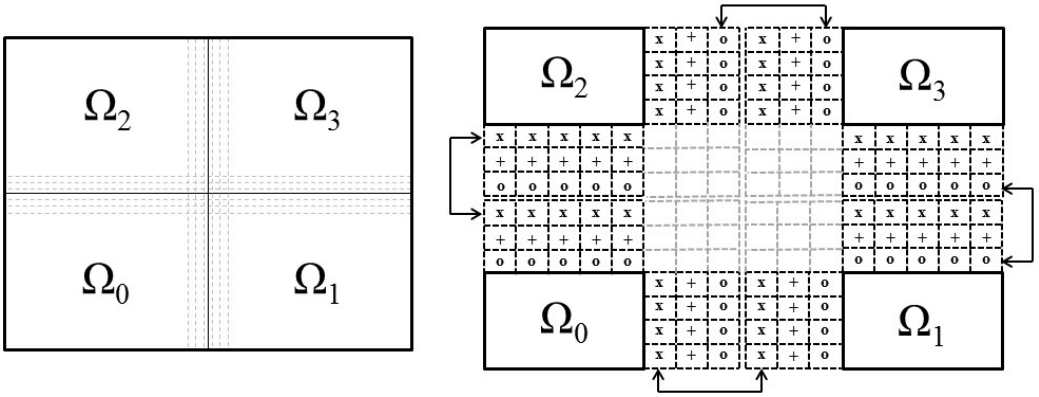

Figure 3.1: Representation of the communication between 4 sub-domains using layers of 3 ghost cells. The drawn cells correspond to the pressure mesh.

3.2.2 OpenMP implementation

OpenMP is used for fine-grained or loop-based parallelisation. The parallel regions are created as a fork operation where the work is distributed among different

threads, Aversa et al. [2005]; Chorley and Walker [2010]. A PARALLEL DO directive is placed at the parallelised loop which is executed by a certain number of threads ($N_{threads}$). Rabenseifner et al. [2009]; Zhang et al. [2004] studied the impact of different schedule directives on the OpenMP performance verifying it can provide important advantages. Table 3.1 describes briefly the standard Static, Dynamic, Guided and Runtime directives that are compared later on. The schedule directives aim at providing a better load balance in the sequential operations. Hence, they can provide an additional code speedup without increasing the hardware resources.

Schedule directive	Description
Static	The number of chunks the loop is split into is equal to the number of threads. This is the schedule directive set by default.
Dynamic	The iterations from the loop are divided in chunks of n-size. By default n is 1 but it can be modified. This schedule works with a first-come first-served basis.
Guided	This is similar to the dynamic. The specified n-size chunk corresponds to the largest piece of work. Thereafter, the new chunk size is approximately equal to the iterations left in the loop divided by the number of threads. This exponential decreasing of the chunk size makes Guided to have fewer synchronisations than the Dynamic but adds an extra computational cost due to communication and distribution.
Runtime	In contrast to the previous directives, Runtime modifies how the work is distributed among the threads throughout the simulation.

Table 3.1: Short description of the OpenMP Schedule directives.

3.2.3 Hybrid MPI/OpenMP stategy

The use of a mixed parallelisation strategy using MPI and OpenMP in Hydro3D aims at gathering the benefits from each model, and enhancing the speedup from the pure MPI strategy, He and Ding [2002]; Smith and Bull [2001]. In the proposed scheme, Hydro3D benefits from coarse-grained message-passing parallelism in the Eulerian calculations, and from fine-grained multi-threading mechanism in the Lagrangian loops calculations. The solution of the Poisson pressure equation (Eq. 2.11) constitutes the most time-consuming operation within the fractional-step method (Versteeg and Malalasekera [2007]), and is accomplished in Hydro3D using a multigrid solver that provides a better performance than other widely used methods, e.g. Conjugate-Gradient (Wang et al. [2013]). However, in this work when a large number of solid markers are clustered in a confined region of the Eulerian domain, the computations of the Lagrangian algorithms constitute an important overhead. The addition of a multi-threading environment to the latter intends to improve the code's speedup based on (i) reducing the inter-node communication between MPI cores, and (ii) balancing the load of the Lagrangian computations from the IB method subroutine, which turned into a bottleneck, by sharing the load among threads. Note that the standard MPI_THREAD_SINGLE or *masteronly* concept is used as no MPI calls are made within the OpenMP parallelised loops, which simplifies the present implementation and avoids some common drawbacks of these hybrid schemes, Aversa et al. [2005]; Rabenseifner et al. [2009].

A global layout of the proposed hybrid approach in Hydro3D is outlined in Fig. 3.2 considering the 4 MPI sub-domains setup depicted in Fig. 3.1 and 3 OpenMP threads forking the calculation of the IB method equations. Firstly, the predicted Eulerian velocities are calculated by each rank according to Eq. 2.14. The next step is to distribute the Lagrangian points among the different MPI tasks. The present strategy accomplishes the particle allocation combining the "master-slave" concept from Uhlmann [2003] with "scattering-and-gathering" distributions from Wang et al. [2013], thus it can be denoted as "master-scatter-gather" strategy.

The master processor (hereinafter referred to as master) gathers the general

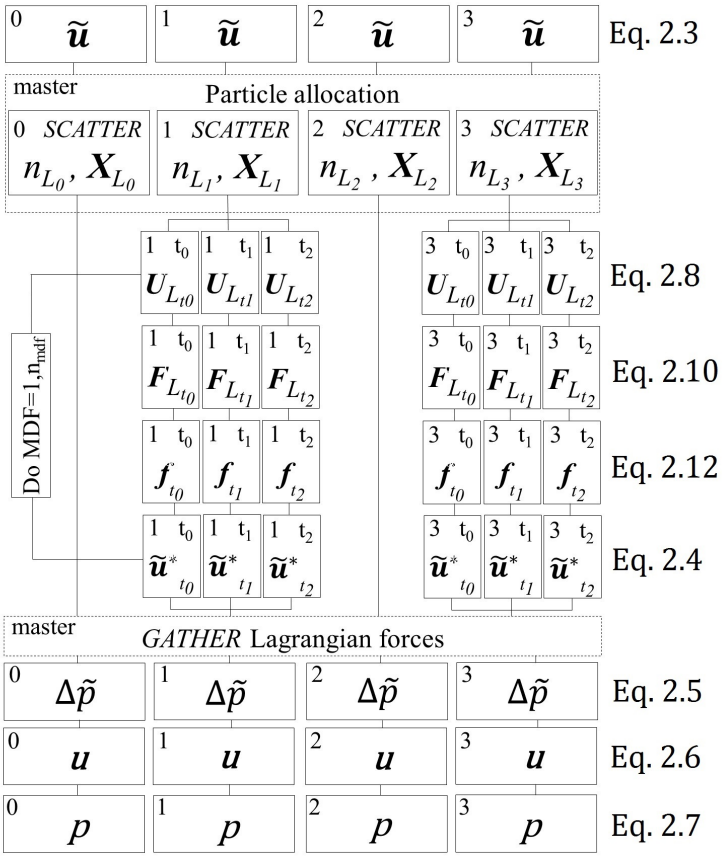

Figure 3.2: Schematic representation of the solving procedure in Hydro3D using 4 MPI tasks configuration. In this example, sub-domains 1 and 3 have Lagrangian particles and are provided with 3 OpenMP threads. Top left box indices indicates the MPI rank and t_i indicates the OpenMP thread number. MDF indicates Multi-Direct Forcing.

information from the Lagrangian markers, e.g. their coordinates. The master calculates in which MPI sub-domain each Lagrangian belongs to regarding its position, and generates a vector X_{L_i} that contains the index of the markers located in the sub-domain i. The latter is distributed via SCATTER together with the integer n_{L_i} indicating the number of markers within the sub-domain i. Depending on whether the marker is dynamic or fixed, the particle allocation and scattering-and-gathering processes are done at every time step or just at the first one, respectively.

In this strategy, each MPI task dealing with Lagrangian particles computes

the IB method equations (Eq. 2.14, 2.16, and 2.18). This differs from Wang et al. [2013]'s strategy where only the master deals with these operations. Actually their strategy is efficient as long as the number of Lagrangian points remains low. In the present cases the amount of markers is much higher leading to important load unbalance. Once the Lagrangian forcing correction on the Eulerian field is done, an inverse operation is performed sending the Lagrangian forces from the processors to the master via GATHER. The latter is just needed for those cases where the Lagrangian forces are meaningful at some extend, such as in the analysis of tidal turbines needed to compute the force coefficients. The final step is to compute the pseudo-pressure $\tilde{p}$, corrected velocity $\mathbf{u}$ and pressure p Eulerian fields using Eq. 2.11 to 2.13.

Considering no hyper-threading capabilities or similar in the HPC processors used, the maximum number of threads a multi-core shared-memory computer node provides depends on the number of cores (N_{cores}) and MPI tasks (N_{tasks}) assigned, $N_{threads}$=N_{cores}/N_{tasks}, Shi et al. [2015]. In most hybrid MPI/OpenMP applications every MPI task requires OpenMP threads, while in the presented scheme only few MPI ranks require multi-threading. This adds certain flexibility to the hybrid scheme specially when allocating MPI ranks and OpenMP threads within the same node towards reducing inter-node communications. The environment variable SLURM_TASKS_PER_NODE is used to optimise the distribution of the number of cores. In this framework, the MPI tasks demanding OpenMP threads are placed in different nodes to those that do not need OpenMP. Fig. 3.3 shows a schematic distribution of 38 MPI tasks among 4 nodes for which 12 ranks demand multi-threading with to 2 available threads. Different node distributions are combined: those dedicated to pure MPI ranks, mixed pure MPI and hybrid MPI/OpenMP cores, and exclusively dedicated to hybrid MPI/OpenMP. Node 1 and 3 are underpopulated which is not optimum when it comes to optimise the HPC resources. However, it is not possible to allocate dynamically the threads to those processors demanding hyper-threading.

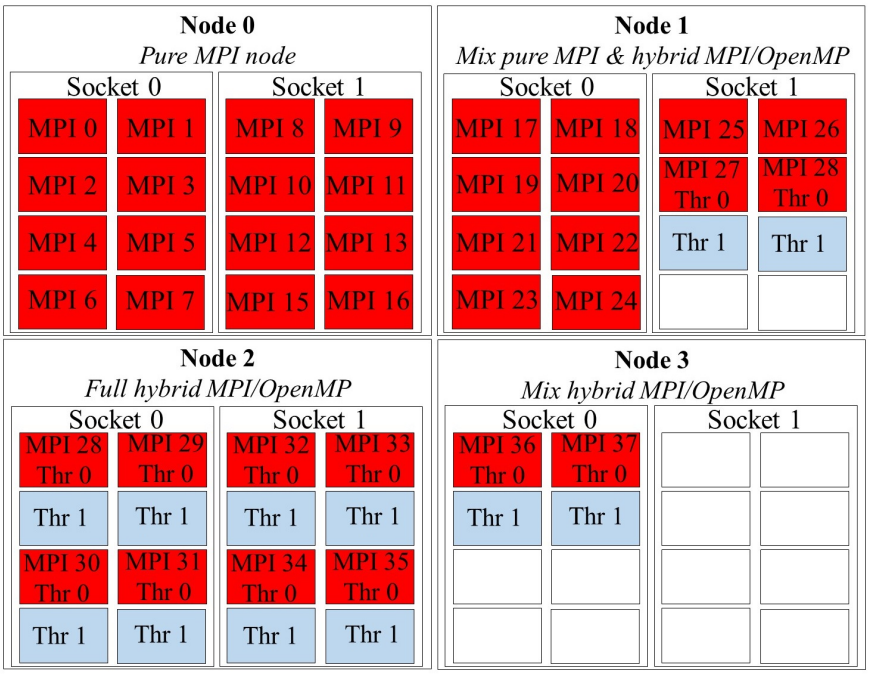

Figure 3.3: Schematic distribution of 38 MPI ranks among 4 SMP nodes for which 12 can demand up to 2 OpenMP threads.

3.3 Parallel performance assessment

Two large eddy simulations employing the IB method are performed using the proposed hybrid MPI/OpenMP parallelisation, and the parallel performance is analysed for each case. Case 1 comprises the flow around a Vertical Axis Tidal Turbine (VATT), and case 2 simulates a pitching airfoil undergoing deep dynamic stall. These cases are selected because they are a new class of particularly challenging engineering flow problems, i.e. interaction of a moving solid structure with a highly turbulent flow. The speedup, S_n, is evaluated as,

$$S_n = T_0/T_n \tag{3.1}$$

Here T_0 is the wall-time or runtime when the configuration with the minimum number of cores is used, and T_n corresponds to the runtime when using n number of cores. These are obtained with the MPI_WTIME() directive, and the generation of input/output files (e.g. IB forces) is avoided during the simulations to purely

limit the analysis to the code computations. For the presented cases, the run times are averaged for 200 iterations (similarly to Wang et al. [2013]) under fully developed flow conditions.

3.3.1 Case 1: Simulation of a Vertical Axis Tidal Turbine

The calculation of fluid-structure interaction of a VATT using the immersed boundary method is a computationally challenging simulation because of the large amount of moving Lagrangian points within a small area of a large computational domain. The IB method adapted to a VATT is described in Section 2.4.2 and is validated in Section 5 based on the experimental tests from Roa et al. [2010]. The ϕ_3^* kernel function is initially used for the interpolation procedures. The fluid domain is $30c$ by $22c$ in x- and y-directions with the turbine centre placed at $x/c = 9$ and $y/c = 11$. The domain spanwise length is $2c$. The turbine has three cambered NACA 0018 blades with a chord length $c = 0.032m$, and the resulting Reynolds number based on the blade's chord is $Re_c = 73,600$ as the incoming velocity U_0 is set to 2.3m/s. The radius of the turbine is $R = 2.73c$ and it rotates at a prescribed rotational speed of $\Omega = 52.57rad/s$ yielding a tip speed ratio of 2.

The efficiency of the hybrid parallelisation scheme is tested with two different mesh resolutions, namely M1 and M2, whose details are presented in Table 3.2. These meshes are chosen based on a mesh convergence study (later discussed in Section 5) where M2 provides a good prediction of the turbine's efficiency compared with experimental data. The scalability of the scheme is discussed using 3 different number of MPI sub-domains, 57, 114 and 171 for M1 while for M2 only the cases with 114 and 171 MPI tasks are used. Each of these configurations are tested with the addition of 2, 3 and 4 threads parallelising the IB method operations. Note that preliminary testing comparing immersed boundary forces output between pure MPI and multi-threading verified that multi-threading does not add any rounding errors and the forces results are the identical.

In the present parallelisation framework the only MPI tasks requiring multi-threading are those that at some point during the simulation deal with IB markers. The procedure to identify these tasks is straightforward for those cases when

Case	Mesh	$\Delta x/c$	N_e	N_L	N_{tasks}	N_{tasks}^{omp}
1.a	M1	0.0125	$6.64{\cdot}10^6$	81,120	57	24
1.b	M1	0.0125	$6.64{\cdot}10^6$	81,120	114	48
1.c	M1	0.0125	$6.64{\cdot}10^6$	81,120	171	72
2.a	M2	0.0100	$31.84{\cdot}10^6$	357,000	114	48
2.b	M2	0.0100	$31.84{\cdot}10^6$	357,000	171	72

Table 3.2: Details of the configurations used to test the hybrid parallelisation scheme in the simulation of a VATT: Eulerian cell size normalised with the chord length, number of Lagrangian markers representing the airfoil, number of MPI tasks, and which of them demand multi-threading.

the body moves with a prescribed motion, e.g. the circular movement described by a VATT. For this case, the sub-domains requiring multi-threading are the ones enclosed within blue boundaries in Fig. 3.4, which shows a zoom-in of the fluid domain with contours of normalised mean streamwise velocity. This figure also highlights the sub-domain division patterns determined to embed the turbine within the fine LMR level. The enclosed region concerns 24 out of the 36 sub-domains that comprise the fine LMR level.

The distribution of cores among the nodes is done attending the MPI tasks assigned to those sub-domains demanding multi-threading. As an example using case 2.b with 3 OpenMP threads, the 171 cores are distributed among 21 nodes, for which 99 are dedicated to pure MPI whilst 72 uses 3 OpenMP threads. The processors dedicated to pure MPI are split into 6 full nodes, i.e. 16x6=96 tasks, and the 3 tasks left are assigned to the 7^{th} node. The latter is a mixed core as it also allocates 3 MPI tasks demanding 3 threads, i.e. in the 7^{th} node 3 cores are allocated for pure MPI and 9 cores are for hybrid MPI/OpenMP. The remaining 69 cores using 3 threads are located in another 14 nodes. Hence, this can be specified as environment variable in the HPC job script as '16(x6),5,5(x14)'.

Fig. 3.5 presents the runtime and speedup achieved for all mesh configurations shown in Table 3.2, dividing the time spent on computing: convection and diffusion operations, Poisson pressure solver, the IB method, and the total time per time step. The Dynamic schedule directive with chunk size of 50 is used, and this is justified later on. The filled squares denote pure MPI configurations whereas

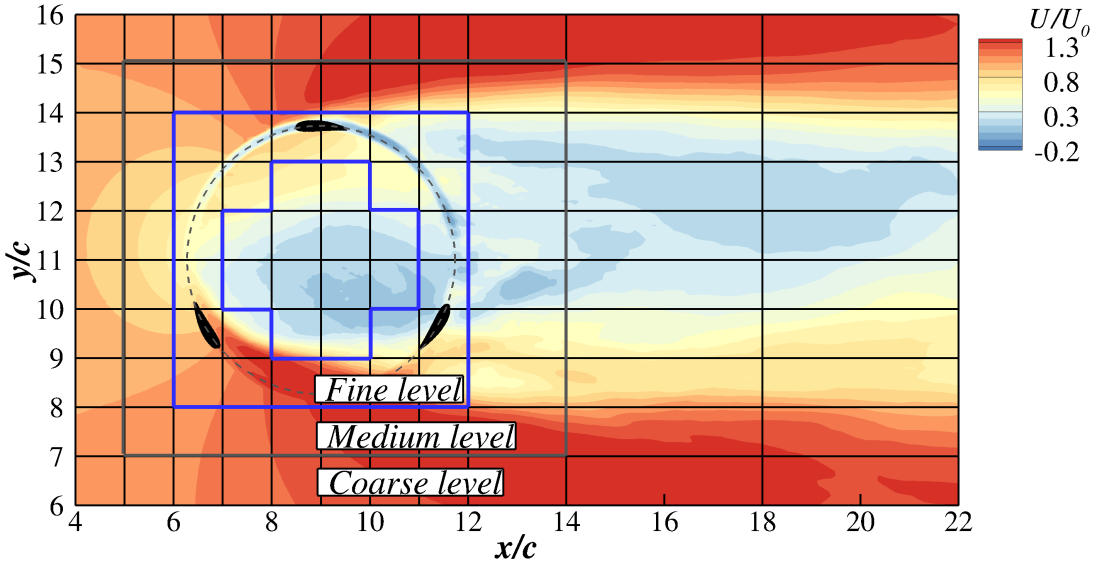

Figure 3.4: Eulerian sub-domains distribution with indication of the LMR levels, and the VATT blades with contours of normalised time-averaged streamwise velocity.

those using hybrid MPI/OpenMP are represented with blank filled symbols. The performance of the proposed mixed scheme for the mesh M1 is shown in Fig. 3.5a) with the runtime values for the different parallelisation configurations. The effectiveness of the hybrid MPI/OpenMP scheme is limited by the time spent solving the Poisson equation that fully depends on the MPI parallelisation. The convection and diffusion operations also rely exclusively on the latter although their computational load is smaller compared to that of solving the pressure equation as depicted in Fig. 3.5a) and b).

The addition of 2 threads to the 57 tasks configuration is able to reduce from 6.6s to 5.4s the total time per time step with just adding 12 cores. Further reduction is achieved using 3 and 4 threads that drop this time down to 4.9s and 4.7s respectively. Nonetheless, the efficiency of the proposed scheme is not optimal yet. The reduction in computing the IB method in a multi-threaded environment has a limited impact on the total time compared to that of computing the pseudo-pressure and convection-diffusion operations between pure MPI environments. For instance, the runtime using 114 pure MPI cores is approx. 1s lower than using a hybrid scheme with 57 MPI tasks and 3 or 4 threads (i.e.

similar number of cores). Additional division of the fluid domain into smaller sub-domains provides a faster computation in the Poisson equation solver and neighbour searching algorithm within the IB method subroutine. For the 114 and 171 tasks configurations, the computation of the IB method is slightly smaller than that of the Poisson solver although these are already balanced when using 2 threads. This fact provokes that the limiting factor goes from the IB method back to the Poisson equation solver. Hence, it is observed the parallelisation is highly conditioned by the pure MPI scheme performance.

Fig. 3.5c) presents the code performance results using mesh M1 in terms of speedup, where the pure MPI configuration is considered as the reference computing time. A larger speedup on the code is achieved for the lowest number of cores as the weight of computing the IB method within the code's load is the largest. The slope on the speedup curves is however flattened once the number of cores dedicated to pure MPI is increased. This is expected as Fig. 3.5a) exhibits that solving the Poisson pressure equation is again the limiting factor in the code performance when using 2 threads onwards.

The results for mesh M2 are somehow similar to those for M1 in terms of the speedup (Fig. 3.5d)), whilst the runtime curve from Fig. 3.5b) shows that the IB method remains as bottleneck until 3 threads or more are used. As a result of this different balance, the gap in runtime for the pure MPI using 171 cores and the mixed scheme with 114 MPI tasks and 2 threads in M2 is relatively smaller compared to that of M1 with the same configurations. In view of the results, the improvements on the performance with the proposed hybrid parallelisation is proportional to the ratio between fluid and solid elements per sub-domain. It is also observed that the impact on the code's performance is higher when using 2 threads whilst this is reduced when adding 3 or 4 threads due to communication overhead. Additionally, Wang et al. [2013] outlined that an efficient paralellisation has to show a good weak scalability, i.e. provide similar performance when the number of processors is increased while the size of the problem is kept. This is achieved and demonstrated for the proposed scheme in the speedup curves for M1 and M2 meshes, as almost the same speedup is achieved using the same number of threads both in the 114 and 171 tasks configurations.

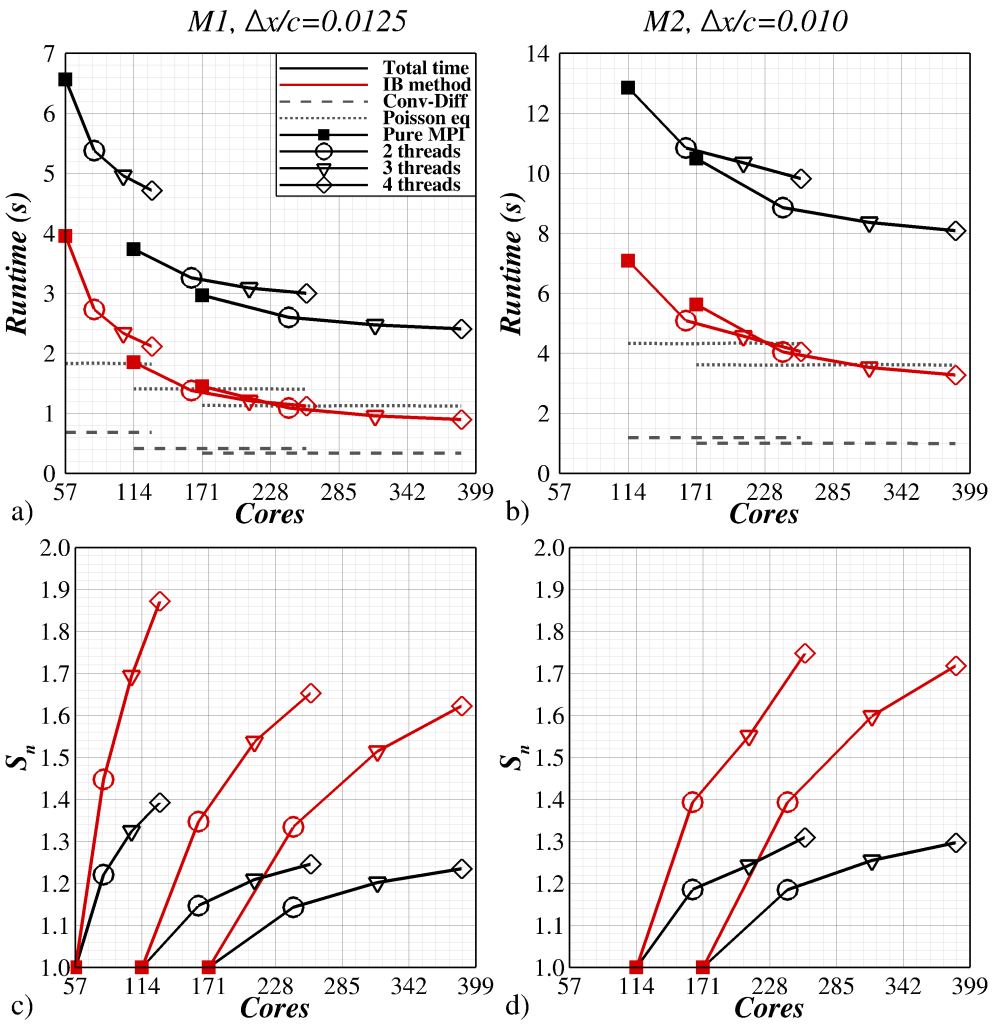

Figure 3.5: Physical average runtime due to computation of convection and diffusion, Poisson pressure equation, and the IB method subroutines, and total time per time step for meshes a) M1 and b) M2. Speedup in the code performance regarding the IB method computations and total time per time step for meshes c) M1 and d) M2.

Analysis of scheduling directives

The impact of different scheduling directives (explained in Section 3.2.2) on the speedup is analysed using 2 and 4 threads. These directives can provide an additional speedup to the current scheme at no extra hardware cost, i.e. do not require more physical resources. Their impact is studied for the case 1.b.

The relative speedup is herein referred to the runtime obtained with the Static directive, as it is the one set by default in OpenMP. The directives Dynamic and Guided offer further refinement in terms of specification of chunk size, so values 1, 50, 200 and 2000 are selected.

Fig. 3.6 presents the results using different OpenMP scheduling directives and number of threads in terms of average execution time of convection, diffusion and pressure calculations, the IB method subroutine, and the total time per time step; together with the relative speedup.

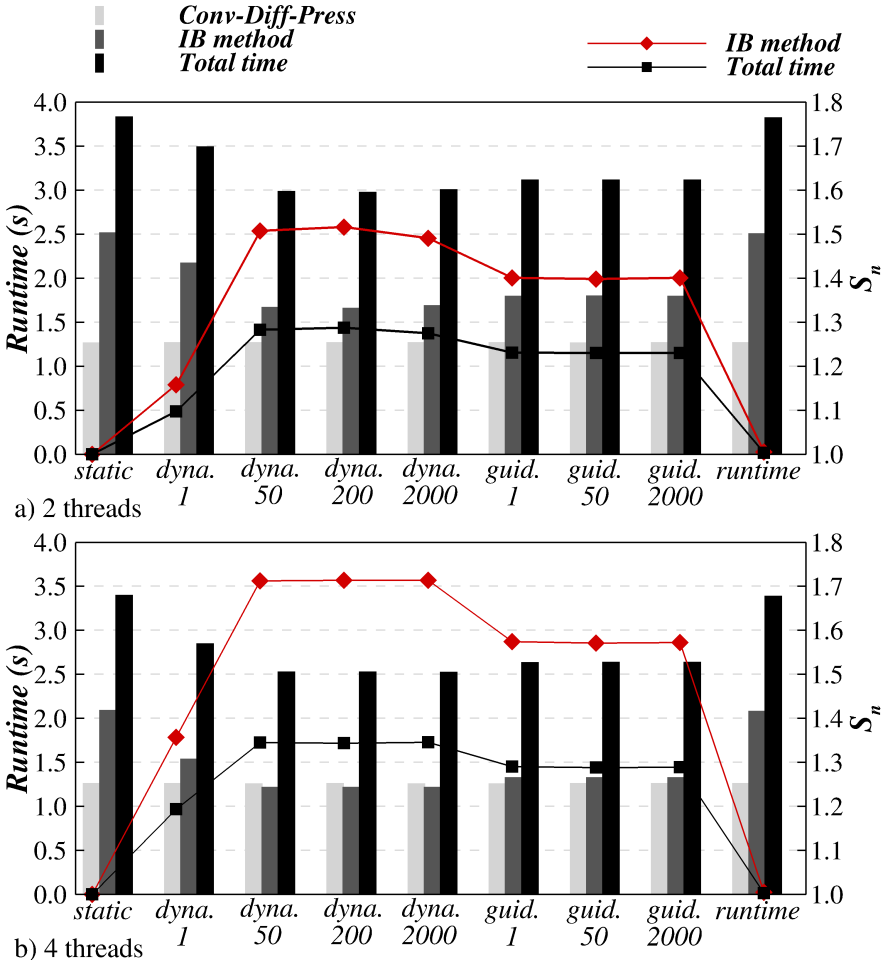

Figure 3.6: Comparison of the physical runtime and speedup due to computing the convection, diffusion and pressure terms, the IB method subroutine, and total time per time step due to schedule directives in OpenMP, using a) 2 threads, and b) 4 threads.

The greatest speedup improvement is achieved when using the Dynamic directive and chunk size of 50 and 200, regardless the number of threads used. Referred to the 2.5s spent by the Static directive, the Dynamic directive reduces the time spent in computing the IB method to 1.65s and 1.2s, when 2 and 4 threads are selected. In terms of code speedup, using the Dynamic directive with chunk 50 improves the code performance computing the IB method by factor 1.5 and 1.7 when using 2 and 4 threads respectively, which in terms of total code speedup these factors are 1.28 and 1.35.

These improvements are remarkable as the increased speedup is obtained without adding extra hardware resources. In the investigation to determine the chunk size that provide the best results using Dynamic and Guided directives, a chunk size of 2000 drops slightly the performance for the 2 threads case although keeps the same speedup values than when using 50 and 200 as chunk size for the 4 threads case. The default chunk size value is 1 which appears to be suboptimal as the achieved speedup is lower than that of the chunk size equal to 50. The results from the Guided directive exhibit an improvement on performance but less notably than the one achieved using the Dynamic directive. The Runtime scheduling directive fails to provide any improvement compared to the Static directive. Hence, the schedule directive provides the best speedup results is the Dynamic with a small chunk size, e.g. 50.

Multi-direct forcing overhead

The multi-direct forcing is based on the argument that the direct forcing equations need to be solved iteratively in order to better fulfil the no-slip condition at the IB's interface, Wang et al. [2008a]. The extra computational time to perform these additional loops is highlighted so as to provide an estimation of the cost to achieve a better satisfaction of the no-slip condition. Fig. 3.7 presents the average physical time to compute the IB method and time per time step using the standard direct forcing algorithm, i.e. no MDF, and MDF using 1, 2 and 4 extra loops. The serial execution of the MDF causes an overhead of 0.7s with each added loop whereas when using 4 threads this extra time is down to 0.6s. This linear increase in time is expected as the initial neighbour searching is done at the

first IB loop (standard direct forcing method), and ever since both neighbours indices and delta function values are stored. The addition of OpenMP threads diminish the times in the MDF computations. For instance, using 2 threads allows to perform 2 MDF loops with similar computing time compared to that of the standard IB method using no MDF loop. Analogously, the overhead when using 3 MDF loops can be balanced providing 4 threads in order to achieve a similar computational effort to the standard direct forcing.

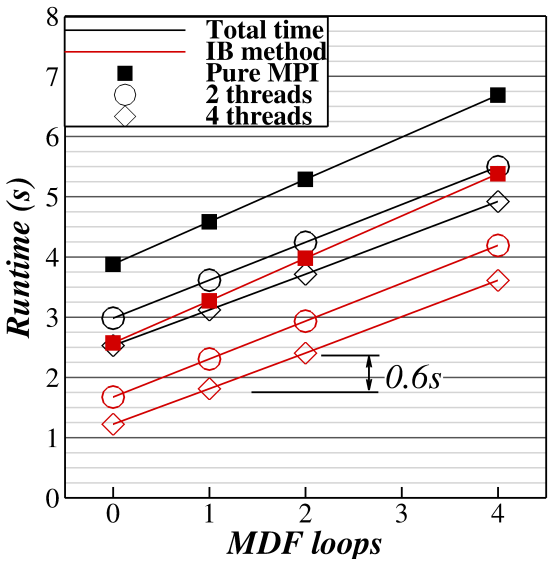

Figure 3.7: Comparison of the overhead on the code computations when using the multi-direct forcing scheme.

Hybrid scheme efficiency using different kernel functions

Increasing the number of neighbours improves the smoothness and accuracy of the interpolation processes, Yang et al. [2009]. However, this increase in accuracy is not free-of-charge as it brings additional increase in time due to a larger number of operations during the neighbour searching. This is investigated using case 1.b. Fig. 3.8a) outlines the differences in runtime executing the IB method using three delta functions featuring each of them with a wider support, and hence larger number of neighbours. The computing time spent on the IB method increases 1.8 and 3.6 times using ϕ_3^* and ϕ_4^* based on that of ϕ_3. The provision of multi-

threading to fork the IB method loops provides a notable improvement on the code speedup with the highest impact for the ϕ_4^* as using 4 threads almost halves the IB method computing time.

Fig. 3.8b) presents the speedup experienced in the different scenarios and outlines that the efficiency of the present hybrid parallelisation is larger when the delta function uses more neighbours. In fact, using ϕ_4^* enlarges the bottleneck due to the IB method, and hence it is expected that the hybrid parallelisation improves the code performance compared to the pure MPI when using a similar number of cores.

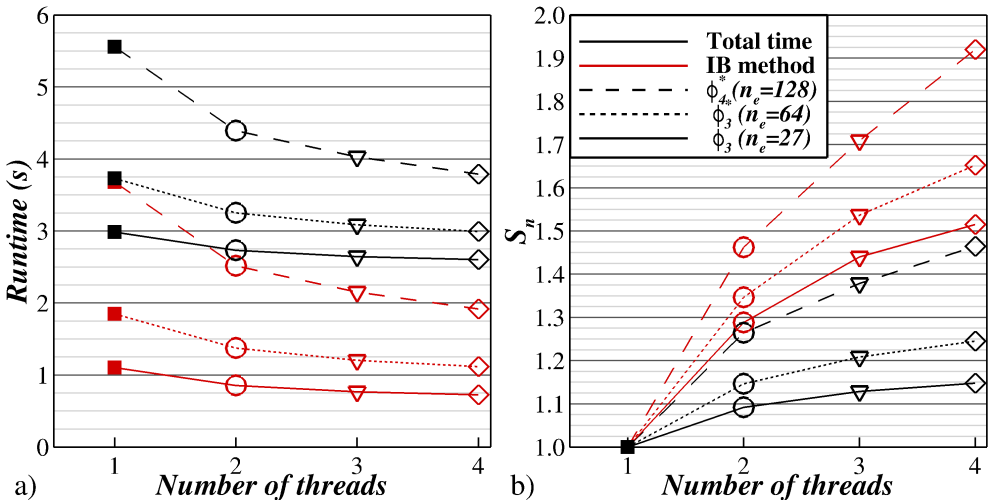

Figure 3.8: Comparison of the extra overhead on the code computations when using different kernel functions.

3.3.2 Case 2: Simulation of a Pitching Airfoil

The present hybrid parallelisation is applied to a NACA 0012 under a pitching motion undergoing dynamic stall. The simulation setup is based on the experiments from Lee and Su [2015], and the validation and results are discussed in Section 4.4.2. In the present case, a NACA 0012 oscillates with a sinusoidal pitching movement where the pitching angle, $\alpha(t)$, described by the airfoil at the

time t reads:

$$\alpha(t) = \alpha_0 + \Delta\alpha \cdot \sin(\omega t) \tag{3.2}$$

Here α_0 is the pre-set angle with value 10°, $\Delta\alpha$ is the angle amplitude equal to 6°, and $\omega = 0.32 rad/s$ is the oscillation frequency. Under this setup the maximum and minimum pitch angles are 16° and 4°, respectively. Details of mesh configurations and number of processors are given in Table 3.3. Note that the resolution is uniform in x- and y-directions while this is half in the spanwise direction, i.e. $\Delta z = 2\Delta x$. The kernel used for the interpolation is ϕ_3^* as it provided a smoother computation of the velocity gradients along the airfoil surface in comparison with ϕ_3, and is less computationally expensive than ϕ_4^*, as previously indicated. Next Section 4 outlines that very fine mesh resolutions required to accurately resolve the complex phenomena involved in the flow around pitching airfoil under deep dynamic stall conditions. The performance of the hybrid MPI/OpenMP scheme is tested using the medium (P1) and fine (P2) meshes presented in Section 4.

Case	Mesh	Δx/c	N_e	N_L	N_{tasks}	N_{tasks}^{omp}
1.a	P1	$3.125{\cdot}10^{-3}$	$6.60{\cdot}10^{6}$	81,120	38	12
1.b	P1	$3.125{\cdot}10^{-3}$	$6.60{\cdot}10^{6}$	81,120	76	24
2.a	P2	$2.500{\cdot}10^{-3}$	$13.32{\cdot}10^{6}$	364,224	38	12
2.b	P2	$2.500{\cdot}10^{-3}$	$13.32{\cdot}10^{6}$	364,224	76	24

Table 3.3: Details of the configurations used to test the hybrid MPI/OpenMP parallelisation in the simulation of the pitching airfoil: grid resolution normalised with the chord length, total number of Eulerian cells, number of Lagrangian markers representing the airfoil, number of MPI tasks, and which of them demand multi-threading.

The sub-domains that at some point during the simulation deal with IB markers are outlined in Fig. 3.9 considering 38 MPI tasks and that four LMR levels are used. In this setup, 12 MPI tasks demand multi-threading whilst in configuration with 76 MPI processors this number is doubled as the difference between setups is that the latter has two domains in the spanwise direction while the former has one. The mesh convergence study (performed in Section 4) determines that

the resolution of mesh P2 provides accurate results to predict the aerodynamic coefficients, i.e. the main phenomena involved in the dynamic stall process is well resolved.

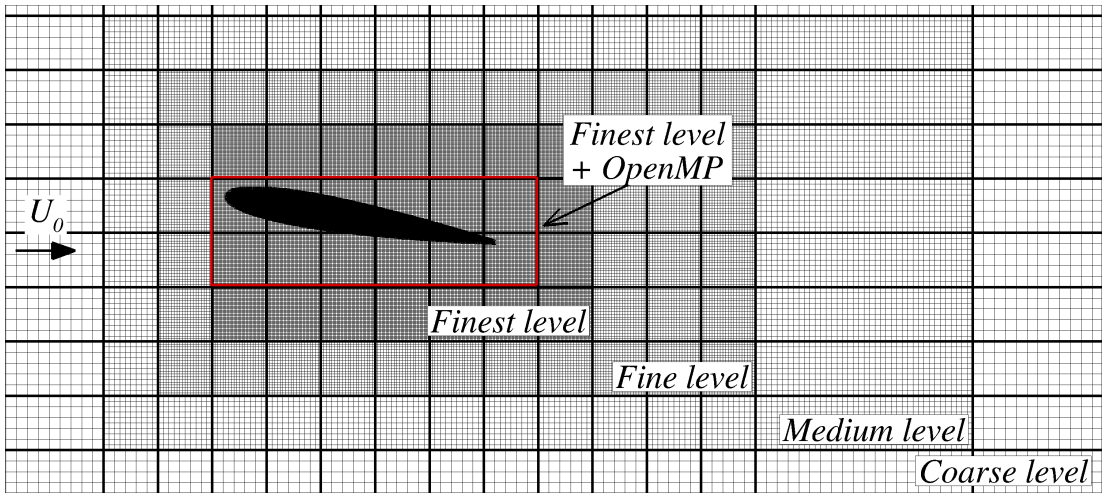

Figure 3.9: Distribution of the LMR levels in the mesh used for the pitching airfoil simulations. The sub-domains enclosed within the red boundaries demand multi-threading.

The effectiveness of the hybrid MPI/OpenMP parallelisation is presented in Fig. 3.10 with the runtime and speedup values from mesh configurations P1 (left column) and P2 (right column). The speedup is related to the pure MPI configuration so as to verify the weak scalability of the parallelisation scheme, Wang et al. [2013]. Fig. 3.10a) presents the results for P1. The addition of multiple threads to the pure MPI configuration with 38 tasks improves the code performance dropping the average time per time step from 5.5s to 4.5s, 4.1s, and 3.95s when using 2, 3 and 4 threads, respectively. In terms of speedup, 2 threads improve the code performance by factor 1.25 on the overall computations, and by factor 1.45 when computing the IB method equations. The results for mesh P2 are very similar either in reduction of the average runtime and speedup. Noteworthy is that similarly to the previous VATT case, the hybrid MPI/OpenMP scheme exhibits a good weak scalability as almost identical results are observed in meshes P1 and P2 in terms of speedup when using the same amount of computational resources.

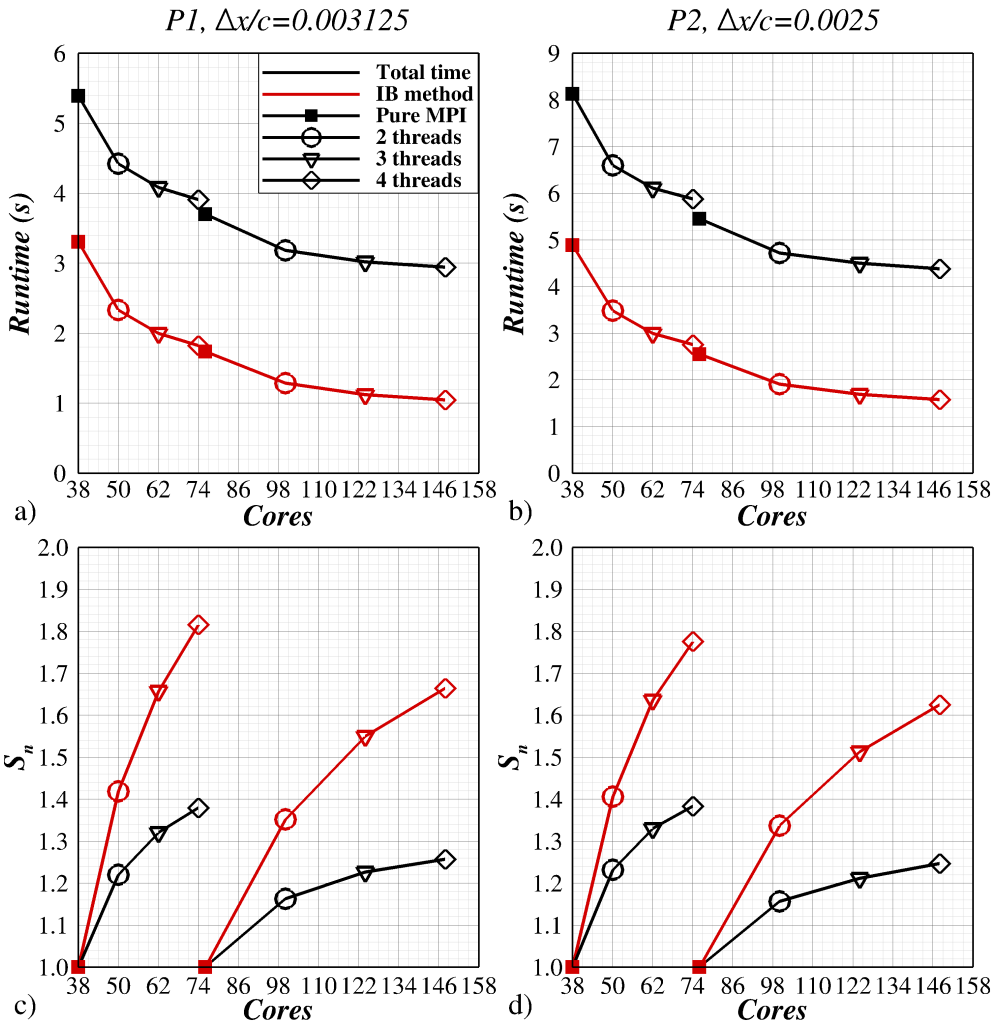

Figure 3.10: Performance of the hybrid MPI/OpenMP parallelisation on the pitching airfoil simulations achieved for the mesh P1 (left column) and P2 (right column).

Considering the computational load from these pitching airfoil simulations, a total of 4 full pitching cycles are simulated and the last 3 are used to average the aerodynamic coefficients. During these simulations a very low time step values are also needed ($\Delta t = \mathcal{O}(10^{-4})$) and simulations run for 300,000 time steps. Hence, considering mesh P2 running with a pure MPI configuration using 76 tasks, the addition of 2 threads (i.e. using 76+24=100 cores) can reduce the mean time per time step from 5.5s to 4.75s, i.e. approx. 15%, which is very considerable for

such long run simulations.

It should also be remarked that the kernel used for the interpolations is ϕ_3^*, which uses 64 neighbours. Additionally if a kernel that uses 128 neighbours is considered, e.g. ϕ_4^*, the mixed MPI/OpenMP parallelisation configuration could provide a higher performance improvement on the code analogously to the ones obtained for the VATT previously shown in Fig. 3.8. In the latter scenario a hybrid scheme would outperform pure MPI computations. These are not computed as ϕ_3^* is the only kernel used in Section 4.

3.4 Summary

A hybrid MPI/OpenMP parallelisation methodology designed for simulations employing a Eulerian-Lagrangian framework has been presented and applied to the in-house code Hydro3D. A multi-threading environment has been added to an existing coarse-grained MPI parallelisation. OpenMP has been included into a complex master-scatter-gather strategy which targets to reduce the overhead from the Lagrangian computations. The efficiency of the strategy was validated in the simulations of two challenging fluid-structure interaction problems. The code performance has been improved ever since the computational load associated to the IB method is larger than that of solving the Poisson pressure equation. Hence, the efficiency of the mixed parallelisation approach depends on whether the IB method is the bottleneck. The results have shown that the speedup gained when using 2 threads is larger than that when using 3 or 4 threads, for which the speedup slope flattens as additional outweigh is added due to thread communication. The OpenMP parallelisation was further refined with the comparison of different Schedule directives. The results suggested that using a Dynamic schedule directive with chunk size of 50 provides the best added performance to Hydro3D.

The performance of the parallelisation strategy was proved to increase when the overhead from the IB method enlarges, e.g. when using kernel functions with larger number of neighbours. In the latter scenario, adding 2 threads reduced the physical time associated to compute the IB method in approx. 31% when

using 128 neighbours whilst this reduced to 22% for the 27 neighbours case. Similar outcomes were obtained for the multi-direct forcing algorithm wherein the provision of OpenMP threads provided a linear reduction on the IB method computation.

Overall, the hybrid MPI/OpenMP method provides an appreciable increased in the code speedup. For the applications shown in this Chapter it, does not overcome the performance from pure MPI schemes as pressure solver is still the major bottleneck. Hence, it is advise to adopt such mixed scheme where not only the standard direct forcing equations are used but when additional fluid-structure interaction algorithms are adopted, such as those used for particle laden flows (Uhlmann [2005]; Wang et al. [2008b]), deformable bodies (Tian et al. [2014]) or simulation of moving filaments (Pinelli et al. [2017]), as they increase the overhead associated to the IBM. The provision of the hybrid parallelisation strategy to fork the additional equations in these algorithms is expected to have a larger impact than for the current direct forcing algorithm. It is also worth to mention that many HPC resources feature hyper-threading capabilities, which allows a physical core to be virtually divided into 2 threads. In this scenario, performing multi-threading computations could be done without any extra cores dedicated to OpenMP.

Chapter 4

Dynamic stall in pitching airfoils

4.1 Introduction

Structural failures in wind and tidal turbines caused by large aero/hydrodynamic loads or fatigue are many times related to dynamic stall on the blades. Hence, there is a need for understanding this phenomenon towards damping or reducing its impact on the structure, McCann [2007]. Over the past decades, the study of dynamic stall has been a crucial step for the industry development in the design of helicopters (Corke and Thomas [2015]), micro-aerial vehicles, and even wind and tidal turbines (Leishman [2002]) for which further research is still needed for improving the actual designs.

The complexity of dynamic stall on moving airfoils was investigated experimentally throughout different motion, such as heaving, plunging and/or pitching, and combinations of them. During extensive experimental studies (Carr et al. [1977]; Lee and Gerontakos [2004]; Lee and Su [2015]; McCroskey et al. [1976]; Mulleners and Raffel [2012]), it was observed that the aerodynamic behaviour of an airfoil undergoing pitching motion is dominated by dynamic stall, which modifies its aerodynamic characteristics compared to steady-state dynamics. Dynamic stall is related to the generation of a Leading Edge Vortex (LEV) at high angles of attack, larger than the static stall angle, which overshoots the lift generation capabilities of the airfoil. Under deep dynamic stall conditions, the shedding of

the LEV provokes large flow separation over the entire suction side of the airfoil, and this is subjected to successive generation and shedding of a series of leading and trailing edge vortices. In this post-stall regime, the airfoil loses its aerodynamic capabilities and experiences large force fluctuations until front-to-rear flow reattachment is achieved during the downstroke motion recovering its ability to generate lift.

Despite all the research undertaken to date, it has not been possible to extract an unique conclusion about the nature of dynamic stall. Choudhry et al. [2014] remarked that dynamic stall in moving air/hydrofoils depends on many factors such as blade geometry (e.g. thickness or cambering), Reynolds and Mach numbers, oscillation frequency or movement pattern (pitching, heaving, plunging or ramp-type motion), among others. Concerning the pitching motion, the three key factors are the pitching oscillation frequency, pre-set angle of attack, and angle of attack amplitude. These determine whether deep or light stall is achieved, i.e. the flow separation region is extended over the entire suction side or just over a short portion of it closer to the trailing edge (Mulleners and Raffel [2012]), respectively.

CFD in understanding dynamic stall

Previously cited experimental studies on dynamic stall started in the 1970s. However, it was not until the 2000s when CFD started to be used as a complementary tool to analyse this phenomenon. Ever since, many authors started to study dynamic stall using numerical simulations as they can provide more detailed information ranging from velocity and pressure fields to the visualisation of turbulent flow structures. A first investigation was carried out by Akbari and Price [2003] who analysed the dynamic stall of a NACA 0012 using a vortex method for a range of low Reynolds numbers ($3 \cdot 10^3$ to $1 \cdot 10^4$). Martinat et al. [2008] simulated a NACA 0012 and compared different turbulence models in 2D and 3D RANS simulations, which appear to have a noticeable influence on the predicted aerodynamic performance results.

Wang et al. [2012] performed a similar analysis using the experimental work from Lee and Gerontakos [2004] to validate the model. Their results show that

the computed aerodynamic coefficients are sensible to the chose turbulence model. Their extension from 2D RANS to 3D RANS and 3D DES provided different prediction on the airfoil behaviour and differences of the predicted flow field became more noticeable at high angles of attack. This highlights that 3D models are required to accurately resolve dynamic stall due to its three-dimensional nature. Gharali and Johnson [2013] improved the previous RANS-based predictions from Wang et al. [2012] using a finer grid while the same turbulence model was used. Kim and Xie [2016] further improved RANS predictions from the previous references using LES. They reproduced different pitching frequency cases from Lee and Gerontakos [2004], and achieved an overall great agreement with the experimental results. These improvements, derived from using LES instead of RANS, outline the capabilities of the former to resolve the instantaneous flow field compared to the time-averaged nature of the latter. The eddy-resolving nature of LES is specially important in the simulation of flows dominated by large-scale structures, such as those found during dynamic stall.

Visbal [2011] studied the behaviour of a heaving airfoil using implicit LES (ILES). The computed flow field pattern achieved a close representation of the vortical structures compared to those observed during the experiments. They highlighted relevant flow phenomena such as Kelvin-Helmholtz instabilities during the downstroke motion onset developed on the upper side of the airfoil, as well as high instabilities within the LEVs or TEVs. The identification of these phenomena were not previously observed with RANS encouraging to use LES or ILES for the accurate simulation of such complicated flows. The use of ILES on moving airfoils was extended by Visbal et al. [2013] with an emphasis on the generated flow structures, which again agreed remarkably well with those observed in the experiments. Worth to mention is the recent work from Rosti et al. [2016] who performed the DNS of an aifoil subjected to ramp-up motion providing relevant insights on the vortex generation and developed pattern during the airfoil motion.

The IB method in the simulation of airfoils at high Re

To date, the use of the IB method for high Reynolds number flows has been limited as the compromise for the accurate resolution of the boundary layer is often questioned as the fluid mesh does not conform to the immersed body shape. Nonetheless, recent publications have demonstrated that the IB method is able to accurately reproduce the flow around airfoils at medium to large Reynolds numbers when adequately fine meshes are used. Castiglioni et al. [2014] performed a LES of a NACA 0012 with fixed angle of angle at $Re_c = 5 \cdot 10^4$ obtaining remarkable outcomes when comparing the aerodynamic coefficients computed using the IB method compared with those from body-fitted models. Tay et al. [2015] compared the aerodynamics of a flapping wing using a body-fitted mesh and different IB methods with experimental data, and achieved an overall good agreement. Zhang and Schluter [2012] studied the influence of the LEV on the lift generation of a flat-plate undergoing a sinusoidal motion for a range of Reynolds number between 440 to 21,000. Their results indicated that the IB method worked well in predicting flow separation and vortex shedding mechanisms.

Aim of the chapter

This chapter aims at improving the understanding of dynamic stall influences the aerodynamic coefficients of a pitching airfoil, and thus shedding some light on the future development of Vertical Axis Turbines (VATs). The effect of blade shape in dynamic stall is analysed with the comparison between straight and cambered airfoils describing a pitching motion undergoing deep stall. As VATs are lift-driven devices, the use of cambered blades may improve the lift-to-drag ratio and hence enlarge the turbine's performance, Elkhoury et al. [2015]; Takamatsu et al. [1991]. According to Choudhry et al. [2014], in reference to the experiments from McCroskey et al. [1981] on the design of helicopter blades, blade profiles with cambered shape tend to experience smaller hysteresis cycles, which is also beneficial for VATs by reducing fatigue load amplitude.

Section 4.2 describes the dynamic stall phenomenon on airfoils under pitching motion and VATs, and the pitching airfoil kinematics. Section 4.3 presents the computational setup. In Section 4.4 the method is validated with experimental

data in the simulation of a NACA 0012 , and a spatial and temporal integration sensibility study is also presented. The comparison between the NACA 0012 and NACA 4412 is shown in Section 4.4.1. Results from simulating a NACA 0012 under different flow conditions and higher pitching frequency, reproducing the experiments from Lee and Su [2015], are described in Section 4.4.2.

4.2 Dynamic stall on Vertical Axis Turbines

In the design of Darrieus-type vertical axis turbines, the determination of its solidity, σ, is a relevant step as it establishes the range of tip speed ratios, λ, at which the turbine operates. The solidity, Eq. 4.1, relates the length covered by the blades along the turbine's swept perimeter, and the tip speed ratio, Eq. 4.2, represents the relative rotational speed of the turbine considered the free-stream velocity. The higher the solidity, the lower the tip speed ratio at which power is extracted, and vice versa, Amet et al. [2009].

$$\sigma = \frac{N_b c}{2\pi R} \tag{4.1}$$

$$\lambda = \frac{\Omega R}{U_0} \tag{4.2}$$

Here N_b is the number of blades, c is the chord length of the turbine blades, R is the turbine's radius, Ω is the rotational velocity, and U_0 is the free-stream velocity. During the rotational motion of a VAT, its blades undergo a constantly varying effective angle of attack, α, relative to the oncoming flow, defined as,

$$\alpha = \text{atan}\left(\frac{-\sin\theta}{\lambda + \cos\theta}\right) \tag{4.3}$$

where θ denotes the rotated angle. Fig. 4.1a) exhibits the variation of α along the upstream motion of the turbine blade, i.e. $0° < \theta < 180°$. At all rotational speeds the blade overcomes the static stall angle, α_{ss}, and at tip speed ratios lower than approx. 3.0 also the dynamic stall angle, α_{ds}. Additionally, the lower the tip speed ratio, the earlier the deep dynamic stall onset, i.e. $\alpha > \alpha_{ds}$, and

thus the larger the extension the turbine blade undergoes full flow separation. Fig. 4.1b) illustrates the stages at which a VAT blade undergoes no dynamic stall ($\alpha < \alpha_{ss}$, blank region), light dynamic stall ($\alpha_{ss} < \alpha < \alpha_{ds}$, light grey region), and deep dynamic stall ($\alpha > \alpha_{ds}$, dark grey region), considering a tip speed ratio of 2.0.

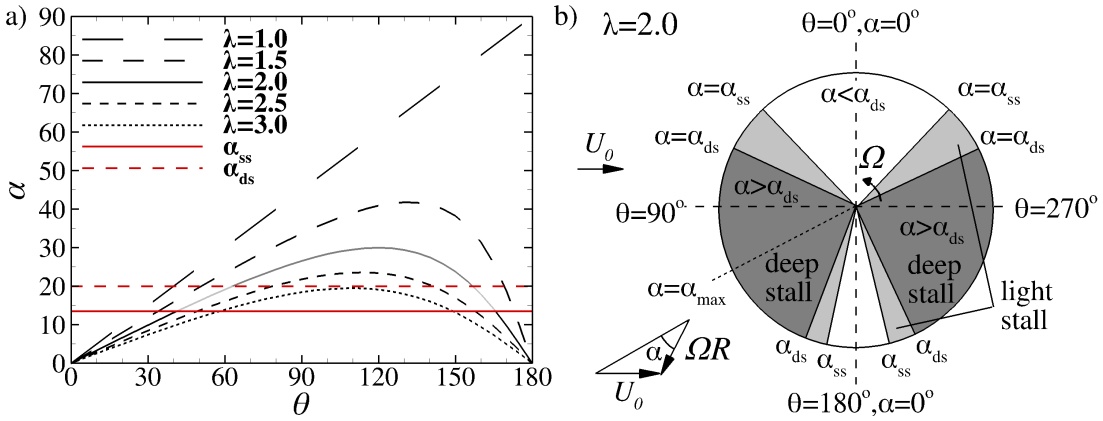

Figure 4.1: a) Effective angle of attack, α, described by a turbine blade during the first half of the revolution for different tip speed ratios, where α_{ss} and α_{ds} denote static and dynamic stall angles respectively. b) Regions of dynamic stall experienced by a VAT blade when rotating at $\lambda = 2.0$.

Noteworthy is that the maximum torque generated by a VATT is often located at $\lambda = 2.0$ with its peak value at $\theta \approx 90°$, Amet et al. [2009]; Kiho et al. [1996]. According to Fig. 4.1a), at this rotated angle the blade is at an effective angle of attack larger than α_{ds}, and hence dynamic stall plays an important role during VATT's optimal operational conditions, Simão Ferreira et al. [2009]. Fig. 4.1b) shows that during maximum power generation conditions, the blades are under deep dynamic stall, and thus in order to simulate accurately the torque generated by a VATT, dynamic stall has to be accurately predicted.

The value of α_{ss} is intrinsic to the airfoil geometry and flow regime, whereas α_{ds} is a function of the described motion, Choudhry et al. [2014]. Understanding dynamic stall of pitching airfoils can help to design VATs, which are highly influenced by this phenomenon, Brochier et al. [1986]. The analysis on how cambering an airfoil profile influences its aerodynamic performance aims at investigating whether this could provide a larger α_{ds} that may reduce or delay the

development of full flow separation over the blade, i.e. delaying $\alpha > \alpha_{ds}$, towards improving the VAT performance.

The kinematic factors that define the VATs and pitching airfoils motions are the tip speed ratio and the reduced pitching frequency, κ (Eq. 4.4), respectively. Laneville and Vittecoq [1986] introduced an equivalent reduced rotational frequency associated to VATs, here denoted as κ^* and defined in Eq. 4.5. The latter depends both on the geometrical properties of the VAT (represented by the solidity) and its motion in terms of tip speed ratio and α_{max}, which stands for the maximum effective angle described by the turbine at a certain tip speed ratio, defined in Eq. 4.6.

$$\kappa = \frac{\Omega}{U_0}\frac{c}{2} \tag{4.4}$$

$$\kappa^* = \frac{c}{R}\frac{1}{\lambda - 1}\frac{1}{2\alpha_{max}} = \sigma\frac{2\pi}{N_b}\frac{1}{\lambda - 1}\frac{1}{2\alpha_{max}} \tag{4.5}$$

$$\alpha_{max} = \text{atan}\left(\frac{1}{\sqrt{\lambda^2 - 1}}\right) \tag{4.6}$$

Fig. 4.2 presents how the parameter κ^* depends directly on the curvature parameter, c/R, and in turn on the turbine solidity. The value of $\kappa^* = 0.05$ was adopted as threshold above which a pitching airfoil experiences a strong dynamic stall, Amet et al. [2009]. According to their statement and observed in Fig. 4.2, for VATTs operating at low tip speed ratios, i.e. $\lambda < 2$, dynamic stall is somehow present at all rotational speeds. VATTs are often designed with higher solidity than their wind counterpart as they have to stand larger forces, and thus they operate at lower tip speed ratios, Amet et al. [2009]. In consequence, a larger turbine solidity leads to a higher reduced rotational frequency, i.e. VATTs are more prone to dynamic stall than VAWTs.

Another feature of low solidity turbines is that their blades suffer less from deep dynamic stall, i.e. they do not experience full flow separation. Consequently, they experience smaller load amplitudes which reduce their fatigue loads, Elkhoury et al. [2015]. Therefore, the design of VATTs requires to optimise design factors, such as solidity, towards achieving an optimal behaviour regarding: self-starting capabilities, torque generation (energy production), fatigue loads,

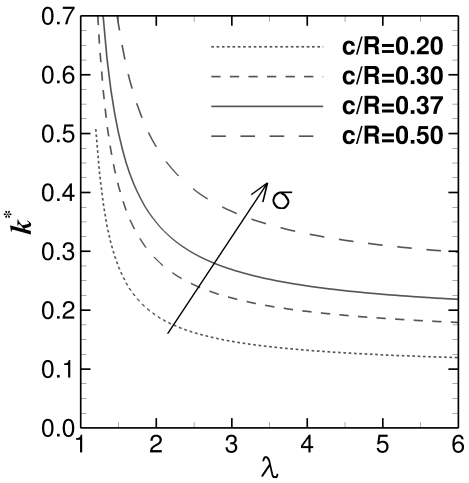

Figure 4.2: Evolution of the reduced frequency, k^*, with the tip speed ratio, λ, considering different curvature parameters, c/R.

and also noise generated when the turbine operates at high tip speed ratios.

4.3 Computational setup

Three different cases of an airfoil describing a sinusoidal pitching motion undergoing deep dynamic stall conditions are simulated. The experimental work undertaken by Lee and Gerontakos [2004] is selected for the baseline simulation, as it was reproduced using RANS (Gharali and Johnson [2013]; Wang et al. [2010, 2012]), DES (Wang et al. [2012]), and more recently with LES (Kim and Xie [2016]). In this baseline case, namely case I.a, a NACA 0012 is simulated, and this setup is adopted for the sensibility study using different mesh resolution and time step values. In case I.b, the effect of blade cambering on dynamic stall is analysed using a NACA 4412 under the flow and kinematic conditions of case I.a. Additionally, case II is adopted to simulate a NACA 0012 with a lower Re_c and higher κ, and results are compared with the experiments from Lee and Su [2015].

The geometrical parameters and forces considered during the simulation of a pitching airfoil are sketched in Fig. 4.3. The pitch angle at the time t is calculated as $\alpha(t) = \alpha_0 + \Delta\alpha \cdot sin(\Omega t)$, where α_0 is the pre-set pitching angle, $\Delta\alpha$ is the angle amplitude, and Ω is the pitching frequency calculated from the reduced

frequency (Eq. 4.4). Note that upstroke movement, i.e. increasing of the pitching angle, is denoted with ↑ whilst ↓ indicates the opposite downstroke movement.

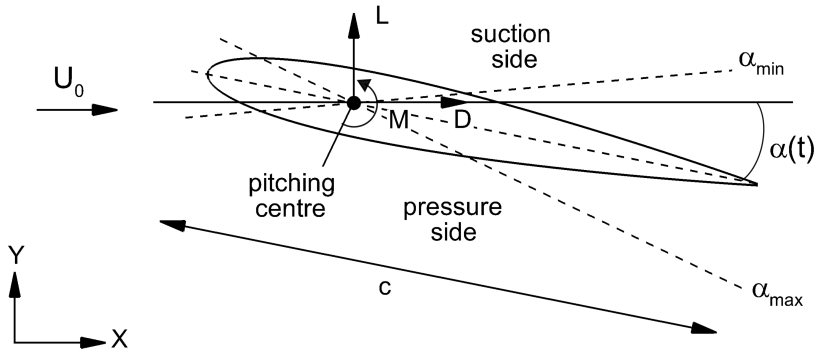

Figure 4.3: Representation of the pitching cycle described by a NACA 0012. α_{max} and α_{min} represent the maximum and minimum pitch angles.

The main aerodynamic forces are the lift (L), drag (D) and pitching moment (M), although from hereinafter these are referenced in terms of aerodynamic lift (C_L), drag (C_D) and moment (C_M) coefficients, calculated as:

$$C_L = \frac{L}{1/2\rho U_0^2 A} \tag{4.7}$$

$$C_D = \frac{D}{1/2\rho U_0^2 A} \tag{4.8}$$

$$C_M = \frac{M}{1/2\rho U_0^2 A c} \tag{4.9}$$

where A corresponds to the spanwise length used in the computational domain.

Table 4.1 presents the details for the three cases of: airfoil shape, Reynolds number, pitching motion parameters, maximum (α_{max}) and minimum (α_{min}) pitch angle values, and reference of the experiments used for the validation of the numerical approach.

The simulations run for four pitching cycles being the first one discarded from the phase averaging of the aerodynamic coefficients (similar to Kim and Xie [2016]), although during the experiments (Lee and Gerontakos [2004]; Lee and Su [2015]) this was done for more than 100 cycles. Both experimental campaigns of cases I.a (Lee and Gerontakos [2004]) and II (Lee and Su [2015]) were performed

Case	NACA	Re_c	α_0	$\Delta\alpha$	α_{min}	α_{max}	κ	Experiments
I.a	0012	135,000	10°	15°	-5°	25°	0.10	Lee and Gerontakos [2004]
I.b	4412	135,000	10°	15°	-5°	25°	0.10	-
II	0012	36,000	10°	6°	4°	16°	0.16	Lee and Su [2015]

Table 4.1: Description of the main parameters characterising the pitching airfoil cases and the experimental campaigns used as reference.

in a suction-type wind tunnel measuring $L = 2.7m$ $(18c)$ x $H = 1.2m$ $(8c)$ x $B = 0.9m$ $(6c)$, which are kept in the numerical domain presented in Fig. 4.4. Note that during previous numerical studies of case I.a (Gharali and Johnson [2013]; Kim and Xie [2016]; Wang et al. [2010, 2012]) the domain length in the y-direction (H) was set to $20c$, reducing the experimental wind tunnel blockage effect and thus leading to some differences between their results and the present ones. The airfoil pitching centre is placed at $0.25c$ from the leading edge and is situated $4c$ downstream the inlet and centred in the transversal y-direction. In the experiments the airfoil had a spanwise length of $2.5c$ and was equipped with end-plates. The present computational domain considers a spanwise airfoil length of $0.2c$ as it would be unaffordable to perform the present LES with the experimental tunnel dimensions considering the HPC resources available to the authors. Such assumption is deemed valid as Lee and Gerontakos [2004] outlined that the flow over the airfoil can be assumed as two-dimensional, and is also supported with the numerical results from Kim and Xie [2016] regarding the influence of the spanwise length using values of $0.5c$ or $1.0c$, which provided very similar aerodynamic coefficients prediction. Using finite spanwise domains is a common practice in the study of airfoils using LES and DNS as seen in Shan et al. [2005] or Sandberg and Jones [2011].

Concerning the boundary conditions, uniform free-stream velocity is set at the inlet while convective boundary condition is set at the outlet. Symmetric boundary conditions are set on the spanwise direction and no-slip conditions are imposed on the upper and lower bounds of the numerical domain representing the wind tunnel walls. The computational domain is decomposed into 264 sub-domains, as depicted in Fig. 4.4. Four LMR levels are used to achieve a fine

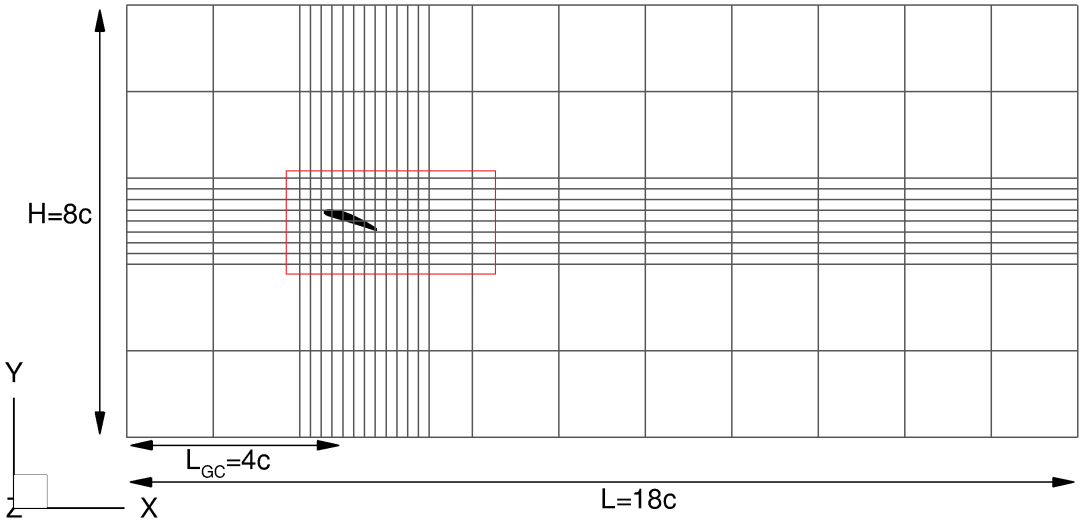

Figure 4.4: Dimensions of the numerical domain used for the pitching airfoil simulations.

mesh resolution close to the airfoil while coarsening it far from it, as highlighted previously in Fig. 3.9. The simulations run in 76 CPUs and each simulation using the finest mesh resolution requires about 300,000 iterations with a computational load of approx. 38,000 CPU hours.

4.4 Code validation

The present computational approach is firstly validated with a mesh resolution and time step sensibility analysis using as reference the aerodynamic coefficients from case I.a. Table 4.2 presents the details of the three Eulerian fluid mesh resolutions used at the finest LMR level, i.e. area enclosing the airfoil (see Fig. 3.9), namely Δx_1, Δx_2 and Δx_3, and number of Lagrangian IB markers along each two-dimensional section of the airfoil's boundary, N_L. The mesh resolution is uniform in x- and y-directions, so the number of points distributed along the upper and lower surfaces of the airfoil is the same, whereas in the spanwise direction the mesh resolution is $\Delta z = 2\Delta x$. Note that there is one Lagrangian marker per Eulerian cell in order to accomplish that the total force exchanged between solid and fluid grids is constant, as explained in Section 2.4.

Mesh	$\Delta x/c$	N_L
Δx_1	$6.250\ 10^{-3}$	324
Δx_2	$3.125\ 10^{-3}$	642
Δx_3	$2.500\ 10^{-3}$	802

Table 4.2: Details of the normalised mesh resolutions and the number of divions along the airfoil's surface used during the sensibility study for case I.a.

The mesh resolutions are compared to other references that used body-fitted meshes with reference to the number of solid markers N_L, as the IB method is non body conformal, i.e. no boundary-layer cells are built along the airfoil's surface. In RANS, the finest resolution was used by Gharali and Johnson [2013] with 500 divisions along every airfoil surface section. Kim and Xie [2016] performed most of their LES in a mesh with 579 division (386 on the upper side), although they tested a finer mesh with 893 divisions that did not provide remarkable improvements. Hence, meshes Δx_2 and Δx_3 are expected to be fine enough to provide a good resolution of the flow phenomena. The time step analysis is performed using the finest mesh resolution (Δx_3) with three different values: $\Delta t_1^* = 8 \cdot 10^{-4}$, $\Delta t_2^* = 4 \cdot 10^{-4}$, and $\Delta t_3^* = 2 \cdot 10^{-4}$, where Δt^* is the normalised time step calculated as $\Delta t^* = \Delta t U_0/c$.

Fig. 4.5 presents the phase averaged lift and drag coefficients computed for the different mesh resolution and time steps, experimental data and 3D DES results from Wang et al. [2012]. The results obtained with the coarser mesh fail to predict C_L and C_D values along the pitching cycle, featuring a premature drop in the lift forces. From flow visualisations, it is appreciated that this mesh is not fine enough to accurately resolve the velocity gradients along the airfoil surface, which are fundamental to correctly represent the generated flow field. The increase in mesh resolution provides an appreciable improvement in both aerodynamic coefficient results. The medium mesh, Δx_2, gives accurate C_L predictions for $\alpha < 20°$ with a very good agreement during the downstroke motion. Further improvements are achieved using the finest mesh, Δx_3, as the C_L prediction gets closer to the experimental data during the upstroke motion. The LEV detachment is responsible for the dramatic drop in lift forces during the upstroke motion. Its

shedding prediction with Δx_2 is yet too premature whilst Δx_3 features a delay on this phenomenon and achieves a closer match to the experiments. Nonetheless, Δx_3 results are still differing from the experimental data during the downstroke, which is probably because of the reduced number of averaged cycles.

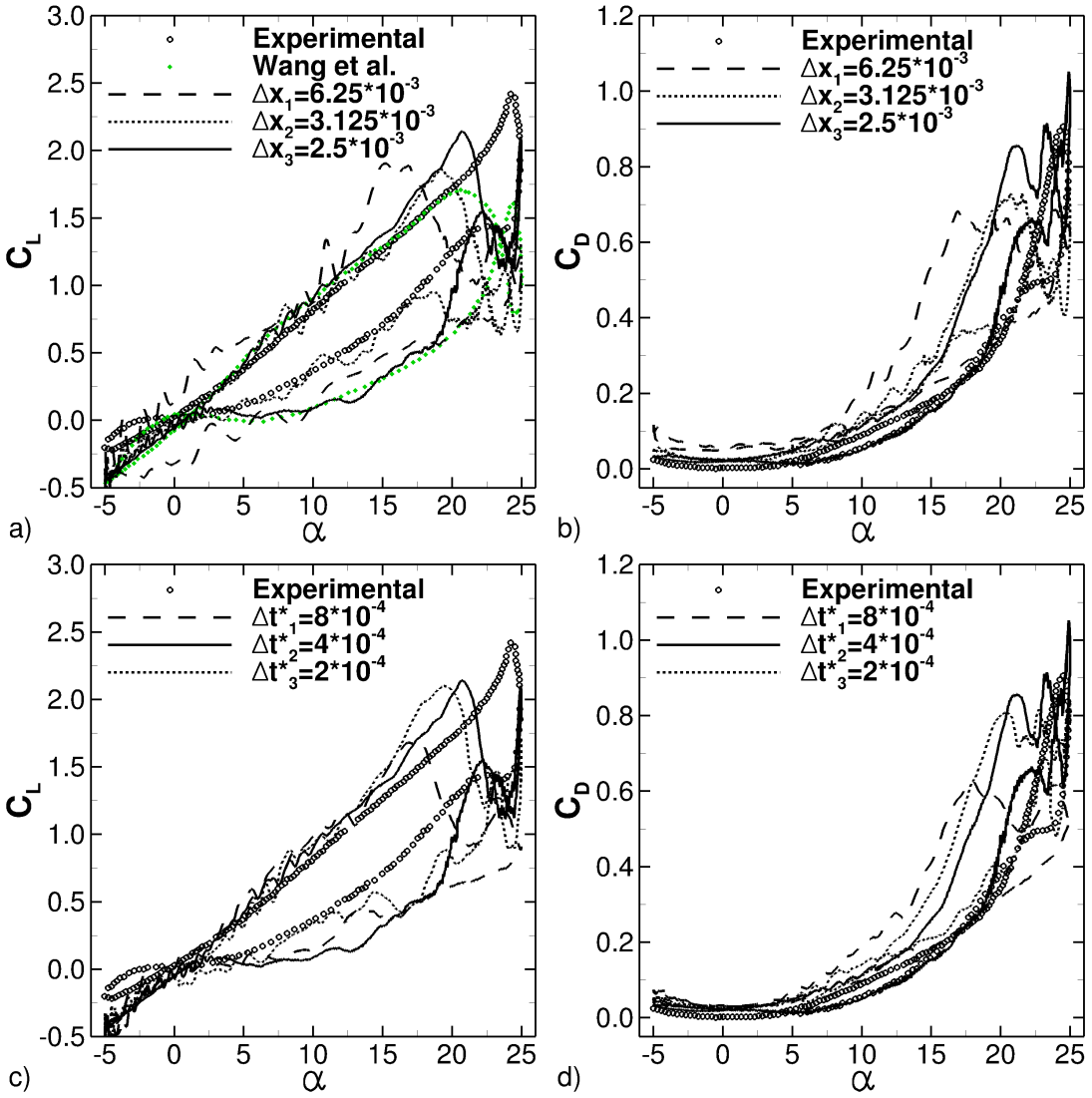

Figure 4.5: Phase averaged aerodynamic coefficients from case I.a. a) Lift and b) drag coefficients using different mesh resolutions, and c) lift and d) drag coefficients with different time step values. Comparison of the present LES with experiments (Lee and Gerontakos [2004]) and 3D DES (Wang et al. [2012]).

Results from LES agree with those of DES for $\alpha < 20°$, although LES im-

proves the lift overshoot prediction due to the LEV and post-stall conditions, as explained later in Section 4.4.1. Similar to the findings of Martinat et al. [2008], the downstroke motion features large flow separation, which leads to larger differences in the aerodynamic forces among cycles in comparison to the upstroke before stall occurs. The coefficient of drag describes a similar pattern for the two fine meshes with an appreciable reduction of drag values with mesh refinement. The drag overprediction compared to experiments are similar to the ones observed in the LES results from Kim and Xie [2016].

The sensibility to the time step is studied using Δx_3, and results of C_L and C_D are presented in Fig. 4.5c) and d), respectively. The large time step, Δt_1^*, features an early LEV shedding and consequently the post-stall conditions are not accurately predicted. Further reduction of the time step improves the prediction of the LEV formation. Some differences between Δt_2^* and Δt_3^* are observed during the downstroke motion, with the latter providing a better match with experiments at $5° \downarrow < \alpha < 18° \downarrow$.

These results show evidence that small time step together with fine mesh resolution are required to achieve a good representation of the complex flow phenomena. Considering that the number of iterations associated to Δt_3^* is double than that of Δt_2^*, i.e. double computational load, mesh Δx_3 with fixed time step value of Δt_2^* are selected as the best configuration for the following simulations.

The presented aerodynamic coefficients results show a similar pattern to that observed in other numerical works using 2D RANS (Wang et al. [2010]), 3D RANS (Wang et al. [2012]) and LES (Kim and Xie [2016]). Noteworthy is that the present and cited numerical studies coincide that the LEV shedding occurs at $\alpha \approx 20° \uparrow$ (large drop in lift coefficient), differently to the experimental results where the LEV is shed when the upstroke motion is almost finished. A good agreement is found comparing both C_L and C_D of the present LES adopting the IB method for the airfoil representation with those from Kim and Xie [2016] who used body-fitted meshes.

4.4.1 Cases I.a and I.b

The effect of blade cambering on the development of dynamic stall is analysed comparing the results of the previously validated NACA 0012 with a cambered NACA 4412. The flow and kinematic conditions are identical for both cases, i.e. $Re_c = 1.35 \cdot 10^5$ and $\kappa = 0.10$. This aims at investigating whether blade cambering could delay the LEV shedding and further enlarge the lift capabilities of the airfoil.

The flow field generated over the NACA 0012 and NACA 4412 is visualised to allow quantitative comparisons of the hydrodynamics of dynamic stall. For sake of simplicity, the pitching motion is divided into three stages: upstroke pitching from the minimum angle of incidence until LEV shedding (Fig. 4.6), upstroke pitching under deep stall conditions (Fig. 4.7), and downstroke motion (Fig. 4.8). The flow pattern is visualised in Fig. 4.6 to 4.8 using instantaneous normalised z-vorticity ($\omega_z c/U_0$) contours at a plane at half the spanwise length of the domain, i.e. $z/c = 0.1$. The aerodynamic loads for both airfoils are analysed later on in order to link the force generation with the developed flow field.

Upstroke pitching previous to deep stall

During the first instances of the upstroke motion, $\alpha > \alpha_{min} = -5°$ (see Fig. 4.8e)), the entire suction side of the NACA 0012 features a laminar shear layer without flow separation, whereas the cambered shape of the NACA 4412 induces the generation of a short laminar-to-turbulent transition along the trailing edge. Increasing the pitch angle, at 6.23° ↑ (Fig. 4.6a)), this shear layer remains quite unaffected for the straight airfoil with a vortex shedding at the trailing edge. The NACA 4412 develops rear-to-front flow reversal that shortens progressively the laminar shear layer on the suction side with the generation of coherent vortices. As Fig. 4.6b) shows, at 9.99° ↑ the flow reversal in the latter is extended over more than half of the suction side. The NACA 0012 also experiences flow reversal that breaks down the laminar shear layer due to an adverse pressure gradient induced by the pitching motion. This provokes the onset of Kelvin-Helmholtz instabilities with generation of shear layer vortices. Such phenomenon was also highlighted during experimental work by McAlister and Carr [1979] and Carr et al. [1977],

and numerical simulations from Visbal [2011]. Note that a fine grid resolution is required to accurately resolve such phenomena, as the prediction of these flow instabilities in the simulations with meshes Δx_1 and Δx_2 is not smooth and force fluctuations on C_L are triggered at $5° \uparrow < \alpha < 15° \uparrow$ (see Fig. 4.5a)).

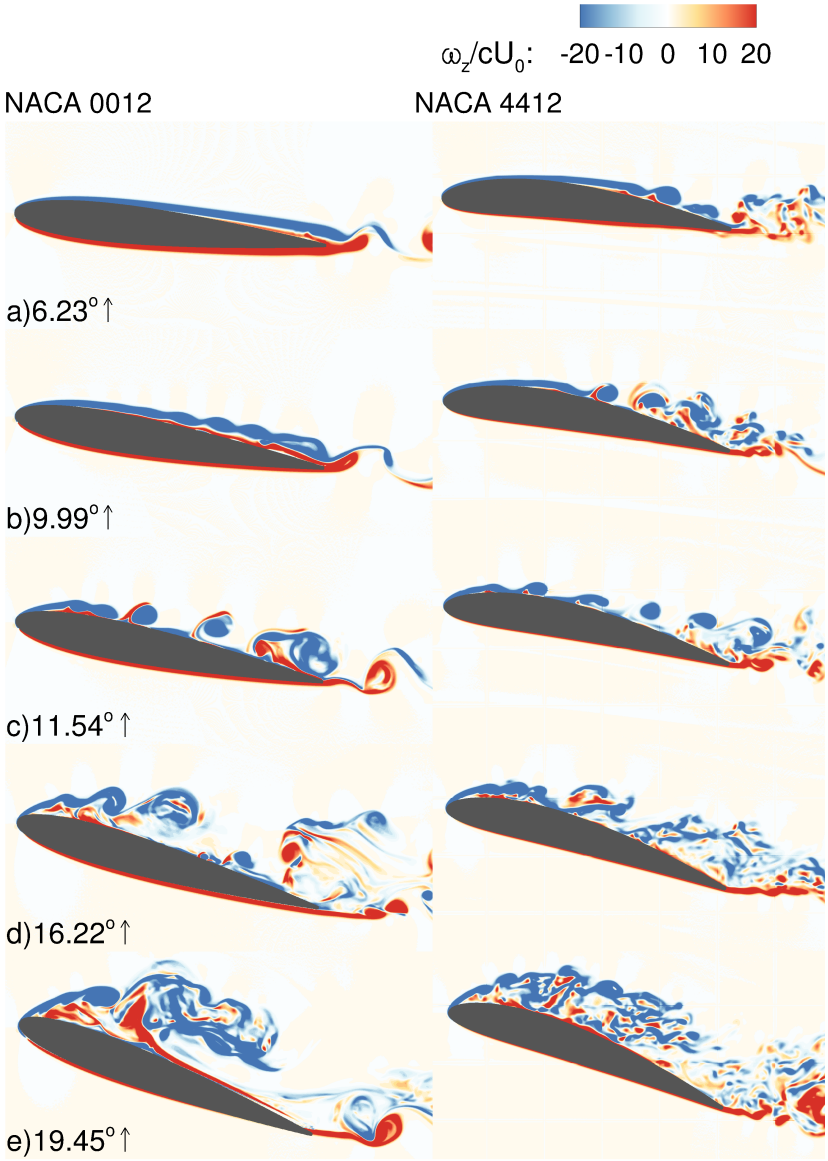

Figure 4.6: Description of the flow pattern developed for the NACA 0012 (left) and NACA 4412 (right) at different phases of the upstroke pitching motion previous to deep stall with normalised z-vorticity ($\omega_z c/U_0$) contours.

Fig. 4.6c) depicts the flow field at $11.54° \uparrow$ before the airfoil reaches the static

stall angle value of $\alpha_{ss} = 13°$ (reported by Lee and Gerontakos [2004]). The suction side of both airfoils shows an analogous situation where a series of coherent vortices are convected along the upper surface, and a small bubble is being formed at the leading edge and extends up to $x/c < 0.10$. This turbulent bubble is the premature formation of the LEV during the first instances of dynamic stall. Fig. 4.6d) exhibits the flow field at 16.22° ↑ where the LEV starts to develop but is already separated from the NACA 0012 whereas in the NACA 4412 it is attached until $x/c \approx 0.3$ where the its separation occurs. Noticeable differences on the flow field between the two airfoils are observed in Fig. 4.6e) at 19.45° ↑ especially of the LEV behaviour. For the straight airfoil, this large-scale flow structure is detached from the upper surface and there is a recirculating bubble along the first quarter of the chord. Meanwhile, the cambered airfoil permits the LEV to be generated and develop attached to the upper surface.

Upstroke pitching at onset of stall and post-stall conditions

The increase of pitch angle induces the LEV to grow in size and to extend over almost the entire upper surface of both airfoils, as depicted in Fig. 4.7a). At this stage, the LEV distribution is similar for both NACA 0012 and 4412 as it is not completely attached to any of the airfoils, and is accompanied by a recirculating area (enclosed bubble) along the first half of the suction side. At an angle of 21.17° ↑, the straight airfoil overcomes the dynamic stall angle of $\alpha^s_{ds} \approx 20.8°$ ↑ and hence is already under post-stall conditions. On the other hand, the NACA 4412 dynamic stall angle is $\alpha^c_{ds} \approx 21.3°$ ↑ so at α=21.17° ↑ the LEV is still attached but close to be shed and the airfoil to stall. Note that the LEV formation process is a critical stage affecting the airfoil forces behaviour as it is the responsible for the lift overshoot during dynamic stall, and its shedding causes a dramatic drop in the aerodynamic coefficients.

During the remaining upstroke motion, both airfoils are under deep dynamic stall conditions and thus lack of lift generation capabilities. At 22.74° ↑, Fig. 4.7b), the LEV moves away from both airfoils, and its clockwise rotation induces the generation of a Trailing Edge Vortex (TEV) that features a counter clockwise rotation. This primary TEV increases gradually and becomes the dominating

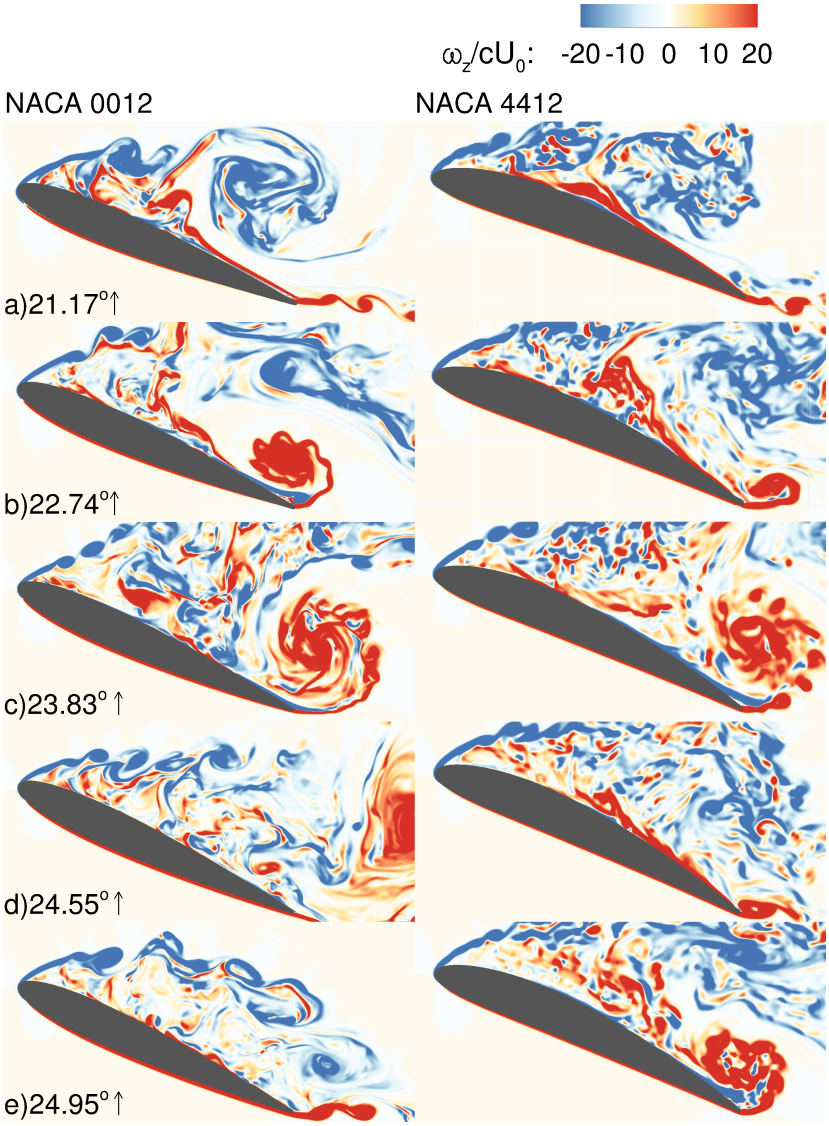

Figure 4.7: Description of the flow pattern developed for the NACA 0012 (left) and NACA 4412 (right) at different phases of the upstroke pitching motion during post-stall conditions with normalised z-vorticity ($\omega_z c/U_0$) contours.

large-scale flow structure at 23.83° ↑, Fig. 4.7c). Before the maximum pitch angle is reached, the TEV is eventually shed allowing the enclosed recirculating bubble to extend over the upper surface of both airfoils, as observed in Fig. 4.7d). Near to completion of the upstroke motion, at $\alpha = 24.95°$ ↑, a secondary TEV is formed at the NACA 4412 trailing edge, whilst in the NACA 0012 this is not

appreciated and the enclosed recirculating area dominates the airfoil suction side.

Downstroke pitching

Fig. 4.8a) shows the normalised vorticity contours at 24.52° ↓. The development of a secondary TEV on the NACA 0012 is observed shortly after the downstroke movement started. This provides evidence of the rapid formation and shedding of large-scale structures during post-stall conditions. In the cambered airfoil, the TEV formed during the last stages of the upstroke motion is still attached. Once the airfoil pitches down, this TEV is shed and the flow field becomes again dominated by the recirculating bubble followed by front-to-rear flow reattachment and irregular shedding of LEVs and TEVs. At 13.90° ↓, Fig. 4.8b), the shear layer developed from the leading edge extends along the suction side for both airfoils. Fig. 4.8c) shows that reducing the pitching angle further results in flow reattachment until $x/c \approx 0.1$. At 0.00° ↓, the NACA 4412 exhibits a laminar shear layer until $x/c \approx 0.85$ while for the straight airfoil it covers the first half of the suction side. In the flow field at the minimum angle of attack ($\alpha = -5°$ ↓, Fig. 4.8e)), there is an absence of any turbulent flow phenomena over the upper surface of both airfoils, whilst on their pressure side the shear layer breaks down and roll-up vortices are generated and shed. The latter phenomenon is more accentuated in the NACA 4412 due to its convex shape pressure side, which shortens the laminar shear layer compared to that of the NACA 0012.

Flow three-dimensionality

Turbulence structures and three-dimensionality of the flow over the pitching NACA 4412 airfoil are visualised in Fig. 4.9 and 4.10. Three-dimensional views of iso-surfaces of the spanwise vorticity and contours of streamwise velocities at half spanwise domain width ($z/c = 0.1$) are depicted in Fig. 4.9. At 11.54° ↑, the free shear layer at the leading edge of the airfoil exhibits two-dimensionality and laminar separation until it becomes unstable and transitions to three-dimensionality in the form of rollers due to Kelvin-Helmholtz instabilities. Such vortices are fairly coherent in the spanwise direction initially due to the absence of turbulent

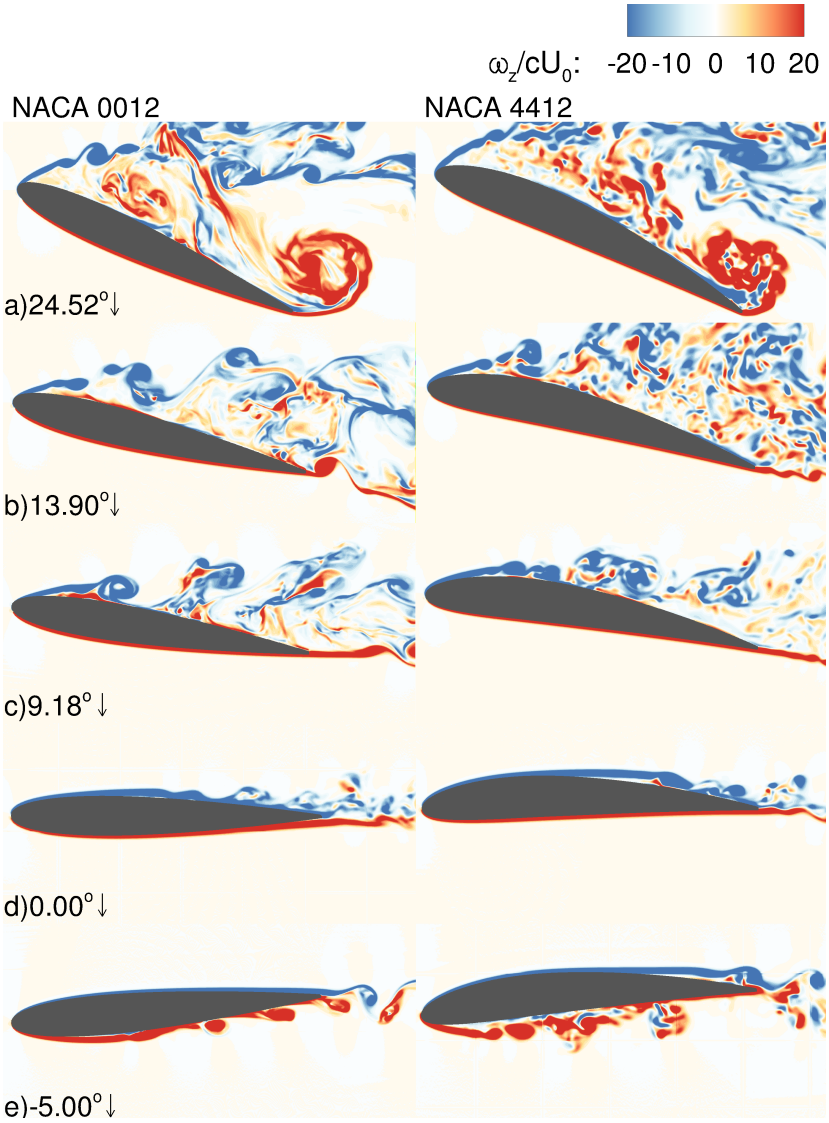

Figure 4.8: Description of the flow pattern developed for the NACA 0012 (left) and NACA 4412 (right) at different phases of the downstroke pitching motion with normalised z-vorticity ($\omega_z c/U_0$) contours.

instabilities. Nonetheless, spanwise instabilities emerge as the shear layer rollers exhibit some undulation in this direction. Fig. 4.10 presents two iso-surfaces of streamwise vorticity with opposite sign and identifies the onset of coherent periodic instabilities in the rollers that are close to the leading edge. A total of four instabilities are depicted along the spanwise domain ($H = 0.2c$) and their wave-

length is $d_w = 0.2c/4 = 0.05c$ being constant in the first three rollers depicted here. It is noteworthy that the spanwise wavelength remains constant irrespective of their size. Similar pattern of these perturbations were observed in the DNS of a static NACA 0012 by Jones et al. [2008]. Additionally, Visbal [2011] identified an analogous onset of spanwise perturbations in their ILES of a SD7003 plunging airfoil and the size of the developed spanwise instabilities was found to be $d_w \approx 0.04c$ which agrees well with the present observations.

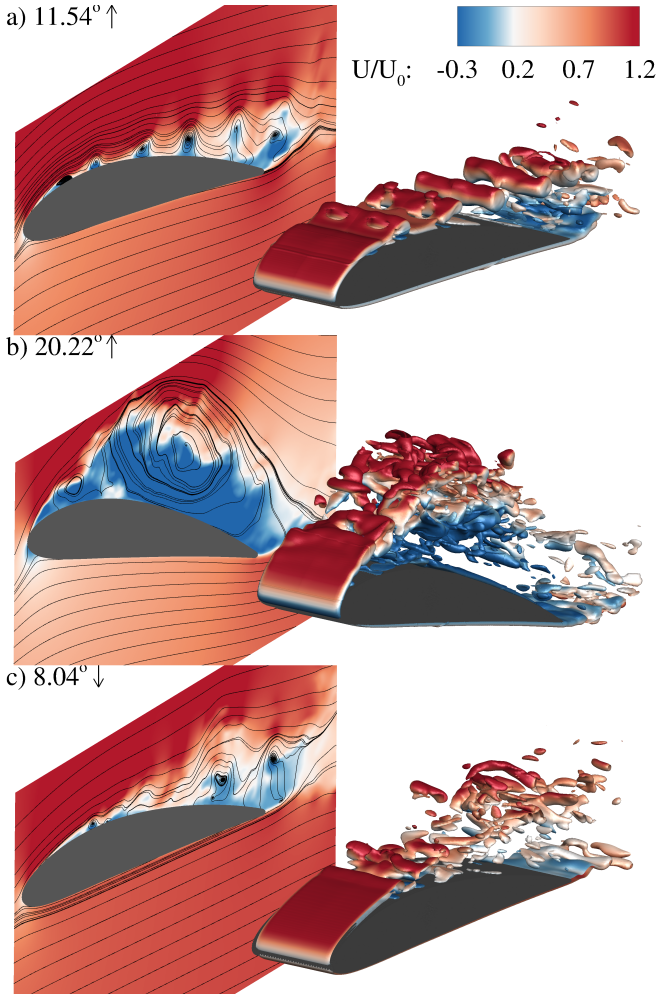

Figure 4.9: Iso-surfaces of normalised spanwise vorticity ($\omega_z c/U_0 = \pm 30$) coloured with normalised streamwise velocity (U/U_0) for the NACA 4412 at three pitch angles.

At 20.22° ↑ the large-scale LEV vortex dominates the airfoil as streamlines

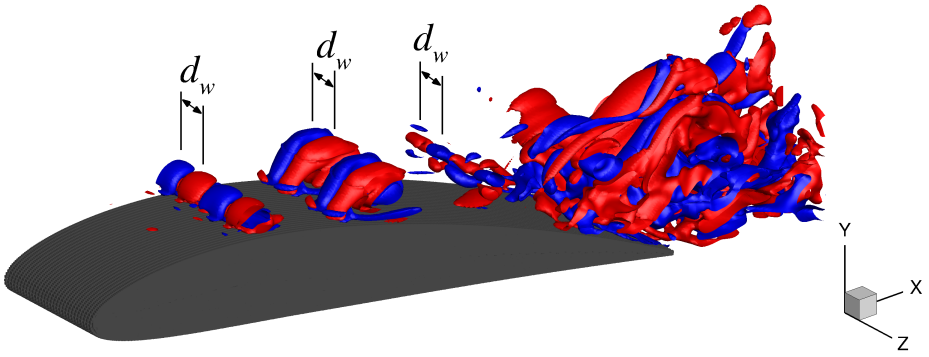

Figure 4.10: Iso-surfaces of normalised streamwise vorticity for the NACA 4412 at 11.54° ↑, with blue and red surfaces corresponding to $\omega_x c/U_0 = 8$ and -8, respectively.

and iso-surfaces plotted in Fig. 4.9(b) show. The z-vorticity iso-surfaces suggest an almost instant transition from the 2D shear layer to 3D structures which are predominant around the LEV. At this pitch angle the flow over the upper surface is dominated by flow reversal (blue areas in the velocity contours) whose interaction with the free-stream velocity above results in strong velocity shear at the interface and causing strong turbulence.

During downward pitching, at 8.04° ↓ (Fig. 4.9(c)), the laminar shear layer extends further downstream along the upper surface. Full flow separation over the second half of the upper surface is observed during the entire pitch-down cycle. Shear layer turbulence in the form of fairly incoherent small scale structures is found towards the tail of the airfoil. Such complex front-to-rear reattachment is notably different from the smooth laminar-to-turbulent transition experienced during the pitch-up motion as shown in Fig. 4.9(a). These visualisations suggest that after the airfoil undergoes deep stall, with the separated flow over the upper surface being fully three-dimensional, the process of flow relaminarisation and hence the airfoil's ability to generate lift is delayed in comparison to the pitch-up process.

Flow phenomena such as shear layer transition, flow separation or reattachment are key in the aerodynamics around pitching airfoils. Fig. 4.11 shows various of these events developed at different stages of the pitching cycle using iso-surfaces of Q-criterion=300 (Hunt et al. [1988]) coloured with streamwise

velocities with top-views of the airfoil from (a) to (g) whereas (h) shows a bottom-view at $\alpha = -5° \downarrow$. During upstroke motion previously to the generation of the LEV ($\alpha < \alpha_{ss}$), the turbulence above the upper surface of the airfoil features a roller-like shape as shown in Fig. 4.11(a) to (c). The onset of spanwise instability is again observed from the top-view of Fig. 4.11(c). During the development of the LEV at 21.17° ↑, coherent iso-surfaces of Q-criterion are found until $x/c = -0.1$ corresponding to the stable free shear layer. Following a quick turbulent transition, the flow becomes unstable shortly after the shear layer breakdown and non-coherent small-scale structures are distributed over the LEV influence area.

The complexity of the front-to-rear flow reattachment during the downstroke cycle is depicted in Fig. 4.11(e) and (f) for which after $x/c = 0.0$ the shear layer breaks into three-dimensional smaller-scale structures that evidence the chaotic turbulent structures distribution in the area of full flow separation. Close to completion of the downstroke motion, at 0.00° ↓ the flow over the upper surface of the airfoil still features some separation due to the convex shape of the NACA 4412's upper surface. Finally, the bottom view of Fig. 4.11(h) presents the flow development along the pressure side of the airfoil. Due to the cambered shape of the NACA 4412, there is a prompt flow separation on this side compared to that exhibited during pitch-up motion at a similar angle of attack.

Effect of blade cambering on the aerodynamic coefficients

The effect of blade cambering on the aerodynamic coefficients is quantified in Fig. 4.12, where the right column shows the values of C_L, C_D and C_M between $19° < \alpha < \alpha_{max}$ of the aerodynamic coefficients from the left column plots. α^s_{ds} and α^c_{ds} stand for the dynamic stall pitch angle for the straight and cambered airfoils, respectively.

Fig. 4.12a) exhibits how using a cambered profile the lift capabilities are enlarged along both upstroke and downstroke. This is appreciated throughout the cycle except when the airfoil stalls, i.e. $\alpha > \alpha_{ds}$. The NACA 4412 hysteresis loop, i.e. the difference on C_L values at the same angle of attack between upstroke and downstroke phases, is smaller compared to that of the NACA 0012. These findings agree with Choudhry et al. [2014] who stated that the hysteresis loops on

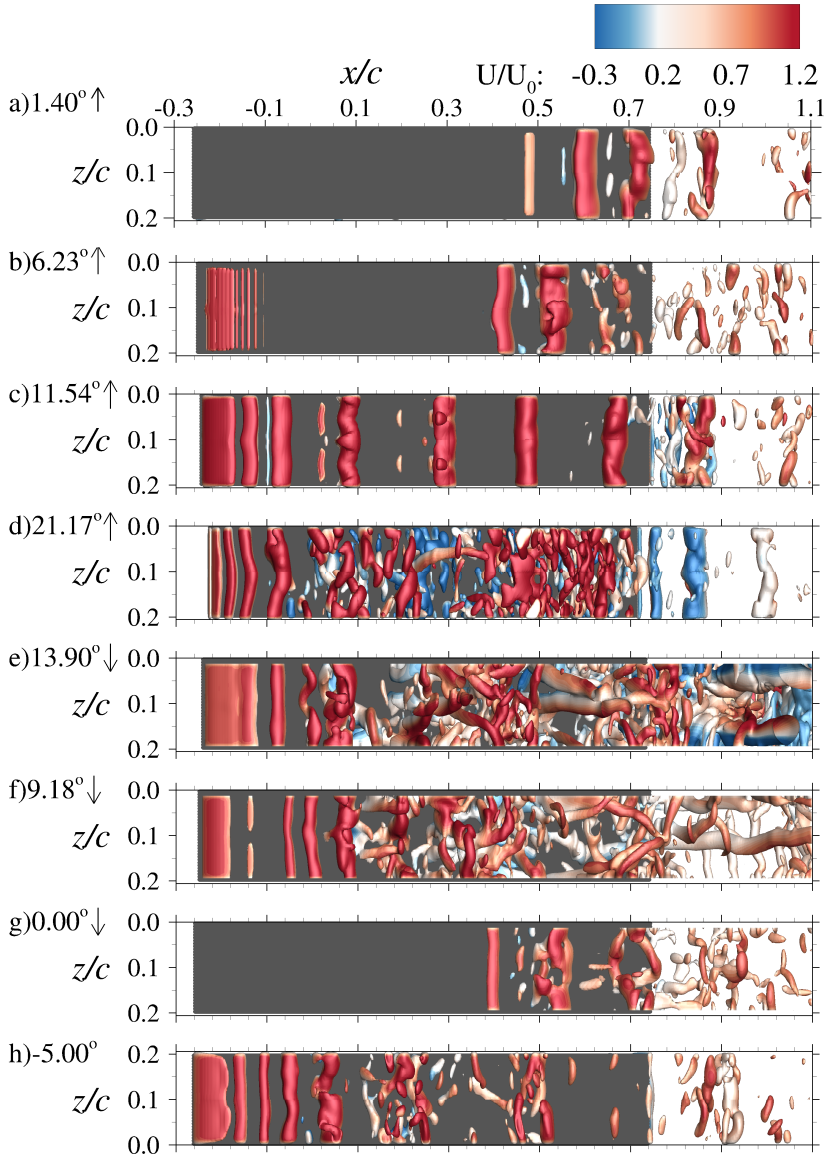

Figure 4.11: Plan-view of the turbulent structures generated during the pitching cycle of the NACA 4412 represented with iso-surfaces of Q-criterion=300 coloured with instantaneous streamwise velocities. (a) to (g) show the top-view at different pitch angles, and (h) shows the bottom-view at the minimum angle of attack of $\alpha = -5°$.

cambered airfoils are smaller.

The onset of the LEV provokes a lift overshoot in both airfoils starting at $\alpha \approx 17°$ until its shedding at $\alpha = \alpha_{ds}$. During this high lift generation stage,

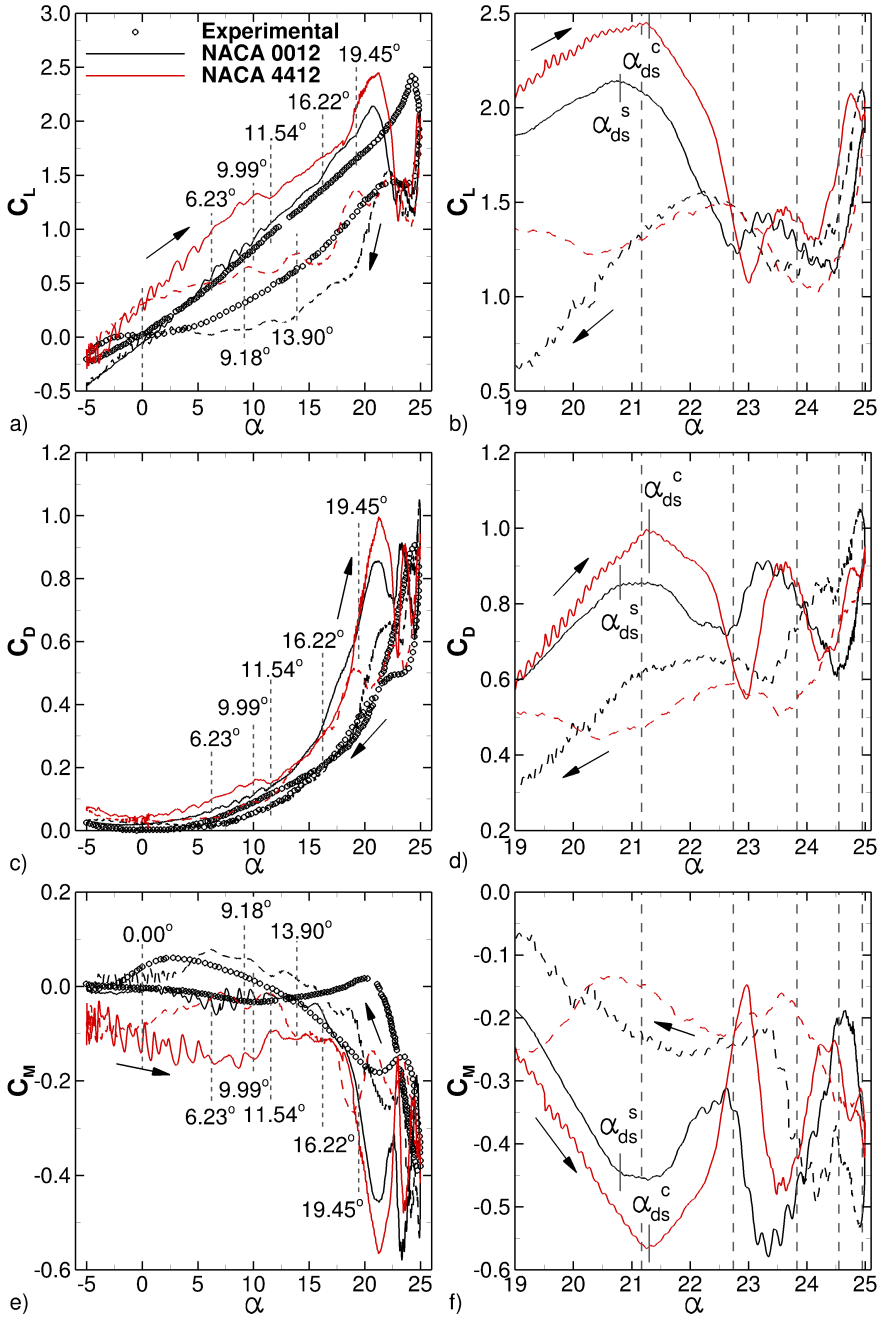

Figure 4.12: Comparison of the phase averaged computed C_L (a) and b)), C_D (c) and d)) and C_M (e) and f)) for the NACA 0012 and 4412 and experimental results (Lee and Gerontakos [2004]). Straight and dashed lines denote upstroke and downstroke movements respectively.

the NACA 4412 generates larger values compared with those of the NACA 0012 together with a steeper C_L slope. Carr et al. [1977] identified this stage as when moment stall occurs, in which the C_M slope suffers a notable value increase due to the LEV action, as depicted in Fig. 4.12e). The difference in lift generation between airfoils is a consequence of the LEV remaining attached closer to the suction side of the NACA 4412 than to the NACA 0012, as depicted in Fig. 4.6e) with $\alpha_{ds} = 19.45° \uparrow$. This flow development also triggers larger C_m values for the cambered airfoil.

The fact that the LEV is slightly away from the airfoil upper surface makes it more vulnerable to the free-stream flow and hence easier to be shed. As a result of this, the dynamic stall angle for the straight airfoil α^s_{ds} is approx. $20.7° \uparrow$, whereas for the cambered is $\alpha^c_{ds} \approx 21.3° \uparrow$. Thus, cambering the airfoil provides a short delay on the LEV shedding as well as an additional lift overshoot. Maximum C_L values are depicted from Fig. 4.12b) showing that at α_{ds} the NACA 0012 exhibits a peak of 2.1 whilst this increases up to 2.45 for the cambered airfoil. Therefore, the cambered airfoil generates approx. 15% more maximum lift than the straight airfoil.

The post-stall behaviour ($\alpha > \alpha_{ds}$) is characterised by the shedding of the LEV causing a dramatic drop on C_L, C_D and C_M. These coefficients show very similar patterns during post-stall conditions irrespective of the airfoil profile. This is in line with the findings from McCroskey et al. [1981], who stated that under post-stall conditions the blades lose their aerodynamic capabilities, i.e. they behave similarly to simple bluff bodies.

During the downstroke motion, the flow starts to develop front-to-rear reattachment since $\alpha \approx 20° \downarrow$ wherein the coefficients start to stabilise. Flow recovery is characterised by the shear layer formed at the leading edge, and whose extension increases along the upper surface as the airfoil decreases its pitch angle. The airfoil cambering provides an improvement on this boundary layer reattachment process, and hence its capability to generate lift again. This is related to the flow field observed in Fig. 4.8b) to d), where the flow relaminarisation on the upper surface of the NACA 4412 is quicker than for the NACA 0012. Consequently, since $\alpha \approx 10° \downarrow$ the NACA 4412 produces values of $C_L \approx 0.5$, in contrast to the NACA 0012 that generates negligible values of lift. At negative pitch angle

values, the latter always exhibits negative lift coefficient values with minima of approx. -0.5, whilst in the former the change from positive to negative C_L values is achieved at $\alpha \approx -2.5°$, and a minimum value of $C_L = -0.25$ is found.

Coefficient of drag results are shown in Fig. 4.12c) and d). The NACA 4412 produces larger amount of drag when $\alpha < 10°$, i.e. before overcoming the static stall angle, while it remains similar to the NACA 0012 in the rest of the C_D curve. At the shedding of the LEV, $\alpha \approx \alpha_{ds}$, the overshoot of lift forces produced by the cambered airfoil is also accompanied by a drag increase. Under post-stall conditions both airfoils generate same the amount of drag. During the pitch-down and after $\alpha < 20° \downarrow$, the quicker boundary layer reattachment on the NACA 4412 leads to higher C_D values which are maintained until $\alpha \approx 12° \downarrow$ when both bodies generate similar values of C_D.

The C_M results are depicted in Fig. 4.12e) and f). The cambered shape of the NACA 4412 leads to a constantly larger generation of pitching moment until post-stall conditions are reached. Note that it constantly generates negative C_M values whilst the NACA 0012 experiences positive values during the downstroke motion. Discrepancies between the computed results and the experimental data Lee and Gerontakos [2004] are observed at high angles of attack, similarly to those found by Kim and Xie [2016]. They argued that in the experiments the pressure probes covered 91% of the airfoil surface from the leading edge whereas in the numerical models the forces are integrated along the whole airfoil chord. Hence, the C_M results are not close the experimental maximum values as the latter do not account for the forces in the last $0.09c$ of the airfoil, which is the part with highest TEV influenced, as previously observed in Fig. 4.7b) and c).

Fig. 4.12a) and b) exhibit that the larger C_L peak of the NACA 4412 compared to the NACA 0012 goes along a drag increase, as observed in Fig. 4.12c) and d). This lift overshoot during dynamic stall is positive towards designing VATs as they are lift-driven devices. The increased drag is suboptimal as it enlarges the friction of the blades reducing the turbine's performance and self-starting capabilities. The lift-to-drag ratio (C_L/C_D) for large angles of attack, i.e. $\alpha > 19°$, is presented in Fig. 4.13. Under the post-stall conditions, the cambered NACA 4412 achieves a larger C_L/C_D ratio compared with the NACA 0012. Thus, the benefits of enlarging the lift forces is greater than the drawback associated to

the drag increase. These findings invite to consider that using a NACA 4412 could over-perform the VAT characteristics compared to those when using a NACA 0012.

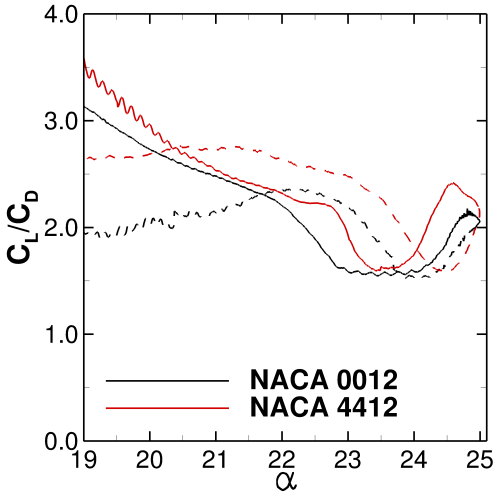

Figure 4.13: Comparison of the phase averaged computed lift-to-drag coefficient (C_L/C_D) for the NACA 0012 and 4412. Straight and dashed lines denote upstroke and downstroke movements respectively.

4.4.2 Case II

A NACA 0012 is now subjected to a pitching motion with higher pitching frequency, $\kappa = 0.16$, and lower Reynolds number, $Re_c = 36,000$. The higher pitching oscillation also induces the airfoil to undergo deep dynamic stall. The reduced angle amplitude, compared to case 1.a, diminishes the time to accomplish flow reattachment as explained in the following. This case targets at representing a closer scenario where small-to-medium scale VATs operate in compared to case I.a. The mesh resolution Δx_3 and time step value Δt_2^* are again adopted.

Fig. 4.14 presents the contours of normalised z-vorticity at 10 different stages of the pitching cycle during both pitch-up and pitch-down motions. At the lowest pitch angle, $\alpha = 4.00° \uparrow$, the boundary layer remains attached allowing the first half of the suction side followed by laminar-to-turbulent transition, as depicted in Fig. 4.14a). Once the upstroke movement commence, the shear layer shortens and

breaks into large-scale roll-up vortices. This onset of Kevin-Helmholtz instability differs from case I.a, where the laminar shear layer extends along the upper side and forms roller vortices due to adverse pressure gradient. Note that in case II the upper surface features laminar-to-turbulent transition and vortex shedding similarly to the flow over a static airfoils from Castiglioni et al. [2014]; Jones et al. [2008]; Shan et al. [2005].

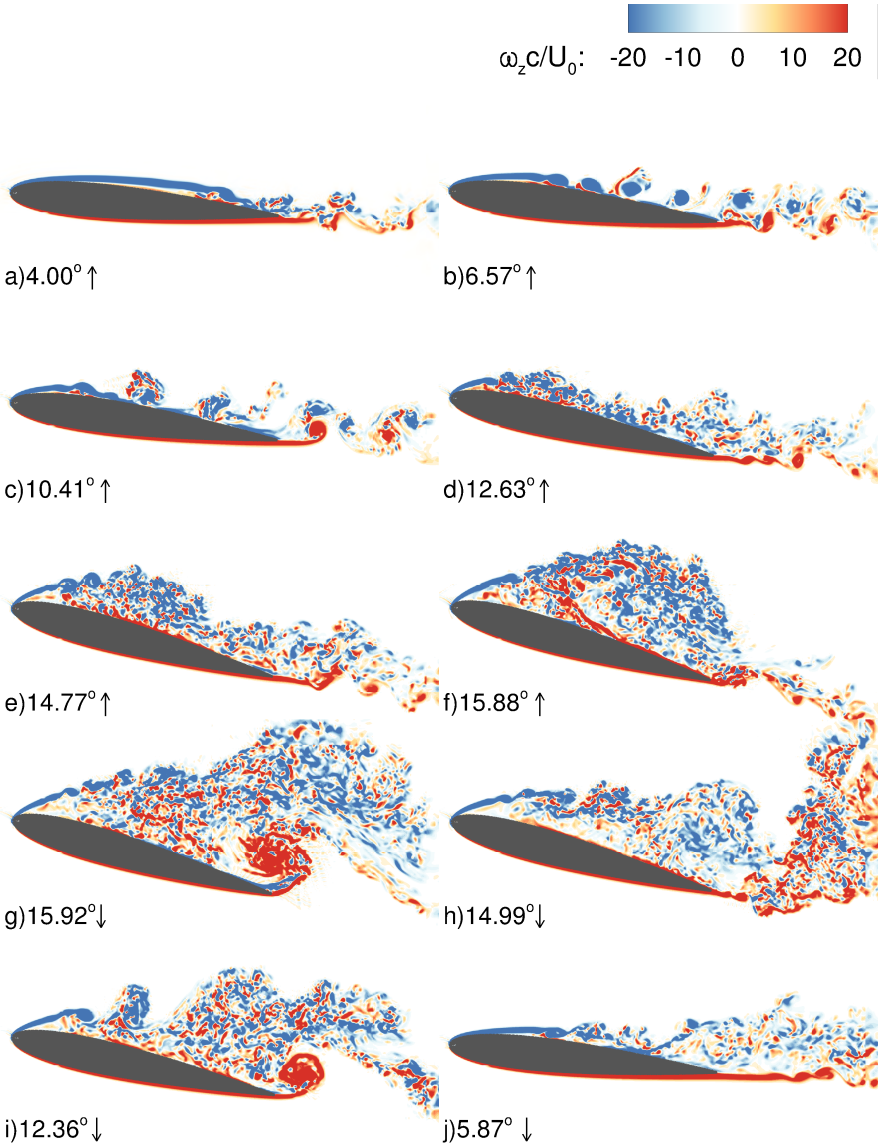

Figure 4.14: Contours of $\omega_z c/U_0$ describing the flow pattern experienced by the NACA 0012 during 10 phases of the pitching cycle in case II.

The progressive shortening of the laminar shear layer is observed at $\alpha = 6.57° \uparrow$ which is extended over a quarter chord length from the leading edge and is further reduced at $\alpha = 10.41° \uparrow$, Fig. 4.14c). This angle represents the flow field shortly before overcoming the static stall angle of $\alpha_{ss} = 10.5°$, reported by Lee and Su [2015]. Ever since this is accomplished ($\alpha > \alpha_{ss}$), the lift overshoot in the airfoil corresponds to the LEV generation after the shear layer breakdown. The onset of the latter is appreciated in Fig. 4.14d). Its size increases together with the pitch angle and continuously grows to occupy a larger extension over the upper surface, as depicted in Fig. 4.14e) with $\alpha \approx 14.77° \uparrow$. At this stage, the enclosed wake features a larger instability compared that found in the previous case I.a (see Fig. 4.7a), which is invites to consider that higher pitching rates induce larger instability in the enclosed region. At $\alpha = 15.88° \uparrow$, the airfoil approaches the maximum pitching angle and the LEV extends over the full upper surface of the airfoil, as observed in Fig. 4.14f). This pitch-up movement is accomplished before the generation of a TEV.

During the first instances of the downstroke ($\alpha = 15.92° \downarrow$) a TEV is rapidly generated induced by the upwards movement of the trailing edge of the airfoil. This energetic flow structure is quickly convected towards the LEV inducing the shedding of the latter due to their opposite rotation. At $\alpha = 14.99° \downarrow$, the TEV is shed and a secondary LEV is formed. A shedding sequence of TEVs and LEVs characterises the remaining downstroke movement in conjunction with a progressive reattachment of the laminar shear layer from the leading edge, as appreciated in Fig. 4.14h) to j).

Lift and moment coefficients for case II are compared with the experimental results from Lee and Su [2015] in Fig. 4.15. The computed C_L shows an over-prediction along the upstroke motion, which is enlarged at large values of α. Similar to the reported by Kim and Xie [2016] for case I.a, this difference is because in the experimental pressure probes cover the leading 91% of the airfoil length while the computational model integrates the forces over the whole chord length. This is also source of discrepancies in the moment coefficient for $\alpha > 14° \uparrow$, as seen in Fig. 4.15b).

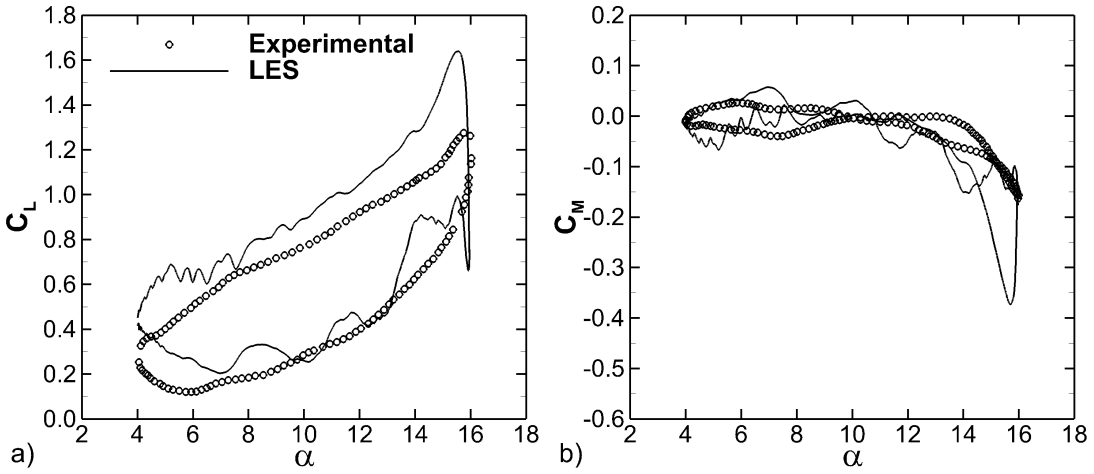

Figure 4.15: Computed coefficients for the case II. Comparison of the experimental results from Lee and Su [2015] with the computed a) C_L and b) C_M.

4.5 Summary

The large eddy simulation of three different pitching airfoil cases undergoing deep dynamic stall has been presented. Cases I.a and II have been validated with experimental data and numerical results from other authors confirming the accuracy of the LES-IB approach. A fine mesh resolution and small time step were required to achieve a correct representation of the flow phenomena, characterised by a wide range of large-to-small scale flow structures.

The airfoil cambering influence was analysed comparing a NACA 0012 and a NACA 4412 under same flow and kinematic conditions. Results shown significant aerodynamic performance variation during pre-stall conditions highlighted by larger lift generation of the cambered airfoil as well as smaller dynamic hysteresis loop. The dominating LEV produced an extra lift overshoot for the cambered airfoil accompanied by a short delay on its shedding. Under post-stall conditions, both airfoils behaved almost identically with a successive generation and shedding of LEVs and TEVs causing an irregular generation of aerodynamic forces. Such flow development under deep stall conditions agreed well with other experimental findings, outlining that during full flow separation the airfoil loses its aerodynamic capabilities, and thus blade cambering effects are lost. During the downstroke motion, the NACA 4412 has featured a quicker boundary layer

reattachment together with a larger lift generation.

A third case was reproduced with closer flow and kinematic conditions to where medium scale vertical axis turbines operate in. The computed lift and moment coefficients achieved an overall good agreement with experimental data. These successful comparisons confirmed the accuracy of the LES-IB approach for the simulation of complex flows. The presented results shown that blade cambering could be beneficial in the design of VATs in terms of (i) delaying the onset of deep dynamic stall, (ii) enlarging lift generation capabilities, and (iii) reducing the dynamic hysteresis loop, which potentially diminish fatigue loads on the turbine.

Chapter 5

Simulation of Vertical Axis Tidal Turbines

5.1 Introduction

Most of the current knowledge on the performance of VATTs has been obtained from experimental work. One of the first experimental campaigns was conducted by Brochier et al. [1986], who visualised the flow field generated after a VATT and highlighted that these devices are highly influenced by dynamic stall. Shortly after, studies on this turbine typology targeted at improving their efficiency, such as Takamatsu et al. [1991] who analysed the performance using different hydrofoil profiles. Kiho et al. [1996] tested a Darrieus-type turbine under different velocity conditions in order to study how its power generation capacity changes. Roa et al. [2010] analysed the performance of a VATT in a confined water tank with and without ducts. The influence of the turbine's solidity was studied by McLaren [2011] while Fiedler and Tullis [2009] focused on turbine parameters such as blade and shaft shapes, pitch angle, and location of blade attachment to the shaft. At a larger scale, Han et al. [2013] carried out an extensive field testing of a pre-commercial prototype that obtained an approx. 32% efficiency. Other recent studies looked at the effects of blade roughness (Priegue and Stoesser [2017]) or turbine helicity (Bachant and Wosnik [2015]) on the performance of VATTs. A

complete review of recent tidal turbine technologies is provided by Khan et al. [2009].

Experimental studies are costly and time-consuming and the available information from these tests is not enough to fully understand the complex fluid-structure interaction of VATTs. Numerical models, if accurate and trustworthy, can provide a more complete picture of the complex flow-turbine-interplay. However, highly turbulent flows and the complex fluid-structure interaction of a rotating device calls for advanced computational models. One of the simplest numerical approaches is the vortex panel method (Islam et al. [2008]) which offers some understanding of the turbine's hydrodynamics but has severe limitations, such as assuming that lift and drag coefficients are constant over one revolution or the omission of the effects of unsteadiness and turbulence.

CFD has become a powerful tool for predicting the operation and performance of tidal turbines. Tidal turbine CFD simulations are generally based on the RANS equations as they are less demanding in terms of computational cost than other CFD closures. Maître et al. [2013] used a 2D RANS k-ω SST model to reproduce the experimental results from Roa et al. [2010], and they found that this approach tends to overestimate the experimental results which was related to the lack of consideration of 3D effects in the model. McNaughton et al. [2014] reproduced the setup from Maître et al. [2013] adding the Low-Reynolds number Effect (LRE) correction to the 2D RANS k-ω SST model which tries to improve the provide more accurate representation of the transitional effects, e.g. laminar to turbulent, near the walls improving the production/dissipation rate predictions. The results were improved with the change of the turbulence model although they were still unable to match the experimental data. Similar analysis was done by Howell et al. [2010] using 2D and 3D RANS with the $k-\varepsilon$ RNG turbulence model for a VAWT. The lack of accuracy of the 2D RANS model was again obvious, highlighted by a large overestimation of the power coefficient, whilst the 3D model reduced the overestimation significantly demonstrating the importance of reproducing the 3D nature of the flow around vertical axis turbines. Marsh et al. [2015] analysed the influence of different helicolidal configurations on a VATT using 3D RANS, and provided relevant outcomes to understand the impact of this geometrical variation onto the device's performance.

One reason for the lack of accuracy of RANS based approaches to predict flow-turbine interaction is that these are governed by large-scale turbulence. The method of LES is, in theory, more suited to simulate these interactions due its demonstrated higher accuracy compared to RANS in predicting flows dominated by large-scale energetic vortices. However, the computational requirements of LES are much higher than those of RANS and this is a limitation to most researchers and practitioners, Kear et al. [2015]; Rodi et al. [2013]; Stoesser [2014]. Most LES studies are in the area of VAWTs: Iida et al. [2007] compared results of momentum theory-based calculations with LES achieving a good match between them although no comparison with experimental data was performed. Li et al. [2013] performed a more complete analysis comparing outputs of 2D and 3D RANS and LES with performance data of a VAWT previously tested by McLaren [2011]. They demonstrated the higher accuracy of LES compared to RANS but pointed out that the vertical extension of the domain may have an impact on the final results. Elkhoury et al. [2015] performed the LES of a full 3D VAWT model including the analysis of the effects of blade shape and fixed or variable pitch angle on the VAWT's performance. Their results agreed well with experimental data. Furthermore, their complementary LES and experiments demonstrated that the power coefficient of the VAWT can be increased by employing variable-pitch turbine blades. Recently, Posa et al. [2016] performed the LES of a VATT using the immersed boundary method. The numerical results were well validated with experimental data in terms of wake velocity and turbulent kinetic energy profiles, although they do not report the performance predicted with LES and compare it with experimental data.

Aim of the chapter

The objective of this chapter is to demonstrate the applicability and accuracy of the LES-IB approach to simulate a VATT, and to provide insights into the complex blade-vortex interactions of the device operating at different rotational speeds, i.e. at different flow regimes.

The chapter is organised as follows: the LES-IB model is thoroughly validated for a VATT subjected to a 2D laminar approach flow in Section 5.2. Section 5.3

shows an in-depth study of a VATT subjected to turbulent flow: error convergence of the LES-IB method, hydrodynamic coefficients, wake downstream, and power performance compared to the results from RANS-based approaches and experiments. The visualisation of the blade-vortex interaction at different tip speed ratios and the power spectral density of the velocity series from a point located inside the turbine's swept area are also presented with the goal to shed some light on the complex flow-turbine interaction.

5.2 VATT subjected to laminar flow

The first validation test is a three-bladed Darrieus turbine subjected to laminar flow. This VATT has been simulated previously with sophisticated body-fitted CFD models by Ferrer and Willden [2015] and Ramírez et al. [2015] who employed a high-accuracy Galerkin method and a high-order finite volumes method, respectively, and their results are used for model comparison. The chosen test-case allows quantitative assessment of the accuracy of the predictions of normal and tangential forces, and the method's ability to resolve the fluid-structure interaction which generates the torque at the turbine shaft. Further, the absence of the effects of turbulence eliminates uncertainties regarding the accurate representation of laminar-to-turbulent boundary layer transition or the impact of small-scale turbulence.

The setup and boundary conditions of a 3-bladed VATT driven by laminar flow are chosen analogue to the ones of Ferrer and Willden [2015] and Ramírez et al. [2015]. All dimensions are normalised by the chord length of the turbine blade. The radius of the VATT is $R = 2c$, the prescribed fixed rotational velocity is $\Omega = 0.5$ rad/s, and the inlet velocity is set to $U_0 = 0.5$. The resulting Reynolds number based on the chord is 100 and the tip speed ratio is 2. The numerical domain extends $24c$ in the streamwise and $18c$ in the spanwise direction. The turbine centre is placed at $9c$ from the inlet and in the middle of the channel with regards to the spanwise direction. The mesh resolution is similar to the two reference cases and is approximately $\Delta x = \Delta y = 0.02c$. Three different constant time step sizes are used, i.e. CFL=0.8, 0.45 and 0.2 (where $CFL = U_{tip} \cdot \Delta t / \Delta x$,

and $U_{tip} = \Omega R$ stands for the tip speed), in order to assess the effect of time step size on the accuracy of the simulation.

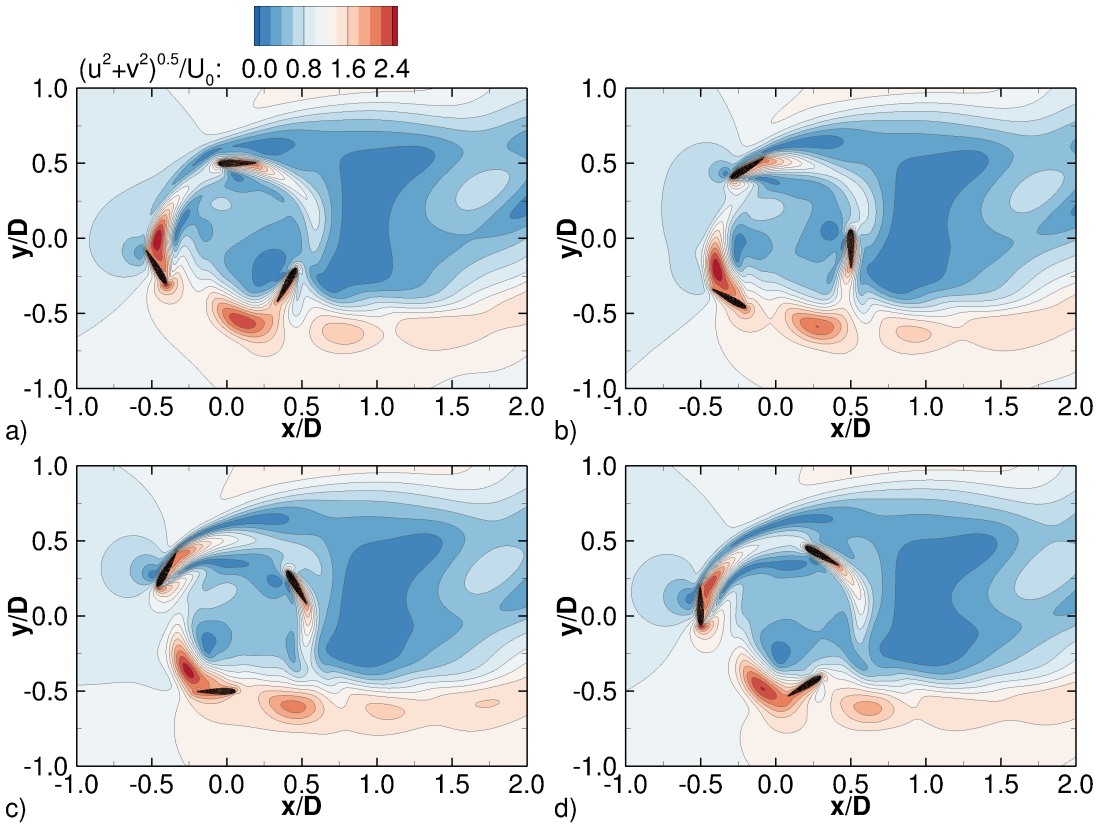

Figure 5.1: Normalised velocity magnitude contours at θ = a) 0°, b) 30°, c) 60°, and d) 90° after the first VATT blade has rotated three full revolutions with the laminar flow conditions.

Fig. 5.1 presents the normalised velocity magnitude contours at four instants in time. The velocity contours near the blades at $\theta = 1080°$ (Fig. 5.1a)) are smooth and comparable with the ones presented by Ramírez et al. [2015]. Noteworthy are the distinct features of VATTs as: (i) formation of high-velocity wakes (red colour areas) behind the blades specially the formed in their inner side along the upstream side of the rotation, i.e. $0° < \theta < 180°$, and (ii) significantly varying near-field hydrodynamics around the turbine with a low-velocity wake region developed immediately downstream the device (blue colour areas).

A quantitative validation of the simulation outputs is obtained through Fig. 5.2 which shows the normal and torque coefficient for $360° \leq \theta \leq 1080°$. A remark-

ably good agreement of the coefficients predicted by the present IB-based simulation with the ones from the body-fitted models is achieved. There is some sensitivity of the results to the time-step value, and the smallest gives the best agreement of predictions with the data from the reference calculations. In terms of the torque coefficient predictions there appears to be a better agreement with Ramírez et al. [2015] on the upstream side of the revolution whilst a closer match with Ferrer and Willden [2015] is obtained on the downstream side. Regarding the normal coefficient, the solution with the smallest time-step shows a good agreement with the referenced data both in maxima and minima values as well as in the overall distribution. Overall, the IB method reproduces well the turbine-flow interaction and the resulting hydrodynamic coefficients. The torque and normal force coefficient curves are continuous and smooth as a result of using constant time step values.

5.3 VATT subjected to turbulent flow

A more complex test case is the simulation of a VATT comprised of three cambered NACA 0018 blades subjected to a turbulent approach flow. This challenging test case is chosen because experimental data of Roa et al. [2010] and numerical results of Maître et al. [2013] and McNaughton et al. [2014] are available to assess the accuracy of the present method. Both Maître et al. [2013] and McNaughton et al. [2014] employed body-fitted meshes and their calculations were performed with two-dimensional RANS models with k-ω SST turbulence closures. The present VATT simulations are carried out in a quasi-3D domain, i.e. using a finite 3D domain without considering turbine end-effects.

The geometrical dimensions of the test case are similar to those of Maître et al. [2013] with a domain size of $30c$ x $22c$ in x- and y-directions respectively. The turbine centre is placed $9c$ away from the inlet and in the middle of the domain regarding the lateral direction. The computational domain is extruded in the vertical by $H = 2c$, which is expected to provide accurate results. Posa et al. [2016] demonstrated in their VATT simulations that using a vertical extension of $2c$ and $4c$ provided similar results. The radius of the turbine is $R = 2.73c$ so the

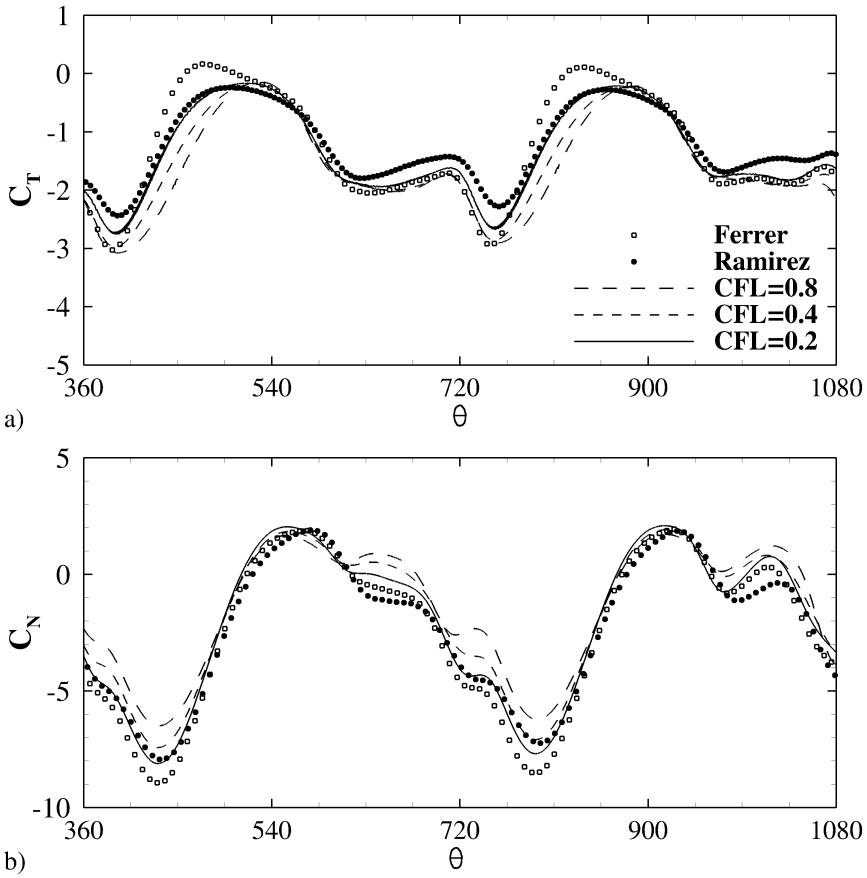

Figure 5.2: Hydrodynamic a) torque and b) normal coefficients of the VATT under a laminar flow. Comparison between the present results using different time step values, and those from body-fitted models of Ferrer and Willden [2015]; Ramírez et al. [2015].

resulting turbine's solidity value is 0.175, calculated according to Eq. 4.1, and the Reynolds number based on the chord length is $Re_c = 73,600$.

A uniform velocity distribution of U_0=2.3m/s is imposed at the inlet and a convective outlet condition is set at the domain's outlet. Periodic boundary conditions are set at the top and bottom boundaries while no-slip conditions are imposed on the domain sides representing the experimental hydraulic flume walls. VATT simulations are performed for λ=1.0, 1.5, 2.0, 2.5, and 3.0, to obtain the performance curve and to compare in detail the present LES with the experimental results (Roa et al. [2010]) and 2D numerical data (Maître et al. [2013];

McNaughton et al. [2014]). The fluid domain is divided into 504 sub-domains as depicted in Fig. 5.3 where the domain decomposition pattern is drawn. Three LMR levels are used (see Fig. 3.4) to optimise the computational requirements, and the simulations run on 171 cores. These run initially for a period of two turbine revolutions in order to develop fully the flow around the turbine, and power coefficients are computed and averaged over another four revolutions.

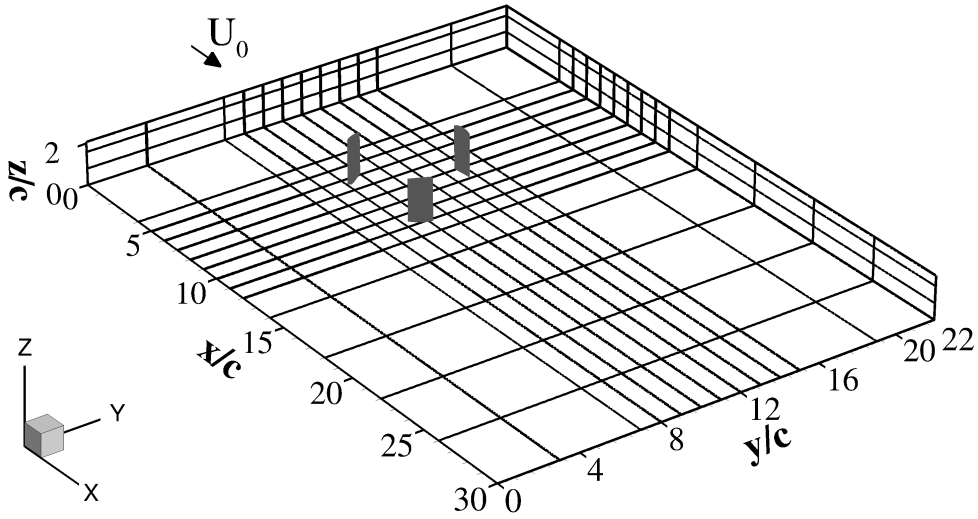

Figure 5.3: Sketch of the domain used for the LES of the VATT under turbulent flow. The sub-domain divisions is represented by straight lines.

5.3.1 Grid size and time step sensitivity

A grid size and time step sensitivity study is carried out for the turbine rotating at $\lambda = 2.0$. Table 5.1 lists the details of grid spacing normalised by the chord length, number of solid markers distributed over each section of the blades boundary, and predicted power coefficient. These values refer to the horizontal plane where the mesh is uniform in x- and y-directions, i.e. $\Delta x = \Delta y$, while the resolution in the vertical direction is set as $\Delta z = 2\Delta x$. The effect of time step on the predictions is analysed for the finer mesh resolution using constant time steps of $\Delta t^* = \Delta t U_0/c = 7.2 \cdot 10^{-4}$, $4.0 \cdot 10^{-4}$, $1.0 \cdot 10^{-4}$, corresponding to CFL=0.046, 0.026, 0.006, respectively. The impact on the coefficient of power among the different time step values is quite reduced compared to the sensitivity to the

mesh resolution. Thus, in order to balance the already high computational effort $\Delta t^* = 4.0 \cdot 10^{-4}$ is the value adopted for the following calculations.

Mesh	Δx/c	N_L	C_P	$\Delta C_P/\Delta x/c$
Δx_1	0.0250	82	0.252	-
Δx_2	0.0125	162	0.313	0.488
Δx_3	0.0100	202	0.328	0.300

Table 5.1: Details of mesh resolutions tested, number of divions along the airfoil's surface, N_L, and time-avergared power coefficient generated by the 3 blades.

Fig. 5.4 presents the instantaneous values of power coefficient obtained for one blade over one revolution for the three different meshes using $\Delta t^* = 4.0 \cdot 10^{-4}$. A notable variation of C_P is observed with each refinement of the mesh. The meshes Δx_1 and Δx_2 show a larger and sharper C_P peak during the blade upstroke movement with a maximum of $C_P \approx 0.55$ while the finest mesh achieves a maximum of $C_P \approx 0.48$. The latter also shows a smoother curve around the maximum C_P in comparison to the pointy peaks predicted by the coarser meshes, which can be attributed to a more accurate representation of dynamic stall processes by the fine grid simulation, as explained later in Section 5.3.4. Table 5.1 shows that with successive mesh refinement the predicted power coefficient achieves a closer match to the experimental value of $C_P = 0.336$ reported in Maître et al. [2013], with Δx_3 obtaining only a 2.5% error. Additionally, it also shows that mesh convergence is also achieved from the smaller differences in the increased power coefficient when reducing the mesh size accounted by $\Delta C_P/\Delta x/c$.

The numerical simulation of a rotating turbine blade using an IB method is a challenging task. An important measure to the stability and accuracy of any immersed boundary method is to eliminate/minimise artificial residual velocities inside the moving immersed boundary, Kara et al. [2015]; Wang et al. [2008a]. These can be quantified with the L_2 norm error, calculated as,

$$L_2 = \sqrt{\frac{\sum_{L=1}^{N_L} (\mathbf{U}_L^* - \mathbf{U}_L)^2}{N_L}} \tag{5.1}$$

Here N_L indicates the total number of Lagrangian markers comprising one

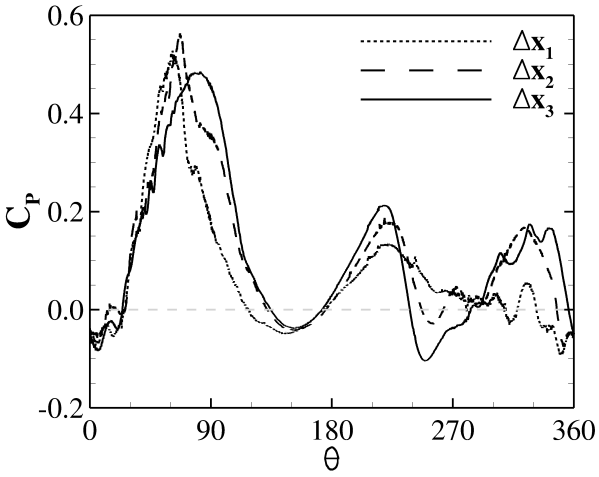

Figure 5.4: Comparison of the computed power coefficient generated by one blade using the different mesh resolutions.

blade. The lower the L_2 norm error, the better is the achievement of the no-slip condition at the solid boundary (Wang et al. [2008a]). Hence, the residual velocities inside the blades are quantified through the L_2 norm error for different spatial resolutions with $CFL = 0.026$. Fig. 5.5a) plots the error as a function of grid spacing (solid line) together with sloped (dashed) lines indicating the order of the scheme. The data line is parallel to the 1st-order slope, and hence the method is 1st-order accurate in space. Simulations to investigate the effect of temporal resolution on the L_2 norm error are carried on the Δx_2 grid. Fig. 5.5b) plots the L_2 norm error as a function of time step (solid line) and demonstrates that the method is 2nd-order accurate in time.

Noteworthy is the fact that for a rotating VATT the accuracy in space is only linear whereas both Uhlmann [2005] and Wang et al. [2008a] demonstrated 2nd-order accuracy of the direct forcing method, however for stationary immersed boundaries. Similar error convergence rates to the present ones are found by Taira and Colonius [2007] or Li et al. [2016a], who attributed this deviation to the interpolation procedures or to the effects of turbulence, respectively.

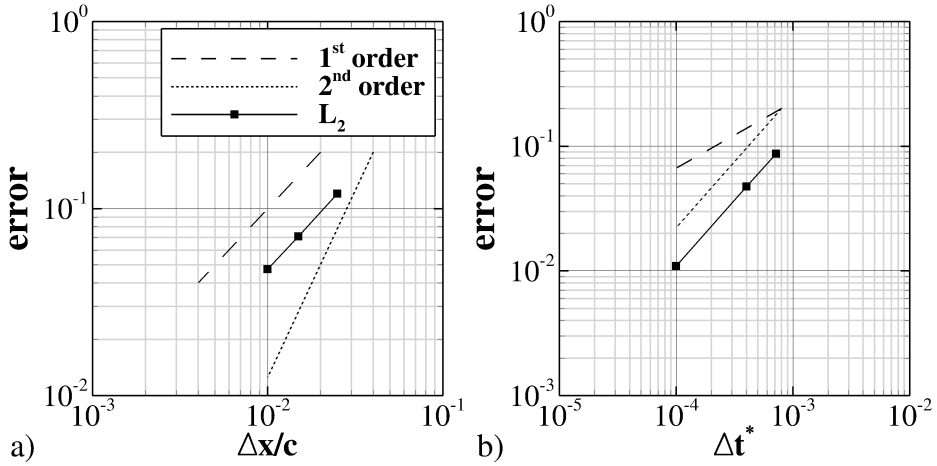

Figure 5.5: L_2 norm error analysis for the turbine under turbulent flow regarding the different values of normalised a) mesh resolution and b) time step size.

5.3.2 Turbine Performance

A blade resolved high-resolution numerical simulation of a VATT operating in fully turbulent conditions is able to reveal important flow-turbine physics, and can aid in improving their design or understanding why some VATT designs perform better than others. A crucial step in this process is to validate the numerical approach and to assess its credibility. Thus, the present LES method is first validated with data from experiments and previous numerical simulations from Maître et al. [2013] and McNaughton et al. [2014].

Fig. 5.6 presents the power curve, i.e. mean coefficient of power as a function of tip speed ratio, obtained from the experiments of Roa et al. [2010], the RANS simulations from Maître et al. [2013]; McNaughton et al. [2014], and the present LES. It is observed that overall LES provides accurate predictions of the mean power coefficient. In particular, LES is able to predict the behaviour of the turbine during all phases of the operation, whereas RANS predictions show significant overestimation of the power coefficient for tip speed ratios greater than 2.0, i.e. in the transition and secondary effects regions.

A better understanding of power generation of a VATT is provided with the help of Fig. 5.7, which presents the distribution of the phase-averaged power coefficient over one full turbine revolution for one blade (upper row) and for

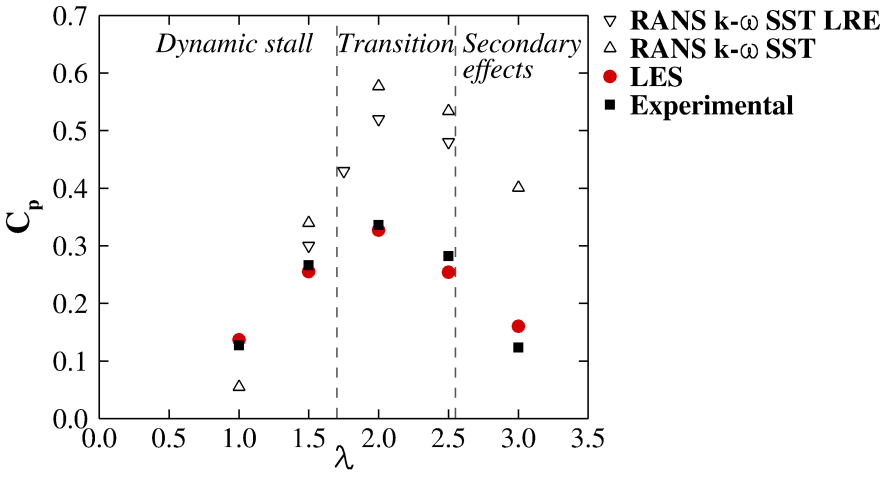

Figure 5.6: Mean power coefficient for the entire turbine versus tip speed ratio curve: Experimental (Roa et al. [2010]), RANS (Maître et al. [2013]; McNaughton et al. [2014]) and present LES results.

the sum of the three blades (lower row) at different tip speed ratios. Fig. 5.7 demonstrates the inherent peculiarity of a vertical axis turbine in that the power generation is very uneven over one revolution. The majority of power is generated on the upstream side of the revolution, i.e. $0° \leq \theta \leq 180°$, and there are phases where C_P drops below zero or is close to zero, which means that one blade opposes the power generation of the two other blades. Hence, and as seen from the lower row of Fig. 5.7, the power generation of a three-bladed VATT takes on a sinusoidal pattern per revolution with three peaks and three troughs. The overall distribution of C_P of the single blade is quite similar amongst all numerical approaches irrespective of the tip speed ratio, particularly on the upstream side of the turbine ($0° \leq \theta \leq 180°$). Noteworthy is that the maximum C_P value predicted by LES and $k-\omega$ SST LRE (McNaughton et al. [2014]) closures is quite similar for λ=1.5 and 2.0, while k-ω SST features a notable overestimation at all rotational speeds. More pronounced differences between the numerical approaches are observed for $180° \leq \theta \leq 270°$, i.e. during the first half of the downstream side of the rotation, for which only LES predicts a rather significant secondary C_P peak. This secondary peak is due to the lift overshoot experienced by the blade on the outer side as a result of the onset of a secondary trailing edge vortex, which is visualised and discussed later in Section 5.3.4. RANS models

also predict secondary peaks, however these are smaller in magnitude than the LES predictions and occur at a later stage in the revolution, i.e. $\theta \approx 330°$.

The power coefficient of the 3-bladed VATT is shown in Fig. 5.7d) to f) as predicted by the two RANS models, LES, and measured experimentally. The LES predictions for $\lambda = 1.5$ match the experimental values both in phase and extreme values. At maximum efficiency, i.e. $\lambda = 2.0$, LES slightly overestimates the maximum C_P and similarly underestimates the troughs of the curve. The LES predicted C_P curve also features a slight shift in the location of the peaks and troughs, possibly due a slight shift of the $\theta = 0°$ position in the experiments. At a higher tip speed ratio of $\lambda = 2.5$, LES predicts well the mean value but fails in the prediction of the maxima and minima values, which is probably due to the omission of end-effects, which have a greater effect at higher rotational velocities. The author acknowledges that there is a mismatch in RANS $k-\omega$ SST LRE results from Fig. 5.7 and 5.6 as the averaging of the power coefficient curve does not agree with the average value reported in those publications, and it is not corrected as the source of error is unknown.

The accurate prediction of the lift coefficient of individual blades by the numerical model is of great importance and essential for geometry-resolved Darrieus-type VATT simulations, because they are lift driven devices. A detailed analysis of hydrodynamic lift forces is enabled by Fig. 5.8, which presents the lift coefficient, C_L, as a function of angle of attack, α, for tip speed ratios of $\lambda = 1.5$, 2.0 and 2.5. Significant differences between LES and RANS are found along the C_L curve irrespective of the rotational speed. The most relevant differences concern the lift generated during the first half of the blade's upstroke movement ($0 < \alpha < \alpha_{max}$ and $0° \leq \theta \leq 90°$), where LES predicts a higher generation than RANS approaches at all λ with differences up to a 20%. This agrees with the RANS underestimated lift generation shown in the pitching airfoil analysis in Section 4.

Fig 5.8a) shows the lift hysteresis loop for λ=1.5 and suggests large differences among the different numerical approaches. LES predicts the transition of power generation to loss of lift occurs at $\theta \approx 70°$ while this is delayed until $\theta \approx 80°$ in the RANS predictions. Consequently, LES predicts that at $\theta = 90°$ (blade is perpendicular to the oncoming flow) $C_L \approx 1.8$ whereas RANS models predict

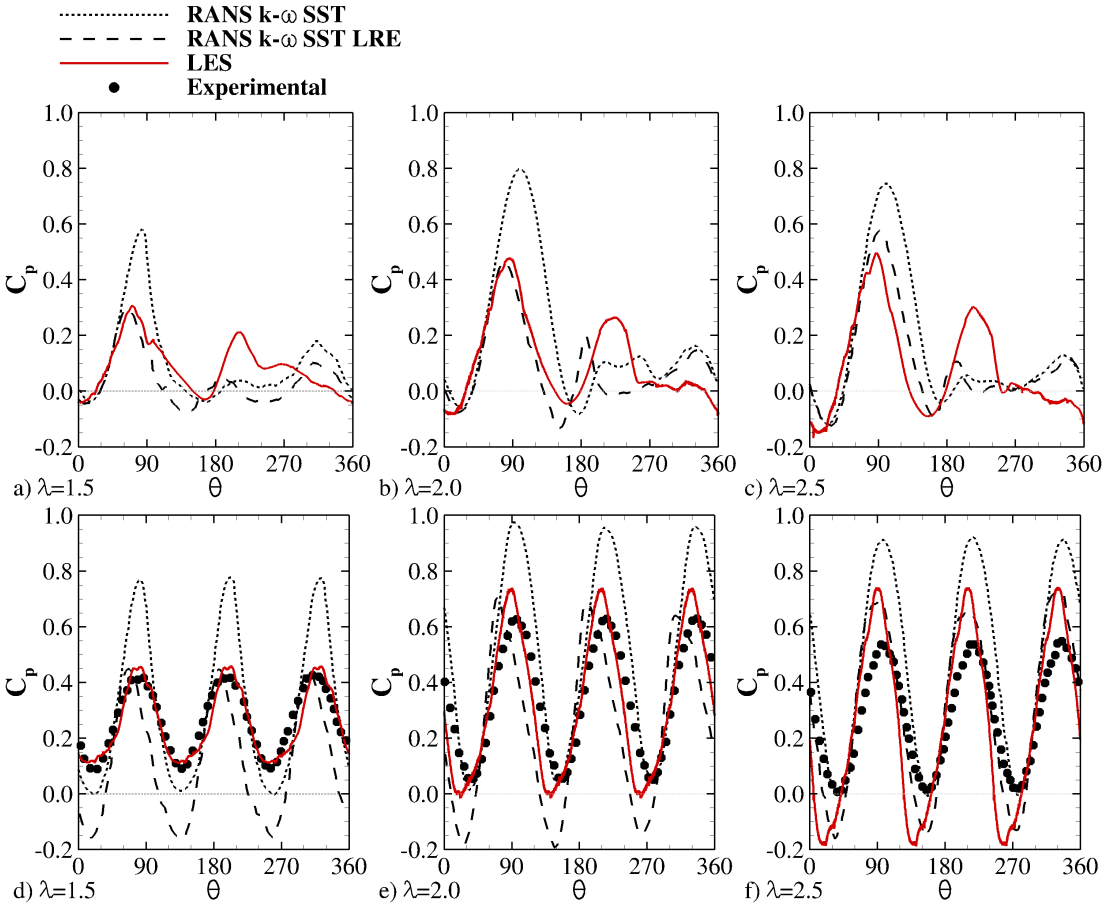

Figure 5.7: Coefficient of power, C_P, as a function of rotated angle, θ, of one turbine blade for λ= a) 1.5, b) 2.0 and c) 2.5, and C_P of the entire turbine for λ= d) 1.5, e) 2.0 and f) 2.5. Comparison between experiments and RANS k-ω SST (Maître et al. [2013]), RANS k-ω SST LRE (McNaughton et al. [2014]), and present LES.

$C_L \approx 2.8$, reflecting the differences between approaches in predicting the energetic flow structures that dominate the flow over the blade. Nonetheless, at the maximum effective angle of attack ($\alpha = 40°$, $\theta = 130°$) the three approaches converge to the same value of C_L. At this angle, the blade suffers from detachment of the dominating large-scale structure (as shown later in Section 5.3.4) causing the lift to drop dramatically. The considerable differences between numerical approaches are due to their different prediction of dynamic stall that dominates the VATT physics at low tip speed ratios, $\lambda < 1.7$, Maître et al. [2013]. In the last quarter

of rotation ($270° \leq \theta \leq 360°$), the generated lift is negative as the large-scale vortices are formed on the blade's outer surface, and where LES predicts less generation of lift in comparison to RANS models.

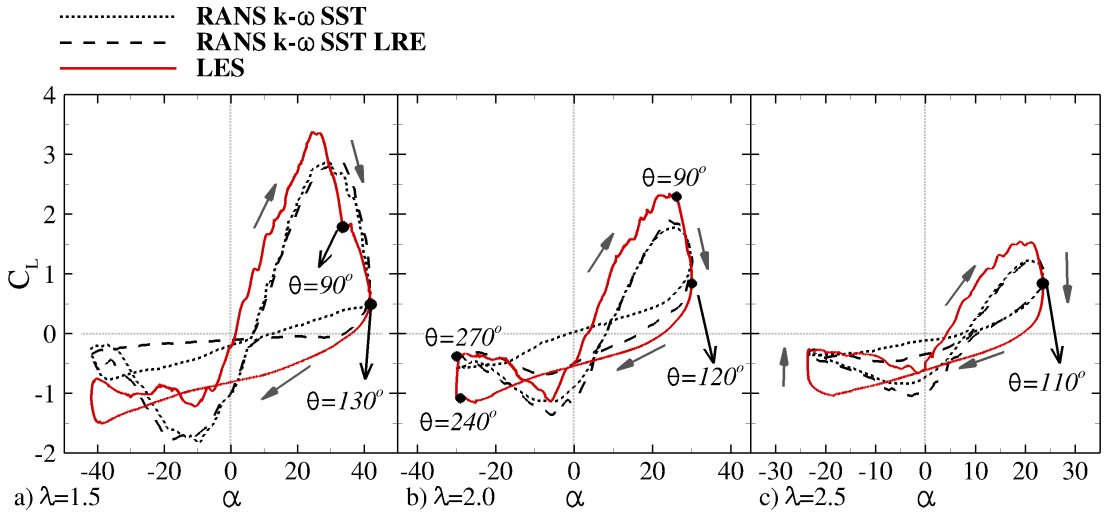

Figure 5.8: Coefficient of lift, C_L, as a function of effective angle of attack, α, of one turbine blade for λ= a) 1.5, b) 2.0 and c) 2.5. Comparison of present LES with RANS results from Maître et al. [2013]; McNaughton et al. [2014].

The hysteresis lift curves for λ=2.0 and 2.5 are presented in Fig. 5.8b) and c), respectively. The difference in the predictions of lift during $\alpha > 0$, where LES consistently exceeds the magnitude of C_L compared to that of RANS, exists for almost the entire upstream rotation for both rotational speeds. However, the peak of C_L is predicted to occur at $\theta \approx 90°$ for $\lambda = 2.0$ and 2.5 irrespective of the numerical approach. Larger differences are again observed for the downstream side of the revolution especially for $270° \leq \theta \leq 360°$. The source of the differences is the resolution of the blade-vortex interaction as RANS approaches tend to underestimate the formation of leading and trailing edge vortices, which are the principal responsible for the generation of lift on the blades.

5.3.3 Downstream wake prediction for λ=2

The accurate representation of the downstream wake depends on the resolution of the large-scale energetic eddies shed from the blades during both upstream

and downstream sides of the revolution. Hence, the eddy-resolving nature of LES supposes a valuable benefit to accomplish an accurate prediction of the turbine's wake hydrodynamics. The developed wake with the turbine spinning at $\lambda = 2$ is analysed and results are compared with experimental measurements and RANS predictions reported by Mercier et al. [2014]. The simulation is initially run until the flow downstream the turbine is well-developed (approx. after two spins). Then first order statistics are averaged for four revolutions whilst second order statistics are collected during another two.

Fig. 5.9 shows the contours of normalised streamwise velocity and z-vorticity ($\omega_z c/U_0$) at half spanwise length, i.e. $z/c = 1$. A low-velocities area is found between these two regions and is extended until $x/D \approx 2.5$ wherein the high-momentum streams start to converge. Along the wake expansion areas, two high-vorticity streams distributed along $y/D \approx \pm(0.6-0.7)$ are found, which coincides with the experimental observations. Noteworthy is that these areas are extended laterally until maximum values of y/D$\approx \pm 0.85$ representing a considerable wake expansion compared to the maximum value of $y/D = 0.5$ swept by the blades.

A qualitative comparison of the wake prediction is shown in Fig. 5.10 with the comparison of mean normalised streamwise velocities and TKE profiles with experimental and RANS results from Mercier et al. [2014]. The profiles adopted for the comparison are outlined in Fig. 5.9 and are placed downstream the device since $x/D = 1.0$ until 2.5 each 0.5D. Note that TKE is calculated analogously to Mercier et al. [2014] with two-dimensional velocity components, i.e. $k = 0.5(\overline{u'^2} + \overline{v'^2})$, where $u' = U - u$ is the time-averaged velocity fluctuation, U is the time averaged velocity, and u is the instantaneous velocity.

At the closest location to the turbine, i.e at $x/D = 1.0$ shown in Fig. 5.10 a), the LES streamwise velocity distribution achieves a good agreement with both experimental and RANS results. However, in the TKE distribution at this location (Fig. 5.10 e)), LES overestimates the peak values, although the location and distribution of the two areas containing the highest TKE peaking at $y/D \approx \pm 0.6$ are well predicted. This mismatch can be attributed to the different amount of revolutions used for the TKE averaging, as in the present simulation the TKE values are obtained from averaging two revolutions while Mercier et al. [2014] averaged the experiments and RANS data for a single revolution.

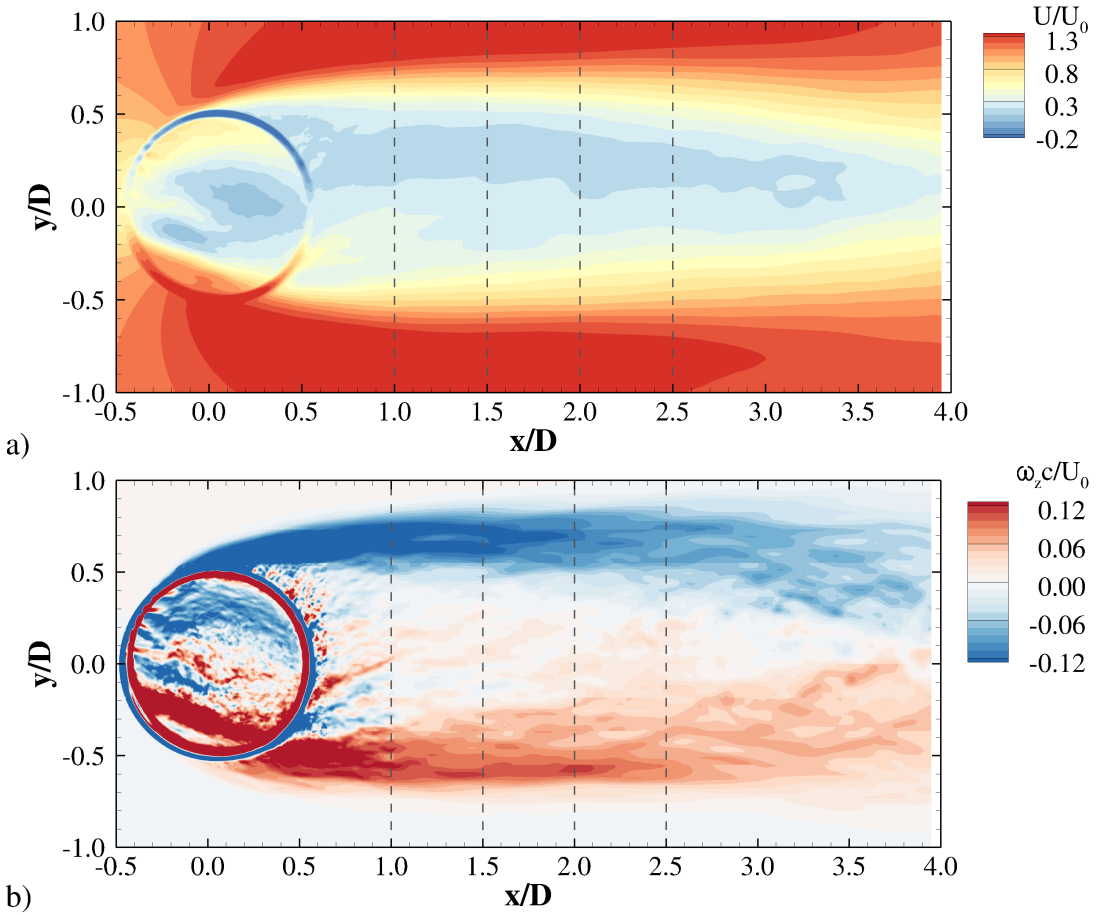

Figure 5.9: Contours of normalised a) streamwise velocity and b) z-vorticity at $z/c = 1$ for the turbine rotating at $\lambda = 2.0$.

The velocity distribution close to the turbine shows a "U" shape, and is smoothly evolving into a more "V" shape as soon as the two high-vorticity alleys come closer, as depicted in Fig. 5.9. This wake recovery behaviour is well predicted by LES as in the velocity profiles at x/D =1.5, 2.0 and 2.5 (Fig. 5.10 b) to d)) matches the experimental values specially at the low-momentum area, i.e. $|y/D| < 0.5$. Fig. 5.10 f) to h) show the TKE profiles at these location for which LES also shows an excellent match with experiments both in peak values and their location, while RANS results underestimate the velocity fluctuations.

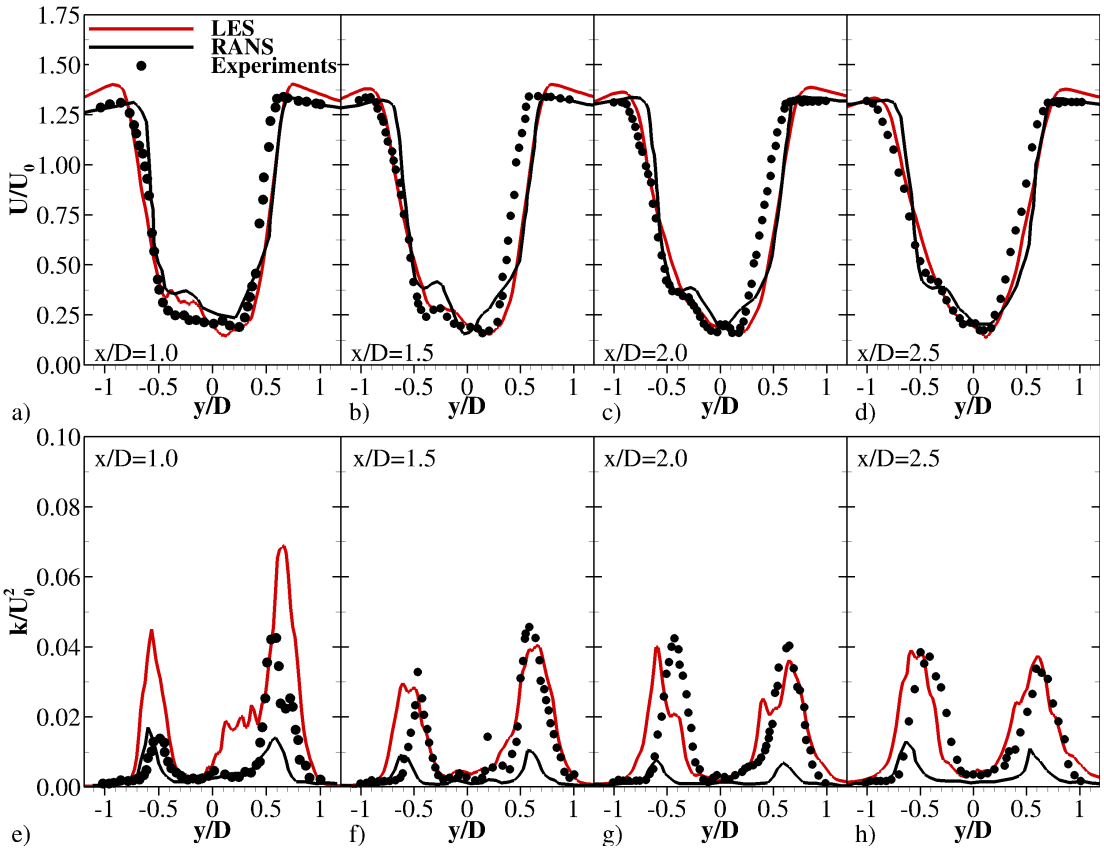

Figure 5.10: Profiles of normalised mean streamwise velocity profiles at $x/D =$ a) 1.0, b) 1.5, c) 2.0, and d) 2.5; and normalised mean TKE at $x/D =$ e) 1.0, f) 1.5, g) 2.0, and h) 2.5 with comparison of the present LES results with RANS and experimental data from Mercier et al. [2014].

5.3.4 Blade-vortex interaction

An inherent fluid-structure interaction phenomenon of Darrieus-type VATTs is dynamic stall. This is characterised by the shedding of leading and trailing edge vortices from the blade in motion (as shown in Section 4), which is more pronounced on the upstream side of the circumference that the blade describes. These vortices are consequently convected through the swept area of the rotor, and hence they may interact again with the blade during its rotation on the downstream half of the circumference. The complex vortex shedding and blade-vortex interaction is sketched in Fig. 5.11, as proposed by Brochier et al. [1986] who investigated experimentally dynamic stall characteristics of a three-bladed

VATT rotating at $\lambda = 2.14$. From their observations, various vortex shedding mechanisms take place, mainly in the form of LEVs and TEVs, denoted as ***a*** and ***b*** respectively. Fig. 5.11 illustrates their loci of generation, growth and pathways of travel through the rotor's swept area.

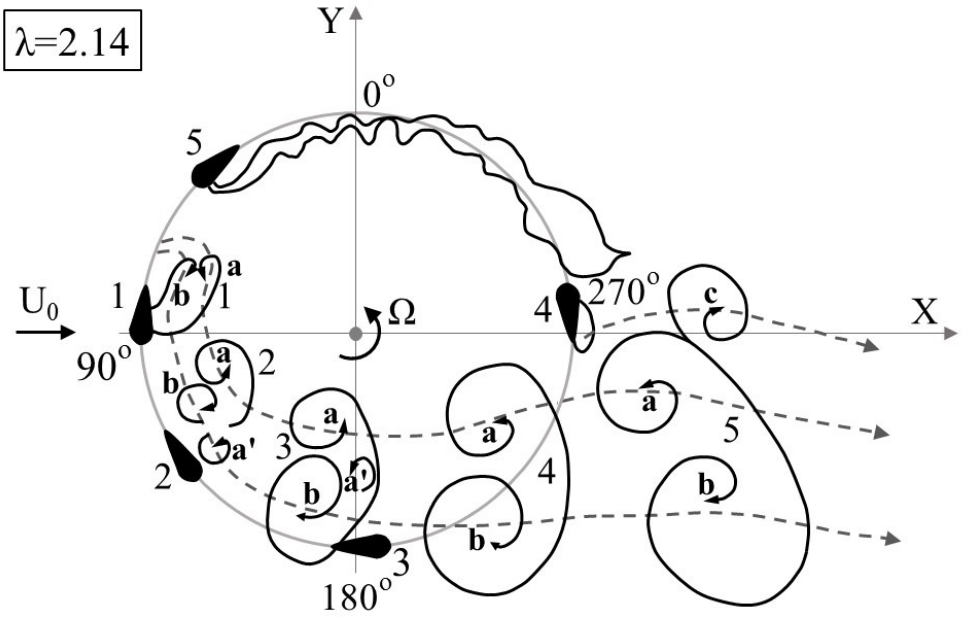

Figure 5.11: Schematic of the vortex shedding sequence in the flow around a VATT rotating at $\lambda = 2.14$ described by Brochier et al. [1986].

The ability of LES to resolve the large-scale structures present in the instantaneous velocity field together with a geometry-resolved approach permits studying in detail dynamic stall and vortex-blade interactions of a VATT. This varies notably depending on the tip speed ratio as explained previously in Section 4.2. Three different scenarios are analysed: λ=1.0, 2.0 and 3.0. At λ=1.0 and 1.5 deep dynamic stall occurs and the turbine stops operating or experiences a severe drop in performance, respectively. At higher tip speed ratios, e.g. λ=2.5 and 3.0, the inertia of the blades dominates over viscous effects and the chosen turbine "overspins", in other words it does not operate at its peak. For the turbine under investigation the peak performance is at $\lambda \approx 2.0$, see Fig. 5.6, which appears to be the best compromise between maximum lift on the upstream portion of the revolution and minimum negative lift on the downstream portion of the revolution.

Fig. 5.12 visualises coherent vortices through iso-surfaces of the spanwise vorticity for $\lambda = 2.0$ illustrating the blade-vortex interaction and vortex evolution at 9 different rotated angles. The iso-surfaces are coloured in blue and orange indicating whether their rotation is clockwise and counter-clockwise, respectively. At position I ($\theta \approx 30°$), the blade does not experience any vortex shedding and only minor trailing edge turbulence is observed. Once the blade passes the dynamic stall angle, i.e. at position II, onset of dynamic stall occurs with the generation of an energetic LEV denoted ***a***, and at the instant depicted it already occupies most of the blade's suction side. The blade generates the maximum torque at $\theta \approx 90°$ (see Fig. 5.7b) probably because of the LEV ***a***. At position III, vortex ***a*** is considerably larger but has been already advected away from the suction side of the blade and is replaced by the TEV ***b***, which is rotating in the opposite direction to the LEV. The TEV grows as the blade continues its motion and other smaller LEVs are generated, such as vortex ***a'***. At position IV, the primary LEV ***a*** is fully detached from the blade and is now advected through the inside of the rotor whereas the TEV ***b*** grows and dominates the blade's hydrodynamics. The TEV ***b*** is eventually shed from the blade at $\theta \approx 180°$, as is observed at position V. At tip speed ratio of 2.0, vortices shed during the upstream side of the motion interact with the blades mostly within the third quarter of the rotation, i.e. $180° < \theta < 270°$. This is visible at position V, $\theta \approx 200°$, where the blade interacts with the advected TEV ***b*** from the previous blade, whilst its own TEV ***b*** is completely detached. At position VI the blade starts to generate a secondary LEV ***c*** on its outer side, and the blade now interacts with the LEV ***a*** of the previous blade. Once the blade reaches position VII, no more blade-vortex interaction takes place and only small leading and trailing edge vortices are formed, detached and transported into the downstream area of the turbine. In the fourth quarter, there is no influence of upstream turbulence and the blades at positions VIII and XI experience only vortex shedding at the trailing edge, and in absence of relevant flow separation. The dotted lines indicate the path described by the centre of the vortices ***a*** and ***b***, and all of these findings and observations agree remarkably well with Brochier et al. [1986]'s sketch.

A larger presence of dynamic stall is observed when the turbine rotates at $\lambda = 1.0$ and this is appreciated with help of Fig. 5.13. At position I, only laminar

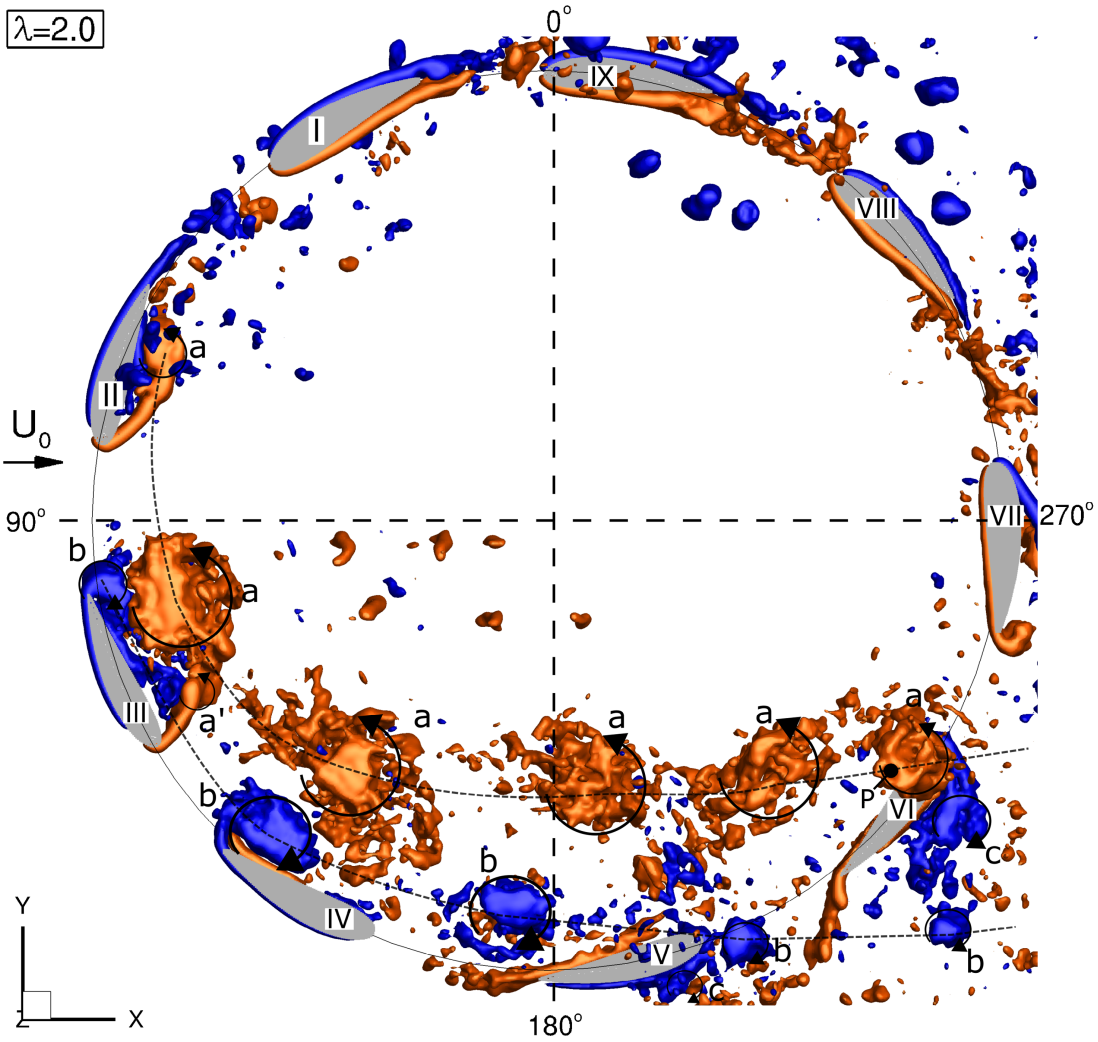

Figure 5.12: Blade-vortex interaction of the VATT at $\lambda = 2.0$.

shear layers on both sides of the blades are visible. The rapid onset of dynamic stall, massive flow separation in the form of a LEV ***a*** is appreciated already at position II meanwhile a TEV ***b*** starts to form as well. Both vortices, ***a*** and ***b***, are shed even before the blade approaches $\theta \approx 90°$. At position III, a secondary LEV ***a'*** is generated and shed before the blade advances to position IV whilst the secondary TEV ***b'*** remains attached. Note that at tip speed ratio of 1.0 at an angle of $\theta = 180°$ the relative velocity between the blade and free-stream is zero. This provokes that at position V the vortex ***b'*** travels close to the blade at similar velocity but they are physically detached. The vortex ***b'*** quickly loses

coherence due to its interaction with vortex ***a'***, which rotates in the opposite direction. The same is true for the main vortices ***a*** and ***b***, they interact with each other on their way through the turbine and for the scenario depicted here the TEV has lost its coherence almost entirely by the time it exits the rotor on the downstream side.

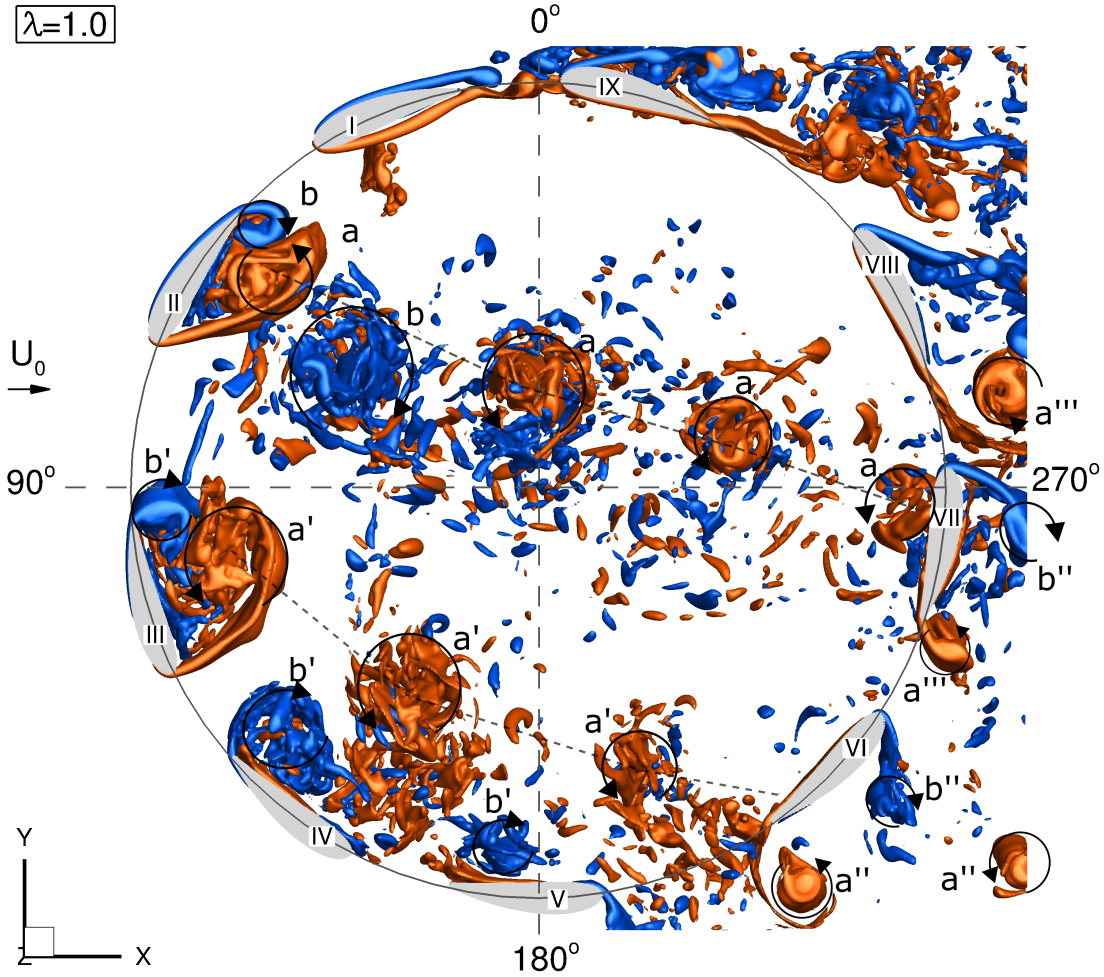

Figure 5.13: Blade-vortex interaction of the VATT at $\lambda = 1.0$.

Significant LEV ***a"*** and TEV ***b"*** are being generated and shed at position VI. At position VII, the blade experiences interaction with vortices ***a*** and ***b***, shed during the first quarter of the revolution and another trailing edge vortex appears (***a"'***). The interaction continues until position VIII, and appears to affect the shedding of ***a"'***. Leading edge flow separation is still observed at position VIII

and is also clear at position IX. Full recovery of the boundary layer on the outer side of the blade is not achieved until the blade passes $\theta = 0°$.

Fig. 5.14 visualises blade-vortex interactions when the turbine rotates at $\lambda = 3.0$, and this is when the turbine overspins and operates below its peak efficiency. The turbine does not undergo deep dynamic stall. At positions I and II, only minor trailing edge vortices form and shear layers on both sides are still attached to the blade. The LEV ***a*** is generated at position III and shed shortly after because of the fast motion of the blade. At position IV the blade is under light stall with a short region of flow separation closer to the trailing edge, which generates small-scale flow structures. This behaviour is expected as Fig. 4.1a) shows that α is never larger than α_{ds} for $\lambda = 3.0$, and thus deep dynamic stall conditions are not developed. Note that light or deep stall conditions are differentiated by the extension of the separated flow region, extending only over a short portion of the blade's surface or over the entire length of the blade, respectively.

The region of flow separation near the inner side of the blade is already reduced at position V and gone entirely by position VI. In contrast, there is no flow separation at the outside of the blade at position V, while at VI a secondary LEV ***a'*** is generated and is already located close to the trailing edge. The vortex ***a*** (shed at position III) interacts with the following blade somewhere between position V and VI. At position VII, vortex ***a"*** is already detached and advected downstream of the turbine. Minor but not insignificant vortex formation and shedding is observed for the remainder of the revolution until position I.

Visualised by Fig. 5.12 to 5.14 the blade-vortex interaction depends strongly on the tip speed ratio λ. Noteworthy is the difference in the pathways described by the vortices shed on the upstream side of the revolution. For $\lambda = 1.0$, the vortices travel in the direction of the main flow as the low rotational velocity allows for a larger entrainment of fluid into the turbine's swept area. The swept area is more isolated from the approach flow in the cases of $\lambda = 2.0$ and 3.0 and consequently the vortices are deflected to the right, e.g. in the case of $\lambda = 3.0$ by approx. 45°.

The regions of dynamic stall depending on the rotational speed are exhibited in Fig. 5.15 for the tip speed ratios previously visualised. For $\lambda = 1.0$, the blades undergo deep dynamic stall along most of the revolution whilst this is notably

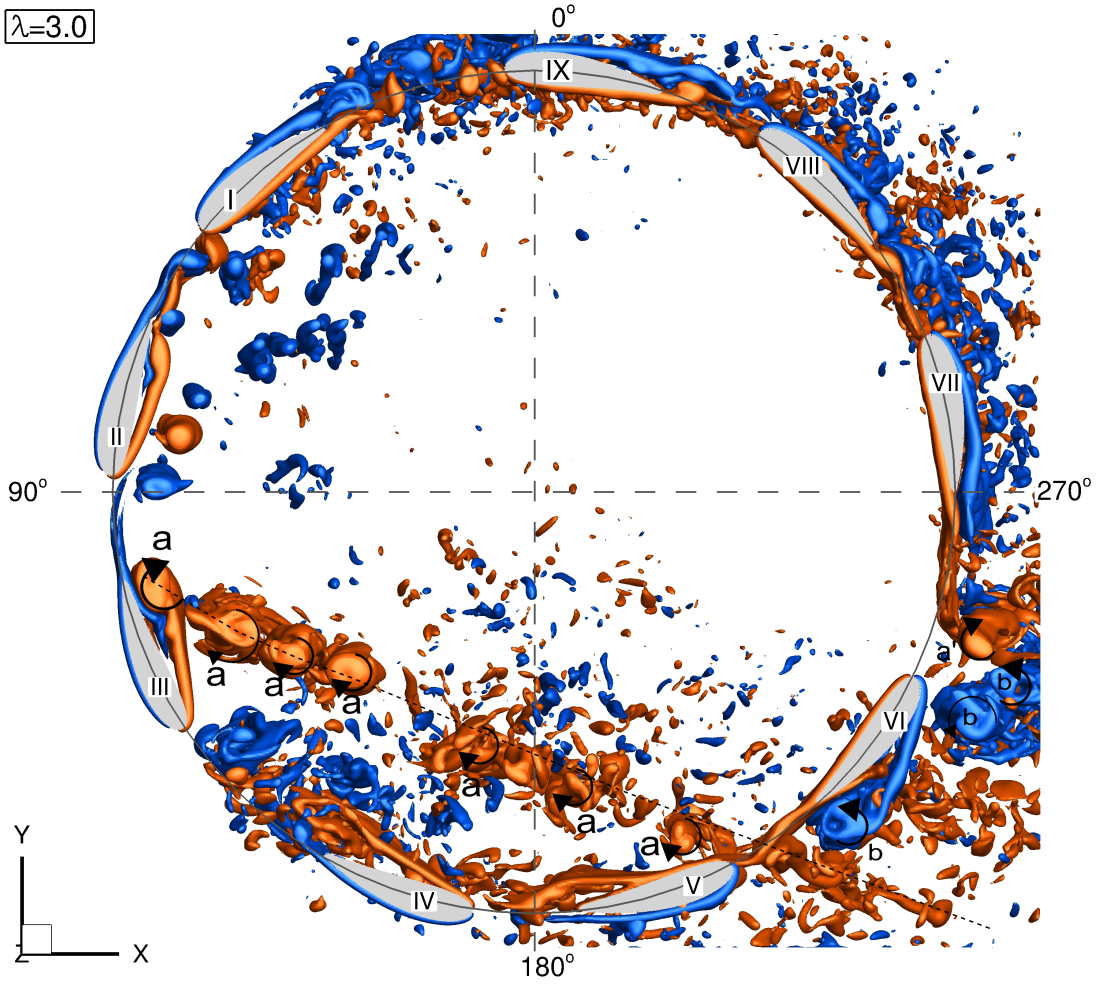

Figure 5.14: Blade-vortex interaction of the VATT at $\lambda = 3.0$.

reduced for $\lambda = 2.0$. In the latter, light dynamic stall area is increased but also the area for which no flow separation is developed, i.e. the blades do not stall. For the over-spinning case at $\lambda = 3.0$, there is an almost equal distribution of no-stall and light stall areas throughout the revolution which agrees with the blade-vortex development from Fig. 5.14.

5.3.5 Power spectral density

Signals of instantaneous u- and v-velocity are collected at a point located at $x/R = 0.80$ and $y/R = -0.60$, denoted as "P" in Fig. 5.12, for the case of the

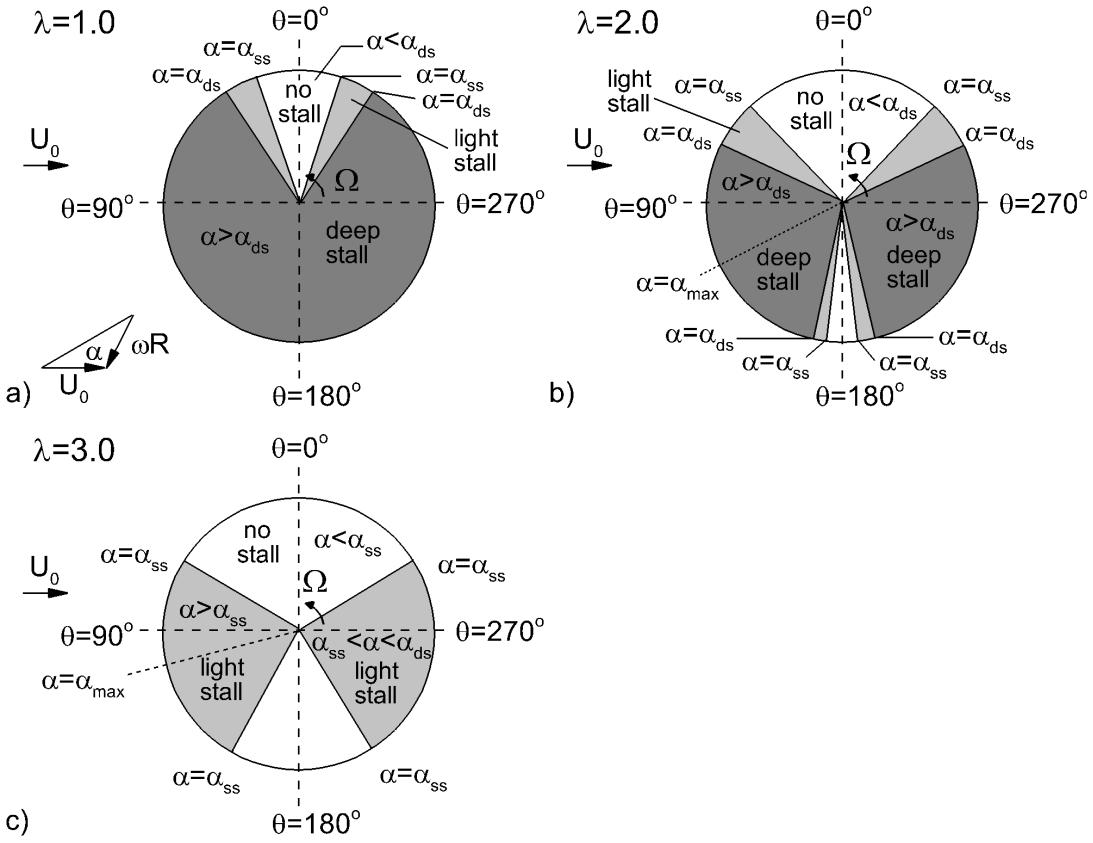

Figure 5.15: Dynamic stall regions along the revolution of a VATT at tip speed ratios of a) 1.0, b) 2.0, and c) 3.0.

turbine rotating at $\lambda = 2.0$. This point is placed within the pathway of the LEV $\boldsymbol{a}$ vortices that are shed during dynamic stall at around $\theta = 90°$. The angular velocity of the turbine is $\Omega = 52.57 rad/s$, which results into a blade frequency of $f_b = 25.1 s^{-1}$, calculated as,

$$f_b = (\Omega/2\pi) * N_b \tag{5.2}$$

The blade period of $T_b = 1/f_b = 0.04s$ is used to normalise the time values of the velocity signals from Fig. 5.16a). The Power Spectral Density (PSD) from the velocity signals is presented in Fig. 5.16b). A large energy peak associated with the passing blade is identified at f_b in both PSDs together with another distinct peak at a lower frequency of $f_r = 3.8 s^{-1}$. The latter is the frequency of the circular

flow motion inside the turbine swept area induced by the rotation of the turbine's rotor, and which was also observed by Brochier et al. [1986] from transversal velocity spectra. A secondary, high-frequency peak is also present in the spectra and this is due to the fact that previously shed vortices are convected through the rotor's swept area, and hence are out of sync with the blade movement, showing up as additional energetic spikes in the spectra.

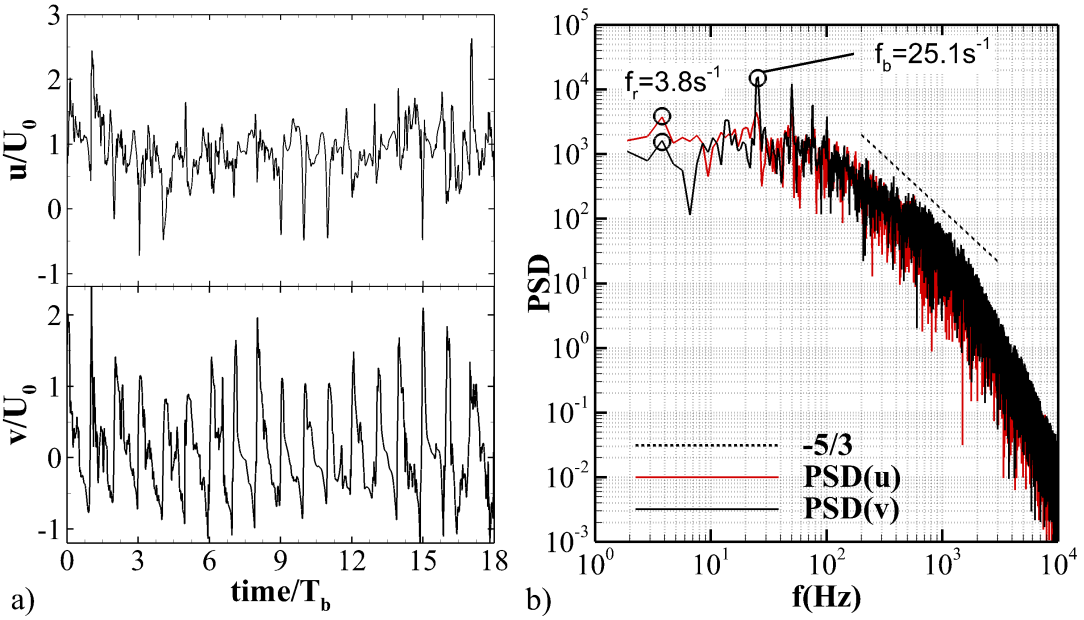

Figure 5.16: a) Time series of u- and v-velocities and their b) power spectral density at the point P located at $x/R = 0.80$, $y/R = -0.60$. Dashed line represents the -5/3 slope from Kolmogorov's law.

The low-frequency peak of the circular fluid motion and the blade-vortex PSD peaks are found in the production range of the spectrum. As Fig. 5.16b) shows the energy cascade of the u and v spectra exhibit a certain range of isotropic turbulence decay following the expected -5/3 decay, and from approximately 10^3 Hz onwards energy dissipation takes place, mainly induced by the SGS model. The selected mesh resolves approx. three frequency decades of the flow, between the production of energetic large-scale vortices and dissipation of small-scale turbulence, further demonstrating the adequacy of the chosen mesh, Fröhlich et al. [2005].

5.4 Summary

In this chapter the LES-IB approach for the simulation of Darrieus-type vertical axis tidal turbines has been introduced, validated and applied. In the first instance, a 3-bladed turbine subjected to laminar flow was simulated and results were compared with two highly-accurate body-fitted methods. Predicted torque and normal coefficients were generally in good agreement with the outputs of the two methods used for comparison, and this has demonstrated the stability and accuracy of the LES-IB method in absence of turbulence.

Then the approach has undergone detailed performance assessment by comparing simulation results with experimental and RANS-based model data for a 3-bladed VATT subjected to turbulent flow. A mesh resolution and time step sensibility study was carried out first to assess optimal grid and time step sizes for this case. The turbine performance curve was reproduced with the predicted power predictions, which agreed very well with the ones obtained from experiments. Further, it demonstrated that the LES-IB method outperformed the RANS-based models, in particular when the turbine spin at tip speed ratios above its optimal value. The detailed analysis of generated power and acting lift forces over a single revolution revealed significant differences in terms of when power/lift is generated during the rotation. The present analysis also highlighted that important blade-vortex interaction takes place. In particular, the largest differences between LES and RANS predictions in the lift coefficient were achieved at a tip speed ratio of 1.5, which is when dynamic stall dominates the VATT's hydrodynamics and RANS model appear to struggle to reproduce this phenomenon accurately.

The visualisation of the blade-vortex interaction at three different tip speed ratios outlined that the generation and transport of energetic large-scale flow structures depends strongly on the rotational speed of the turbine. At low to moderate rotational speeds, the blades undergo deep dynamic stall, i.e. massive flow separation from the leading edge of the blade and formation of leading edge vortices that are approximately the size of the blade chord length. On the contrary, at high rotational velocities the blades experienced light dynamic stall and vortices are less significant. The analysis of power density spectra confirmed the

presence of deep stall vortices and quantified their dominating frequency, and also provided further insight into the complex blade-vortex interaction mechanism at play.

Chapter 6

Simulation of Horizontal Axis Tidal Turbines

6.1 Introduction

Early experimental works on HATTs have been mainly focused on their hydrodynamics and performance. Bahaj et al. [2007] studied the effect of free surface proximity, yaw angle and different flow speeds on the performance of a tidal turbine. Mycek et al. [2014a] studied the wake produced downstream of the turbine and its interaction with other turbine(s) towards the design of tidal stream turbine farms, and complementary to this Vennell et al. [2015] presented an extended vision of the future of big tidal turbine farms. With a more structural loadings focus, Milne et al. [2015] investigated the structural loading of a 3-bladed HATT subjected to a sinusoidal motion under uniform flow conditions, and Blackmore et al. [2016] studied the influence of different turbulence intensities and eddy length scales in the approaching flow onto the turbine loadings and performance.

The interest in developing numerical approaches that can reproduce the complex flow in the near-field of tidal turbines has been growing in the last decade. These computational models are meant to be used in parallel to experiments reducing their costs but also providing more detailed information including velocity fields or performance data when modifying the rotor's design. Early works

employed the Blade Element Method (BEM) and the actuator disk theory. However, the latter does not consider flow unsteadiness, and the former discretises the turbine geometry by a set of single points representing some blade sections with constant hydrodynamic coefficients. Such simplifications resulted in methods which are computationally cheap, and which gave good results in the turbine's far field wake (Sarlak et al. [2015]; Sorensen and Shen [2002]; Yang et al. [2015]). Nonetheless, they are unable to reproduce the physics around the turbine rotor, and hence returned relatively poor results in the near-field of the rotor.

The complex and highly turbulent flow around tidal turbines is governed by fluid-structure interaction phenomena including dynamic stall, trailing vortex wake generation, or hydrodynamic load unsteadiness. Advanced and accurate models, such as blade resolved methods, are needed to simulate these flow characteristics, Leishman [2002]. In general, blade resolved methods use three-dimensional meshes that represent explicitly the turbine geometry, and the flow field is computed using RANS or LES closures. RANS models are widely used as the computational requirements are affordable (Frost et al. [2015]; Mason-Jones et al. [2013]) although the time-averaging of the velocity field does not accomplish a realistic representation of the instantaneous fluid-blade interaction. On the other hand, LES resolves the large-scale flow structures present in the velocity field (Stoesser [2014]) as the so-called dynamic stall. The main drawback of LES is the large number of computational resources required to run the demanded fine meshes although the exponentially increasing availability of computational resources is making LES more accessible to the research community, Sotiropoulos [2015].

There has been few studies applying LES to study the hydrodynamic performance of HATTs. These are summarised in Table 6.1 with the number of CPUs and the geometry approached used to represent the turbine's geometry, where GR stands for geometry resolved, and AL for actuator line which bases on embedding a BEM into a CFD model (Masters et al. [2013]). Noteworthy is the difference in the number of CPU used when adopting the IB method compared to wall-resolved simulations. Every of the referenced LES-based works obtained an excellent match with experimental data showing the potential and accuracy of the method of LES for the simulation of HATTs.

Reference	Geometry approach	Number of CPUs	CPU hours
Kang et al. [2011]	GR (IBM), AL	-	-
Kang et al. [2012]	GR (IBM)	800	-
Afgan et al. [2013]	GR (wall-resolved)	2048	-
Churchfield et al. [2013]	AL	800	-
Bai et al. [2014]	GR (IBM)	800	-
Lloyd et al. [2014]	GR (wall-modelled)	-	-
Present flat-channel case	GR (IBM)	144	31,000
Present dune case	GR (IBM)	456	475,000

Table 6.1: List of references of some high-fidelity numerical simulations of HATT that used the LES closure. Both body geometry description typology, number of CPUs used to run the simulations are specified, and CPU hours of the simulated cases.

During the lifetime of tidal turbines, they are subjected to harsh and highly turbulent environmental conditions. This compromises their structural design in order to avoid any major failure during the project lifespan or at least reduce as much as possible the costly in site maintenance by reducing risks. Therefore, it is essential to identify and quantify the main stresses on the turbine. To date, few research has been dedicated to tidal turbines loadings due to the inherent difficulty of experimentally determining the acting forces, Milne et al. [2013]. Nicholls-Lee et al. [2013] determined the structural loads on the blades made of composite materials, while Blackmore et al. [2016] focused on the effect of turbulence on hydrodynamic loads on a HATT. Recently, numerical studies that quantified the loadings on tidal turbines have been also performed. Mason-Jones et al. [2013] studied the stanchion shape influence on the structural and hydrodynamic behaviour of a HATT, Frost et al. [2015] studied the variation of thrust and bending moments in a HATT with stanchion subjected to different flow directions, and Tatum et al. [2016] analysed the effect of modelling the free-surface on the performance and bending moments. These analyses were carried out using RANS models which, due to its time-averaging nature, do not resolve the details of the instantaneous flow.

Aims of the chapter

This chapter aims at verifying the suitability of the LES-IB method to predict the wake hydrodynamics, power performance, and structural loadings at the blade-hub junction of a HATT. The method is validated with experimental data and different inlet conditions are analysed in order to evaluate the behaviour of the marine device. The validation is done reproducing the flat-bed channel flow used during the experiments, while the device is also simulated over a bed of dunes. The latter case provides relevant features on how bed-induced turbulence affects the rotor forces and the wake developed downstream changes according to the bed shape.

The results from experimental tests of a HATT prototype are presented in Section 6.2. These results are used for the hydrodynamic validation of the LES-IB model in Section 6.3. Section 6.4 presents the results for the developed wake hydrodynamics, and analyses the structural bending and torsional moments at the blade root. The effect of the oncoming turbulence on the turbine's performance and structural loads is analysed in Section 6.5 with a comparison to uniform inflow conditions. Finally, the HATT is simulated over a bed of dunes so as to assess the impact of bed-induced turbulence on its performance and loadings, and results are presented in Section 6.6.

6.2 Experimental setup description

Ahead of sea deployment, the performance and control strategy of a 1:30-scale commercial horizontal axis tidal turbine model was tested, Harrold et al. [2016]. The 0.4m diameter (D) turbine prototype was placed in a $15m$ long, $1.20m$ wide and $1.0m$ deep recirculating flume located in Cardiff University's hydraulics laboratory. The turbine was suspended in the tank from a Y-shaped frame that was fixed to a platform sitting above the flume, leaving the rotor positioned approximately in the center of the tank's cross-section. The rotor blades were 3D printed and fitted with circular pins to position into holes on the circumference of the turbine hub. The correct pitch angles were set by resting the blades on 3D printed molds aligned with the back of the hub. Once the pitch angles were

set, screws inside the hub were tightened to prevent the pins from moving. The model turbine in the flume is depicted in Fig. 6.1.

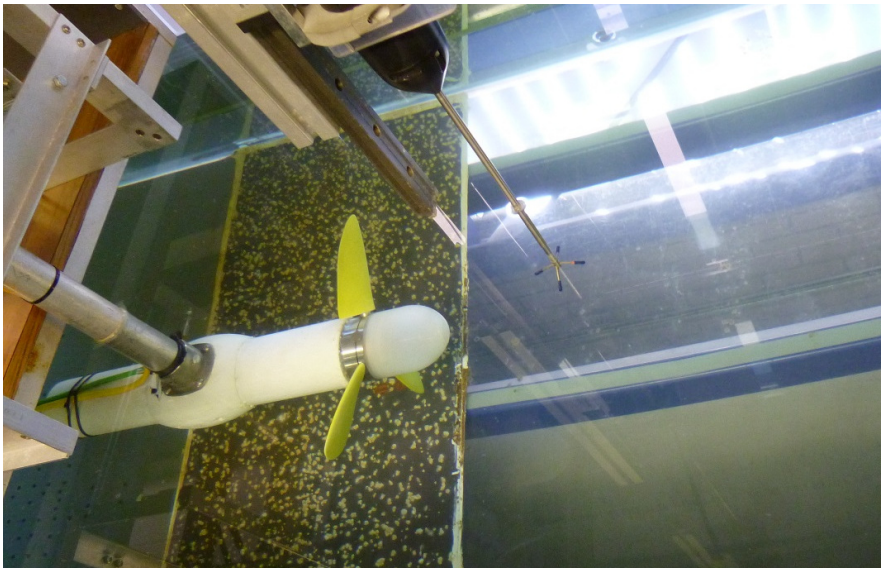

Figure 6.1: The 1:30-scale HATT prototype tested at Cardiff University's hydraulic flume.

The turbine was controlled via a programmable servomotor, used previously for similar tidal turbine tests, Mason-Jones et al. [2012]; Tedds et al. [2011], and hydrodynamic loads from the rotor were opposed by the torque of the servomotor. The software that accompanied the servomotor drive allowed the turbine to be controlled in either rotational speed or torque mode. Measurement data of these two parameters were sampled at 10Hz. A detailed description of the servomotor and its method of operation can be found in Mason-Jones [2010].

A Nortek Acoustic Doppler Velocimeter (ADV) positioned upstream and in line with the centre of the rotor was used to measure the flow velocity in the tank. The instrument was configured to sample at 25Hz, with all measurements subsequently quality controlled for low correlation and signal to noise ratios (SNR) in post-processing. Additionally, any measurements found to be outside ± 3 standard deviations from the mean value were removed. Fig. 6.2 shows a 300s sample of the streamwise velocity with a bulk velocity of $U_0 = 0.76m/s$ and a water depth of $H = 0.64m$. A free-stream turbulence intensity $I = 10\%$ was found from the sample and used in the further numerical analysis aiming at investi-

gating the effect of realistic inflow turbulence on the turbine's performance and hydrodynamic loads.

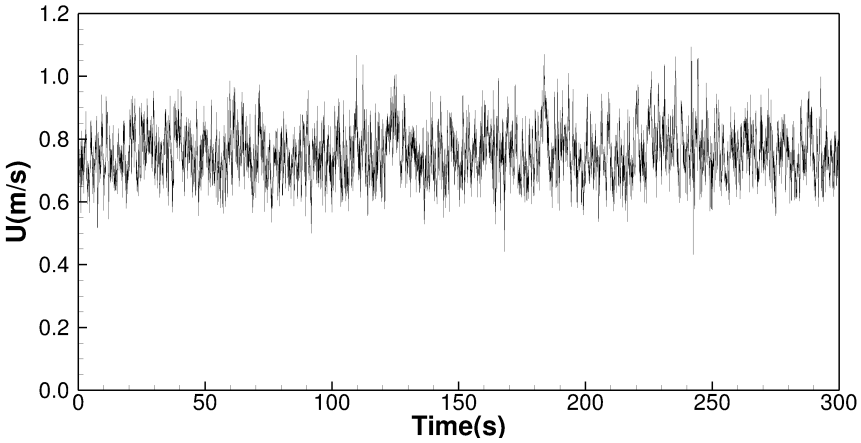

Figure 6.2: Streamwise velocity signal obtained with ADV placed upstream the turbine for 300s.

6.3 Hydrodynamics validation

6.3.1 Simulation setup

The numerical domain presented in Fig. 6.3 is $L = 8D$ long (x-direction), $B = 3D$ wide (y-direction), equalling the width of the laboratory flume. It has a domain height that matches the water depth in the laboratory experiment, i.e. $H = 1.6D$. The turbine diameter is $D = 0.4m$ and is same as the diameter of the laboratory turbine. The device is centred in the cross-section and is placed $1.5D$ away from the inlet. The approaching velocity profile was not measured experimentally. Nonetheless, the oncoming flow is considered to be fully developed upstream of the turbine, so $1/7^{th}$ power law vertical and horizontal velocity profiles are prescribed at the inlet. This distribution is commonly accepted in channel flows, and is recommended to be adopted in the simulation of tidal stream turbines when no velocity profile data is available, DNV-GL [2015]. The bulk velocity of U_0=0.76m/s found from the ADV signal in Fig. 6.2 is prescribed as inflow condition at the upstream end of the domain. The Reynolds number based on

the turbine's diameter ($Re_D = DU_0/\nu$) is $3.04 \cdot 10^5$, and the Froude number ($Fr = U_0/\sqrt{gH}$) is 0.3. No-slip boundary conditions are employed at the side and bottom channel walls while a shear-free condition is used at the water surface. At the downstream end of the domain a convective outflow boundary condition is employed. In order to reduce the computational effort, the length of the hub is shortened compared to the real prototype dimensions. The influence of the length of the hub is deemed small, which was also demonstrated by Kang et al. [2012].

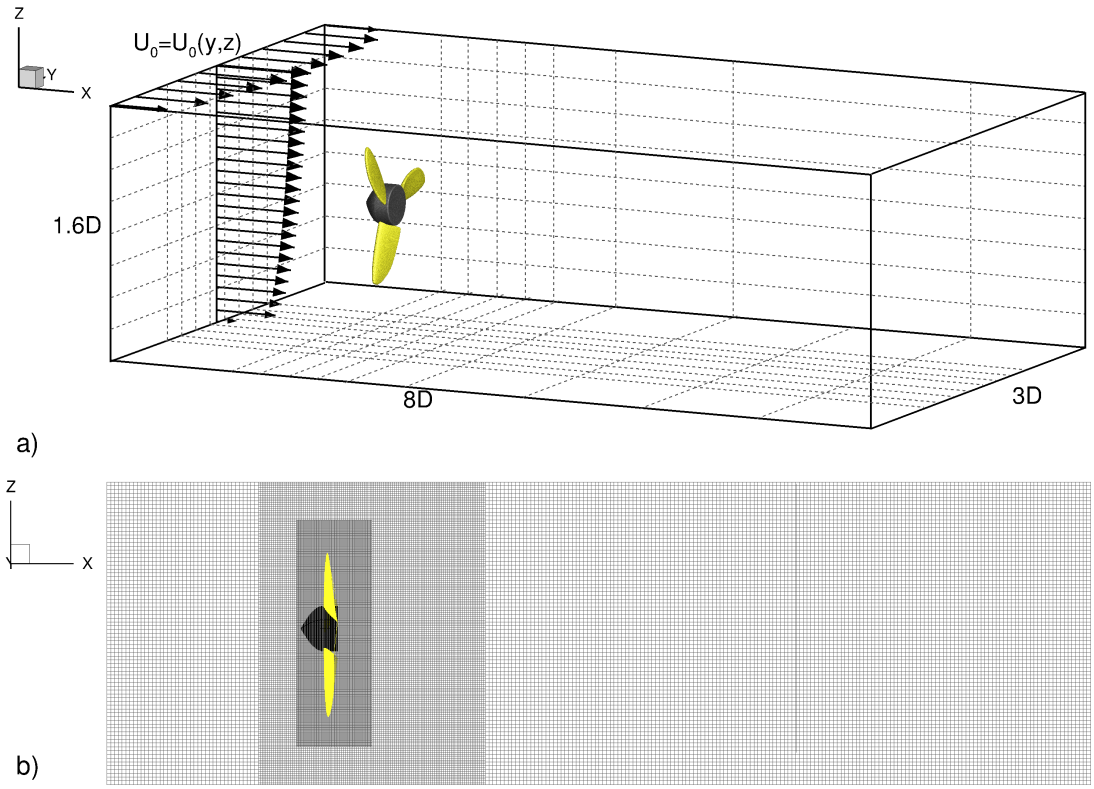

Figure 6.3: a) Numerical domain with the inlet velocity profile sketched; b) Longitudinal plane along $y/D = 1.5$ (through centre of rotor) showing the mesh distribution with increased resolution around the rotor using local mesh refinement.

The entire domain is decomposed into 720 sub-domains and the division is sketched out via dashed lines in Fig. 6.3a). Fig. 6.3b) depicts the three levels of LMR employed with the goal to achieve an adequate resolution in the proximity

of the rotor. The turbine rotates for three revolutions as the generated torque converges after approximately one revolution, as demonstrated in Fig. 6.4a). The simulations are then continued for another two revolutions to obtain average quantities. The simulations are performed on 144 cores and each simulation consumes approximately 31,000 CPU hours.

6.3.2 Numerical parameter sensitivity and validation

The method of LES is grid-dependent, i.e. the finer the numerical grid the more length-scales of turbulence are resolved explicitly. In order to ensure that all relevant turbulent scales are properly resolved it is necessary to carry out at least two LESs on different grids. Here, simulations with two different mesh resolutions and three different time steps are performed. The details of each mesh, which is uniform in the three spatial directions, are provided in Table 6.2 and refer to the Eulerian mesh resolution at the finest level. The sensitivity of the time step is evaluated on the finest mesh and at rotational speed $\lambda = \lambda_{opt}$ at which the turbine performance is maximum. Fixed time steps of $\Delta t_1^* = 28.5 \cdot 10^{-5}$s, $\Delta t_2 = 17.1 \cdot 10^{-5}$s, $\Delta t_3 = 14.25 \cdot 10^{-5}$s are tested, where $\Delta t^* = \Delta t^* U_0/D$. The CFL condition based on the rotor's tip speed ($CFL = U_{tip}\Delta t/\Delta x$, where $U_{tip} = \Omega R$), is CFL=0.036, 0.0216 and 0.018 respectively, small enough to resolve the relevant and most energetic turbulent scales in the flow.

Mesh	$\Delta \mathbf{x}$ (m)	Sections along blade	Blades IB markers	Hub IB markers
I	0.0015	100	55,110	25,642
II	0.0010	150	113,775	44,006

Table 6.2: Details of the meshes used during the spatial resolution sensibility study of the HATT simulation.

Due to the commercial sensitivity of the experimental data, the computed torque, power coefficient, and tip speed ratio are normalised by the experimental torque value T_{exp}, the experimental maximum power coefficient $C_{p_{max}}$ and the tip speed ratio λ_{opt} at which C_p=$C_{p_{max}}$, respectively. The normalised torque obtained from the simulations on the different meshes and time steps are plotted as a

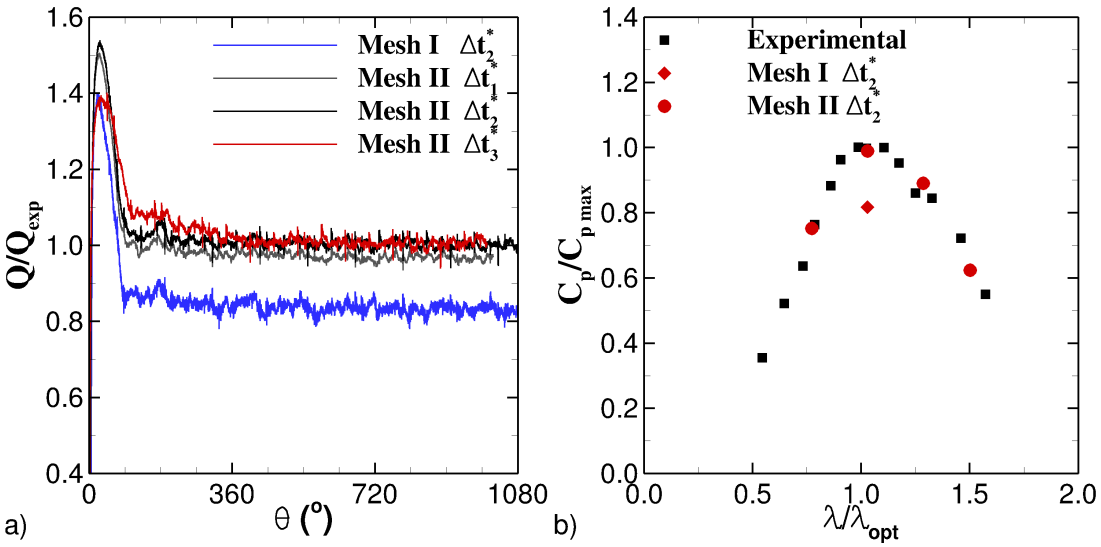

Figure 6.4: a) Instantaneous normalised torque along 3 revolutions with the turbine rotating at λ=λ_{opt} when using different meshes and time steps. b) Normalised computed power coefficient compared with the experimental results for the four different tip speed ratios analysed.

function of rotated angle in Fig. 6.4a). The normalised mean power coefficient is presented in Fig. 6.4b) as a function of normalised tip speed ratio for the two meshes using Δt_2^*. It is observed that the impact of the mesh resolution is quite considerable, the simulation on the coarse mesh predicts approximately 20% less torque than the simulation on the fine grid, and this is reflected in the normalised power coefficient in Fig. 6.4b). In contrast to this, the effect of the time step on the fine mesh is relatively small: the simulation using Δt_1^* predicts only 3% less torque than the simulations employing Δt_2^* or Δt_3^*. Four simulations on the finest mesh using Δt_2^* are performed covering four different normalised tip speed ratios, λ/λ_{opt}, so that the turbine characteristic curve can be plotted. As seen from Fig. 6.4b), the computed normalised power coefficient shows very good agreement with the one obtained from the experiments for all values of λ/λ_{opt}, confirming the accuracy of the method.

6.4 Results and Discussions

6.4.1 Hydrodynamics during turbine operation

The complex flow past the tidal turbine rotor is visualised in Fig. 6.5 depicting instantaneous pressure iso-surfaces, a commonly accepted method to educe coherent flow structures, Rodi et al. [2013]. The helicoidal tip vortices are generated as a result of the shear layer roll-up between the fast flow just above the tip of the blade, and the low velocity wake downstream of the rotor. The helicoidal tip vortices are comparable with the ones visualised experimentally by Chamorro et al. [2013b] and in the LES from Kang et al. [2012]. As Fig. 6.5 suggests, these structures are quite coherent and persist over a considerable period of time: the first vortex generated by blade 1, here denoted as vortex 1b, is still fairly intact while vortex 1a is procreated. The tip vortices are constantly being convected downstream and their spacing, η, is approximately, $\eta = U_b \times 2\pi/\Omega/3$. Between the tip vortices and the hub there is an area of high, quite incoherent turbulence, in the form of small-scale turbulence structures observed after the blades trailing edge, an indication of flow separation along the suction side of the blades.

The hub creates a recirculation zone immediately downstream and a distinct low-momentum inner wake, in the form of a spiral vortex, as is appreciated in Fig. 6.5. This inner vortex starts to meander at about two turbine diameters downstream, approximately where the tip vortices lose their coherence, and which appears to allow greater entrainment of ambient flow into the wake. Fig. 6.6a) presents contours of the instantaneous streamwise velocity in a horizontal plane at $z/H = 0.42$ together with streamlines, which indicate that the inner wake rotates clockwise in contrast to the counter-clockwise rotation of the rotor. The inner wake is characterised by low streamwise velocities and pockets of low streamwise velocity are also found inside the tip vortices. In Fig. 6.6b) flow structures, visualised using iso-surfaces of λ_2-criterion (Jeong and Hussain [1995]), are plotted together with contours of instantaneous streamwise velocity in a horizontal plane cutting through the middle of the turbine (at $z/H = 0.5$). The tip vortices are skewed as they are convected downstream by the flow. In addition, smaller, elongated rollers are generated in the shear layer at the edge of the inner wake

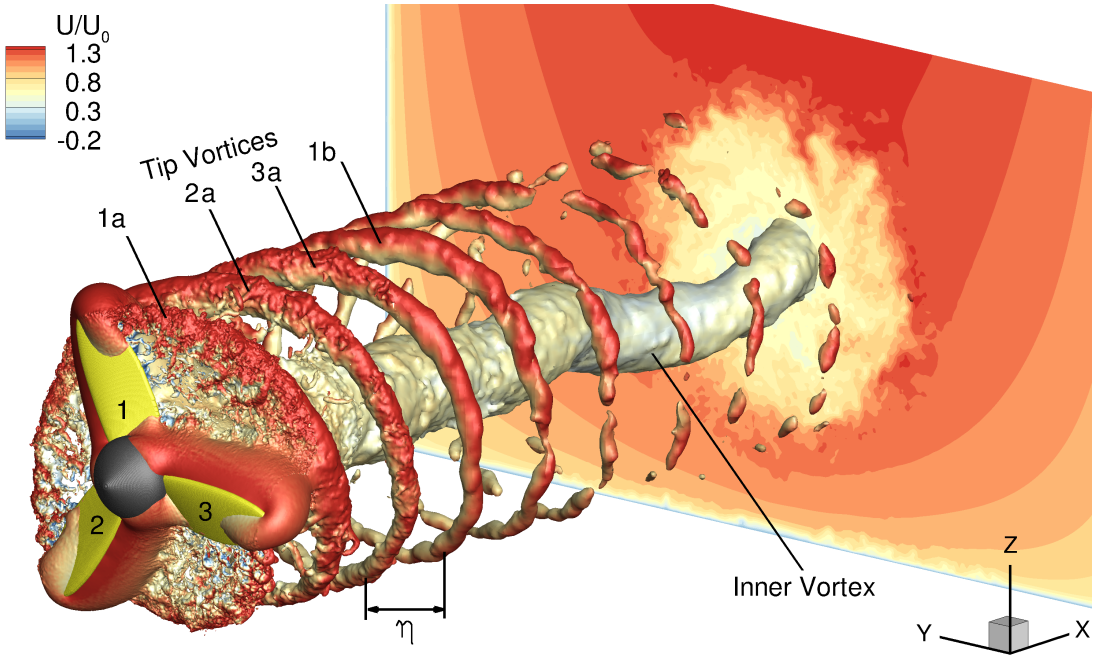

Figure 6.5: Visualisation of the flow structures generated by the turbine rotating at $\lambda = \lambda_{opt}$ represented by pressure iso-surfaces coloured with instantaneous non-dimensional streamwise velocity values.

and are also being convected downstream with the wake.

6.4.2 Hydrodynamic loadings at the blade-hub juncture

The aim of this section is to quantify bending and torsional moments at the blade root, a critical structural juncture with regards to the survivability of the rotor, McCann [2007]. The present study analyses the contribution of both thrust and tangential forces to these moments, previously defined in Section 2.4.3. The former is due to the action of the oncoming fluid onto the turbine's rotor, and the latter is mainly caused by the rotational movement of the blades. The value of these moments are obtained for the four simulated tip speed ratios as they are expected to vary with the rotational speed of the rotor.

Fig. 6.7 shows the instantaneous values of the structural moment coefficients of one blade during the second and third revolutions ($360° < \theta < 1080°$) when the turbine is rotating at λ=0.75, 1.00 and $1.25\lambda_{opt}$. The distribution of the

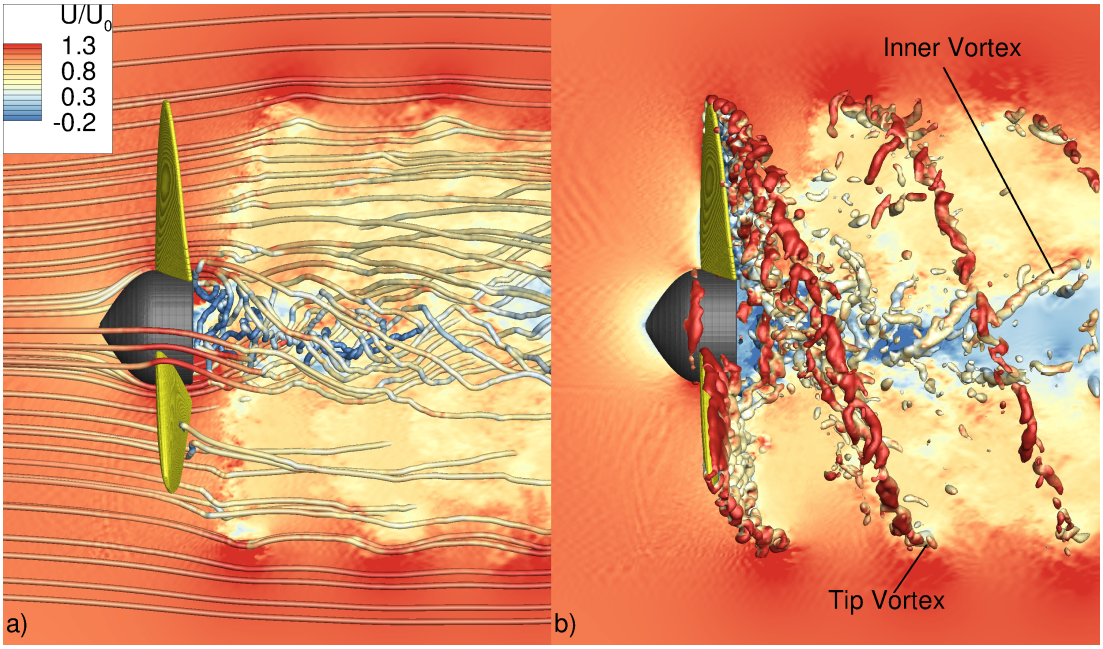

Figure 6.6: Top view of the HATT rotating at λ=λ_{opt}. a) 3D streamlines and vertical contour plane at $z/H = 0.42$ both coloured with the non-dimensional instantaneous streamwise velocity. b) Generated flow structures downstream the turbine's rotor represented with iso-surfaces of $\lambda_2 D/U_0 = -420$ with a z-plane at $z/H = 0.50$.

coefficients oscillate sinusoidally and the curve exhibits clear peaks and troughs every 360°. The blade tip is at the top when $\theta = 360°$, 720° and 1080°, and it is at these angles when the blade experiences the maximum bending moments, as seen in Fig. 6.7a) and b). At this location the highest velocities occur in the channel due to the logarithmic/exponential distribution of velocity in open-channel flows as depicted from the velocity contours in the cross-section plotted in Fig. 6.5. Bending moments are smallest when the blade tip is at the lowest point in the water column, which is where the streamwise velocities are lower than near the water surface.

Maximum and minimum moment coefficients vary for different tip speeds. From Fig. 6.7a), the maximum $C_{M_\theta^T}$ values are found at $\lambda = \lambda_{opt}$ and $1.25\lambda_{opt}$ and are similar in magnitude. Minima of $C_{M_\theta^T}$ are found at λ=$0.75\lambda_{opt}$ and at λ_{opt}. With the turbine rotating at λ=$0.75\lambda_{opt}$ and $1.00\lambda_{opt}$ the $C_{M_\theta^Q}$ curves are very similar over the entire rotation. At tip speed ratio of $\lambda = 1.25\lambda_{opt}$ the

magnitude of $C_{M_\theta^Q}$ drops by approx. 30%, which might be also related with the decrease on the turbine's performance compared to the other tip speed ratios. This reflects the non-linearity of the flow around tidal turbines and suggests that the structural design of tidal turbines requires the consideration of a range of tip speed ratios keeping in mind that tidal turbines overspeed/underspeed in marine environments.

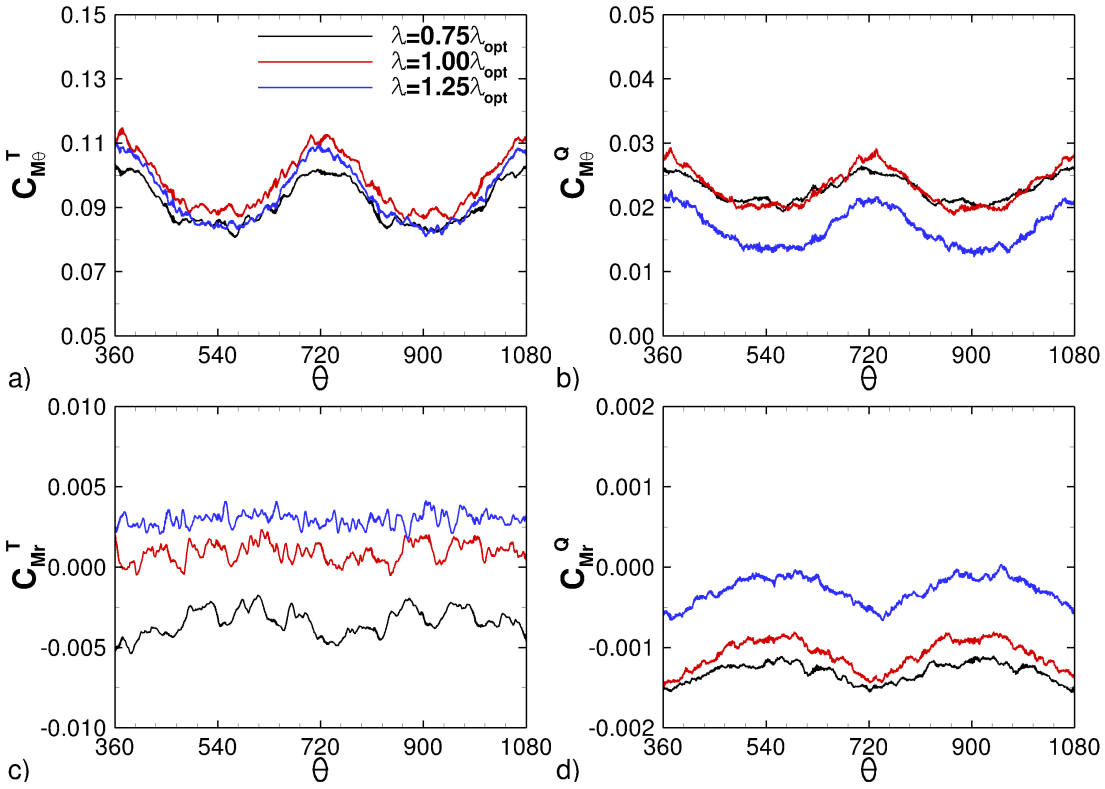

Figure 6.7: Evolution along the second and third revolutions ($360° < \theta < 1080°$) when the turbine rotates at λ=0.75, 1.00 and $1.25\lambda_{opt}$ of: the bending moment coefficients due to a) thrust ($C_{M_\theta^T}$) and b) tangential ($C_{M_\theta^Q}$) forces, and the pitching moments coefficients due to c) thrust ($C_{M_r^T}$) and d) tangential ($C_{M_r^Q}$) forces.Results for a single blade.

The torsional moment causes the blades to pitch around the blade-hub junction, and hence inducing shear forces that can lead to structural failure. Fig. 6.7c) and d) shows that the torsional moments are one to two orders of magnitude lower than the bending moments. The pattern of $C_{M_r^T}$ along the two revolutions shown in Fig. 6.7c) varies notably depending on the rotational velocity. For the higher

case shown, $\lambda = 1.25\lambda_{opt}$, the moment coefficient shows a higher irregularity compared to the other two tip speed ratios. However, reducing the rotational speed to $\lambda = 0.75\lambda_{opt}$, $C_{M_r^T}$ shows somehow a global sinusoidal pattern also found in the bending moments, while the instantaneous values have a smoother distribution than those at $\lambda = 1.00$ and $1.25\lambda_{opt}$. Hence, when the turbine spins faster the effect of the inertial forces is larger than the ones from the oncoming flow, which leads to a more uniform values and irregular distribution of $C_{M_r^T}$.

The tangential forces showed in Fig. 6.7d) contribute to generate negative values of the pitching moment $C_{M_r^Q}$ with a similar pattern previously seen in the bending moments distributions from Fig. 6.7b). It is observed that the tangential forces contribution to the pitching moment values $C_{M_r^Q}$ are smaller than that from thrust $C_{M_r^T}$. This difference is mainly due to the length of the lever arms (see Eq. 2.44 and 2.45) shown in Fig. 2.9b), where d_{r_L} used for the $C_{M_r^T}$ calculations that can be up to 0.75 times the chord length of the blade (distance from the trailing edge to the gravity center of each blade section), whereas d_{x_L} values are based on half the blade thickness that is much smaller than the chord length.

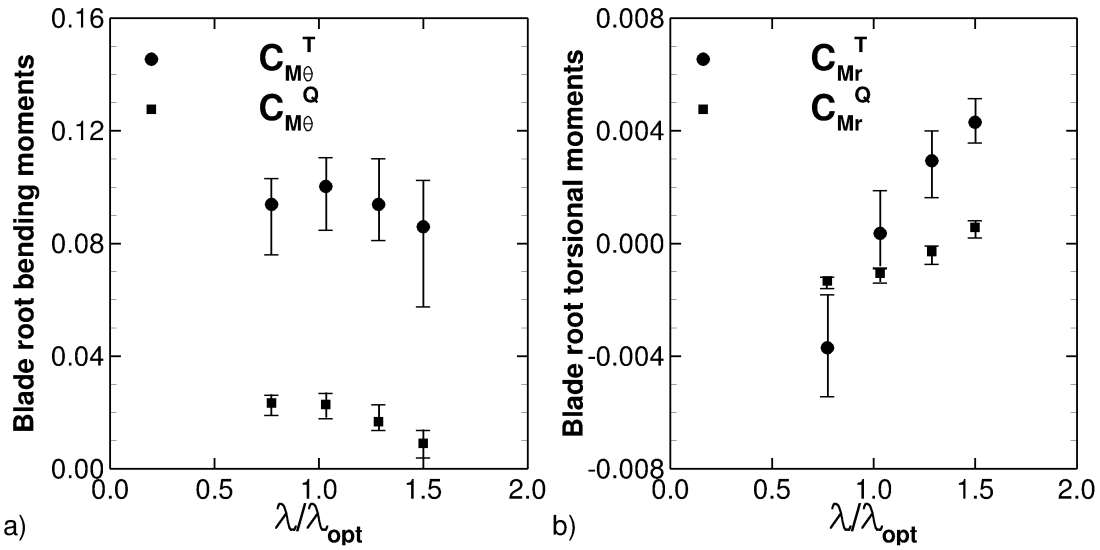

Figure 6.8: Average value and fluctuation range of the a) blade root bending moment coefficients, $C_{M_\theta^T}$ and $C_{M_\theta^Q}$, and b) the blade root torsional moment coefficients, $C_{M_r^T}$ and $C_{M_r^Q}$.

The averaged values of bending and torsional moment coefficients obtained

at various tip speed ratios are presented in Fig. 6.8a) and b), and are plotted with their range of fluctuation bounded by the maxima and minima values. The distribution of bending moments ($C_{M_\theta^T}$ and $C_{M_\theta^Q}$) as a function of tip speed ratio is similar to the C_P curve and maximum values are found at $\lambda = \lambda_{opt}$. Noteworthy is the fact that the greatest difference between maximum and minimum bending moment is obtained at $\lambda = 1.25\lambda_{opt}$, the highest rotational speed considered herein. This is in line with the experimental results of Blackmore et al. [2016]. The thrust component, $C_{M_\theta^T}$, contributes almost to 80% of the total bending moment at the root and exhibits greater variation than $C_{M_\theta^Q}$. There are no experimental data to validate the numerically predicted moments, yet Milne et al. [2013] and Blackmore et al. [2016] reported very similar values from their experimental campaigns for $C_{M_\theta^T} \approx 0.09 - 0.12$ and $C_{M_\theta^Q} \approx 0.01 - 0.025$.

The averaged values of the torsional moment, C_{M_r}, increase when the tip speed ratio is larger as Fig. 6.8b) shows. The range of fluctuation decreases with an increase in rotational speed suggesting that when the turbine rotates faster has a larger inertia and hence it is less sensible to the fluctuating velocities from the oncoming turbulent flow. At the lowest simulated tip speed ratio ($\lambda = 0.75\lambda_{opt}$), $C_{M_r^T}$ attains a negative value compared to the positive values at the higher rotational speed values. Average values of $C_{M_r^Q}$ are around zero so the contribution of torsional moment from tangential forces is much less than that from thrust forces.

6.5 Effect of free-stream turbulence on rotor hydrodynamics

The turbine rotor is now subjected to a turbulence intensity (I, Eq. 6.1) of 10%, similar to the one obtained from the experimental velocity signal (see Fig. 6.2). This is added to the mean velocity at the inlet via turbulent fluctuations generated using the Synthetic Eddy Method (SEM) explained in Appendix A, considering

an eddy length, l_e, value of $0.25H$.

$$I(\%) = \frac{\sqrt{\frac{1}{3}(\overline{u'^2} + \overline{v'^2} + \overline{w'^2})}}{U_0} \cdot 100 \tag{6.1}$$

The effect of free-stream turbulence on the rotor performance, the wake downstream of the rotor, and the structural bending moments is assessed. In this analysis, only the case with the HATT rotating at $\lambda = \lambda_{opt}$ is simulated using mesh II and Δt_2^*. The simulation is run for 7 revolutions ($\theta = 2520°$). In order to allow comparison of turbulence statistics, the uniform inflow simulation ($I = 0\%$) is run for another 4 revolutions. The flow statistics of both simulations are not fully converged, as it would require to run over several more revolutions (Kang et al. [2014]), which is deemed computationally too expensive. Nonetheless differences in the turbine hydrodynamics and structural loadings with and without free-stream turbulence are obvious enough after the chosen period of time.

6.5.1 Influence on the turbine hydrodynamics

The time-averaged normalised streamwise velocity contours in the XY-plane through the middle of the channel depth, i.e. $z/H = 0.5$, are shown in Fig. 6.9a) and c) for the $I = 0\%$ and 10% cases respectively. These contour plots demonstrate that the wake recovery is shortened due to the presence of free-stream turbulence. The low velocities, represented by the blue colour areas, extend to $x/D \approx 3.5$ downstream the turbine for the uniform inlet case, while for the $I = 10\%$ case this is reduced to $x/D \approx 1.5$.

XY-planes of the instantaneous normalised streamwise velocities are presented in Fig. 6.9b) and d) after the turbine rotates 2440°. The tip vortices are appreciated in the turbine's wake along $y/D = -0.5$ and 0.5 and high-velocity streams above the tip vortices are discerned irrespective of the approach flow velocity. However, the signature of the tip vortices is observable until $x/D \approx 3.0$ in the uniform inlet case, Fig. 6.9b), whereas in presence of free-stream turbulence the tip vortices are obvious only until $x/D \approx 1.5$, see Fig. 6.9d). This latter is a result of the oncoming turbulence accelerating the filling of the low-momentum

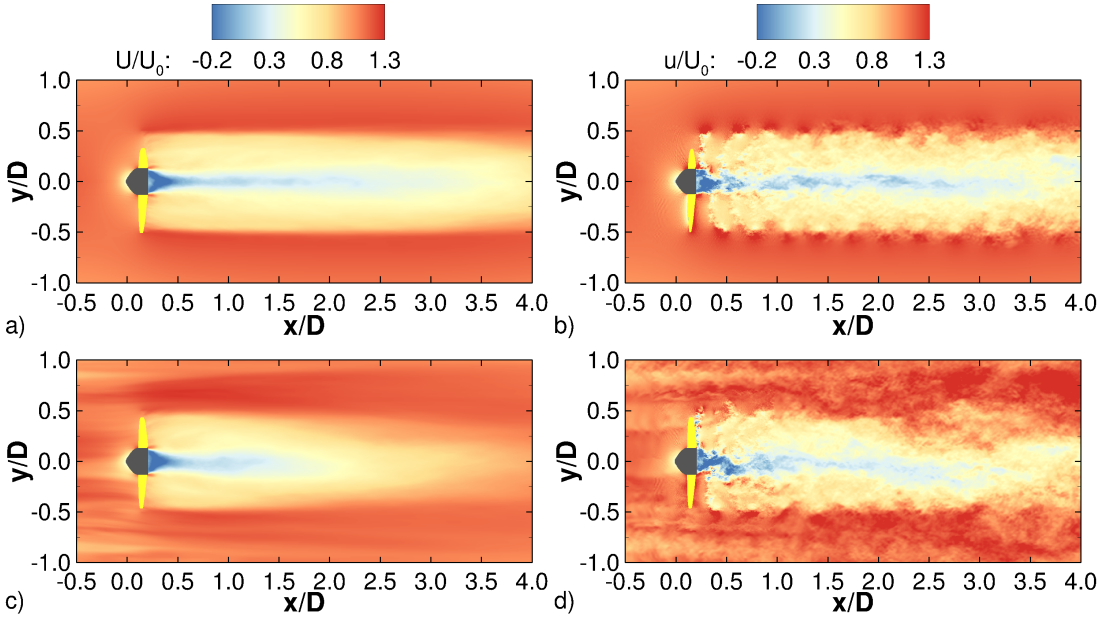

Figure 6.9: XY-planes at the middle of the channel ($z/H = 0.5$) representing the turbine's wake after it rotates 2240°. a) Mean and b) instantaneous non-dimensional streamwise velocity for the uniform inflow case, and c) mean and d) instantaneous non-dimensional streamwise velocity for the turbulent inflow case.

wake behind the rotor and results in shearing and stretching of the tip vortices, and leads to a loss of their coherence. Also, the instantaneous velocity contours of Fig. 6.9b) and d), suggest that the rotor's wake experiences an earlier onset of meandering in the presence of free-stream turbulence compared to the uniform inlet case. The wake instability is visible already after $x/D \approx 1.5$ for the former while the wake becomes unstable at $x/D \approx 3.0$ for the latter case. The absence of turbulence in the flow sustains the shear layer between outer flow and rotor wake, and hence promotes a delay of wake meandering. The opposite situation is found for the $I = 10\%$ case where after $x/D \approx 1.5$ the entrainment of ambient flow into the wake triggers the rotor's wake instability.

The present computational domain, that represents the hydraulic flume, extends vertically 1.6 times the turbine's diameter with a clearance of $0.3D$ between the blade tips and both the flume's bottom and water surface. This setup results in a notable variation of the hydrodynamics in the vertical direction. This is observable in the normalised streamwise velocity distribution in a longitudinal

plane along the channel centre ($y/B = 0.5$) presented in Fig. 6.10. The normalised time-averaged streamwise velocities contours are presented in Fig. 6.10a) and c), for the uniform and turbulent inlet velocity conditions respectively, and they show that in both cases the velocity above the turbine ($z/D \geq 0.5$) is considerably higher than below it ($z/D \leq 0.5$). The difference in wake recovery, already observed in the XY-planes from Fig. 6.9a) and c), is again appreciated in Fig. 6.10a) and c). Noteworthy is that the turbine's low-momentum wake tends to move upwards the water surface where the high-momentum ambient velocities are found, in particular for the free-stream turbulence case as seen from Fig. 6.10c). This is in line with the findings by Vybulkova et al. [2016] who investigated the effects of a parabolic approach flow velocity distribution on the wake of a HATT in comparison with an uniform approach flow.

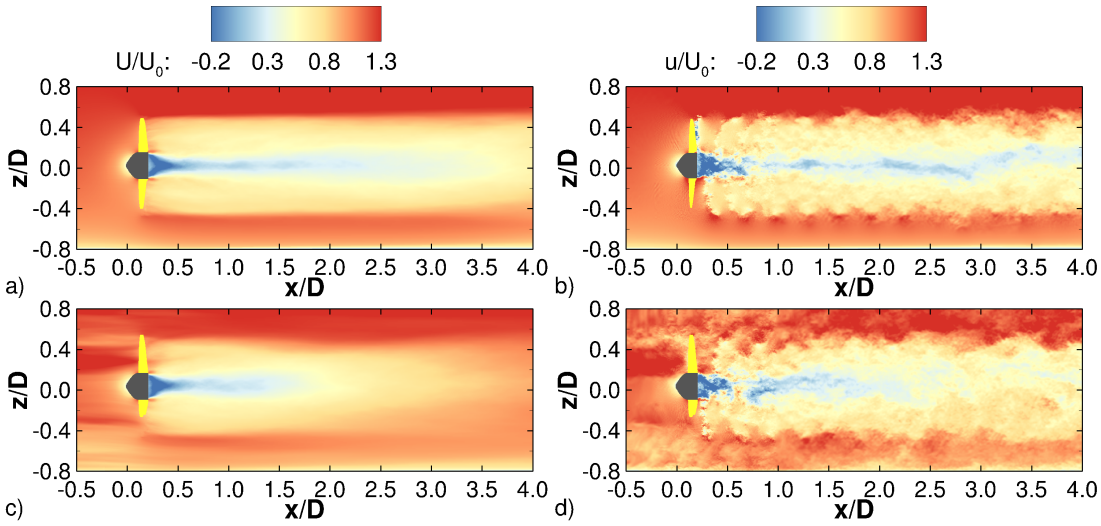

Figure 6.10: XZ-planes at the middle of the channel ($y/B = 0.5$) representing the turbine's wake after rotating 2240°. a) Mean and b) instantaneous normalised streamwise velocity with uniform inflow ($I = 0\%$), and c) mean and d) instantaneous non-dimensional streamwise velocity with turbulent inflow ($I = 10\%$).

From the instantaneous normalised streamwise velocity contours from the $I = 0\%$ case presented in Fig. 6.10b), the tip vortices get mixed with the ambient channel flow faster when they are close to the free-surface compared with their evolution closer to the channel's bottom. The blade tip velocity is constant (the turbine rotational velocity is prescribed) and hence the shear induced by

the blade's tip on the ambient flow is higher when the difference in velocities is larger, i.e. the blades induce a larger shear on the bottom than at the top of the channel. As a consequence, the shear layer generated by the convection of the tip vortices is more stable closer to the channel bed ($z/D = -0.5$) than closer to the surface ($z/D = 0.5$). Similar wake evolution is observed also in Fig. 6.10d) for the turbulent inflow case where the described mixing between the free-stream flow and the turbine's wake happens earlier. As a final consideration, the different stability on the shear layer along the vertical direction seems to drag the inner wake towards the top of the channel, as observed in Fig. 6.10b). This latter consideration sums to the observations seen in Fig. 6.9b) to explain the spiral evolution of the inner vortex showed in Fig. 6.5.

Fig. 6.11 plots the velocity deficit, U_D, which is defined as $U_D = (U_0 - \overline{U})/U_0$, giving more quantitative evidence of the quicker wake recovery when the approaching flow is more turbulent. This agrees well with the experimental findings of Mycek et al. [2014b] and Myers et al. [2013], and results from numerical simulations using actuator disk theory from Blackmore et al. [2014], who reported that the velocity deficit recovery in the turbine wake is faster when the turbulence intensity is greater.

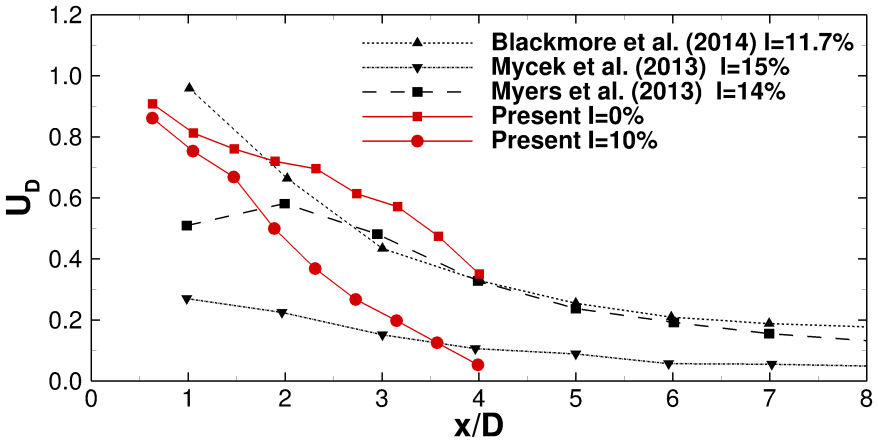

Figure 6.11: Profiles of velocity deficit along the turbine's wake centreline. Results from the LES with turbulent and non-turbulent inflow conditions are plotted together with data from experimental (Myers et al. [2013]) and numerical studies (Blackmore et al. [2014]).

The velocity fluctuations experienced in the turbine's wake are analysed by

means of time-averaged TKE ($k = 1/2(\overline{u'^2} + \overline{v'^2} + \overline{w'^2})$) and instantaneous TKE ($k' = 1/2(\overline{(u-U)^2} + \overline{(v-V)^2} + \overline{(w-W)^2})$), being both variables are normalised by U_0^2. Contours of time-averaged TKE for the $I = 0\%$ and 10% cases are plotted in Fig. 6.12a) and c) respectively, showing small differences in the TKE distribution until $x/D \approx 1.0$. In this near-wake area, the signature from the tip vortices is observed with a region of large TKE values (red colour areas) along $z/D = -0.5$ and 0.5. They are slightly higher for the $I = 10\%$ case in comparison with the $I = 0\%$ due to the ambient turbulence contributing to the velocity fluctuations. Individual tip vortices are easy to discern as pockets of high TKE along $z/D = -0.5$ and $z/D = 0.5$ are depicted from the contours of instantaneous TKE in the right column of Fig. 6.12. Downstream of the hub there is an area of elevated TKE until $x/D \approx 0.75$ which corresponds to the turbulence in the immediate recirculation zone behind the hub's wake, where the large velocity fluctuation area corresponds to the low streamwise velocity values from the hub's wake shown in Fig. 6.10a) and c).

Downstream this near-wake area, a transition mid-wake region with reduced TKE values is developed. This area begins afterwards the hub's wake influence ($x/D \approx 0.75$) until the TKE values increase again due to the meandering of the inner wake that triggers velocity fluctuations. Such intermediate region in the wake has a different length in each of the simulated cases, with an extension between $x/D \approx 1.0$ until $x/D \approx 2.5$ for the $I = 0\%$ case, and between $x/D \approx 1.0$ and $x/D \approx 1.5$ for the $I = 10\%$ case. This difference in the downstream bound of the mid-wake region is directly related with the region where the ambient channel flow entrains within the turbine's wake.

The most noteworthy difference in the distribution of mean and instantaneous TKE between the turbulent and uniform inflow cases is the far-wake region. An area of high TKE is observed after $x/D \approx 2.5$ and $x/D \approx 1.5$ for the $I = 0\%$ and 10% cases respectively. The meandering of the inner vortex, visualised in Fig. 6.5, is responsible for significant velocity fluctuations, and hence results in high values of the TKE values. From both, mean and instantaneous TKE plots, it is observed that wake meandering starts earlier in the $I = 10\%$ than in the $I = 0\%$ case, and also the magnitude of TKE is greater in the $I = 10\%$ case. Clearly, the earlier break-down of the tip vortices due to the turbulent ambient

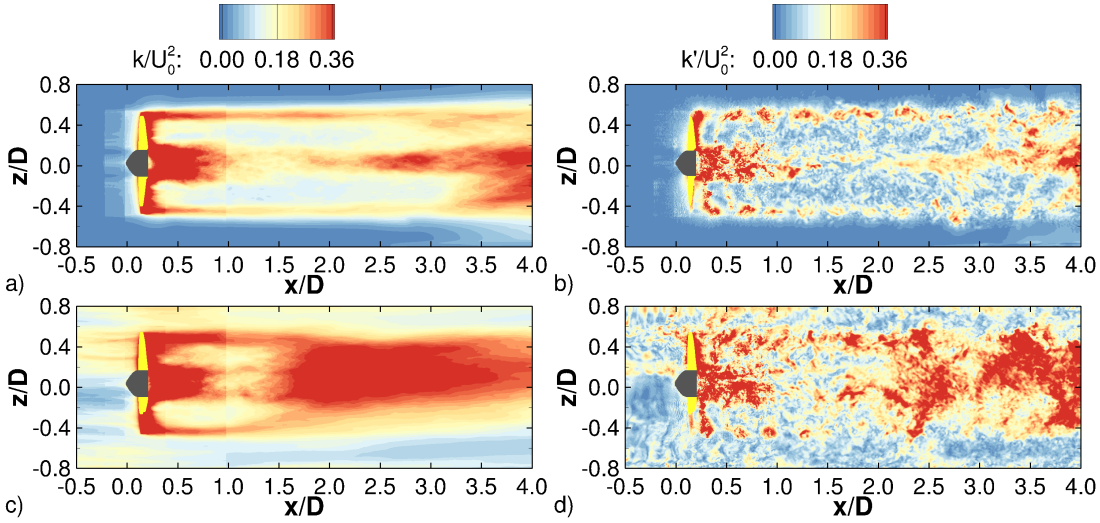

Figure 6.12: XZ-planes at the middle of the channel ($y/B = 0.5$) representing the turbine's wake after rotating 2240°. a) Mean and b) instantaneous non-dimensional turbulent kinetic energy for the uniform inflow, and c) mean and d) instantaneous non-dimensional turbulent kinetic energy for the $I = 10\%$ case.

flow leads to an earlier entrainment of fluid into the low-momentum rotor wake, and vortex meandering/oscillation appears to be enhanced by the outskirts fluid entrainment. The turbine's wake analysed and reported herein share several of the characteristics revealed from the LES by Kang et al. [2014]. Some of the differences are most likely the result of the higher blockage of the current channel in comparison with their setup (Edmunds et al. [2014]).

Fig. 6.13 presents normalised time-averaged turbulent kinetic energy contours at four cross-section downstream of the rotor located at $x/D = 0.33$, 1.0, 2.0 and 3.5. These locations are selected to cover the near-wake region ($x/D = 0.33$), the transition between near- and far-wake ($x/D = 1.0$) and the far-wake region for the turbulent inflow case ($x/D = 2.0$) and non-turbulent inflow case ($x/D = 3.5$), respectively. In the near-wake, Fig. 6.13a) and b), TKE level contours are highest in the area of the tip-vortices (coinciding with the circumference of the rotor) and in the hub's recirculation zone. There is nearly zero TKE outside of the rotor's swept area in the $I = 0\%$ case in contrast to the ambient turbulence of the $I = 10\%$ case. In the intermediate wake region, at $x/D = 1.0$, Fig. 6.13c) and d), the areas with higher values of TKE look similar among the two cases, and

the magnitude of TKE is reduced in comparison to $x/D = 0.33$. The decay in velocity fluctuations suggests reduced strength of the tip vortices.

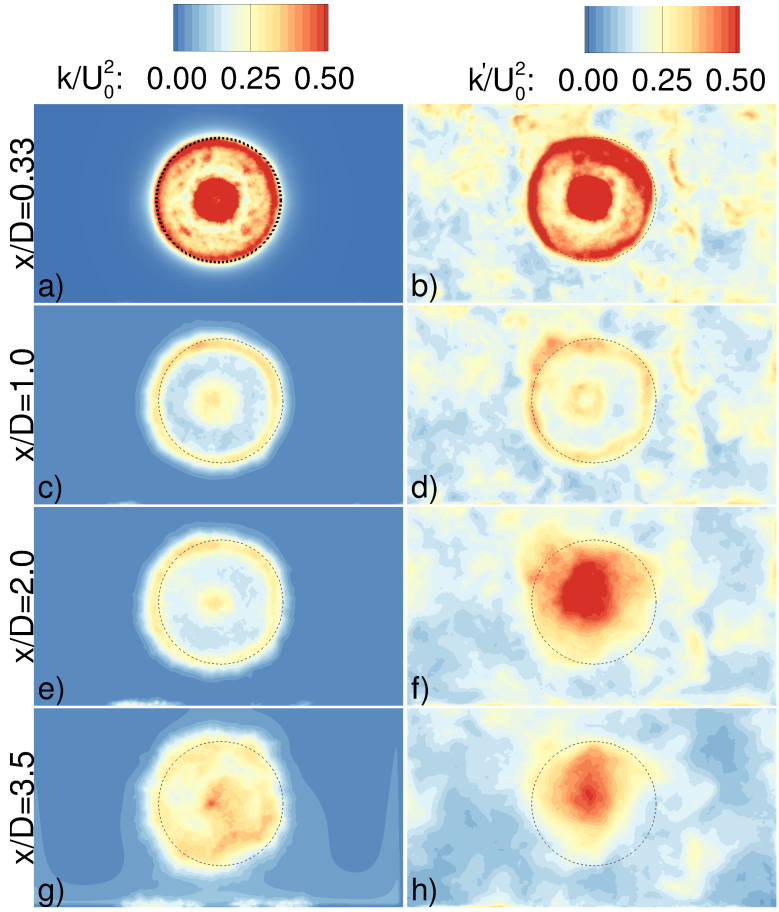

Figure 6.13: X-planes located at 0.33D, 1.0D, 2.0D and 3.5D downstream the turbine representing the non-dimensional turbulent kinetic energy contours when an inlet turbulence intensity of a) $I = 0\%$ and b) $I = 10\%$ is used. The dotted circle represents the turbine's swept area.

As seen from Fig. 6.13e), at $x/D = 2.0$ the mean TKE distribution and magnitude is very similar than at $x/D = 1.0$, which underlines that the tip vortices remain coherent over a certain period of time in the uniform inflow case. In contrast, the mean TKE distribution at $x/D = 2.0$ is significantly different from the one at $x/D = 1.0$ for the $I = 10\%$ case as observed from Fig. 6.13f). The $x/D = 2.0$ plane can be considered to be already in the far-wake region and therefore high values of TKE are observed in a ring-shape area within the

turbine's swept area, as the result of large velocity fluctuations stemming from the meandering of the inner vortex. Noteworthy is the fact that at $x/D = 2.0$ the tip vortices have lost their coherence. In the $x/D = 3.5$ cross-sections, the far-wake developed under turbulent inflow conditions (Fig. 6.13h)) still exhibits a concentrated region of high TKE albeit the magnitude is reduced compared to $x/D = 2.0$. At this distance downstream of the turbine, the low-momentum zone has been filled with outer fluid and hence the velocity deficit is reduced as also shown in the mean streamwise velocity contours from Fig. 6.10c). On the contrary, at $x/D = 3.5$ for the uniform inlet case (Fig. 6.13g)), the unstable far-wake starts to develop with an increase in the TKE levels within the turbine's swept area. At this location the wake does not exhibit the same extent and magnitude of high TKE as in the $I = 10\%$ case, however the signature of the tip vortices is still visible and this appears to hinder the development of the inner vortex of the $I = 0\%$ case.

The primary Reynolds shear stresses for the uniform and turbulent inflow cases are presented in Fig. 6.14a) and b) respectively. For the laminar inflow case, the stream behind the hub due to the inner wake is well depicted and also the signature of the tip vortices. In the turbulent inflow case the far-wake is again characterised by the triggering of $u'v'/U_0^2$ values since $x/D \approx 1.5$, whilst this is observed at $x/D \approx 2.5$ for the $I = 0\%$ case. This correlates well with the pattern observed in the TKE contours of Fig. 6.12. The contour plots also show that immediately behind the rotor the wake rotates contrarily to the counter-clockwise motion of the turbine, whereas the far-field features an opposite sign in the primary Reynolds shear stresses indicating that it has a contrary rotation motion to that of the near-wake, and thus that of the turbine.

6.5.2 Effect of free-stream turbulence on hydrodynamic loadings

Fig. 6.15 presents the instantaneous normalised torque values between $180° < \theta < 1260°$ comparing the results with $I = 0\%$ and $I = 10\%$ prescribed at the inlet. The absence of inflow turbulence results into a quasi-uniform torque distribution

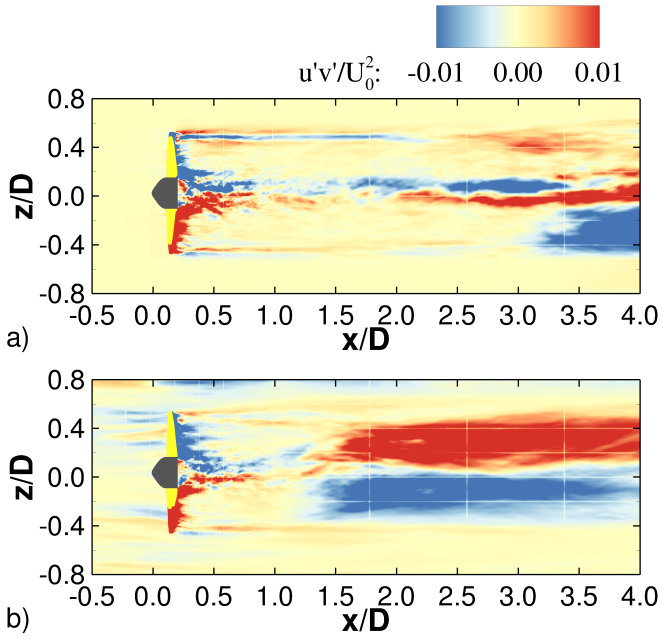

Figure 6.14: Contours of time-averaged primary Reynolds shear stresses, $u'v'/U_0^2$, at a XZ-plane at $y/B = 0.5$ when the turbine rotates 2240° for a) laminar and b) artificial turbulent inflow cases.

while for the turbulent inflow case the torque describes an obvious oscillating pattern with the peaks occurring when one blade is at its highest vertical position. Additionally, the inflow turbulence causes more irregularity on the instantaneous torque due to the interaction of the blades with the oncoming turbulent structures, resulting in sudden pressure fluctuations on the blades. An increase in torque fluctuation with an increase in the approach flow turbulence was also observed by McCann [2007]. Despite the obvious difference in the distribution of instantaneous torque, the average power coefficient achieved with $I = 10\%$ is almost identical to one obtained for the uniform inflow case. This is in line with the findings from Mycek et al. [2014b] who tested experimentally a tidal turbine under two free-stream turbulence intensity levels of 3% and 15%. They concluded that the turbine experiences little variation in its mean performance when the turbulence intensity is increased while large differences were observed in the wake recovery (also observed herein).

The instantaneous bending and torsional coefficients for one blade over $180° < \theta < 1260°$ when using uniform or turbulent inflows are shown in Fig. 6.16 a) to

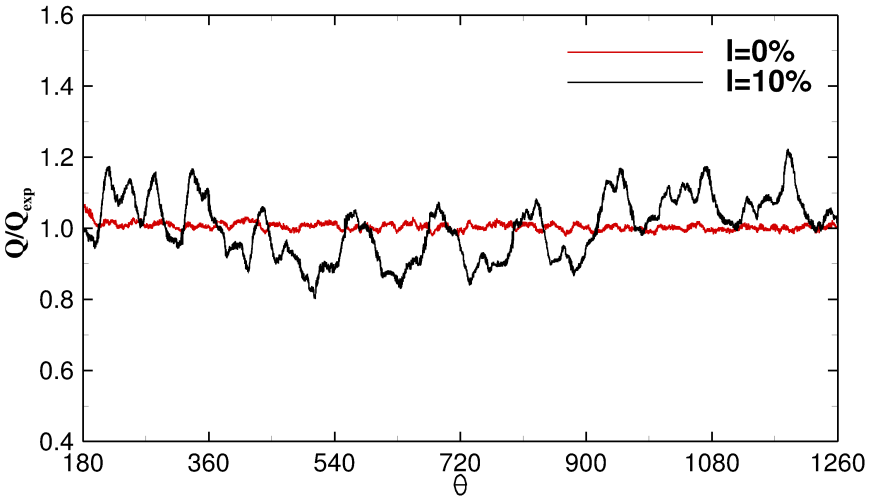

Figure 6.15: Instantaneous normalised torque value generated by the turbine blades along $180° < \theta < 1260°$ when $I = 0\%$ and $I = 10\%$ are prescribed at the inflow.

d). All structural coefficients obtained from the $I = 10\%$ case follow basically the same pattern as the ones obtained from the zero inlet turbulence case. However, the interactions of the blade with the oncoming turbulent flow provoke considerable instantaneous variation of the moment coefficients. For instance sudden moment fluctuations are appreciated at $\theta \approx 720°$, for all four coefficients, and similarly at $\theta \approx 360°$ or $\theta \approx 900°$. Such sudden variations in hydrodynamic loadings due to the oncoming turbulence result in violent and repeated force accelerations on the blades that could consequently lead to material fatigue and eventually to blade failure.

The average, maximum and minimum values of the structural coefficients for the $I = 0\%$ and 10% cases are summarised in Table 6.3. In a similar fashion than the non-dimensional torque from Fig. 6.15, the time-averaged values of the structural coefficient exhibit little variation when prescribing turbulence compared to the uniform inflow simulation. There is a significant increase in the maximum values of the bending moment coefficient with $C_{M_\theta^T} = 0.1305$ when using $I = 10\%$, which is almost 20% larger than that obtained for the laminar inflow case. The maximum bending moment coefficient from the tangential forces, $C_{M_\theta^Q}$, is larger when there is free-stream turbulence (up to a 30% more) although it is consid-

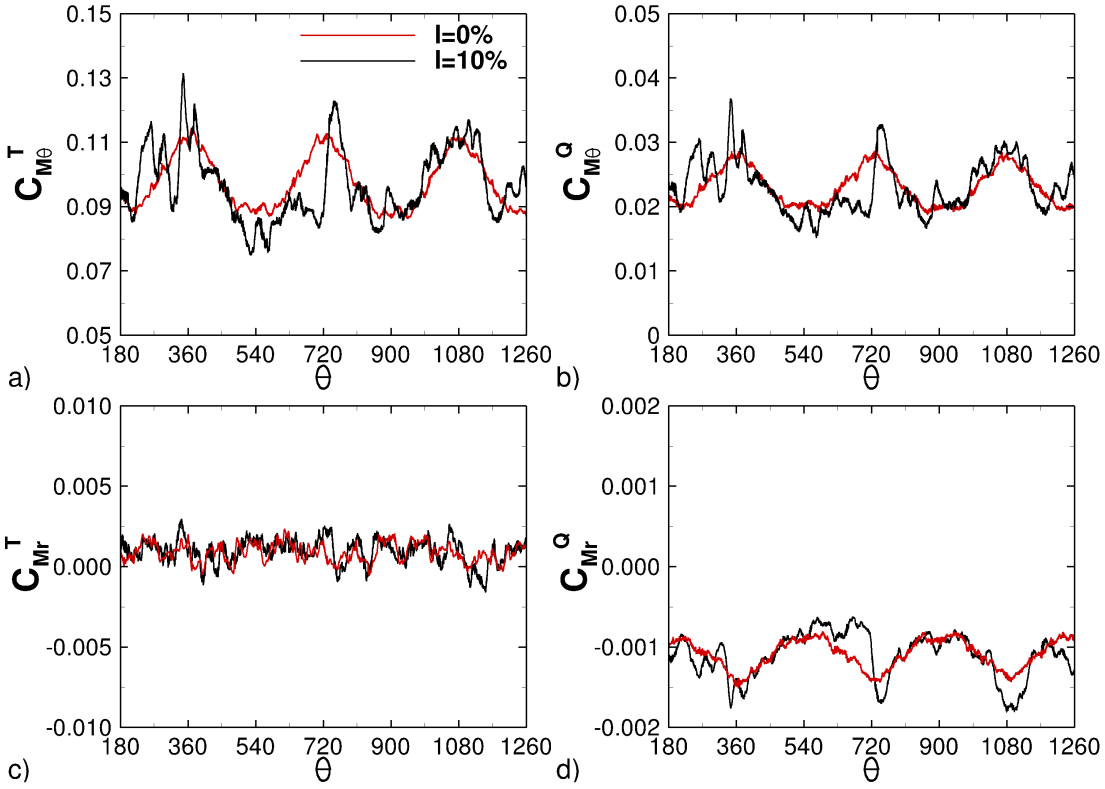

Figure 6.16: Distribution during $180° < \theta < 1260°$ of bending moment due to a) thrust and b) tangential forces, and pitching moments due to c) axial and d) tangential forces, when the turbine rotates at $\lambda = \lambda_{opt}$ influenced by the free-stream turbulence.

erably smaller than the contribution from thrust, $C_{M_\theta^T}$. The increase in extreme loadings during turbulent approach flows is translated into a wider range of load values to be sustained by the rotor. This has to be taken into consideration during the design process to avoid future failures. On the contrary, lower impact is predicted for the pitching moment, C_{M_r}, where both mean and extreme values are quite similar for both cases.

6.6 HATT over a bed of dunes

The previous simulations provided relevant insights of the effect of oncoming turbulence on the hydrodynamics of a marine device. Prescribing an artificial turbu-

Structural Moment	Value	I=0%	I=10%
$C_{M_\theta^T}$	Max	0.1113	0.1305
	average	0.1003	0.0964
	Max-min	0.0258	0.0545
$C_{M_\theta^Q}$	Max	0.0276	0.0365
	average	0.0228	0.0230
	Max-min	0.0090	0.0206
$C_{M_r^T}$	Max	0.00196	0.00206
	average	0.00036	0.00098
	Max-min	0.00115	0.00132
$C_{M_r^Q}$	Max	-0.00079	-0.00109
	average	-0.00106	-0.00146
	Max-min	0.00067	0.00065

Table 6.3: Value of the bending moment coefficients obtained at different turbulence intensity values with the turbine rotating at $\lambda = \lambda_{opt}$.

lent velocity inflow using the SEM generates the targeted turbulence intensity and eddy length scale, but it does not necessarily reproduce realistic turbulent fields tidal stream turbines find at the deployment sites. In this Section, the HATT is simulated over a dune-shape bathymetry channel flow, which aims at analysing its performance, hydrodynamic loadings, and generated downstream wake under realistic nature-like turbulent conditions. Note that the planned deployment site of this HATT is Ramsey Sound (Wales, UK), which features a very irregular bathymetry, as exhibited in Fig. 6.17 from the work of Evans et al. [2015].

The dune-shape channel bed is adopted as many authors simulated two-dimensional dunes using both body-fitted meshes (Omidyeganeh and Piomelli [2011]; Stoesser et al. [2008]; Temmerman et al. [2003]; Xie et al. [2013]; Yue et al. [2006]), and non-body conformal methods (Grigoriadis et al. [2009]). The main characteristic of the flow over a bed of dunes is the generation of large-scale turbulent structures at the lee side, e.g. horseshoe, roller and hairpin vortices, which are advected downstream. These energetic flow structures are now expected to interact with the turbine rotor. The simulation of the fluid-device interaction pretends to provide evidences on how large velocity fluctuations due to energetic

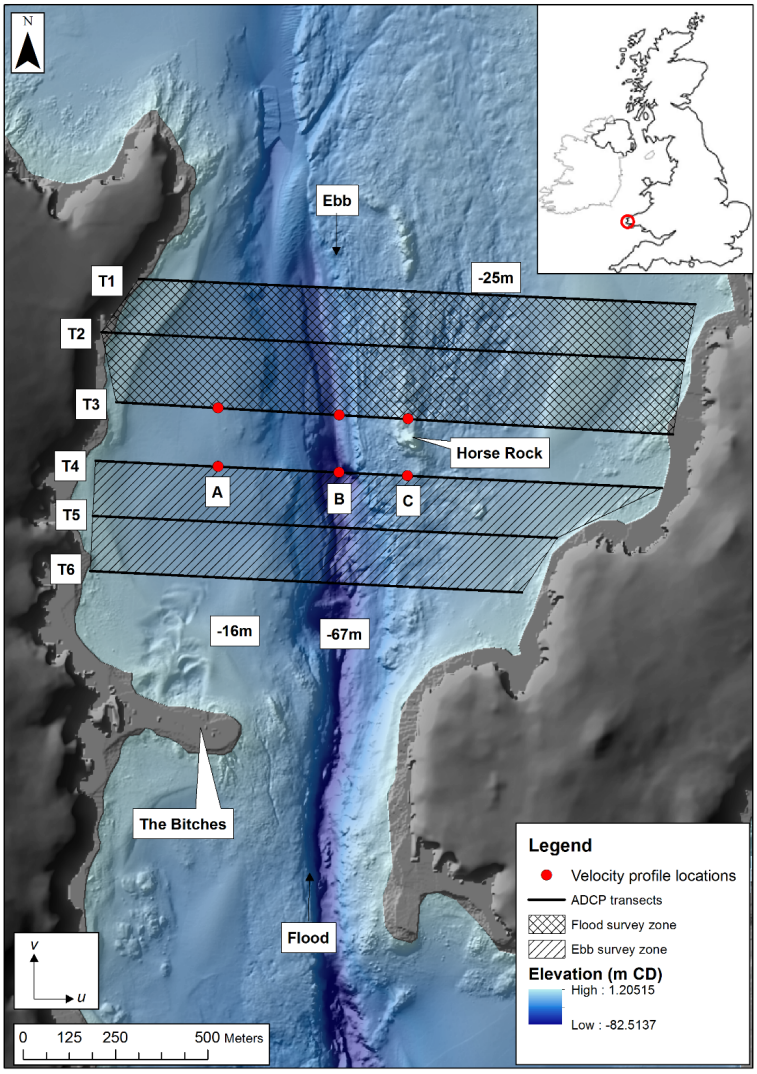

Figure 6.17: Bathymetry of Ramsey Sound (Wales) where the HATT is designed to be deployed. From: Evans et al. [2015].

turbulent structures challenge the survivability of tidal stream turbines. The outcomes pretend to provide relevant insights for tidal turbine developers in order to enhance the resilience of the marine hydrokinetic devices in the long-term from both points of view of extreme loadings and fatigue load cycles.

6.6.1 Single dune precursor simulation

A precursor simulation is performed in order to validate the generated velocity field reproduces realistic and coherence turbulent flow conditions. This initial setup comprises a single dune without placing the turbine. Periodic boundary conditions on the streamwise direction are imposed, and the flow is driven by a pressure gradient which keeps constant the flow rate. On the contrary to the other numerical works, no-slip conditions are set to the side-walls of the domain in order to keep the same flow and domain characteristics from the previous simulations. Inlet planes from this initial simulation are stored as they are uses as inflow conditions in the larger simulation setup later on adopted for the HATT.

Fig. 6.18 represents the full domain with two dunes used later on for the turbine simulation. The precursor simulation domain comprises a single dune occupying the extension $0 \leq x/k \leq 20$ according to Fig. 6.18, where k stands for the dune's height (not to be confused with TKE) and is equal to 0.16m. The flow conditions used in previous flat-bed channel flow simulations are maintained, i.e. free-stream velocity is set to 0.76m/s, and water depth H at the inlet is $0.64m$ $(4k)$ so same water height at the turbine's position as in previous setup is kept. Nonetheless, the variable bathymetry of the dune leads to a maximum water depth of $5k$ between $2.5 < x/k < 4$. In the spanwise direction, the domain is $7.5k$ wide. The free-surface is treated as shear free rigid lid. The dune is represented using the IB method, whose accuracy to represent the flow over a bed of dunes was already proven by Grigoriadis et al. [2009].

The mesh resolution is kept uniform in the whole domain with $\Delta x = 4{\cdot}10^{-3}$m, and consists of 800 x 300 x 200 grid points in the x-, y- and z- directions respectively, yielding to a total of 48 million fluid elements. Variable time step is used satisfying a CFL condition of 0.3 in order to guarantee numerical stability. The simulation is initially run until the flow is fully developed. First order statistics are then collected for 250 eddy turn-over times (h/U_0) before starting to collect second order statistics, which is performed for another 150 h/U_0. The resolution in wall-units calculated from the resulting friction velocity u_* is $\Delta y^+ = 5.8$, which justifies the use of no-slip conditions at the side-walls. The domain is divided into 900 sub-domains which runs in 100 processors.

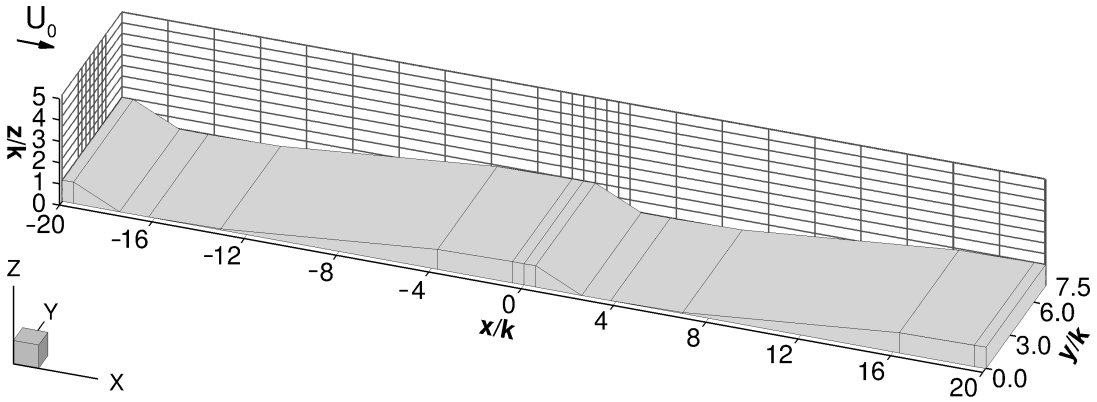

Figure 6.18: Complete domain representation of the channel with dune-bed bathymetry used for the HATT simulation.

Validation

Fig. 6.19 shows the time-averaged streamwise velocity contours. The main flow features are well captured in the simulation, such as the recirculation area on the lee side, providing evidence that the IB method represents with accuracy the velocity field over the dune's geometry. Between $2 < x/k < 12$, an expansion of the streamwise velocities is observed, i.e. when the water depth is largest, whilst along the stoss side the velocities get contracted achieving the highest velocities at the crest, where the HATT is placed later on.

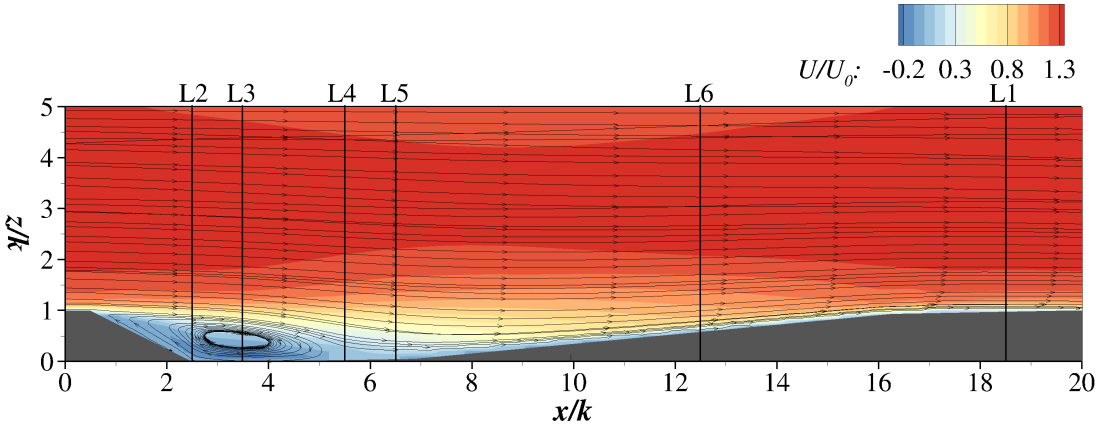

Figure 6.19: Time-averaged normalised streamwise velocity contours and streamlines for the precursor dune simulation.

First and second order statistics at six verticals, namely L1 to L6 depicted in Fig. 6.18, are presented in Fig. 6.20 comparing the present LES and experimental data reported by Stoesser et al. [2008]. Note that the actual bulk velocity is more than 2.5 times that of the cited work, thus the comparison has a quantitative point of view focused on the overall distribution and magnitude of the mean and fluctuating velocities instead of matching the velocity values. Fig. 6.20a) shows that good agreement is found for normalised time-averaged streamwise velocity up to a water depth of $z/k \approx 3$. Above this water height the x-velocities from the current LES are reduced compared to experiments. This deviation is because the current simulation adopts side-walls in the spanwise direction instead of periodic boundary conditions, which generates secondary currents. Moreover, the actual water depth is also higher than that of Stoesser et al. [2008]. At profiles L2 to L5 between $0 < z/k < 1$, the LES velocity distribution agrees well with the experimental data showing that the separated shear layer at the recirculating area, and boundary layer along the dune stoss side are well captured.

Normalised streamwise (u'/U_0) and spanwise (v'/U_0) velocity fluctuations presented in Fig. 6.20b) depicts that distribution and values of both quantities match the reference data at every profile location. The distribution of vertical velocity fluctuations (w'/U_0) follows the LES data from Stoesser et al. [2008] although in the present case these are larger above $z/k = 2$ caused by the secondary recirculation due to the use of side-walls. Overall the validation profiles show that the turbulent flow field in this precursor simulation is fully developed. Hence, inlet planes can be fed into the following case with the tidal turbine simulation.

6.6.2 HATT over a bed of dunes

The HATT is simulated using the full computational domain depicted in Fig. 6.18, which comprises two dunes placed alongside with the device situated at their transition. The turbine is then centred at $\mathbf{x}_{hub}(x/k = 0, y/k = 3.75, z/k = 3.1)$ according to the measures in Fig. 6.18. Mesh resolution II at the fine LMR level and fixed time step value of Δt_2^* are kept. The domain has a total of $2{,}5{\cdot}10^8$ mesh elements, and is divided into 2250 sub-domains that run in 456 processors. The simulation runs for 500,000 iterations yielding to an equivalent computational

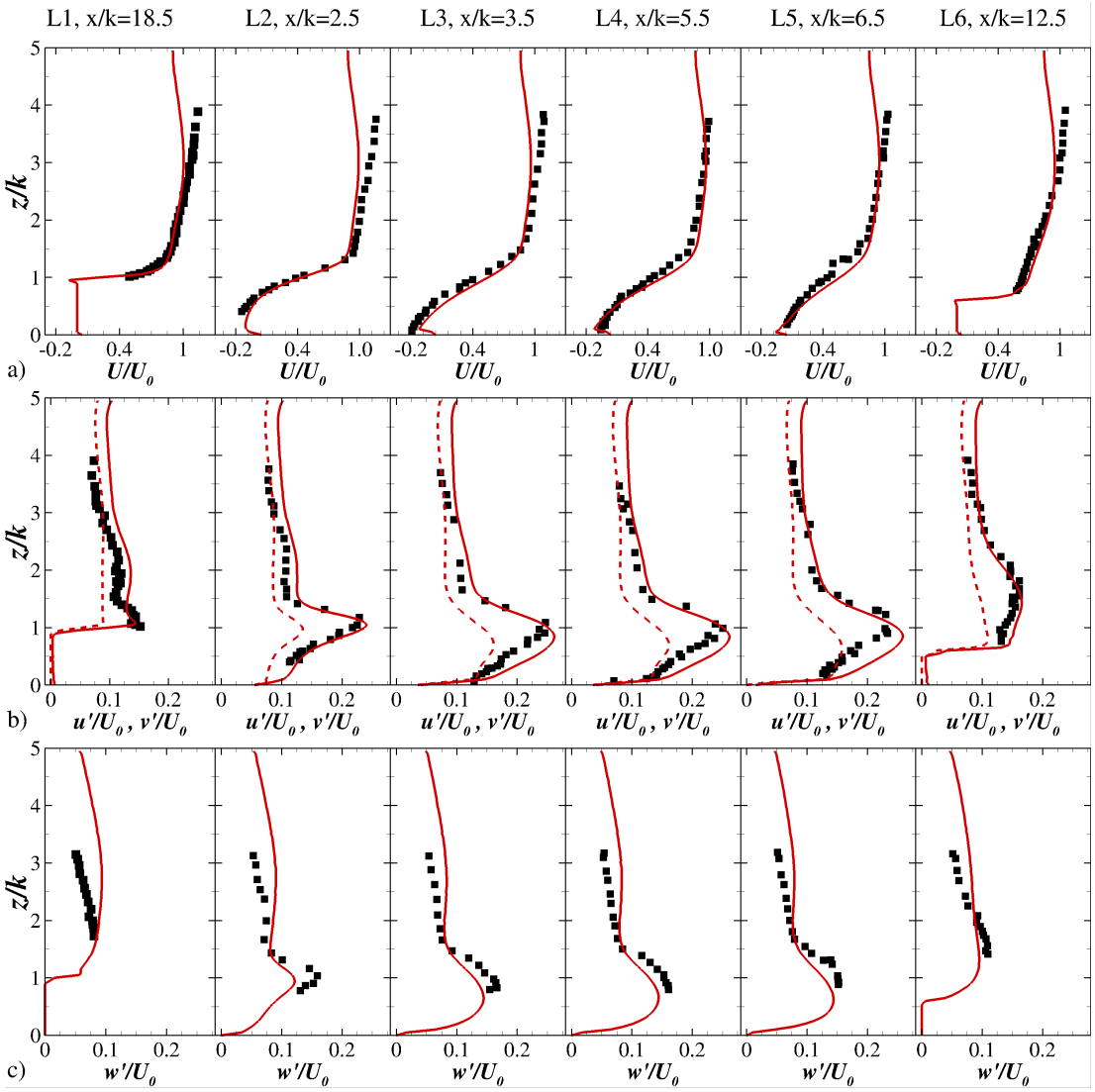

Figure 6.20: Comparison of present results (red line) with experiments (symbols) from Stoesser et al. [2008] of normalised mean: a) streamwise velocities, b) streamwise (straight line) and cross-flow (dashed line) direction velocity fluctuations, c) vertical velocity fluctuations.

load of 475,000 CPU-hours. As this simulation is computationally very expensive, only the case with the turbine rotating at its maximum efficiency, i.e. $\lambda = \lambda_{opt}$, is performed. Inlet planes from the precursor simulation are used for inflow conditions in the current domain which initially runs for 2 flow-through before placing the turbine. Convective boundary condition is set at the outlet. First

order statistics are collected after the turbine initially rotates 4 full revolutions, whilst second order statistics are collected after another 4 revolutions during 6 revolutions, as the turbine is simulated for a total of 14 revolutions.

Mean flow field

The time-averaged flow field is presented in Fig. 6.21 with contours and vectors of streamwise velocity and turbulent kinetic energy. Streamwise velocities augment on the stoss side of the upstream dune (also observed in the precursor simulation, Fig. 6.19). This causes that high velocities are distributed along the whole water depth at $x/D = -0.5$, as shown in Fig. 6.21a). The turbine interacts with the oncoming flow and obstructs it to continue its movement downstream. This interaction generates two high-momentum areas over its top and bottom tips locations, which are indicated with dotted lines in Fig. 6.21a).

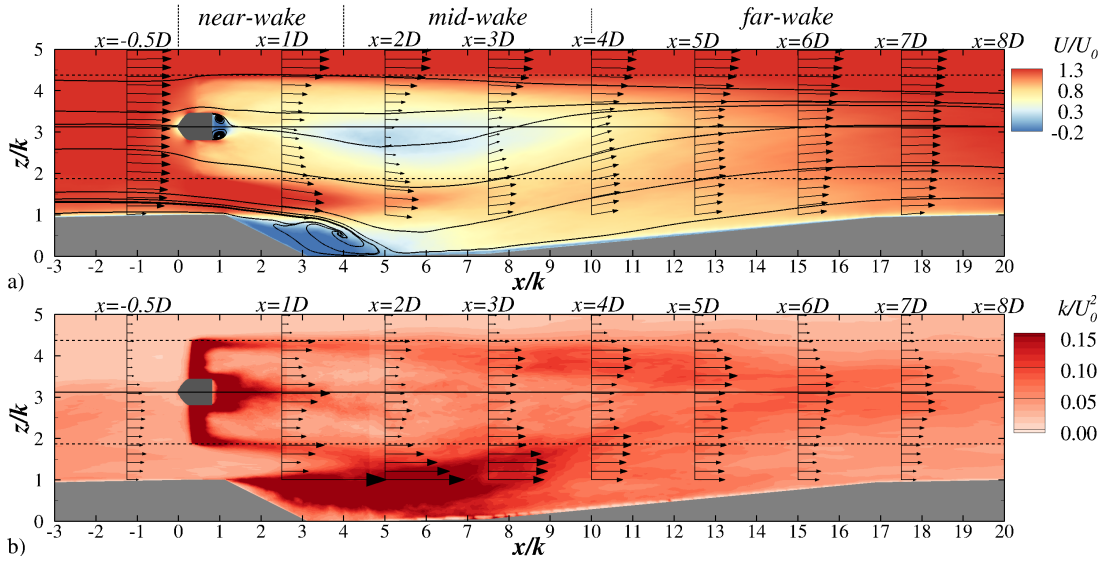

Figure 6.21: Contours of time-averaged values of a) streamwise velocities and b) TKE, corresponding to the simulation of the HATT over a bed of dunes.

The depression of the second dune generates a low-pressure area that drags the flow below the rotor and strengthens the high-velocity stream below the turbine bottom tip. The velocity vectors at $x/D = 1$ and 2 and between $1 < z/k < 2$ point downwards indicating that the flow enters into the dune recirculation area.

Above the turbine top tip, i.e. $z/k > 4$, high velocities are observed through the whole wake length. The turbine's wake is distributed in between these two high-momentum streams, and is divided into three regions according to the properties of the developed flow field, analogously to the previous flat-bed simulations. The near-wake extends along $0 < x/D < 1.5$ featuring a short recirculation enclosed to the hub. The low-velocity wake along $1.5 < x/D < 4$, represented by blue areas in Fig. 6.21a), is the most remarkable characteristic of the mid-wake region. Compared to the results from Fig. 6.10, the generated wake lacks of vertical symmetry as the low-pressure in the lee side of the downstream dune drags the wake inducing the low-velocities to be distributed more predominantly towards $z < z_{hub}$. This is deduced in the streamline departing from $z/k \approx 3$ at the hub's enclosed recirculation as $2D$ downstream the rotor is at a water depth of $z/k \approx 2.5 < z_{hub}$. In the onset of the far-wake region, at $x/D = 4 - 5$, a fast wake recovery is observed. At $x/D = 6 - 7$ the x-velocity profile exhibits an exponential profile characteristic of the boundary layer flow developed along the stoss side of the second dune, which is similar to that found at $x/D = -0.5$ upstream the turbine.

The vectors of mean TKE at $x/D = -0.5$ (Fig. 6.21b)) reveal that the turbulence developed along the first dune and approaching the tidal turbine is predominantly distributed along $z < z_{hub}$, which agrees with the streamwise turbulence intensity distribution at L1 shown in Fig. 6.20b). The main high TKE regions in the near-wake (red areas in Fig. 6.21b)) are due to blade passing effects, tip vortices, recirculation area and inner vortex behind the hub, similar to Fig. 6.12. At $x/D = 1$ these regions are still the most predominant as depicted from the TKE vector peaks located at z_{hub}, $z_{hub} + R$ and $z_{hub} - R$. In the mid-wake, the distribution of TKE along the upper and bottom parts of the channel changes. The former experiences a decay in TKE intensity as top tip vortices diffuse due to the interaction with the outskirts flow. In the latter the large velocity fluctuations generated in the recirculation area of the second dune's depression, at $x/D = 1.5 - 3$, merge with those from the bottom tip vortices, thus triggering TKE pockets. At $x/D = 2$ and 3, as a result of these wakes interaction, the highest turbulence intensities are found within $1 < z_{hub} < 2$.

At the beginning of the far-wake ($x/D = 4$), the interaction of tip vortices

with the ambient flow increases the TKE levels. The vertical profile of TKE exhibits two peaks, one above z_{hub} and the other below it. Analogously to the results from Section 6.5, the far-wake region is characterised by the inner wake meandering which becomes predominant after $x/D = 6$ noticed by the "bell-shape" distribution of TKE, whose maxima are located at half water depth.

Centreline plots

The distribution of time-average values along the centreline of the channel at $z = z_{hub}$, represented by a straight line in Fig. 6.21, are analysed. Fig. 6.22a) shows the streamwise velocity and turbulence intensity whilst primary Reynolds stresses and turbulence kinetic energy are plotted in Fig. 6.22b). Along the first dune ($-8 < x/D < 0$), the fluctuation of vertical velocity (w'/U_0^2) is the main contribution to the TKE, specially observed at $-2 < x/D < 0$ due to the generated turbulent structures on the first dune's depression, e.g. roller vortices, which are swept downstream (Stoesser et al. [2008]). At a distance of $x/D = -0.5$, the approaching flow conditions values upstream the device are $U_{hub} \approx 1.3U_0$ and $I_{hub} \approx 14.5\%$, which are referred to as values at the hub.

The near-, mid- and far-wake regions are well identified from both Fig. 6.22a) and b). The near-wake is highly influenced by the recirculation area enclosed to the hub (see Fig. 6.21a)), which features low streamwise velocities and the shedding and reattachment of vortices triggers velocity fluctuations with consequent higher levels of turbulence intensity. Primary Reynolds stresses values are reduced between $1.5 < x/D < 4$, i.e. in the mid-wake, coinciding with the lower velocities than those in the near-wake. The main contributors to TKE are both u'/U_0^2 and w'/U_0^2, as depicted in Fig. 6.22b). In the far-wake, two phenomena increase the turbulence intensity levels: the wake meandering causing high levels of u'/U_0^2 (Kang et al. [2014]), and the turbulent structures shed from the second dune's depression that merge with the turbine's wake, thus triggering w'/U_0^2 values. The latter arises as an important feature of bed-induced and turbine-wake interactions on the contrary to flat-bottom channel flows for which this is not characteristic.

A consideration can be made for the future design of turbine arrays for which

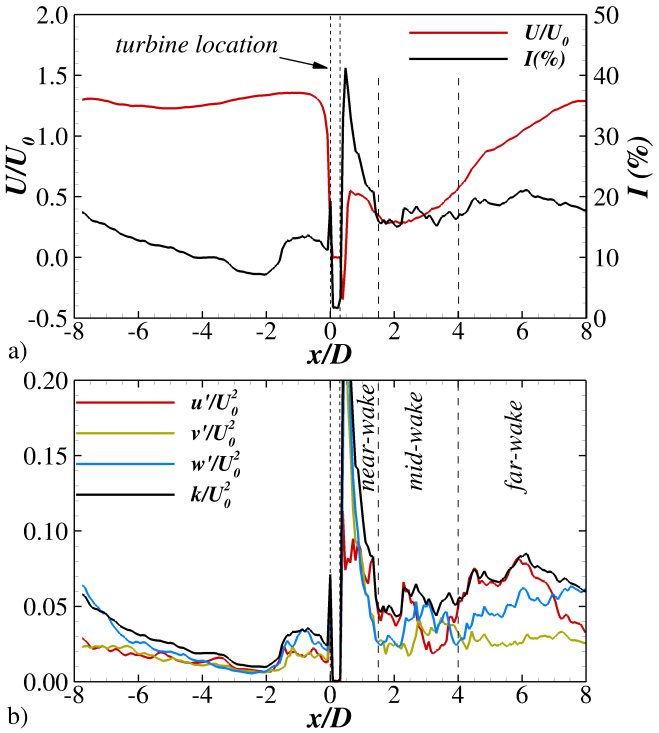

Figure 6.22: Centreline profile at $z = z_{hub}$ with normalised time-averaged values of a) streamwise velocity and turbulence intensity (%), and b) Reynolds stresses and turbulent kinetic energy.

turbine-to-turbine interaction becomes an issue. Fig. 6.21a) shows that the mean streamwise velocity at $x/D = 7$ (far downstream the turbine) exhibits a vertical distribution similar from the one at $x/D = -0.5$ (right upstream the device), whilst TKE contours (Fig. 6.21b)) reveal that the turbine's signature increases the turbulence levels, which are yet relevant even at $x/D = 7$. This is also highlighted in Fig. 6.22 for the values at the centreline of the channel. The velocity further downstream the device seems to get recovered quite well, i.e. U/U_0 at $x/D = 8$ is approximately U_{hub} at $x/D = -0.5$, although the turbulence intensity at $x/D = 8$ increases up to 20% whilst at $x/D = -0.5$ this is 14.5% (I_{hub}). According to the hydrodynamic loading results shown in Section 6.5, the higher level of turbulence intensity at $x/D = 8$, where a secondary turbine would be hypothetically placed, would not decrease its performance although it would cause larger hydrodynamic loading fluctuations, which are suboptimal for standing large fatigue load cycles.

Instantaneous flow field

Fig. 6.23 presents iso-surfaces of pressure fluctuation coloured with mean streamwise velocities and aids to visualise how the large-scale turbulent structures are generated in the depression of the first dune, convected downstream, and interact with the turbine. The oncoming flow separates shortly after the crest of the hill and generates a shear layer which, followed by a Kelvin-Helmholtz mechanism, leads to the formation of elongated vortices denoted as KH. The flow separation in the dune's depression is not uniform along the spanwise direction as the flow is turbulent (Fröhlich et al. [2005]). KH vortices can grow up to the size of the dune's depth and due to the high-velocities above the depression's height are advected downstream. Further downstream Hairpin (HP) vortices are observed which again and whose transversal length is less than half of the domain dimension (Stoesser et al. [2008]). Due to the boundary layer reattachment along the stoss side of the dune, the mentioned large-scale structures move upwards and form vertical rollers (VR) which are observed in Fig. 6.23 approaching the turbine. Finally, due to the action of the secondary currents streamwise-oriented (S) vortices are also developed.

The instantaneous flow field depicted in Fig. 6.24 identifies some of the main turbulent structures generated by the turbine and the second dune, and the interaction of their wakes. The recirculation area enclosed to the rear face of the hub is depicted by the streamwise velocity contours of Fig. 6.24a). Two other low-momentum areas corresponding to the dune recirculation in its geometrical depression are observed as well as the hub's signature wake along the mid-wake extension. It is also appreciated how the high-velocity stream originated between the turbine bottom tip and the dune crest entrains into the low-momentum wakes persisting until $x/D = 2 - 3$.

Top and bottom tip vortices are better identified from the spanwise velocity (v/U_0) contours from Fig. 6.24b). These energetic flow structures are generated from the shear induced by the blades tip, which continuously generate the so-called tip vortices. The blades induce positive v-velocities for $z > z_{hub}$ meanwhile the wake exhibits negative transversal velocity values represented by blue contours in Fig. 6.24b). Similar situation is found for $z < z_{hub}$ although with opposite

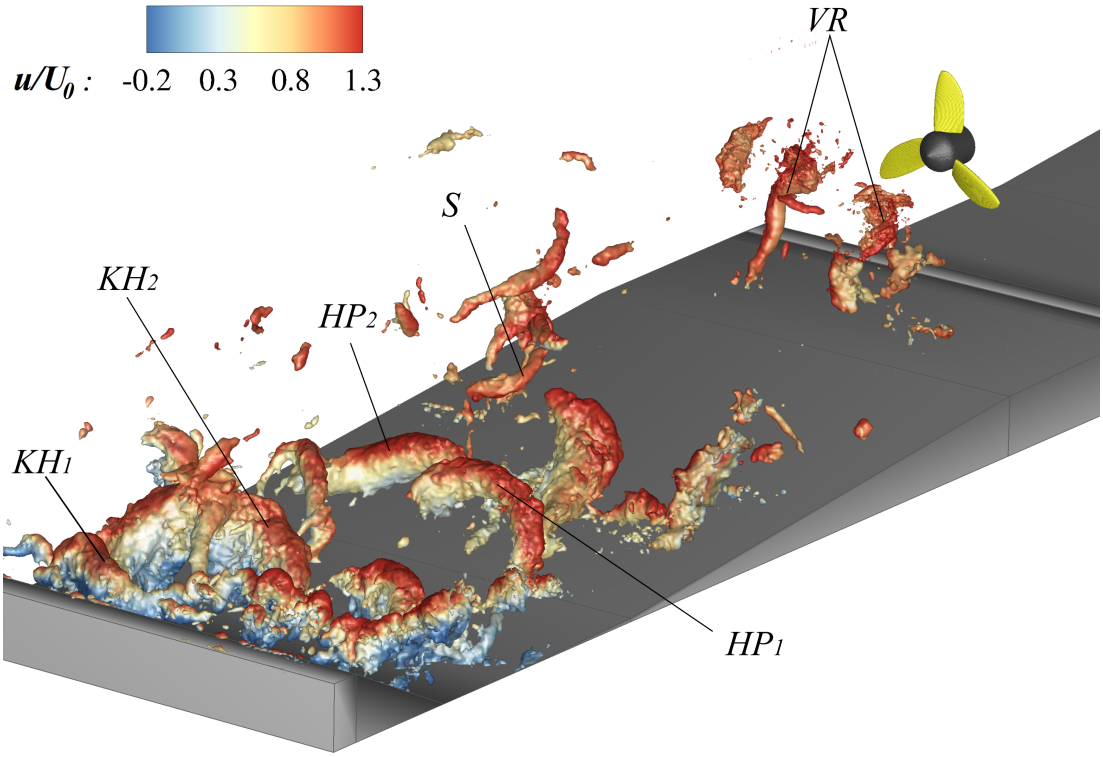

Figure 6.23: Instantaneous flow structures generated in the first dune and which eventually interact with the tidal turbine. Iso-surfaces of pressure fluctuation are coloured with mean streamwise velocity values.

velocity values. Hence, tip and inner vortices are well identified by their opposite rotation to that found on the immediately downstream wake, so they can be depicted in Fig. 6.24b).

The interaction between wakes is not deduced easily from x-velocity contours whilst y-velocities show how the mixing is produced after $x/D = 2$, being more noticeable at $x/D = 3$. The convection of the dune induced turbulent structures towards the low-momentum wake of the turbine is highlighted until $x/D = 5$. This is also reflected in Fig. 6.21b) with TKE profiles evolving from a two-peak profile into a "bell-shape" distribution. The instantaneous TKE contours are plotted in Fig. 6.24c) depicting secondary turbulent structured derived from the wakes interaction. Bottom tip vortices are seen to get diffused quicker in the downstream direction compared to top tip vortices. The latter remains identifi-

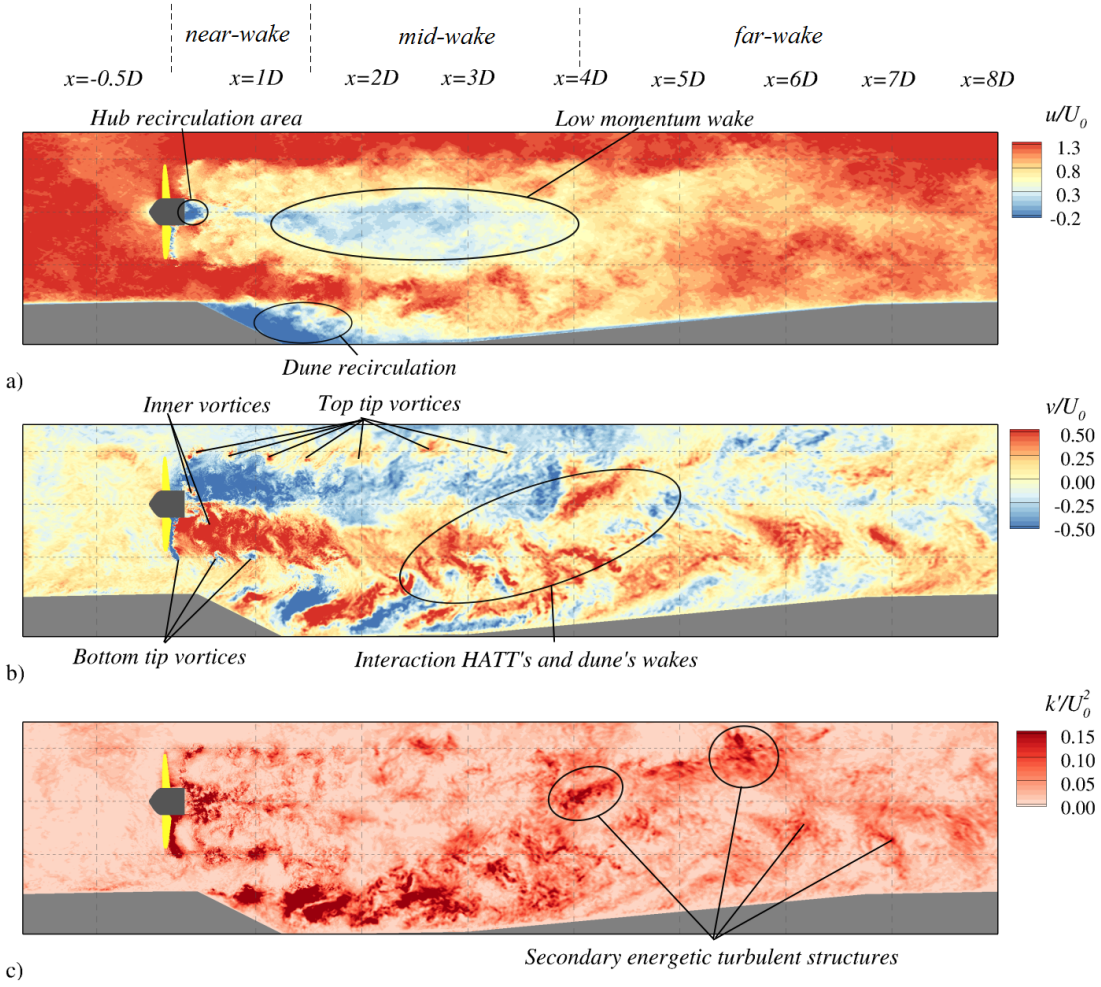

Figure 6.24: Main flow features developed from the fluid-structure interaction of the HATT and the uneven bed shape represented with contours of normalised instantaneous a) streamwise velocities, b) spanwise velocities, and c) turbulent kinetic energy.

able even at $x/D = 3$ whereas the former vortices are just appreciated until one diameter downstream.

The signature of the turbine wake at x-planes located at $x/D = 0.5$, 1.5, 3.5 and 7.5 downstream the device is analysed in Fig. 6.25 using contours of time-averaged streamwise velocity (left column), mean TKE (centre column), and instantaneous TKE (right column). At the closest location to the turbine, the ring-shape wake is depicted from x-velocity contours. Pockets of high TKE

along the swept perimeter due to tip vortices interacting with the ambient flow are appreciated in conjunction with another high TKE region behind the hub due to the enclosed recirculation area. The instantaneous TKE contours depict tip vortices caused by the three blades, the hub's wake, and the presence of turbulence in the oncoming flow.

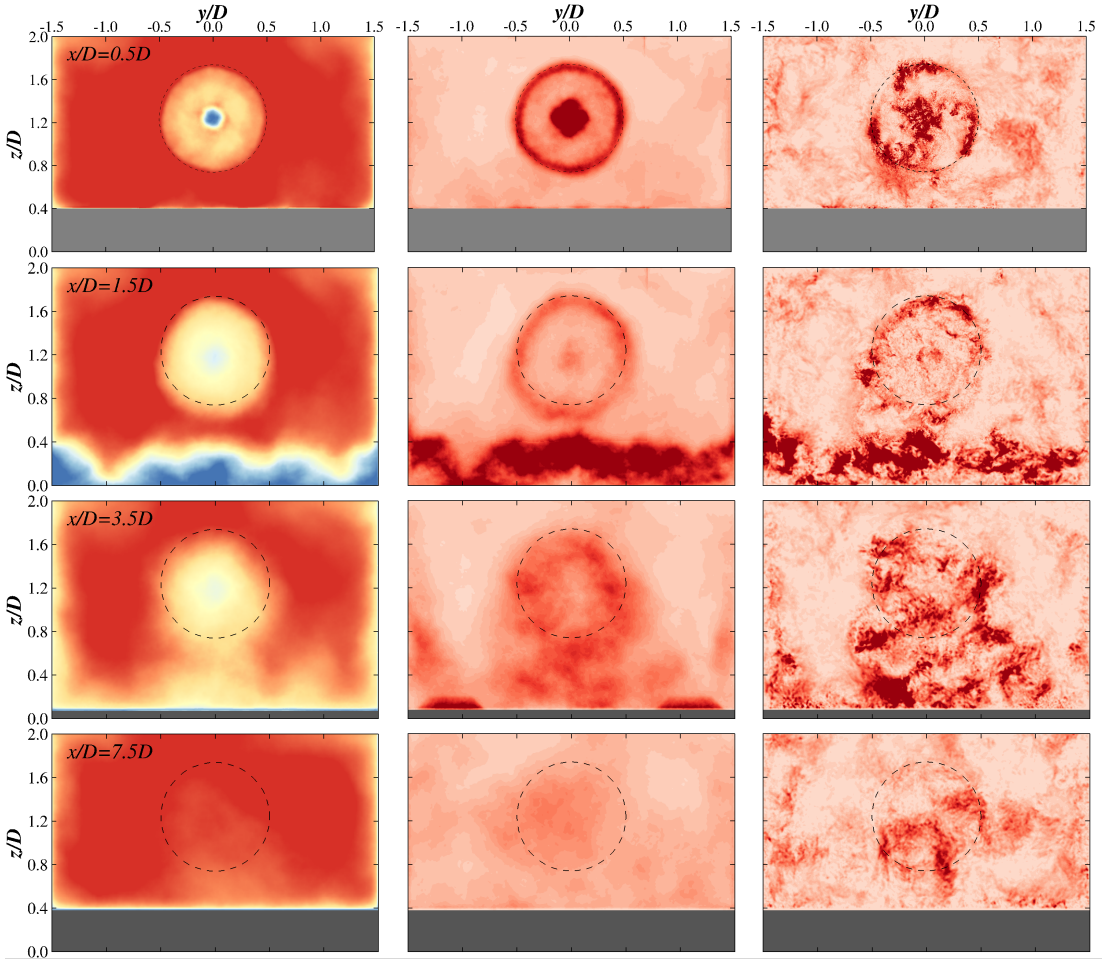

Figure 6.25: X-planes located at x/D=0.5, 1.5, 3.5, and 7.5 downstream the turbine. Left column shows mean streamwise velocities, centre column time-averaged turbulent kinetic energy, and right column instantaneous turbulent kinetic energy. Dashed line depicts the turbine swept perimeter. For legend values the reader is referred to Fig. 6.21.

The plane at $x/D = 1.5$ depicts the instability originated at the dune's depression at $z/D < 0.4$ with high- and low-velocities streaks. The circular shape

of the wake is yet observed in the mean TKE contours although the low-pressure area generated in the dune's depression appears to drag the energetic tip vortices towards the bottom. This interaction is clear in the instantaneous TKE contours where the dune's recirculation area generates large-scale flow structures that are more energetic than the tip vortices, and enhance the mixing between turbine and dune wakes. At $x/D = 3.5$, along the stoss side, the streamwise velocity shows an "inverted-U" distribution shape with the high-momentum areas at the sides and above the turbine's wake. Noteworthy is the plume-shape of the mean TKE contours on the contrary to the previous ring-shape distribution, as tip vortices lost their coherence by mixing with the ambient flow. Finally, further downstream the turbine at $x/D = 7.5$ the large velocity fluctuation areas are due to wake meandering, similarly to Fig. 6.13 from the flat channel bed simulations.

Three-dimensional turbulent structures

A closer view to the generated turbulent structures is presented in Fig. 6.26 using contours of relative pressure ($p - p_0$, where p_0 is the pressure at the inlet) along a XZ-plane at the channel centre, and iso-surfaces of λ_2-criterion. The signature of tip vortices is depicted from low-pressure areas as well as the hub's wake, which meanders further downstream the turbine. Tip vortices are denoted as "1a" corresponding to the latest vortex generated by blade 1, in a similar fashion to Fig. 6.5. Top tip vortices exhibit an irregular spacing, e.g. separation between vortices 2b-3b is larger than that of 3b-1c, on the contrary to Fig. 6.5 where this spacing is fairly uniform. Regarding the bottom tip vortices only 3 of them are well defined in the pressure contours, i.e. 1a, 2a and 3a. Vortex 1b is also appreciated but is segregated into 2 cores. The interaction of vortex 2a with oncoming turbulent structures travelling close to the bottom bed (e.g. a horseshoe vortex highlighted by Grigoriadis et al. [2009]) eases its breakdown into two distinct cores despite it being close to the turbine rotor, and hence not much energy dissipation at this stage is expected.

The turbulent ambient flow accelerates the diffusion of the tip vortices. This becomes more important as soon as the vortex travels downstream and starts losing its coherence and energy, as depicted in Fig. 6.26 comparing the iso-surfaces

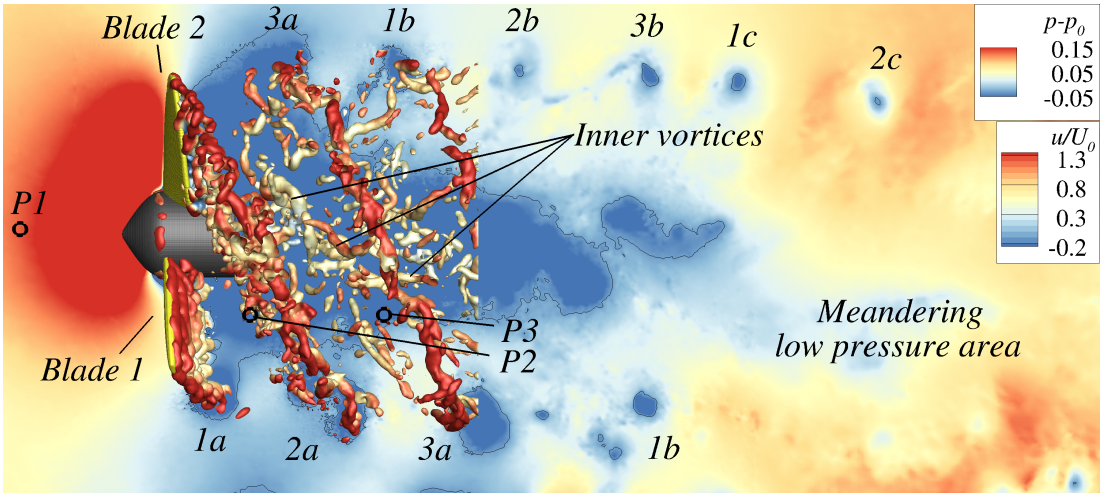

Figure 6.26: Relative pressure contours at $y/D = 0$ with $\lambda_2 D/U_0 = -200$ iso-surfaces coloured with streamwise velocity values. Points P1, P2 and P3 are used to collect velocity signals.

of vortices 2a, 3a, and 1b. The characteristic roller shape representing vortex 1b losses its continuity whilst 3a (which is closer to the rotor) is smoother and compact. This loss of coherence is due to the interference with the turbulent external flow. In the current case, this associated energy decay of tip vortices becomes more appreciable compared to the iso-surfaces shown in Fig. 6.5 for the laminar inflow case.

Chamorro et al. [2013b] visualised experimentally the wake of a HATT using PIV records and also observed tip vortices featuring irregularly spaced patterns. Similar outcomes were found by Yang et al. [2016] with uneven tip vortices distribution in the wake of a full-scale HAWT. Felli et al. [2011] found in the wake generated downstream by a propeller a clear distinction of tip vortices and hub's inner wake.

6.6.3 Impact of bed-induced turbulence on hydrodynamic loadings

Survivability of tidal turbines is directly linked to their ability to support large loading fluctuations due to sudden velocity variations. This Section analyses the

effect of the instantaneous free-stream velocity fluctuations onto the turbine rotor forces. Fig. 6.27 shows the streamwise velocities upstream the turbine obtained at P1 (located at $x_{hub}-0.5D$, y_{hub}, z_{hub}, i.e. half diameter upstream and centred with the hub's centre, see Fig. 6.26) normalised by its mean value U_{hub}, normalised power coefficient C_P, and coefficients of flap-wise ($C^T_{M_\theta}$) and edge-wise ($C^Q_{M_\theta}$) bending moments.

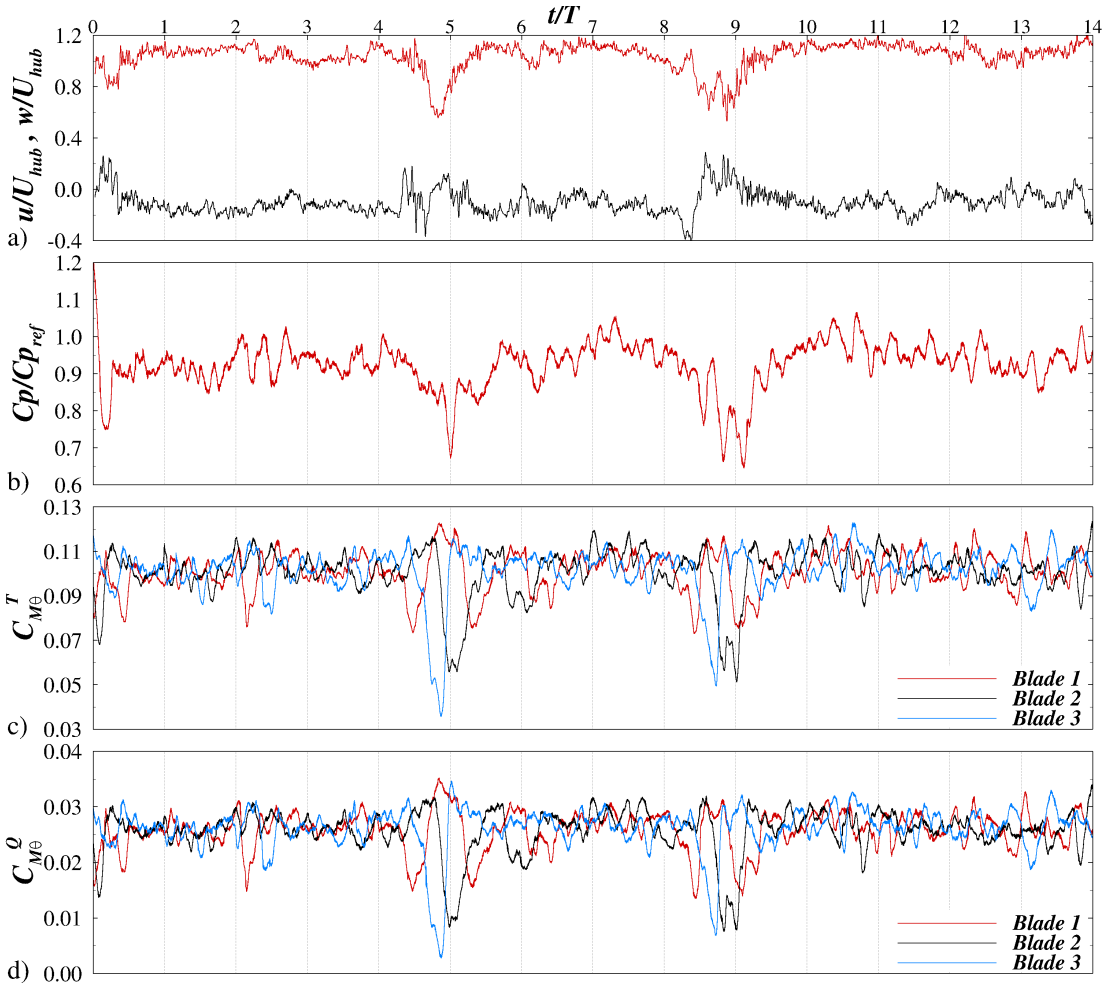

Figure 6.27: Time series of a) streamwise (red line) and vertical (black line) velocities upstream the turbine obtained at P1, b) normalised power coefficient, and c) flap-wise and d) edge-wise bending moments.

The flow over two-dimensional dunes is characterised by recurrent generation of large-scale structures at the dune's depression, and their advection down-

stream. Same phenomena occur in the present simulations as both u- and w-velocity signals at P1 experience periodic and noticeable changes, e.g. at $t/T \approx$0.2, 4.8, and 8.8 where $T = 2\pi/\Omega$ stands as the time the turbine takes to perform a full revolution. In the current simulation, the anisotropic ratio $\sqrt{\overline{u'^2}} : \sqrt{\overline{v'^2}} : \sqrt{\overline{w'^2}}$ is 1:0.64:0.88. These are acceptable values considering the large influence of the dune induced turbulence making vertical velocities predominant over spanwise velocities. According to Mycek et al. [2014b], ratios of mean turbulence intensities are site-depending and vary according to the dominating flow phenomena at the marine site, e.g. large obstacles in the bathymetry as Horse Rock in Ramsey Sound, Evans et al. [2015].

Instantaneous variation of power coefficient due to variable oncoming velocity is depicted in Fig. 6.27b). The turbulent events at $t/T = 4.8$ and 8.8, hereinafter referenced as turbulent events 1 and 2, feature a considerable drop of u-velocities, which causes a sudden reduction of power generation. Nonetheless, the latter recovers quickly as velocity increases further until the onset of the second turbulent event, during which the performance drops again. Fig. 6.27c) and d) present the bending moment coefficients for each of the blades comprising the rotor. Noteworthy is that each blade behaves differently during the referenced turbulent events 1 and 2 as their position is constantly changing. At $t/T \approx 4.8$, the blade 1 tip is at the highest z-position (i.e. closest to the water surface), whereas blades 2 and 3 are closer to the channel bottom where the energetic turbulent structure travels through, and thus inducing on them a larger interference than on blade 1. Table 6.4 presents the main values of the bending moments for the three blades. Noteworthy is that averaged and maximum values are equal for the three blades whereas their difference between the maxima and minima values is notably different, e.g. $C^T_{M_\theta}$=0.0914 for blade 3 against 0.0537 obtained by blades 1. The latter fact is important for future calculations of equivalent fatigue loads for which the maximum loading amplitude is considered, Harper and Hallett [2015].

Despite the time-dependent structural response, time-averaged values are close to those found for the simulations of the turbine over a flat-bed, shown in Table 6.3. The actual time-averaged value of $C^T_{M_\theta}$ is approx. 0.1010 which is similar to the 0.0964 value obtained for the $I = 10\%$ case. Such small differences under different turbulence conditions follow Blackmore et al. [2016]'s findings.

Structural moment	Value	Blade 1	Blade 2	Blade 3
$C^T_{M_\theta}$	Max	0.1267	0.1290	0.1271
	Average	0.1012	0.1009	0.1013
	Max-min	0.0537	0.0777	0.0914
$C^Q_{M_\theta}$	Max	0.0379	0.0380	0.0367
	Average	0.0259	0.0258	0.0261
	Max-min	0.0263	0.0342	0.0343

Table 6.4: Average, maxima, and amplitude of the bending moments for the three blades in the simulation of a HATT over a bed of dunes.

They stated that even though the turbulence intensity value in the flow varies considerably, mean bending moments values lay somehow within certain bounds, i.e. no great differences are expected irrespective of the flow turbulence. Analogous trend is found for $C^Q_{M_\theta}$ with value of 0.0259 for the present case whereas this is 0.0230 for the artificial turbulent inflow case.

These results outline obvious influence of bed-induced turbulent events on the HATT's instantaneous performance and hydrodynamic loadings, which compromise the survivability of the turbine regarding fatigue loadings. The reiterative impact of energetic flow structures onto the turbine can be estimated depending on the periodicity of highly turbulent events. For the dune-bed flow case, these occur with a period of 4.2-4.8s. Hence, considering 20 years life expectancy, a tidal stream turbine is expected to stand approx. 1.30 to $1.50{\cdot}10^8$ fatigue load cycles. This estimated value is in line to that considered by Nicholls-Lee et al. [2013] of 10^8 expected fatigue cycles. Nonetheless, this number of fatigue cycles is both site-depending and variable with the flow conditions, e.g. velocities.

Power spectral density

Velocity signals are collected at three points, namely P1-P3, depicted in Fig. 6.26. P2 and P3 are located $x_{hub} + 0.3D$ and $x_{hub} + 0.6D$, respectively, at a radial distance of $D/2$ from the hub's centre, i.e. at the projected turbine swept perimeter where tip vortices are meant to travel through. PSDs of u- and w-velocities signals obtained at these points are plotted in Fig. 6.28.

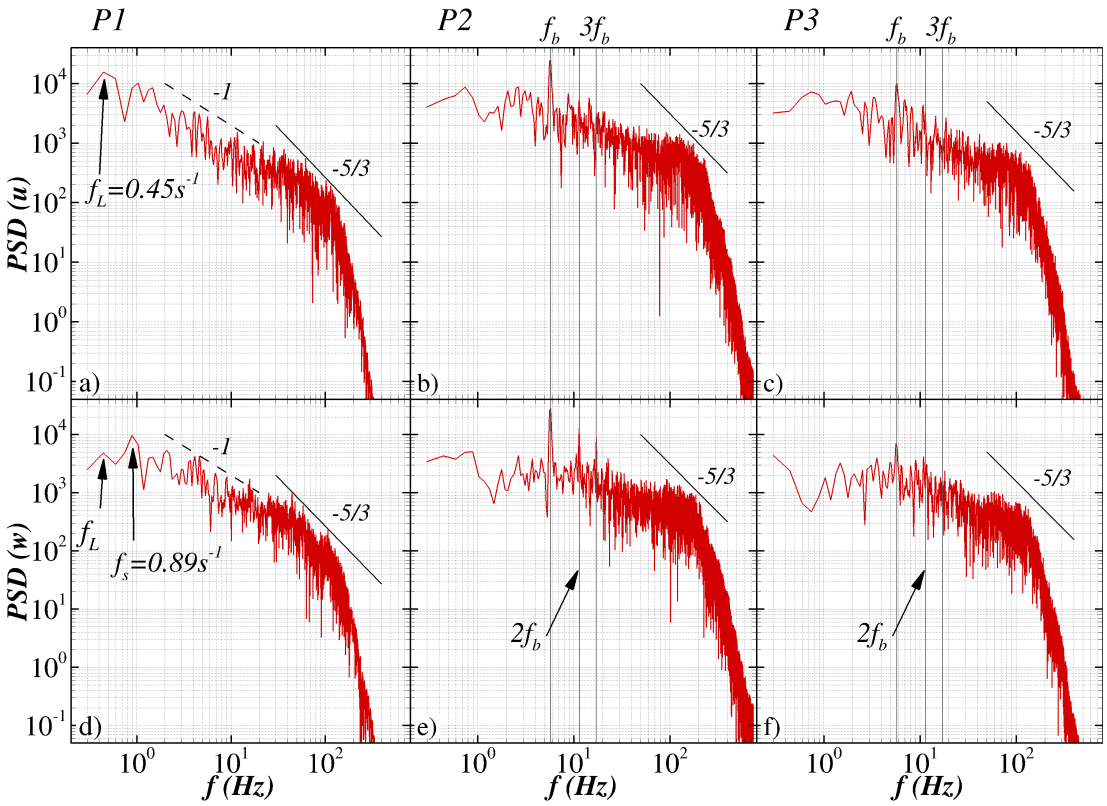

Figure 6.28: Power spectral density of u- and w-velocity signals collected at P1, P2 and P3 for the HATT rotating over a bed of dunes.

At P1 a low-frequency peak is appreciated in the u-velocity spectrum, labelled as $f_L = 0.45s^{-1}$, as a result of the periodic turbulent events 1 and 2 previously observed in Fig. 6.27a). The w-velocity spectrum also depicts this peak although there is one more energetic found at a frequency of $f_s = 0.89Hz$. This is associated to bed-induced turbulent events occurring at higher frequency in time than those contributing for f_L. Spectra of u- and w-velocities feature a decay slope of -1 in the production range prior to the inertial sub-range that follows the -5/3 slope expected from Kolmogorov decay law, and which agrees well with experimental findings from Chamorro and Porté-Agel [2009].

The signature of tip speed vortices at P2 and P3 is reflected in their velocity spectra with energy peaks at f_b, $2f_b$, and $3f_b$, where f_b is the frequency of tip vortices passing by and calculated according to Eq. 5.2. The spectrum of streamwise velocity at P2 features the peak at f_b, although no indication of $2f_b$

or $3f_b$ is appreciated. Further downstream at P3, the spectral energy associated to f_b diminishes due to the loss of coherence and energy decay of tip vortices, as seen in Fig. 6.26. Vertical velocity spectra depict better the presence of these energetic turbulent structures compared to streamwise velocities. Spectrum of w-velocities at P2 do capture the energy peaks at frequency values of f_b, $2f_b$, and $3f_b$, whilst at P3 their associated energy is again diminished even though the peaks are yet well appreciated. These patterns of spectral energy peaks and decay with the increase in distance to the turbine rotor was also found experimentally by Chamorro et al. [2013a], and numerically by Kang et al. [2014] who performed the LES of the tidal turbine based on Chamorro et al. [2013a]'s experiments.

6.7 Summary

The LES-IB approach has been employed to study the hydrodynamics and resulting loads of a horizontal axis tidal turbine prototype. The numerical method has been firstly validated by comparing experimentally obtained with simulated torque values. A spatial and temporal resolution sensitivity analysis has been performed to assess the optimum numerical setup. It has been shown that the simulation in terms of the resulting torque is less sensitive to the time step than the mesh size. Numerically predicted power coefficients at various tip speed ratios agreed well with experimental data provided an adequately fine numerical mesh is employed. After successful validation of the method, further simulations were run with the goal to investigate the turbine's hydrodynamics and the resulting loadings on its blades.

The analysis of the simulation data in terms of hydrodynamics revealed the typical flow structures, including tip and inner vortices, which were visualised using common turbulent structure eduction methods. In terms of hydrodynamic loads, bending and torsional moment coefficients at the blade-hub junction were computed for different tip speed ratios. The results show that there is a considerable fluctuation of the structural moments over one revolution, mainly due to the turbine's operation in a boundary layer flow. It has also been demonstrated that the tip speed ratio at which the turbine operates has an effect on the magni-

tude of the coefficients, most noteworthy that the largest bending moments occur when the turbine operates at the peak of the power curve.

With the goal of reproducing the experimental flow conditions, the turbine rotor was subjected to the same flow conditions plus an artificial free-stream turbulence with a turbulence intensity value of 10%, which was prescribed at the inlet using the Synthetic Eddy Method. The results exhibited a notable change in the hydrodynamics of the turbine's wake. Under free-stream turbulent conditions, the velocity deficit is recovered quicker than under uniform inflow conditions. It was shown that an increase in ambient turbulence reduces the longevity of the tip speed vortices but also that the onset of inner vortex meandering starts closer to the rotor. From contours of the time-averaged and instantaneous turbulent kinetic energy distribution three wake regions were distinguished: a near-field wake with distinct signatures of the tip vortices and the recirculation zone behind the hub, a mid-wake with fairly low turbulence, and a far-field wake an area of high TKE as a result of the meandering of the wake. Ambient turbulence affects the TKE levels and the extent of the three regions: at high levels of ambient turbulence significantly elevated turbulence in the far-field wake and earlier onset of wake meandering were found.

Analysis of the effects of ambient turbulence on hydrodynamic loadings has revealed that the mean structural coefficients are fairly similar irrespective of the level of ambient turbulence. However, the peak values and the difference between maximum and minimum value of the structural coefficients are increased due to turbulence. It has been shown that in the presence of turbulent flow structures can lead to sudden changes in the hydrodynamic loadings, and in particular for high ambient turbulence, minima are followed directly by maxima of the moment coefficients. High levels of ambient turbulence can result in a 20-30% increase of instantaneous bending and pitching moments. The pitching moments have been found to be one to two orders of magnitude lower than the bending moments.

The HATT has been placed over a bed of dune in order to simulate real environmental turbulent conditions. Bed induced turbulence affected the turbine's performance and loadings as large-scale energetic structures impact the turbine's rotor. It has been shown that the response of each blade to these turbulent events was not uniform featuring large differences on the loading amplitude. This is re-

markable when calculating the equivalent fatigue loads the turbine has to support throughout its lifespan. The energetic flow structures generated at the dunes' depression changed the wake pattern to that found for flat-bed channel simulations. Despite the near-wake was fairly equal between cases, large differences were found for the mid-wake where the low-momentum wake was dragged by the low-pressure area generated at the dune's depression, which caused the loss of vertical symmetry of the wake. Two high TKE areas were found, one is distributed above the low-velocity wake while another is near the bottom where the turbine and dune wakes merged triggering velocity fluctuations. This interaction of wakes was recovered sooner than in the flat bed simulations as the turbulence intensities were larger. For this latter case, a quick wake recovery was observed at the end of the second dune. This scenario is favourable for the design of future turbine arrays. The presented high-fidelity simulations also shown that a hypothetical second turbine deployed downstream would generate a similar amount of power compared to the simulated one, whilst it would experience larger loading fluctuations challenging its long-term resilience.

Chapter 7

Conclusions and outlook

Conclusions

A computational approach based on Large-Eddy Simulation (LES) that resolves the flow field and the immersed boundary method to represent the solid bodies has been presented. In this scheme the fluid and solid meshes are decoupled and the simulation of moving boundaries can be performed with more flexibility than if classical body-fitted models were considered. The main advantage of the IB method relies on its good compromise between accuracy and computational cost compared to body-fitted methods as no re-allocation of variables is required. Additionally and despite it could have not been tested, the LES-IB scheme is expected to offer an improved computational speedup than other solvers based on body-fitted models due to the use of a multigrid solver and easy-to-compute numerical schemes, e.g. central differences. The IB method provides similar accuracy than body-fitted models and becomes a promising and powerful approach to be used in conjunction with LES which overcomes the predictions of RANS-based models in every of the cases presented due to its ability to resolve the energetic flow structures.

The calculation in the immersed boundary method was improved with the development of a novel hybrid MPI/OpenMP parallelisation scheme that combines a "master-gathering-scattering" strategy. This scheme was developed with the need for enhancing the computations of the IB method as in cases when the number of solid markers is very large they can led to a computational overhead larger

that of the Poisson pressure solver, which is usually the most time-consuming part in a CFD solver. The mixed approach improved the code performance in all the tested cases and the weak scalability of the scheme was also successfully verified. It was proven that dynamic schedule directives enhance OpenMP's speedup without additional hardware resources , and which is especially interesting when hyper-threading is available. Such hybrid scheme can be easily implemented in any IB method code improving its overall speedup even without adding more HPC resources.

The capability of the LES-IB method to deal with complex flow phenomena, such as dynamic stall or laminar-to-turbulent boundary layer transition in air/hydrofoils, was approached with the simulation of a pitching airfoil. Results verified that the IB method deals well with boundary layer flows whenever appropriately fine mesh resolutions and small time steps are adopted as accurate predictions of the aerodynamic coefficients were obtained. The beneficial effect of blade cambering evidenced with larger lift generation capabilities of the airfoil due to the delay of the shedding of the leading edge vortex which dominates the pre-deep stall conditions. This consequently led to an improved lift-to-drag ratio, that is deemed optimal in consideration to tidal stream turbines.

The application of the LES-IB method to vertical axis tidal turbines obtained an excellent agreement for power coefficient prediction compared with experimental results. The presented LES results outperformed the coefficient of power predicted by RANS-based models, which tend to underestimate the lift generation of the blades. An excellent agreement was found for the wake developed downstream at optimal performance conditions, and the nature of LES to accurately resolve the energetic large-scale flow structures was highlighted in the predictions of turbulence kinetic energy achieving a great match with the experiments. The fluid-structure interaction characteristics happening in the rotor-swept perimeter was visualised in order to envisage the driving physics of these turbines. This analysis showed how the blade-vortex interaction pattern is at different rotational speeds with an accentuated deep dynamic stall happening at low rotation speeds whilst at higher velocities only light dynamic stall (not full flow separation along the blades) is developed. The novelty of this analysis indicates a future research line that will help to optimise the design of vertical axis turbines in terms of their

performance.

Finally, a Horizontal Axis Tidal Turbine (HATT) is simulated and compared with experimental results. The computational approach obtained a great prediction of the generated power coefficient and the main coherent flow structures generated in the wake of a HATT were educed, such as tip and inner vortices. The structural response of bending moments showed that at maximum efficiency conditions, the device undergoes maxima stress values, whilst when the device over-spins the loads fluctuations are triggered.

Influence of turbulence in the flow approaching the turbine was analysed using artificial turbulence and it was observed that large turbulent flow conditions enhances the mixing of the turbine wake with the outskirts flow and accelerates velocity deficit recovery. The fluctuations on the structural bending moments increased when the oncoming turbulent intensity was higher, whereas the mean performance value remained unaffected by the turbulent inflow conditions. Results indicated that maximum load values and fatigue load cycles are enlarged when the incident flow is more turbulent.

The seabed over which HATTs are deployed in reality often features an irregular shape which can be a source of additional turbulence in the already harsh conditions they operate in. With the simulation of the HATT placed over a bed of dunes it was evidenced how the instantaneous power generation and structural moments are affected by the turbulence in the approaching flow. It was highlighted how these energetic flow structures impact differently each of the rotor blades as their spatial length scale value of 75% the radius showed. Recurrent generation of large-scale turbulent structures from the dune's depression have notably modified the wake behind the turbine which under this conditions featured a notable asymmetry on the contrary to flat-bed channel simulations.

Outlook

The present results have demonstrated the accuracy of the high-fidelity near-field computational model for tidal stream turbines simulations. In the author's view, there are many promising research lines that can continue the investigation accomplished in this thesis. Some of these are briefly described. First, develop-

ment of a coupled computational fluid dynamics-finite element analysis model, where the stresses in the turbine blades are calculated. This CFD-FEM approach would allow to perform a complete structural analysis of these devices under turbulent flow conditions. In this publication the blade root moments are analysed but the blades can also fail due to large stress values or buckling of internal elements. These could be accounted using shell-elements into a finite element analysis framework.

Secondly, the real bathymetry where the turbine is going to be placed can be included in the model following a similar fashion to the case of the HATT over the bed of dunes. This would ease the characterisation of the bed induced turbulence on the turbine loadings as well as the frequency associated to the main turbulent events at the real deployment site. The latter can give a great estimation of the fatigue loads to be supported by the structure so as to prevent an possible structural collapse.

Thirdly, the large amount of computational resources demanded to run large-eddy simulations can be tackled by exploring hybrid turbulence approaches such as Partially Averaged Navier-Stokes (PANS), which is an adjustable balanced hybrid model between RANS and LES. This scheme would allow to perform highly resolved LES near the blade while hybrid RANS-LES away from it. Merging PANS and local mesh refinement would provide a numerical scheme that resolves partially the velocity field in large domains, whereas if RANS is used the turbulence in the flow would be modelled and it would require the generation of artificial turbulence at the transition to LES, for instance using the synthetic eddy method.

Last but not least, developing the coupling of near-field and far-field models would provide an enormous range of applications that are not possible to be approached with the current computational approaches. For instance, the effects of turbine wakes in long distances is yet unknown as the current models performing these simulations are based in RANS and thus underestimate the induced turbulent kinetic energy and predict a quicker recovery of the velocity deficit. Additionally, it would allow to investigate how an array of turbines affect the sediment transport (e.g. erosion/sedimentation), water quality (e.g. bacteria), or even fish mortality using a Lagrangian particle approach. It should be remarked

that this model typology is starting to be used in wind energy industry to optimise the location of the wind turbines, and in atmospheric predictions where meso-scale models are used for inflow conditions to near-field models which use LES.

Appendices

A Synthetic Eddy Method

The consideration of free-stream turbulence is an essential step in order to represent natural environmental flow conditions. Therefore, to accomplish realistic inflow conditions in LES, precursor simulations are often run before the main simulation and then inlet planes fed into the latter (Rodi et al. [2013]). However, this precursor simulations can demand a considerable amount of computational resources as LES require small time steps and fine grid resolutions. To avoid such additional overload, the generation of an artificial turbulent field is done using the Synthetic Eddy Method (SEM). This method was developed by Jarrin et al. [2006] has been widely applied specially for LES and in transition regions between RANS and LES. The SEM is based on the generation of a finite number of eddies, N_{ed}, that are the source of velocity fluctuations on the generated inlet. The number of eddies is calculated based on the length-scale, l_e, and inlet plane dimensions. The resulting instantaneous velocity at the inlet results from the addition of the prescribed mean inlet velocity U_0, and the artificial velocity fluctuation $u_i'(\mathbf{x})$, calculated as a function of the previously described parameters as follows,

$$u_i'(\mathbf{x}) = \frac{1}{\sqrt{N_{ed}}} \sum_{k=1}^{N_{ed}} a_{ij} \varepsilon_j^k f_{\sigma_e}^k \left(\frac{\mathbf{x} - \mathbf{x}^k}{l_e^k} \right) \tag{1}$$

where a_{ij} is a tensor of the Lund coefficients presented in Eq. 2 (Lund et al. [1998]) related to the prescribed Reynolds stresses ($R_{ij} = u_i' u_j'$) from Eq. 2, ε_j^k is a random number between [-1,1] with zero average, $f_{\sigma_e}^k$ corresponds to a Gaussian shape function given to the vortex representation (Jarrin et al. [2006]), and $\mathbf{x}^k$

indicates the centre of coordinated of the k^{th}-eddy.

$$a_{ij} = \begin{pmatrix} \sqrt{R_{11}} & 0 & 0 \\ R_{21}/a_{11} & \sqrt{R_{22} - a_{21}^2} & 0 \\ R_{31}/a_{11} & (R_{32} - a_{21}a_{31})/a_{22} & \sqrt{R_{33} - a_{31}^2 - a_{32}^2} \end{pmatrix} \tag{2}$$

In order to avoid any additional complexity to the generation of the artificial turbulent inflow in the current publication, the turbulence at the inlet is considered isotropic, i.e. $u_i'u_j' = 0$, and homogeneous, i.e. $u_i'u_i' = u_j'u_j' = 2/3k$, Otero [2009]. This yields to a Reynolds stresses tensor presented in Eq. 3. Thus, this method allows to input the same turbulence intensity level measured during the experiments into the numerical simulations.

$$R_{HIT} = \begin{pmatrix} 2/3k & 0 & 0 \\ 0 & 2/3k & 0 \\ 0 & 0 & 2/3k \end{pmatrix} = \begin{pmatrix} (I \cdot U_0)^2 & 0 & 0 \\ 0 & (I \cdot U_0)^2 & 0 \\ 0 & 0 & (I \cdot U_0)^2 \end{pmatrix} \tag{3}$$

During the calculation of the inlet planes at each time step n, the eddies are convected based on the free-stream velocity as,

$$\mathbf{x}^n(t + \Delta t) = \mathbf{x}^n(t) + U_0 \cdot \Delta t \tag{4}$$

where Δt is the time step, which usually is assumed constant as required to obtain smooth forces outputs from the IB method. In LES, the time steps are very small so the relevant temporal scales of the flow can be solved, as seen in the values used in Section 5 and 6. Hence, the number of inlet planes that contain the artificial turbulent velocity fluctuations is quite large so as to achieve a proper continuous inflow condition in the simulation domain. Nevertheless, this methodology remains as a computationally faster and cheaper alternative than running precursor simulations. It also permits to prescribe a determined level of turbulence intensity at the inlet. Fig. 1 shows an example of the inlet velocity distribution using SEM.

As a final consideration, it should be remarked that the artificial turbulent velocity inlet generated with SEM does not fulfil the divergence-free condition

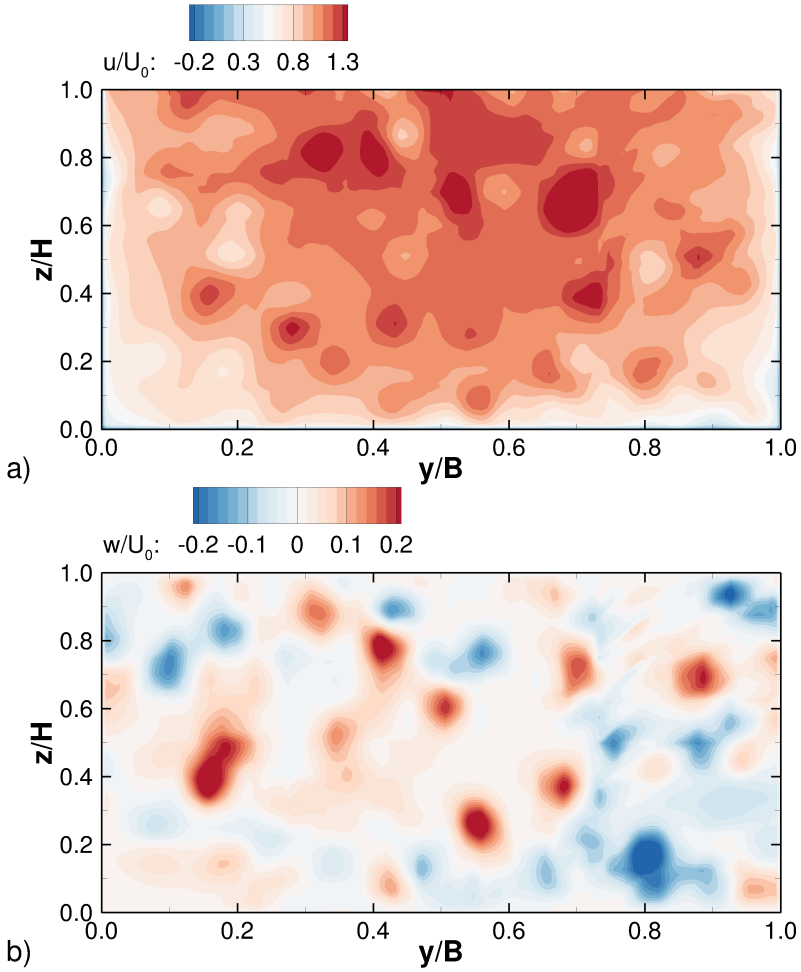

Figure 1: Artificial turbulent velocity field using SEM. Contours of normalised a) streamwise and b) vertical velocities.

and can trigger pressure fluctuations at the inlet. Focused on this issue, Poletto et al. [2013] developed the Divergence-Free SEM (DF-SEM) that addresses these SEM problematic. The upgrade of SEM to DF-SEM in Hydro3D is one of the tasks to be considered in future research.

References

I. Afgan, J. McNaughton, S. Rolfo, D. D. Apsley, T. Stallard, and P. Stansby. Turbulent flow and loading on a tidal stream turbine by LES and RANS. *Int. J. Heat Fluid Flow*, 43:96–108, 2013. ISSN 0142727X. doi: 10.1016/j.ijheatfluidflow.2013.03.010.

A. Afzal, Z. Ansari, A. R. Faizabadi, and M. K. Ramis. Parallelization Strategies for Computational Fluid Dynamics Software: State of the Art Review. *Arch. Comput. Methods Eng.*, pages 1–27, 2016. ISSN 18861784. doi: 10.1007/s11831-016-9165-4.

R. Ahmadian and R. Falconer. Assessment of array shape of tidal stream turbines on hydro-environmental impacts and power output. *Renew. Energy*, 44:318–327, 2012. ISSN 09601481. doi: 10.1016/j.renene.2012.01.106.

M. H. Akbari and S. J. Price. Simulation of dynamic stall for a NACA 0012 airfoil using a vortex method. *J. Fluids Struct.*, 17(6):855–874, 2003. ISSN 08899746. doi: 10.1016/S0889-9746(03)00018-5.

E. Amet, T. Matre, C. Pellone, and J. Achard. 2D Numerical Simulations of Blade-Vortex Interaction in a Darrieus Turbine. *J. Fluids Eng.*, 131(11):111103, 2009. ISSN 00982202. doi: 10.1115/1.4000258.

A. Angeloudis, R. Falconer, S. Bray, and R. Ahmadian. Representation and operation of tidal energy impoundments in a coastal hydrodynamic model. *Renew. Energy*, 99:1103–1115, 2016. ISSN 18790682. doi: 10.1016/j.renene.2016.08.004.

R. Aversa, B. Di Martino, M. Rak, S. Venticinque, and U. Villano. Performance prediction through simulation of a hybrid MPI/OpenMP application. *Parallel Comput.*, 31:1013–1033, 2005. ISSN 01678191. doi: 10.1016/j.parco.2005.03.009.

P. Bachant and M. Wosnik. Performance measurements of cylindrical- and spherical-helical cross-flow marine hydrokinetic turbines, with estimates of exergy efficiency. *Renew. Energy*, 74:318–325, feb 2015. ISSN 09601481. doi: 10.1016/j.renene.2014.07.049.

A. S. Bahaj, A. F. Molland, J. R. Chaplin, and W. M. J. Batten. Power and thrust measurements of marine current turbines under various hydrodynamic flow conditions in a cavitation tunnel and a towing tank. *Renew. Energy*, 32 (3):407–426, 2007. ISSN 09601481. doi: 10.1016/j.renene.2006.01.012.

X. Bai, E. Avital, A. Munjiza, and J. Williams. Numerical simulation of a marine current turbine in free surface flow. *Renew. Energy*, 63:715–723, 2014. ISSN 09601481. doi: 10.1016/j.renene.2013.09.042.

T. Blackmore, W. M. J. Batten, and A. S. Bahaj. Influence of turbulence on the wake of a marine current turbine simulator. *Proc. R. Soc. A*, 470:20140331, 2014. ISSN 1364-5021. doi: 10.1098/rspa.2014.0331.

T. Blackmore, L. E. Myers, and A. S. Bahaj. Effects of turbulence on tidal turbines: Implications to performance, blade loads, and condition monitoring. *Int. J. Mar. Energy*, 14:1–26, 2016. ISSN 22141669. doi: 10.1016/j.ijome.2016.04.017.

G. Brochier, P. Fraunie, C. Beguier, and I. Paraschivoiu. Water channel experiments of dynamic stall on Darrieus wind turbine blades. *J. Propuls. Power*, 2 (5):445–449, 1986. ISSN 0748-4658. doi: 10.2514/3.22927.

I. Buck, T. Foley, D. Horn, J. Sugerman, K. Fatahalian, M. Houston, and P. Hanrahan. Brook for GPUs. *ACM Trans. Graph.*, 23(3):777, 2004. ISSN 07300301. doi: 10.1145/1015706.1015800.

L. W. Carr, K. W. McAlister, and W. J. McCroskey. Analysis of the development of dynamic stall based on oscillating airfoil experiments, NASA TN D-8382. Technical report, TN D-8382, NASA, 1977.

G. Castiglioni, J. A. Domaradzki, V. Pasquariello, S. Hickel, and M. Grilli. Numerical simulations of separated flows at moderate Reynolds numbers appropriate for turbine blades and unmanned aero vehicles. *Int. J. Heat Fluid Flow*, 49:91–99, 2014. ISSN 0142727X. doi: 10.1016/j.ijheatfluidflow.2014.02.003.

M. Cevheri, R. McSherry, and T. Stoesser. A local mesh refinement approach for large-eddy simulations of turbulent flows. *Int. J. Numer. Methods Fluids*, 82: 261–285, 2016. ISSN 02712091. doi: 10.1002/fld.421.

L. P. Chamorro and F. Porté-Agel. A wind-tunnel investigation of wind-turbine wakes: Boundary-Layer turbulence effects. *Boundary-Layer Meteorol.*, 132: 129–149, 2009. ISSN 00068314. doi: 10.1007/s10546-009-9380-8.

L. P. Chamorro, C. Hill, S. Morton, C. Ellis, R. E. A. Arndt, and F. Sotiropoulos. On the interaction between a turbulent open channel flow and an axial-flow turbine. *J. Fluid Mech.*, 716:658–670, 2013a. ISSN 0022-1120. doi: 10.1017/jfm.2012.571.

L. P. Chamorro, D. R. Troolin, S. J. Lee, R. E. A. Arndt, and F. Sotiropoulos. Three-dimensional flow visualization in the wake of a miniature axial-flow hydrokinetic turbine. *Exp. Fluids*, 54(2), 2013b. ISSN 07234864. doi: 10.1007/s00348-013-1459-9.

L. Chen and W. H. Lam. A review of survivability and remedial actions of tidal current turbines. *Renew. Sustain. Energy Rev.*, 43:891–900, 2015. ISSN 13640321. doi: 10.1016/j.rser.2014.11.071.

A. J. Chorin. Numerical solution of the Navier-Stokes equations. *Math. Comput.*, 22(104):745–762, 1968. ISSN 0025-5718. doi: 10.1090/S0025-5718-1968-0242392-2.

M. J. Chorley and D. W. Walker. Performance analysis of a hybrid MPI/OpenMP application on multi-core clusters. *J. Comput. Sci.*, 1(3):168–174, 2010. ISSN 18777503. doi: 10.1016/j.jocs.2010.05.001.

A. Choudhry, R. Leknys, M. Arjomandi, and R. Kelso. An insight into the dynamic stall lift characteristics. *Exp. Therm. Fluid Sci.*, 58:188–208, 2014. ISSN 08941777. doi: 10.1016/j.expthermflusci.2014.07.006.

M. J. Churchfield, Y. Li, and P. J. Moriarty. A large-eddy simulation study of wake propagation and power production in an array of tidal-current turbines. *Philos. Trans. A. Math. Phys. Eng. Sci.*, 371(1985):20120421, 2013. ISSN 1364-503X. doi: 10.1098/rsta.2012.0421.

A. Copping, L. Hanna, J. Whiting, S. Geerlofs, M. Grear, K. Blake, A. Coffey, M. Massua, J. Brown-Saracino, and H. Battey. Environmental effects of marine energy development around the world annex IV final report. Technical Report January, 2013.

T. C. Corke and F. O. Thomas. Dynamic Stall in Pitching Airfoils : Aerodynamic Damping and Compressibility Effects. *Annu. Rev. Fluid Mech.*, 47:479–505, 2015. doi: 10.1146/annurev-fluid-010814-013632.

A. Cristallo and R. Verzicco. Combined Immersed Boundary/Large-Eddy-Simulations of Incompressible Three Dimensional Complex Flows. *Flow, Turbul. Combust.*, 77:3–26, 2006. ISSN 1386-6184. doi: 10.1007/s10494-006-9034-6.

L. Davidson. Large Eddy Simulations: How to evaluate resolution. *Int. J. Heat Fluid Flow*, 30(5):1016–1025, 2009. ISSN 0142727X. doi: 10.1016/j.ijheatfluidflow.2009.06.006.

L. Davidson. Fluid mechanics, turbulent flow and turbulence modeling. Technical report, Chalmers University of Technology, Sweden, 2015.

M. D. de Tullio and G. Pascazio. A moving-least-squares immersed boundary method for simulating the fluidstructure interaction of elastic bodies with ar-

bitrary thickness. *J. Comput. Phys.*, 325:201–225, 2016. ISSN 00219991. doi: 10.1016/j.jcp.2016.08.020.

N. G. Deen, M. V. S. Annaland, and J. a. M. Kuipers. Direct numerical simulation of complex multi-fluid flows using a combined front tracking and immersed boundary method. *Chem. Eng. Sci.*, 64(9):2186–2201, 2009. ISSN 00092509. doi: 10.1016/j.ces.2009.01.029.

DNV-GL. DNVGL-ST-0.164: Tidal turbines. Technical Report October, 2015.

M. Douziech, S. Hellweg, and F. Verones. Are Wave and Tidal Energy Plants New Green Technologies? *Environ. Sci. Technol.*, 50(14):7870–7878, jul 2016. ISSN 0013-936X. doi: 10.1021/acs.est.6b00156.

M. Edmunds, R. Malki, A. J. Williams, I. Masters, and T. N. Croft. Aspects of tidal stream turbine modelling in the natural environment using a coupled BEM-CFD model. *Int. J. Mar. Energy*, 7:20–42, 2014. ISSN 22141669. doi: 10.1016/j.ijome.2014.07.001.

Eel-energy. Accessed 2017-06-12. URL http://www.eel-energy.fr/.

A. El-Hamalawi. A 2D combined advancing front-Delaunay mesh generation scheme. *Finite Elem. Anal. Des.*, 40(9-10):967–989, 2004. ISSN 0168874X. doi: 10.1016/j.finel.2003.04.001.

M. Elkhoury, T. Kiwata, and E. Aoun. Experimental and numerical investigation of a three-dimensional vertical-axis wind turbine with variable-pitch. *J. Wind Eng. Ind. Aerodyn.*, 139:111–123, 2015. ISSN 01676105. doi: 10.1016/j.jweia.2015.01.004.

European Commision. Action needed to deliver on the potential of ocean energy in European seas and oceans by 2020 and beyond. Technical report, 2014a. URL http://ec.europa.eu/maritimeaffairs/policy/ocean{_}energy/documents/com{_}2014{_}8{_}en.pdf.

European Commision. Ocean Energy: Action needed to deliver on the potential of ocean energy by 2020 and beyond. Technical report, 2014b.

P. Evans, A. Mason-Jones, C. Wilson, C. Wooldridge, T. O'Doherty, and D. O'Doherty. Constraints on extractable power from energetic tidal straits. *Renew. Energy*, 81:707–722, sep 2015. ISSN 09601481. doi: 10.1016/j.renene.2015.03.085.

E. Fadlun, R. Verzicco, P. Orlandi, and J. Mohd-Yusof. Combined Immersed-Boundary Finite-Difference Methods for Three-Dimensional Complex Flow Simulations. *J. Comput. Phys.*, 161(1):35–60, 2000. ISSN 00219991. doi: 10.1006/jcph.2000.6484.

J. Favier, C. Li, L. Kamps, A. Revell, J. O'Connor, and C. Brücker. The PELskin projectpart I: fluidstructure interaction for a row of flexible flaps: a reference study in oscillating channel flow. *Meccanica*, pages 1–14, sep 2016. ISSN 0025-6455. doi: 10.1007/s11012-016-0521-0.

M. Felli, R. Camussi, and F. Di Felice. Mechanisms of evolution of the propeller wake in the transition and far fields. *J. Fluid Mech.*, 682:5–53, 2011. ISSN 0022-1120. doi: 10.1017/jfm.2011.150.

E. Ferrer and R. H. Willden. Bladewake interactions in cross-flow turbines. *Int. J. Mar. Energy*, 11:71–83, 2015. ISSN 22141669. doi: 10.1016/j.ijome.2015.06.001.

A. J. Fiedler and S. Tullis. Blade Offset and Pitch Effects on a High Solidity Vertical Axis Wind Turbine. *Wind Eng.*, 33(3):237–246, 2009. ISSN 0309-524X. doi: 10.1260/030952409789140955.

P. L. Fraenkel. Power from marine currents. *Proc. I MECH E Part A J. Power Energy*, 216:1–14, 2002. ISSN 00000000. doi: 10.1243/095765002760024791.

B. Fraga and T. Stoesser. Influence of bubble size, diffuser width, and flow rate on the integral behavior of bubble plumes. *J. Geophys. Res. Ocean.*, 121(6):3887–3904, 2016. ISSN 21699275. doi: 10.1002/2015JC011381.

B. Fraga, T. Stoesser, C. C. Lai, and S. A. Socolofsky. A LES-based EulerianLagrangian approach to predict the dynamics of bubble plumes. *Ocean Model.*, 97:27–36, 2016. ISSN 14635003. doi: 10.1016/j.ocemod.2015.11.005.

J. Fröhlich, C. P. Mellen, W. Rodi, L. Temmerman, and M. a. Leschziner. Highly resolved large-eddy simulation of separated flow in a channel with streamwise periodic constrictions. *J. Fluid Mech.*, 526:19–66, 2005. ISSN 0022-1120. doi: 10.1017/S0022112004002812.

C. Frost, C. Morris, A. Mason-Jones, D. O'Doherty, and T. O'Doherty. The effect of tidal flow directionality on tidal turbine performance characteristics. *Renew. Energy*, 78:609–620, 2015. ISSN 09601481. doi: 10.1016/j.renene.2015.01.053.

M. C. Galbraith, J. A. Benek, P. D. Orkwis, and M. G. Turner. A Discontinuous Galerkin Chimera scheme. *Comput. Fluids*, 98:27–53, 2014. ISSN 00457930. doi: 10.1016/j.compfluid.2014.03.014.

K. Gharali and D. A. Johnson. Dynamic stall simulation of a pitching airfoil under unsteady freestream velocity. *J. Fluids Struct.*, 42:228–244, 2013. ISSN 08899746. doi: 10.1016/j.jfluidstructs.2013.05.005.

D. G. E. Grigoriadis, E. Balaras, and A. A. Dimas. Large-eddy simulations of unidirectional water flow over dunes. *J. Geophys. Res. Earth Surf.*, 114(2): 1–19, 2009. ISSN 21699011. doi: 10.1029/2008JF001014.

W. Gropp, E. Lusk, and A. Skjellum. *Using MPI: portable parallel programming with the message-passing interface*. MIT Press Sci- entific And Engineering Computation Series, Cambridge, MA, USA, 1994. ISBN 9780262527392.

X. Guo, M. Lange, G. Gorman, L. Mitchell, and M. Weiland. Developing a scalable hybrid MPI/OpenMP unstructured finite element model. *Comput. Fluids*, 110:227–234, 2015. ISSN 00457930. doi: 10.1016/j.compfluid.2014.09.007.

S. H. Han, J. S. Park, K. S. Lee, W. S. Park, and J. H. Yi. Evaluation of vertical axis turbine characteristics for tidal current power plant based on in situ experiment. *Ocean Eng.*, 65:83–89, 2013. ISSN 00298018. doi: 10.1016/j.oceaneng.2013.03.005.

Z. Han, D. Zhou, T. He, J. Tu, C. Li, K. C. S. Kwok, and C. Fang. Flow-induced vibrations of four circular cylinders with square arrangement at low

Reynolds numbers. *Ocean Eng.*, 96:21–33, 2015. ISSN 00298018. doi: 10.1016/j.oceaneng.2014.12.002.

P. W. Harper and S. R. Hallett. Advanced numerical modelling techniques for the structural design of composite tidal turbine blades. *Ocean Eng.*, 96:272–283, 2015. ISSN 00298018. doi: 10.1016/j.oceaneng.2014.12.025.

M. Harrold, P. Bromley, P. Clelland, and D. Broudic. Demonstrating a tidal turbine control strategy at laboratory scale. In *ASME 2016 35th Int. Conf. Ocean. Offshore Arct. Eng.*, Busan, South Korea, 2016.

Y. He and C. H. Q. Ding. MPI and OpenMP Paradigms on Cluster of SMP Architectures: The Vacancy Tracking Algorithm for Multi-Dimensional Array Transposition. In *ACM/IEEE SC 2002 Conf.*, 2002. ISBN 0-7695-1524-X. doi: 10.1109/SC.2002.10065.

R. Howell, N. Qin, J. Edwards, and N. Durrani. Wind tunnel and numerical study of a small vertical axis wind turbine. *Renew. Energy*, 35(2):412–422, 2010. ISSN 09601481. doi: 10.1016/j.renene.2009.07.025.

J. Hunt, A. A. Wray, and P. Moin. Eddies, streams, and convergence zones in turbulent flows. Technical report, Stanford University, 1988.

G. Iaccarino. *Immersed boundary technique for turbulent flows with industrial applications*. Phd thesis, Politenico di Bari, 2004.

A. Iida, K. Kato, and A. Mizuno. Numerical simulation of unsteady flow and aerodynamic performance of vertical axis wind turbines with LES. In *16th Australas. Fluid Mech. Conf.*, pages 1295–1298, Australia, 2007. ISBN 1864998946.

Institute Electric Power Research. Environmental Effects of Hydrokinetic Turbines on Fish. Technical report, Electric Power Research Institute, 2012.

M. Islam, D. S. K. Ting, and A. Fartaj. Aerodynamic models for Darrieus-type straight-bladed vertical axis wind turbines. *Renew. Sustain. Energy Rev.*, 12 (4):1087–1109, 2008. ISSN 13640321. doi: 10.1016/j.rser.2006.10.023.

N. Jarrin, S. Benhamadouche, D. Laurence, and R. Prosser. A synthetic-eddy-method for generating inflow conditions for large-eddy simulations. *Int. J. Heat Fluid Flow*, 27(4):585–593, 2006. ISSN 0142727X. doi: 10.1016/j.ijheatfluidflow.2006.02.006.

J. Jeong and F. Hussain. On the identification of a vortex. *J. Fluid Mech.*, 285 (0):69–94, 1995. ISSN 0022-1120. doi: 10.1017/S0022112095000462.

H. Ji, F. S. Lien, and F. Zhang. A GPU-accelerated adaptive mesh refinement for immersed boundary methods. *Comput. Fluids*, 118:131–147, 2015. ISSN 00457930. doi: 10.1016/j.compfluid.2015.06.011.

H. Jin, D. Jespersen, P. Mehrotra, R. Biswas, L. Huang, and B. Chapman. High performance computing using MPI and OpenMP on multi-core parallel systems. *Parallel Comput.*, 37(9):562–575, 2011. ISSN 01678191. doi: 10.1016/j.parco.2011.02.002.

L. Jones, R. Sandberg, and N. Sandham. Direct numerical simulations of forced and unforced separation bubbles on an airfoil at incidence. *J. Fluid Mech.*, 602: 175–207, 2008. ISSN 0022-1120. doi: 10.1017/S0022112008000864.

S. Kang, A. Lightbody, C. Hill, and F. Sotiropoulos. High-resolution numerical simulation of turbulence in natural waterways. *Adv. Water Resour.*, 34(1): 98–113, 2011. ISSN 03091708. doi: 10.1016/j.advwatres.2010.09.018.

S. Kang, I. Borazjani, J. A. Colby, and F. Sotiropoulos. Numerical simulation of 3D flow past a real-life marine hydrokinetic turbine. *Adv. Water Resour.*, 39: 33–43, 2012. ISSN 03091708. doi: 10.1016/j.advwatres.2011.12.012.

S. Kang, X. L. Yang, and F. Sotiropoulos. On the onset of wake meandering for an axial flow turbine in a turbulent open channel flow. *J. Fluid Mech.*, 744: 376–403, 2014. ISSN 0022-1120. doi: 10.1017/jfm.2014.82.

M. C. Kara, T. Stoesser, and R. McSherry. Calculation of fluidstructure interaction: methods, refinements, applications. *Proc. ICE - Eng. Comput. Mech.*, 168(2):59–78, 2015. ISSN 1755-0777. doi: 10.1680/eacm.15.00010.

M. Kear, B. Evans, R. Ellis, and S. Rolland. Computational Aerodynamic Optimisation of Vertical Axis Wind Turbine Blades. *Appl. Math. Model.*, 2015. ISSN 0307904X. doi: 10.1016/j.apm.2015.07.001.

M. Khan, G. Bhuyan, M. Iqbal, and J. Quaicoe. Hydrokinetic energy conversion systems and assessment of horizontal and vertical axis turbines for river and tidal applications: A technology status review. *Appl. Energy*, 86(10):1823–1835, 2009. ISSN 03062619. doi: 10.1016/j.apenergy.2009.02.017.

S. Kiho, M. Shiono, and K. Suzuki. The power generation from tidal currents by darrieus turbine. *Renew. Energy*, 9(1-4):1242–1245, 1996. ISSN 09601481. doi: 10.1016/0960-1481(96)88501-6.

J. Kim, D. Kim, and H. Choi. An immersed-boundary finite-volume method for simulations of flow in complex geometries. *J. Comput. Phys.*, 171(1):132–150, 2001. ISSN 0021-9991. doi: 10.1006/jcph.2001.6778.

Y. Kim and Z.-t. Xie. Modelling the effect of freestream turbulence on dynamic stall of wind turbine blades. *Comput. Fluids*, 129:53–66, 2016. ISSN 0045-7930. doi: 10.1016/j.compfluid.2016.02.004.

A. Laneville and P. Vittecoq. Dynamic Stall: The Case of the Vertical Axis Wind Turbine. *J. Sol. Energy Eng.*, 108(2):140, 1986. ISSN 01996231. doi: 10.1115/1.3268081.

D. V. Le, J. White, J. Peraire, K. M. Lim, and B. C. Khoo. An implicit immersed boundary method for three-dimensional fluid-membrane interactions. *J. Comput. Phys.*, 228(22):8427–8445, 2009. ISSN 00219991. doi: 10.1016/j.jcp.2009.08.018.

J. Lee, J. Kim, H. Choi, and K. S. Yang. Sources of spurious force oscillations from an immersed boundary method for moving-body problems. *J. Comput. Phys.*, 230(7):2677–2695, 2011. ISSN 00219991. doi: 10.1016/j.jcp.2011.01.004.

T. Lee and P. Gerontakos. Investigation of flow over an oscillating airfoil. *J. Fluid Mech.*, 512:313–341, 2004. ISSN 0022-1120. doi: 10.1017/S0022112004009851.

T. Lee and Y. Su. Surface Pressures Developed on an Airfoil Undergoing Heaving and Pitching Motion. *J. Fluids Eng.*, 137(5):1–11, 2015. ISSN 0098-2202. doi: 10.1115/1.4029443.

J. G. Leishman. Challenges in Modeling the Unsteady Aerodynamics of Wind Turbines. *Wind Energy*, 5:85–132, 2002. doi: 10.1115/we.62.

A. Leonard. Energy Cascade in Large-Eddy Simulations of Turbulent Fluid Flows. *Adv. Geophys.*, 18A:237–248, 1975. doi: 10.1016/S0065-2687(08)60464-1.

C. Li, S. Zhu, Y.-l. Xu, and Y. Xiao. 2.5D large eddy simulation of vertical axis wind turbine in consideration of high angle of attack flow. *Renew. Energy*, 51: 317–330, 2013. ISSN 09601481. doi: 10.1016/j.renene.2012.09.011.

R. Y. Li, C. M. Xie, W. X. Huang, and C. X. Xu. An efficient immersed boundary projection method for flow over complex/moving boundaries. *Comput. Fluids*, 140:122–135, 2016a. ISSN 00457930. doi: 10.1016/j.compfluid.2016.09.017.

W. Li, H. Zhou, H. Liu, Y. Lin, and Q. Xu. Review on the blade design technologies of tidal current turbine. *Renew. Sustain. Energy Rev.*, 63:414–422, 2016b. ISSN 18790690. doi: 10.1016/j.rser.2016.05.017.

Y. Li, K. J. Paik, T. Xing, and P. M. Carrica. Dynamic overset CFD simulations of wind turbine aerodynamics. *Renew. Energy*, 37(1):285–298, 2012. ISSN 09601481. doi: 10.1016/j.renene.2011.06.029.

T. P. Lloyd, S. R. Turnock, and V. F. Humphrey. Assessing the influence of inflow turbulence on noise and performance of a tidal turbine using large eddy simulations. *Renew. Energy*, 71:742–754, 2014. ISSN 09601481. doi: 10.1016/j.renene.2014.06.011.

T. S. Lund, X. Wu, and K. D. Squires. On the Generation of Turbulent Inflow Conditions for Boundary Layer Simulations. *J. Comput. Phys.*, 140:233–258, 1998. ISSN 00219991. doi: 10.1006/jcph.1998.5882.

D. Magagna and A. Uihlein. Ocean energy development in Europe: Current status and future perspectives. *Int. J. Mar. Energy*, 11:84–104, 2015. ISSN 22141669. doi: 10.1016/j.ijome.2015.05.001.

T. Maître, E. Amet, and C. Pellone. Modeling of the flow in a Darrieus water turbine: Wall grid refinement analysis and comparison with experiments. *Renew. Energy*, 51:497–512, 2013. ISSN 09601481. doi: 10.1016/j.renene.2012.09.030.

P. Marsh, D. Ranmuthugala, I. Penesis, and G. Thomas. Numerical investigation of the influence of blade helicity on the performance characteristics of vertical axis tidal turbines. *Renew. Energy*, 81:926–935, 2015. ISSN 09601481. doi: 10.1016/j.renene.2015.03.083.

G. Martinat, M. Braza, Y. Hoarau, and G. Harran. Turbulence modelling of the flow past a pitching NACA0012 airfoil at 10ˆ5 and 10ˆ6 Reynolds numbers. *J. Fluids Struct.*, 24(8):1294–1303, 2008. ISSN 08899746. doi: 10.1016/j.jfluidstructs.2008.08.002.

A. Mason-Jones. *Performance assessment of a horizontal axis tidal turbine in a high velocity shear environment*. Phd thesis, Cardiff University, 2010.

A. Mason-Jones, D. M. O'Doherty, C. E. Morris, T. O'Doherty, C. B. Byrne, P. W. Prickett, R. I. Grosvenor, I. Owen, S. Tedds, and R. J. Poole. Non-dimensional scaling of tidal stream turbines. *Energy*, 44:820–829, 2012. ISSN 03605442. doi: 10.1016/j.energy.2012.05.010.

A. Mason-Jones, D. O'Doherty, C. Morris, and T. O'Doherty. Influence of a velocity profile & support structure on tidal stream turbine performance. *Renew. Energy*, 52:23–30, 2013. ISSN 09601481. doi: 10.1016/j.renene.2012.10.022.

I. Masters, R. Malki, A. J. Williams, and T. N. Croft. The influence of flow acceleration on tidal stream turbine wake dynamics: A numerical study using a coupled BEMCFD model. *Appl. Math. Model.*, 37(16-17):7905–7918, 2013. ISSN 0307904X. doi: 10.1016/j.apm.2013.06.004.

K. W. McAlister and L. W. Carr. Water Tunnel Visualizations of Dynamic Stall. *J. Fluids Eng.*, 101(3):376–380, 1979. ISSN 00982202. doi: 10.1115/1.3448981.

G. McCann. Tidal current turbine fatigue loading sensitivity to waves and turbulence a parametric study. In *Proc. 7th Eur. Wave Tidal Energy*, Porto, Portugal, 2007.

W. McCroskey, K. McAlister, L. W. Carr, S. Pucci, O. Lambert, and R. Indergrand. Dynamic stall on advanced airfoil sections. *J. Am. Helicopter Soc.*, 26: 40–50, 1981.

W. J. McCroskey, L. W. Carr, and K. W. McAlister. Dynamic Stall Experiments on Oscillating Airfoils. *AIAA J.*, 14(1):57–63, jan 1976. ISSN 0001-1452. doi: 10.2514/3.61332.

K. McLaren. *Unsteady loading of high solidity vertical axis wind turbines*. Phd thesis, McMaster University, 2011.

J. McNaughton, F. Billard, and A. Revell. Turbulence modelling of low Reynolds number flow effects around a vertical axis turbine at a range of tip-speed ratios. *J. Fluids Struct.*, 47:124–138, 2014. ISSN 08899746. doi: 10.1016/j.jfluidstructs.2013.12.014.

G. Mercier, C. Pellone, and T. Maitre. Experimental characterization of the near-wake of a cross flow water turbine with LDV measurements. In *17th Int. Symp. Appl. Laser Tech. to Fluid Mech.*, pages 1–8, 2014.

I. A. Milne, A. H. Day, R. N. Sharma, and R. G. J. Flay. Blade loads on tidal turbines in planar oscillatory flow. *Ocean Eng.*, 60:163–174, 2013. ISSN 00298018. doi: 10.1016/j.oceaneng.2012.12.027.

I. A. Milne, A. H. Day, R. N. Sharma, and R. G. J. Flay. Blade loading on tidal turbines for uniform unsteady flow. *Renew. Energy*, 77:338–350, 2015. ISSN 09601481. doi: 10.1016/j.renene.2014.12.028.

I. A. Milne, A. H. Day, R. N. Sharma, and R. G. J. Flay. The characterisation of the hydrodynamic loads on tidal turbines due to turbulence. *Renew. Sustain. Energy Rev.*, 56:851–864, 2016. ISSN 18790690. doi: 10.1016/j.rser.2015.11.095.

Minesto Limited. Accessed 2017-06-12. URL minesto.com.

P. D. Mininni, D. Rosenberg, R. Reddy, and A. Pouquet. A hybrid MPIOpenMP scheme for scalable parallel pseudospectral computations for fluid turbulence.

Parallel Comput., 37(6-7):316–326, 2011. ISSN 01678191. doi: 10.1016/j.parco.2011.05.004.

K. Mulleners and M. Raffel. The onset of dynamic stall revisited. *Exp. Fluids*, 52(3):779–793, 2012. ISSN 07234864. doi: 10.1007/s00348-011-1118-y.

P. Mycek, B. Gaurier, G. Germain, G. Pinon, and E. Rivoalen. Experimental study of the turbulence intensity effects on marine current turbines behaviour. Part II: Two interacting turbines. *Renew. Energy*, 68:876–892, 2014a. ISSN 09601481. doi: 10.1016/j.renene.2013.12.048.

P. Mycek, B. Gaurier, G. Germain, G. Pinon, and E. Rivoalen. Experimental study of the turbulence intensity effects on marine current turbines behaviour. Part I: One single turbine. *Renew. Energy*, 66:729–746, 2014b. ISSN 09601481. doi: 10.1016/j.renene.2013.12.036.

L. E. Myers, K. Shah, and P. W. Galloway. Design, commissioning and performance of a device to vary the turbulence in a recirculating flume. In *10th Eur. Wave Tidal Energy Conf.*, Aalborg, Denmark, 2013.

T. Nakata and H. Liu. A fluid-structure interaction model of insect flight with flexible wings. *J. Comput. Phys.*, 231(4):1822–1847, 2012. ISSN 00219991. doi: 10.1016/j.jcp.2011.11.005.

R. F. Nicholls-Lee, S. R. Turnock, and S. W. Boyd. Application of bend-twist coupled blades for horizontal axis tidal turbines. *Renew. Energy*, 50:541–550, 2013. ISSN 09601481. doi: 10.1016/j.renene.2012.06.043.

F. Nicoud and F. Ducros. Subgrid-scale stress modelling based on the square of the velocity gradient tensor. *Flow, Turbul. Combust.*, 62(3):183–200, 1999. ISSN 13866184. doi: 10.1023/A:1009995426001.

M. Omidyeganeh and U. Piomelli. Large-eddy simulation of two-dimensional dunes in a steady, unidirectional flow. *J. Turbul.*, 12(42):1–31, jan 2011. ISSN 1468-5248. doi: 10.1080/14685248.2011.609820.

E. Otero. *Synthetic Inflow Condition for Large Eddy Simulation (Synthetic Eddy Method)*. Msc, KTH, 2009.

P. Ouro, L. Cea, L. Ramírez, and X. Nogueira. An immersed boundary method for unstructured meshes in depth averaged shallow water models. *Int. J. Numer. Methods Fluids*, 81(11):672–688, 2016. ISSN 02712091. doi: 10.1002/fld.4201.

S. Parkinson and W. Collier. Model validation of hydrodynamic loads and performance of a full-scale tidal turbine using Tidal Bladed. *Int. J. Mar. Energy*, 16:279–297, 2016. ISSN 22141669. doi: 10.1016/j.ijome.2016.08.001.

C. Peskin. Flow patterns around heart valves: A numerical method. *J. Comput. Phys.*, 10(2):252–271, 1972. ISSN 00219991. doi: 10.1016/0021-9991(72)90065-4.

C. S. Peskin. The immersed boundary method. *Acta Numer.*, 11:479–517, 2002. ISSN 0962-4929. doi: 10.1017/S0962492902000077.

A. Pinelli, I. Z. Naqavi, U. Piomelli, and J. Favier. Immersed-boundary methods for general finite-difference and finite-volume Navier-Stokes solvers. *J. Comput. Phys.*, 229(24):9073–9091, 2010. ISSN 00219991. doi: 10.1016/j.jcp.2010.08.021.

A. Pinelli, M. Omidyeganeh, C. Brücker, A. Revell, A. Sarkar, and E. Alinovi. The PELskin project: part IVcontrol of bluff body wakes using hairy filaments. *Meccanica*, 52(7):1503–1514, may 2017. ISSN 0025-6455. doi: 10.1007/s11012-016-0513-0.

R. Poletto, T. Craft, and A. Revell. A New Divergence Free Synthetic Eddy Method for the Reproduction of Inlet Flow Conditions for LES. *Flow, Turbul. Combust.*, 91(3):519–539, 2013. ISSN 1386-6184. doi: 10.1007/s10494-013-9488-2.

A. Posa, C. M. Parker, M. C. Leftwich, and E. Balaras. Wake structure of a single vertical axis wind turbine. *Int. J. Heat Fluid Flow*, 61:75–84, oct 2016. ISSN 0142727X. doi: 10.1016/j.ijheatfluidflow.2016.02.002.

L. Priegue and T. Stoesser. The influence of blade roughness on the performance of a vertical axis tidal turbine. *Int. J. Mar. Energy*, 17:136–146, apr 2017. ISSN 22141669. doi: 10.1016/j.ijome.2017.01.009.

R. Rabenseifner, G. Hager, G. Jost, and R. Keller. Hybrid MPI and OpenMP Parallel Programming MPI + OpenMP and other models on clusters of SMP nodes. In *17th Euromicro Int. Conf. Parallel, Distrib. Networkbased Process.*, pages 427–436. IEEE, 2009. doi: 10.1109/PDP.2009.43.

L. Ramírez. *High-order finite volume methods based on Moving Least Squares for Computational Fluid Dynamics. Application to all-speed and incompressible flows on unstructured grids.* PhD thesis, University of A coruna, 2015.

L. Ramírez, C. Foulquié, X. Nogueira, S. Khelladi, J.-C. Chassaing, and I. Colominas. New high-resolution-preserving sliding mesh techniques for higher-order finite volume schemes. *Comput. Fluids*, 118:114–130, 2015. ISSN 00457930. doi: 10.1016/j.compfluid.2015.06.008.

L. Ramírez, X. Nogueira, P. Ouro, F. Navarrina, S. Khelladi, and I. Colominas. A Higher-Order Chimera Method for Finite Volume Schemes. *Arch. Comput. Methods Eng.*, feb 2017. ISSN 1134-3060. doi: 10.1007/s11831-017-9213-8.

RenewableUK. UK Marine Energy Database (UKMED). Accessed 2017-06-12. URL http://www.renewableuk.com/page/UKMED2.

A. M. Roa, V. Aumelas, T. Maître, and C. Pellone. Numerical and experimental analysis of a darrieus-type cross flow water turbine in bare and shrouded configurations. In *25th IAHR Symp. Hydraul. Mach. Syst.*, volume 12, page 012113. IOP Publishing, 2010. ISBN 9786131557002. doi: 10.1088/1755-1315/12/1/012113.

W. Rodi, G. Constantinescu, and T. Stoesser. *Large-Eddy Simulation in Hydraulics.* CRC Press, 2013. ISBN 978-0-203-79757-0.

A. M. Roma, C. S. Peskin, and M. J. Berger. An adaptive version of the immersed boundary method. *J. Comput. Phys.*, 153(2):509–534, 1999. ISSN 0021-9991. doi: 10.1006/jcph.1999.6293.

M. E. Rosti, M. Omidyeganeh, and A. Pinelli. Direct numerical simulation of the flow around an aerofoil in ramp-up motion. *Phys. Fluids*, 28(2):025106, 2016. ISSN 1070-6631. doi: 10.1063/1.4941529.

E. Saiki and S. Biringen. Numerical Simulation of a Cylinder in Uniform Flow: Application of a Virtual Boundary Method. *J. Comput. Phys.*, 123(2):450–465, 1996. ISSN 00219991. doi: 10.1006/jcph.1996.0036.

R. D. Sandberg and L. Jones. Direct numerical simulations of low Reynolds number flow over airfoils with trailing-edge serrations. *J. Sound Vib.*, 330(16): 3818–3831, 2011. ISSN 0022460X. doi: 10.1016/j.jsv.2011.02.005.

H. Sarlak, C. Meneveau, and J. Sørensen. Role of subgrid-scale modeling in large eddy simulation of wind turbine wake interactions. *Renew. Energy*, 77:386–399, 2015. ISSN 09601481. doi: 10.1016/j.renene.2014.12.036.

J. Sarrate, A. Huerta, and J. Donea. Arbitrary Lagrangian-Eulerian formulation for fluid-rigid body interaction. *Comput. Methods Appl. Mech. Engrg.*, 190: 3171–3188, 2001.

H. Shan, L. Jiang, and C. Liu. Direct numerical simulation of flow separation around a NACA 0012 airfoil. *Comput. Fluids*, 34(9):1096–1114, 2005. ISSN 00457930. doi: 10.1016/j.compfluid.2004.09.003.

L. Shi, M. Rampp, B. Hof, and M. Avila. A hybrid MPI-OpenMP parallel implementation for pseudospectral simulations with application to TaylorCouette flow. *Comput. Fluids*, 106:1–11, 2015. ISSN 00457930. doi: 10.1016/j.compfluid.2014.09.021.

S. J. Shin, W.-X. Huang, and H. J. Sung. Assessment of regularized delta functions and feedback forcing schemes for an immersed boundary method. *Int. J. Numer. Methods Fluids*, 58:263–286, 2008. doi: 10.1002/fld.1706.

M. Shives and C. Crawford. Tuned actuator disk approach for predicting tidal turbine performance with wake interaction. *Int. J. Mar. Energy*, 17:30–56, 2017. ISSN 22141669. doi: 10.1016/j.ijome.2016.11.001.

C. Simão Ferreira, G. Van Kuik, G. Van Bussel, and F. Scarano. Visualization by PIV of dynamic stall on a vertical axis wind turbine. *Exp. Fluids*, 46(1): 97–108, 2009. ISSN 07234864. doi: 10.1007/s00348-008-0543-z.

J. Smagorinsky. General circulation experiments with the primitive equations. *Mon. Weather Rev.*, 91(3):99–164, mar 1963. ISSN 0027-0644. doi: 10.1175/1520-0493(1963)091⟨0099:GCEWTP⟩2.3.CO;2.

L. Smith and M. Bull. Development of mixed mode MPI/OpenMP applications. *Sci. Program.*, 9:83–98, 2001.

J. N. Sorensen and W. Z. Shen. Numerical Modeling of Wind Turbine Wakes. *J. Fluids Eng.*, 124:393–399, 2002. ISSN 00982202. doi: 10.1115/1.1471361.

F. Sotiropoulos. Hydraulics in the era of exponentially growing computing power. *J. Hydraul. Res.*, 53(5):547–560, 2015. ISSN 0022-1686. doi: 10.1080/00221686.2015.1119210.

F. Sotiropoulos and X. Yang. Immersed boundary methods for simulating fluid-structure interaction. *Prog. Aerosp. Sci.*, 65:1–21, feb 2014. ISSN 03760421. doi: 10.1016/j.paerosci.2013.09.003.

J. Steger, F. Dougherty, and J. Benek. A Chimera Grid Scheme. In *ASME Mini-Symposium Adv. Grid Gener.*, Houston (USA), 1982.

T. Stoesser. Large-eddy simulation in hydraulics: Quo Vadis? *J. Hydraul. Res.*, 52(4):441–452, 2014. ISSN 0022-1686. doi: 10.1080/00221686.2014.944227.

T. Stoesser, C. Braun, M. García-Villalba, and W. Rodi. Turbulence Structures in Flow over Two-Dimensional Dunes. *J. Hydraul. Eng.*, 134(1):42–55, 2008. ISSN 0733-9429. doi: 10.1061/(ASCE)0733-9429(2008)134:1(42).

K. Taira and T. Colonius. The immersed boundary method: A projection approach. *J. Comput. Phys.*, 225(2):2118–2137, 2007. ISSN 00219991. doi: 10.1016/j.jcp.2007.03.005.

Y. Takamatsu, A. Furukawa, K. Okuma, and K. Takenouchi. Experimental Studies on a Preferable Blade Profile for High Efficiency and the Blade Characteristics of Darrieus-type Cross-flow Water Turbines. *Japan Soc. Mech. Eng.*, 34 (2):149–156, 1991.

S. C. Tatum, C. H. Frost, M. Allmark, D. M. O'Doherty, A. Mason-Jones, P. W. Prickett, R. I. Grosvenor, C. B. Byrne, and T. O'Doherty. Wave-current interaction effects on tidal stream turbine performance and loading characteristics. *Int. J. Mar. Energy*, 14:161–179, 2016. ISSN 22141669. doi: 10.1016/j.ijome.2015.09.002.

W. B. Tay, B. W. van Oudheusden, and H. Bijl. Validation of immersed boundary method for the numerical simulation of flapping wing flight. *Comput. Fluids*, 115:226–242, 2015. ISSN 00457930. doi: 10.1016/j.compfluid.2015.04.009.

S. Tedds, R. Poole, I. Owen, G. Najafian, S. Bode, A. Mason-Jones, C. Morris, T. O'Doherty, and D. O'Doherty. Experimental investigation of horizontal axis tidal stream turbines. In *9th Eur. Wave Tidal Energy Conf.*, Southampton, UK, 2011.

L. Temmerman, M. A. Leschziner, C. P. Mellen, and J. Fröhlich. Investigation of wall-function approximations and subgrid-scale models in large eddy simulation of separated flow in a channel with streamwise periodic constrictions. *Int. J. Heat Fluid Flow*, 24(2):157–180, 2003. ISSN 0142727X. doi: 10.1016/S0142-727X(02)00222-9.

F.-B. Tian, H. Dai, H. Luo, J. F. Doyle, and B. Rousseau. Fluid structure interaction involving large deformations : 3D simulations and applications to biological systems. *J. Comput. Phys.*, 258:451–469, 2014. ISSN 0021-9991. doi: 10.1016/j.jcp.2013.10.047.

Tidalenergytoday.com. Accessed 2017-06-12. URL tidalenergytodal.com.

B. Tutkun and F. O. Edis. An implementation of the direct-forcing immersed boundary method using GPU power. *Eng. Appl. Comput. Fluid Mech.*, 11(1): 15–29, 2017. ISSN 1997003X. doi: 10.1080/19942060.2016.1236749.

M. Uhlmann. Simulation of Particulate Flows on Multi-Processor Machines with Distributed Memory. Technical Report May, Dept. Combustibles Fosiles, CIEMAT, Madrid. Spain, 2003.

M. Uhlmann. An immersed boundary method with direct forcing for the simulation of particulate flows. *J. Comput. Phys.*, 209(2):448–476, 2005. ISSN 00219991. doi: 10.1016/j.jcp.2005.03.017.

M. Vanella and E. Balaras. A moving-least-squares reconstruction for embedded-boundary formulations. *J. Comput. Phys.*, 228(18):6617–6628, 2009. ISSN 00219991. doi: 10.1016/j.jcp.2009.06.003.

A. Vazquez and G. Iglesias. A holistic method for selecting tidal stream energy hotspots under technical, economic and functional constraints. *Energy Convers. Manag.*, 117:420–430, 2016. ISSN 01968904. doi: 10.1016/j.enconman.2016.03.012.

R. Vennell, S. W. Funke, S. Draper, C. Stevens, and T. Divett. Designing large arrays of tidal turbines: A synthesis and review. *Renew. Sustain. Energy Rev.*, 41:454–472, 2015. ISSN 13640321. doi: 10.1016/j.rser.2014.08.022.

H. Versteeg and W. Malalasekera. *An introduction to Computational Fluid Dynamics*. Pearson Prentice Hall, second edi edition, 2007.

M. Visbal, T. O. Yilmaz, and D. Rockwell. Three-dimensional vortex formation on a heaving low-aspect-ratio wing: Computations and experiments. *J. Fluids Struct.*, 38:58–76, 2013. ISSN 08899746. doi: 10.1016/j.jfluidstructs.2012.12.005.

M. R. Visbal. Numerical Investigation of Deep Dynamic Stall of a Plunging Airfoil. *AIAA J.*, 49(10):2152–2170, 2011. ISSN 0001-1452. doi: 10.2514/1.J050892.

L. Vybulkova, M. Vezza, and R. Brown. Simulating the wake downstream of a horizontal axis tidal turbine using a modified vorticity transport model. *IEEE J. Ocean. Eng.*, 41(2):296–301, 2016. ISSN 03649059. doi: 10.1109/JOE.2015.2429231.

D. Walker. Standards for message passing in a distributed memory environment. Technical report, Oak Ridge National Laboratory, 1992.

S. Wang, D. B. Ingham, L. Ma, M. Pourkashanian, and Z. Tao. Numerical investigations on dynamic stall of low Reynolds number flow around oscillating airfoils. *Comput. Fluids*, 39(9):1529–1541, 2010. ISSN 00457930. doi: 10.1016/j.compfluid.2010.05.004.

S. Wang, D. B. Ingham, L. Ma, M. Pourkashanian, and Z. Tao. Turbulence modeling of deep dynamic stall at relatively low Reynolds number. *J. Fluids Struct.*, 33:191–209, 2012. ISSN 08899746. doi: 10.1016/j.jfluidstructs.2012.04.011.

S. Wang, G. He, and X. Zhang. Parallel computing strategy for a flow solver based on immersed boundary method and discrete stream-function formulation. *Comput. Fluids*, 88(8):210–224, 2013. ISSN 00457930. doi: 10.1016/j.compfluid.2013.09.001.

Z. Wang, J. Fan, and K. Luo. Combined multi-direct forcing and immersed boundary method for simulating flows with moving particles. *Int. J. Multiph. Flow*, 34(3):283–302, 2008a. ISSN 03019322. doi: 10.1016/j.ijmultiphaseflow.2007.10.004.

Z. Wang, J. Fan, and K. Luo. Parallel computing strategy for the simulation of particulate flows with immersed boundary method. *Sci. China, Ser. E Technol. Sci.*, 51(8):1169–1176, 2008b. ISSN 10069321. doi: 10.1007/s11431-008-0144-3.

S. Waters and G. Aggidis. Tidal range technologies and state of the art in review. *Renew. Sustain. Energy Rev.*, 59:514–529, 2016. ISSN 18790690. doi: 10.1016/j.rser.2015.12.347.

S. Worasinchai, G. Ingram, and R. Dominy. The Physics of H-Darrieus Turbine Starting Behaviour. *J. Eng. Gas Turbines Power*, 138(062605):1–11, 2016. ISSN 15288919. doi: 10.1115/1.4031870.

Z. Xie, B. Lin, R. Falconer, and T. Maddux. Large-eddy simulation of turbulent open-channel flow over three-dimensional dunes. *J. Hydraul. Res.*, 51(5):494–505, 2013. ISSN 00221686. doi: 10.1080/00221686.2013.835287.

S. Yakubov, B. Cankurt, M. Abdel-Maksoud, and T. Rung. Hybrid MPI/OpenMP parallelization of an euler-lagrange approach to cavitation modelling. *Comput. Fluids*, 80(1):365–371, 2013. ISSN 00457930. doi: 10.1016/j.compfluid.2012.01.020.

J. Yang and F. Stern. A simple and efficient direct forcing immersed boundary framework for fluid-structure interactions. *J. Comput. Phys.*, 231(15):5029–5061, 2012. ISSN 00219991. doi: 10.1016/j.jcp.2012.04.012.

J. Yang and F. Stern. Robust and Efficient Setup Procedure for Complex Triangulations in Immersed Boundary Simulations. *J. Fluids Eng.*, 135(10):101107–1–11, 2013. ISSN 0098-2202. doi: 10.1115/1.4024804.

X. Yang, X. Zhang, Z. Li, and G. He. A smoothing technique for discrete delta functions with application to immersed boundary method in moving boundary simulations. *J. Comput. Phys.*, 228(20):7821–7836, 2009. ISSN 00219991. doi: 10.1016/j.jcp.2009.07.023.

X. Yang, K. B. Howard, M. Guala, and F. Sotiropoulos. Effects of a three-dimensional hill on the wake characteristics of a model wind turbine. *Phys. Fluids*, 27(2), 2015. ISSN 10897666. doi: 10.1063/1.4907685.

X. Yang, J. Hong, M. Barone, and F. Sotiropoulos. Coherent dynamics in the rotor tip shear layer of utility-scale wind turbines. *J. Fluid Mech.*, 804:90–115, 2016. ISSN 0022-1120. doi: 10.1017/jfm.2016.503.

W. Yue, C.-L. Lin, and V. C. Patel. Large-Eddy Simulation of Turbulent Flow over a Fixed Two-Dimensional Dune. *J. Hydraul. Eng.*, 132(7):643–651, 2006. ISSN 0733-9429. doi: 10.1061/(ASCE)0733-9429(2006)132:7(643).

X. Zhang and J. U. Schluter. Numerical study of the influence of the Reynolds-number on the lift created by a leading edge vortex. *Phys. Fluids*, 24(6), 2012. ISSN 10706631. doi: 10.1063/1.4718322.

Y. Zhang, M. Burcea, and V. Cheng. An Adaptative OpenMP Loop Scheduler for Hyperthreaded SMPs. In *PDCS-2004 Int. Conf. Parallel Distrib. Comput. Syst.*, 2004.